Molecular Bistability in Transition Metal Complexes: Electric Field-Induced Switching and Surface Plasmon Resonance Detection.

Tarik Mahfoud, Azzedine Bousseksou, Gábor Molnár

THÈSE

En vue de l'obtention du

DOCTORAT DE L'UNIVERSITÉ DE TOULOUSE

Délivré par *l'Université Toulouse III - Paul Sabatier*
Discipline ou spécialité : *Physique et Nanophysique*

Présentée et soutenue par *Tarik MAHFOUD*
Le *06 Juillet 2011*

Titre : *Bistabilité moléculaire dans des complexes de métaux de transition : commutation par un champ électrique et détection optique par résonance des plasmons de surface.*

JURY
- Pr. Marc VERELST,Professeur à l'Université Paul Sabatier, Toulouse, Président
- Pr.Corine MATHONIERE, Professeur à l'université de Bordeaux 1, Bordeaux, Examinateur
-Dr. Gabor MOLNAR, Chargé de recherche au CNRS, Toulouse, Examinateur
- Dr. Azzedine BOUSSEKSOU, Directeur de recherche au CNRS, Toulouse, Examinateur
- Pr. Philippe DEMONT, Professeur à l'Université Paul Sabatier, Toulouse, Membre invité
*- Dr. Zouheir SEKKAT, Directeur de recherche à l'Institut d'Innovation et de Recherche (MAScIR),
Rabat, Maroc, Membre invité*

Ecole doctorale : *Sciences de la Matière*
Unité de recherche : *Laboratoire de chimie de coordination, UPR CNRS 8241*
Directeur(s) de Thèse : *Dr Azzedine BOUSSEKSOU / Dr Zouheir SEKKAT*
Rapporteurs : *Pr. Jorge LINARES, Professeur à l'Université de Versailles, Versailles
Pr. Anne BLEUZEN, Professeur à l'Université Paris-sud 11, Orsay*

Pour finir, je remercie l'ensemble de mes proches et en particulier mon frère Nabil, mes sœur Imane et la petite Aya et enfin mes parents pour leur soutien et leurs encouragements.

Contents

General introduction

Manufacturing nanomaterials with new functional capabilities appears today as a promising way to develop sustainable and cost-efficient processes and specific applications. Especially, the high versatility and possibility to tune properties of switchable molecular materials such as **spin crossover and valence-tautomeric complexes**, in which a switching between the two electronic states can be induced by various external perturbations (temperature, pressure, magnetic field, light, etc…), [Vols. 233-235, Topics in Current Chemistry series 2004] confers a promising market potential on these compounds in potential applications, such as memories, switching devices and sensors. The main advantage of using such molecular materials is that:

1) They have the possibility to show a transition at nanometer scales.
2) They involve a change of the electronic states, resulting in a very fast and sharp transition between these metastable states.
3) They provide a wide range of flexibility to design new materials.

The switching between the two electronic states implies important changes of crystal structure, bond lengths and that of the molecular volume. Therefore, the bistability is accompanied with a **spectacular change of various physical properties**. Beside the well-known magnetic, mechanical and colour changes, our group among others have shown that the spin state change is accompanied also by an **important variation in the dielectric constant** (ε) in a wide frequency range (kHz-THz-vis) and even hysteresis loops of ε have been observed around room temperature. [Bousseksou et al. J. Mater. Chem. 13, 2003, 2069; Ohkoshi et al. J. Mater. Chem. 15, 2005, 329, Loutete-Dangui et al. Phys. Rev. B 75, 2007, 184425.] Using this property, capacitance or photonic measurements can be used to "read" the state of the system.

Most work on spin crossover (SCO) complexes is performed on powder samples using temperature, pressure, light irradiation (at low temperatures) and intense magnetic field as stimuli for the occurrence of the spin transition. These triggers are usually not compatible with industrial needs. Moreover the typical methods devoted to investigate the SCO phenomenon become limited and inappropriate when one reaches the nanoscale size (thin

films). To overcome these limitations we propose the development of alternative methods. In this thesis, we have worked on these two important problems:

The first objective is to seek a **new trigger for switchable molecular compounds**, which is the **application of an external electric field**. To this aim we have identified a promising family of compounds – valence tautomeric complexes – in which the bistability is associated with an electron transfer between different metal ions. The second objective is to find an **appropriate investigation tool for nanometer sized spin crossover compounds**. To this aim we have selected **surface plasmon resonance spectroscopy**, which can sense the refractive index and thickness changes upon SCO in ultrathin films.

C**hapter I** of the thesis introduces briefly the reader to the rich properties of switchable molecular materials. The effects of different external stimuli (temperature, pressure, magnetic field, light irradiation, and chemical species), which can induce a transition between the two states and the tools used to investigate the spin or phase transition are discussed. The state of the art in the size reduction of these materials (thin films and nanoparticles) is also introduced.

Chapter II is devoted to the electrical investigations. We propose for the first time the application of an external electric field as a trigger, which can induce a transition between the two meta-stable states in valence tautomeric complexes. In parallel we will investigate the charge transport and dielectric properties of these valence tautomeric complexes. We will also investigate the dielectric properties of the SCO complex $[Fe(HB(pz)_3)_2]$ both in the bulk and thin film forms, and propose a non-volatile read-only memory device, which can store information by high and low resistance states.

C**hapter III** presents an introduction to the surface plasmon resonance spectroscopy (SPR). We will demonstrate theoretically as well as experimentally that the SPR spectroscopy is a powerful tool to determine the refractive index and thickness even in ultra thin films of SCO complexes as well as the changes of these properties upon the SCO.

The second chapter is based on the following papers:

- G. Molnár, S. Cobo, <u>T. Mahfoud</u>, et al, Interplay between the charge transport phenomena and the charge-transfer phase transition in $Rb_xMn[Fe(CN)_6]_y.zH_2O$, **J. Phys. Chem. C** 133 (2009), 2586.

- <u>Tarik Mahfoud</u>, et al, Electric-Field-Induced Charge-Transfer Phase Transition: A Promising Approach Toward Electrically Switchable Devices, **J. Am. Chem. Soc,** 131 (2009), 15049.

- L. Salmon, G. Molnár, S. Cobo, <u>T. Mahfoud</u>, et al. Re-investigation of the spin crossover phenomenon in the ferrous complex $[Fe(HB(pz)_3)_2)]$, **New J. Chem**, 33 (2009), 1283.

- <u>T. Mahfoud</u>, et al. Thin films of the $[Fe(HB(pz)_3)_2]$ spin crossover complex: electrical properties and non-volatile memory effect, **Appl. Phys. Lett.** submitted.

The third chapter is based on the following published paper:

- Carlos Bartual-Murgui, Lionel Salmon, Amal Akou, Christophe Thibault, Gabor Molnar, <u>Tarik Mahfoud</u>, Zouheir Sekkat, Jose Antonio Real and Azzedine Bousseksou, high quality nano-patterned thin films of the coordination compound $\{Fe(pyrazine)[Pt(CN)_4]\}$ deposited layer-by-layer, **New J. Chem**., (2011), DOI:10.1039/c1nj20212j.

Chapter I: Introduction to the molecular bistability

I.1 Spin crossover complexes

About 80 years ago, a fascinating change in the spin multiplicity of some *3d* transition metal compounds was discovered. The phenomenon was observed in certain complexes of metal ions having a *3d^n* (n = 4 to 7) electron configuration with (pseudo) - octahedral (O_h) molecular symmetry, where six donor atoms form an octahedron around the metal ion, and for some d^8 configurations where the molecular symmetry is lower than O_h. Cambi and co-workers had been the pioneers of this work [Cambi 31, Cambi 37]. Their measurement of the unusual magnetism of iron (III) derivatives of various tris-dithiocarbamate complexes led to the first recognition of the inter-conversion of two spin states as a result of variation in temperature, according to an equilibrium between the two states predicted as possible ground states for an octahedrally coordinated metal ion having five electrons in the d-shell. These two states are called the low-spin (LS) and the high-spin (HS) state. Later the spin crossover phenomenon was discovered for the first iron(II) complex [Fe(phen)$_2$(NCS)$_2$] (phen =1,10-phenanthroline) [Baker 64]. This compound marks the beginning of a very deep research in this field. Actually, this effect is found essentially for iron(II), iron(III) and cobalt(II) complexes, but also occasionally in complexes of nickel(II), cobalt(III) and manganese(III). However, the majority of known spin crossover complexes today have iron(II) as central metal ion and several in depth studies on a number of iron(II) complexes addressing many different aspects of spin crossover have been published [Gütlich 04]. In the following, we will try to explain and describe how spin crossover occurs using iron (II) compounds as an example.

In a perfectly octahedral coordination, the five *3d* orbitals of a the iron(II) ion are split into a subset of three orbitals, namely d$_{xy}$, d$_{yz}$ and d$_{zx}$, which are basis to the irreducible representation t$_{2g}$, and a subset of two orbitals, namely d$_{z2}$ and d$_{x2-y2}$, which are basis to the irreducible representation e$_g$ in O_h symmetry (Fig.I.1). The t$_{2g}$ orbitals are basically non-bonding and are therefore at lower energy than the anti-bonding e$_g$ orbitals. The splitting between the two sets is called the ligand field splitting and is characterized by the ligand field strength, 10Dq. 10Dq depends on the metal-ligand distance as 1/r^n, with n = 5–6 and it has to be determined experimentally.
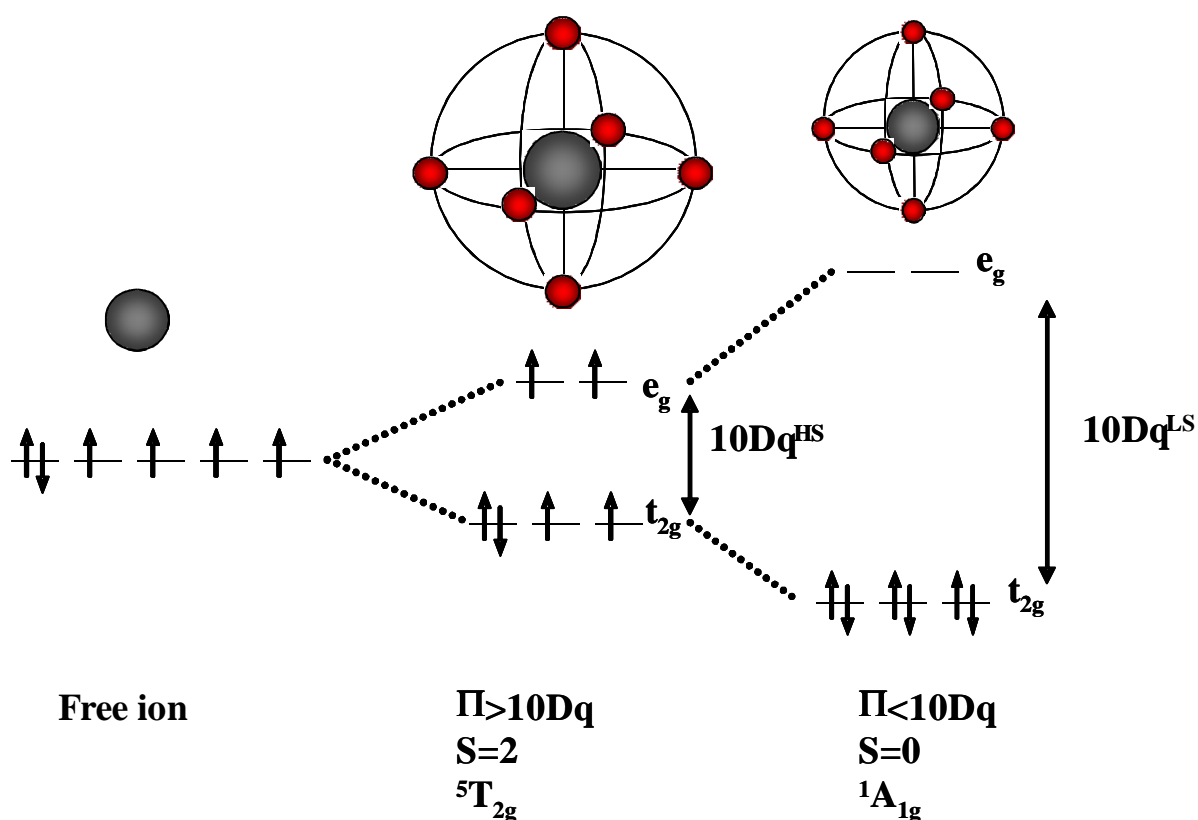
Fig.I.1: The electronic configurations of the two possible ground states for iron(II) in an octahedral complex.

The ligands, which cause a small splitting of the d orbitals, are referred to as weak-field ligands. We have to consider in addition to the ligand field, the electron-electron repulsion, named spin-pairing energy Π. When the value of Π is larger than *10Dq*, it is easier to put electrons into the higher energy set of orbitals than it is to put two into the same low-energy orbital, according to Hund's rule. Subsequently we get maximum spin multiplicity $^{5}T_{2g}$ (t_{2g}^{4} e_{g}^{2}) and we call this paramagnetic ground state the ***high-spin (HS)*** state. Conversely, complexes with a ligand-field, which cause a larger splitting, are referred to as strong-field ligands. If *10Dq* is large compared to the electron-electron repulsion, the six *d* electrons will pair up in the t_{2g} orbitals. Therefore, the lower set of orbitals is completely filled before population of the upper set starts resulting in a diamagnetic, ***low-spin (LS)*** $^{1}A_{1g}$ (t_{2g}^{6}) ground state (Fig.I.1).
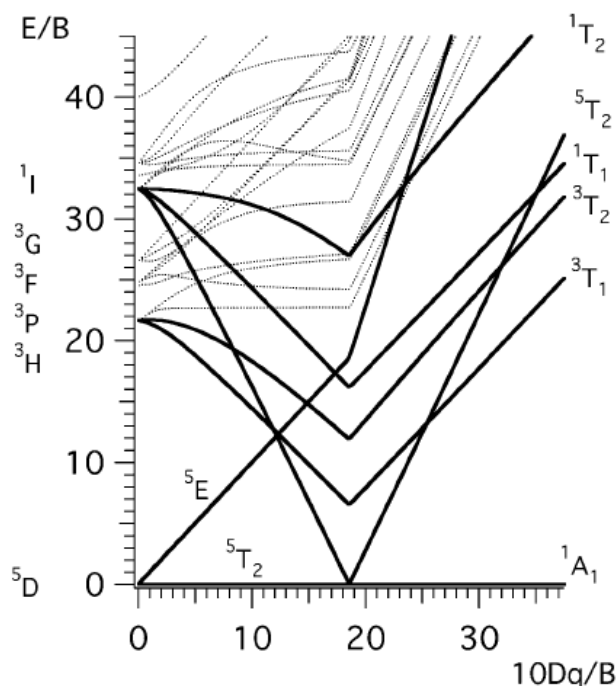
Fig.I.2: *Tanabe-Sugano diagram for a transition metal ion with six d electrons, showing the energy of the excited ligand-field states in units of the Racah parameter of electron-electron repulsion B relative to the respective ground state, versus the ligand-field strength 10Dq also in units of B.* [Sugano 70, Hauser 04]

The metal ligand bond lengths of the *HS* compounds with occupied anti-bonding e_g orbitals are substantially larger than those of *LS* compounds. The difference between the two metal-ligand bond lengths is typically around 0.2 Å, which corresponds to a change of *ca.* 10 %. (This bond length change is accompanied also by the change of bond angles.) However, the ligand field strength is a strong function of the metal – ligand distance (*10Dq* $\alpha\, r^{-6}$). One has to keep in mind also that, contrary to *10Dq*, the electron-electron interaction depends only weakly on *r*. During the transition the metal-ligand bond length changes abruptly and therefore 10Dq changes abruptly, too. The ratio of the ligand field strengths in the two spin states is given by the equation:

$$\frac{10Dq^{BS}}{10Dq^{HS}} = \left(\frac{r_{HS}}{r_{BS}}\right)^{n} \qquad\qquad \textbf{(I.1)}$$

with n = 5–6. Using average values of r_{LS} = 2.0 Å and r_{HS} = 2.2 Å and n = 6, this ratio is estimated to be ~1.75.

From the condition that the zero-point energy difference ΔE^0_{HL} between the two states, $\Delta E^0_{HL} = E^0_{HS} - E^0_{LS}$, must be of the order of thermally accessible energies, $k_B T$, we can define ranges for the ligand field strength 10Dq for each state (Figure I.3):

a) $10Dq^{HS} < 10000$ cm^{-1}, $\Delta E^0_{HL} < 0$:

The HS state is the thermodynamically stable state at all temperatures (at atmospheric pressure).

b) $10Dq^{LS} > 23000$ cm^{-1}, $\Delta E^0_{HL} > 2000$ cm^{-1}:

The LS state remains the thermodynamically stable state up to very high temperatures.

c) Finally, we define the narrow range for which the phenomenon of a thermal spin crossover can be expected: $10Dq^{HS} = 11000 - 12500$ cm^{-1} for the HS state, $10Dq^{LS} = 19000 - 22000$ cm^{-1} for the LS state and $\Delta E^0_{HL} = 0 - 2000$ cm^{-1}.
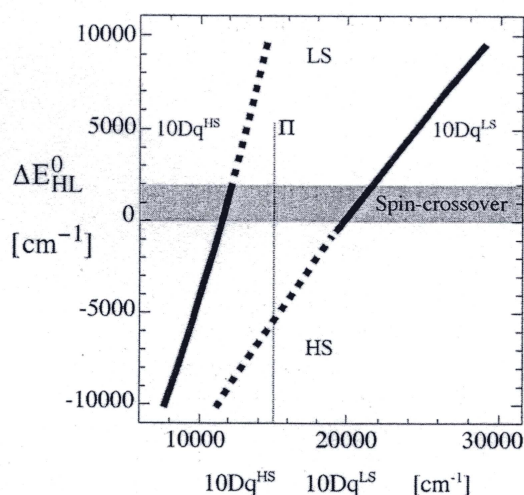
Fig.I.3: *Regions of stability of the HS and LS states as a function of 10Dq.* [Hauser 04]

Considering the dependence of the ligand field strength on the metal-ligand distance r, and the Tanabe-Sugano diagram [Sugano 70] (figure I.2), which depicts the electronic energies of the exited states relative to the respective ground state as a function of the ligand-field strength 10Dq, we can estimate in function of *r* an appropriate potential surface for each $^5T_2$ and $^1A_1$ states. In the configurational coordinate diagram (figure I.4) along the totally symmetric stretching vibration, the minima of the two potential wells are displaced relative to each other, both vertically and horizontally. Based on such a diagram, the condition for a thermal spin crossover to occur becomes apparent: the zero-point energy difference ΔE^0_{HL} has to be of the order of thermally accessible energies. If such is the case, only the LS ($^1A_1$) state as the ground

state is occupied at very low temperatures. However, as the temperature increases an almost quantitative entropy driven population of the *HS* ($^5T_2$) state will take place.
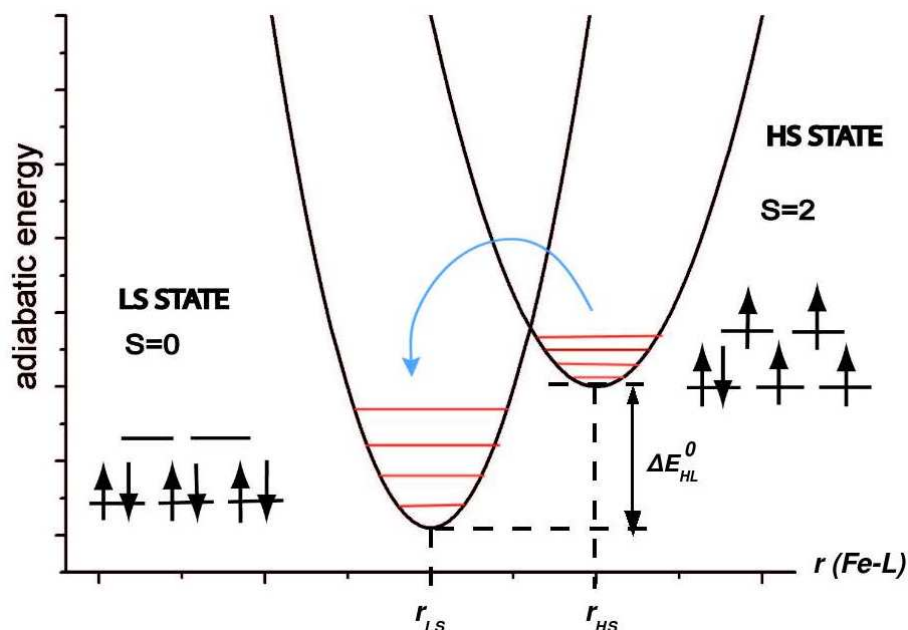
Fig.I.4: Adiabatic potentials for the high-spin and the low-spin states along the most important reaction coordinate for spin crossover, namely the totally symmetric metal-ligand stretching vibration denoted r(Fe-L).

I.1.1 The thermal spin crossover phenomenon

Under various constraints such as temperature variations, pressure, light irradiation, or magnetic field, the spin crossover phenomenon can be induced. The spin crossover induced by the change of temperature remains the most common way of monitoring a spin transition. The reversible thermal spin transition is entropy driven and occurs from the *LS* state at low temperatures to an almost quantitative population of the *HS* state at elevated temperatures. A spin transition curve is conventionally obtained from a plot of high spin fraction (γ_{HS}) vs. temperature (*T*).

The thermally induced spin transition may be understood on the basis of simple thermodynamic considerations. The variation of the spin state involves equilibrium between the two possible states, expressed by the ***Gibbs free energy*** equation: $\Delta G = G_{HS} - G_{LS} = \Delta H - T\Delta S$, where the variation of the Gibbs free energy ΔG is a function of the enthalpy ($\Delta H = H_{HS} - H_{LS}$) and entropy variations ($\Delta S = S_{HS} - S_{LS}$). In a first approximation the variation of the

enthalpy is directly related to the electronic contribution ΔH_{el}. (Here, we did not take into account the vibrational contribution as $\Delta H_{vib} << \Delta H_{el}$.) On the other hand the variation of the entropy ΔS ($\Delta S = S_{\text{élec}} + \Delta S_{vib} + \Delta S_{conf} + \Delta S_{rot} + \Delta S_{trans}$) includes two important contributions, one resulting from the variation of the spin state $\Delta S_{spin} = R \ln[(2S+1)_{HS}/(2S+1)_{LS}] = R\ln(5) = 13.4$ J K^{-1} mol^{-1}, where $(2S+1)_{HS}$ et $(2S+1)_{LS}$ are respectively the spin multiplicity of the HS and LS states. Sorai and Seki [Sorai 74] measured heat capacities of Fe(II) spin crossover complexes. They found a phase transition for [Fe(NCS)$_2$(phen)$_2$] at 176.29 K with an entropy change of $\Delta S = (48.8 \pm 0.7)$ J K^{-1}mol^{-1}. This entropy value is extremely large in comparison with the entropy gain, $\Delta S = R\ln5 = 13.38$ J K^{-1}mol^{-1}, expected for a conversion from the low-spin (LS) state $^1A_{1g}$ to the high-spin (HS) state $^5T_{2g}$. The remainder must be attributed to vibrational contributions from a change of the vibrational density of states. This latter arises mainly from the change in the stretching and deformation modes of the coordination core. This vibrational part constitutes in general the largest contribution for the total entropy change (ΔS). [Sorai 74] Note that the orbital entropy change {$\Delta S_{orbital} = R \ln [(2L+1)_{HS}/(2L+1)_{LS}$ } will be omitted here, assuming that the symmetry of the spin crossover molecules are in general not perfectly O_h. On the LS $\rightarrow$ HS transition, the electronic degeneracy and hence the electronic entropy is higher in the *HS* phase than in the *LS* phase. Moreover, in the HS phase, the metal-ligand bond lengths are, on average, longer, so that the vibrational entropy is also higher in this phase. Subsequently the resulting ΔS is also positive.
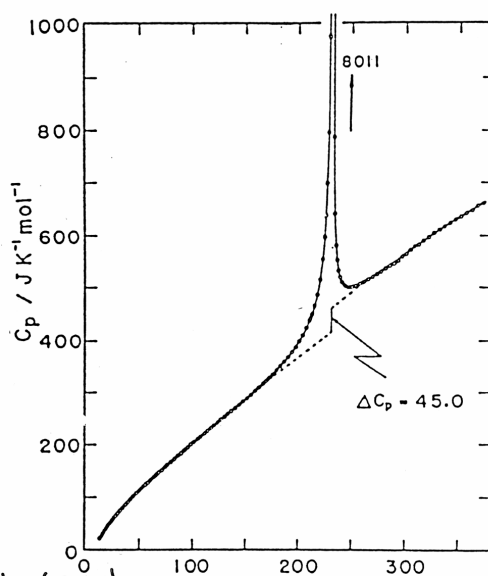
Fig.I.5: *Molar heat capacity of [Fe(NCS)$_2$(phen)$_2$]. Broken curves indicate the normal heat capacities.* [Sorai74]

We conclude that the temperature-induced spin crossover is an entropy-driven phenomenon and coupling between the electronic states and the phonon system plays a fundamental role in the spin crossover transition [Sorai74].

Although the origin of the spin crossover is purely molecular, the macroscopic property of the solid is the result of cooperative interactions between the molecules that make up the material. A macroscopic approach for the simulation of the thermal spin crossover curve is the ***Slichter and Drickamer model*** [Slichter 72]. In this model, the standard Gibbs free energy of the system at a given temperature is:

$$G = \gamma_{HS} G_{HS} + \gamma_{LS} G_{LS} - T\Delta S_{mix} + \Gamma \gamma_{HS}(\gamma_{LS}) \tag{I.2}$$

where γ_{HS} is the high spin fraction as defined before and the associated low spin fraction is denoted $\gamma_{LS} = 1 - \gamma_{HS}$, G_{HS} and G_{LS} are respectively the molar Gibbs free energies of the pure HS and LS phases, Γ denotes the intermolecular interaction parameter and finally S_{mix} represents the ideal mixing entropy, which fulfils the relation $S_{mix} = -R[\gamma_{HS} \ln(\gamma_{HS}) + \gamma_{LS} \ln(\gamma_{LS})]$. If we consider $G_{LS} = 0$ as a reference energy, then the equation (1.1) can be expressed as:

$$G = \gamma_{HS}\Delta H + \Gamma\gamma_{HS}(1-\gamma_{HS}) - RT\left[\gamma_{HS}\ln(\gamma_{HS}) + (1-\gamma_{HS})\ln(1-\gamma_{HS}) + \frac{\gamma_{HS}\Delta S}{R}\right] \tag{I.3}$$

Using the equilibrium condition for the system $(\partial G/\partial \gamma_{HS})_{T,P} = 0$, we can express the temperature vs. the high spin fraction (γ_{HS}), thereby providing the simulation of the spin crossover curve as a function of T:

$$T = \frac{\Delta H + \Gamma(1-2\gamma_{HS})}{R\ln\left(\dfrac{1-\gamma_{HS}}{\gamma_{HS}}\right) + \Delta S} \tag{I.4}$$

Depending upon the value of the interaction parameter (Γ), tree possible limits exist (Figure I.6). The transition is abrupt when the interaction parameter is equal to a critical value $\Gamma_c = 2RT_{1/2}$, whereas for $\Gamma < \Gamma_c$ the transition is gradual. Inversely for $\Gamma > \Gamma_c$ we obtain a first-order phase transition with hysteresis loop.
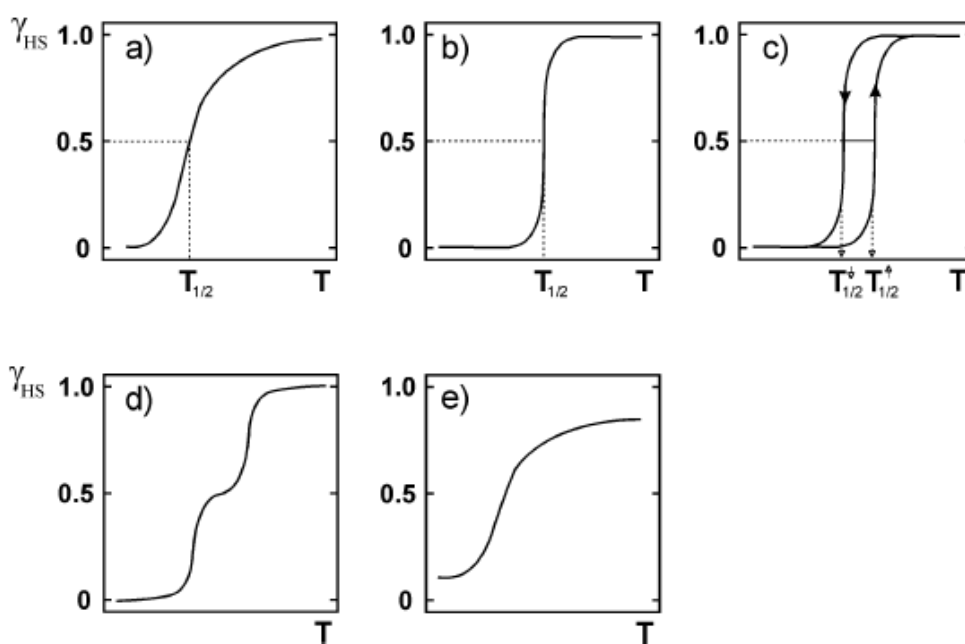
Fig.I.6: *Schematic representation of the different types of spin crossover: a) gradual, b) abrupt, c) with hysteresis, d) in two steps, e) gradual and incomplete.*

I.1.2 Pressure induced spin state change

After the thermal effect on the SCO complexes, it was soon realized that pressure can also be a trigger for the SCO phenomenon. Because the low spin state (LS) has a smaller molecular volume than the high spin (HS) state, it becomes the favored state as pressure increases [Varret 02, Gütlich 04]. Application of pressure increases the relative vertical displacement of the potential wells (Fig.I.7). The gap between the zero point energies of the low spin and high spin states increases by the work term $P\Delta V_{HL}$, where $\Delta V_{HL} = V_{HS} - V_{LS}$ is the volume difference between the *HS* and *LS* states. The new gap can be expressed by the equation $\Delta E^{0}_{HL}(P) = E^{0}_{HL} + P\Delta V_{HL}$. Indeed, at elevated pressure the spin transition will occur at higher temperatures than at ambient pressure. The displacement of the spin transition curve to higher temperature values can be expressed as: $\partial T_{1/2}/\partial P = \Delta V_{HL}/\Delta S_{HL}$. For iron (II) spin crossover complexes the shift in the transition temperature was found, in general, to be about 15-20 *K/kbar* [Slichter 72]. It means that a relatively small external pressure of a few *kbar* is sufficient to strongly affect the thermal spin transition curve.
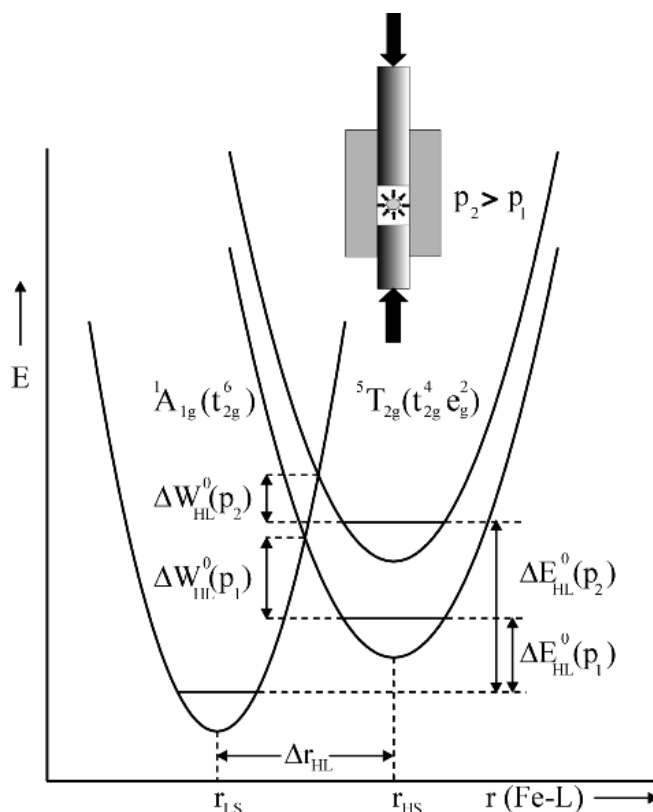
Fig.1.7: *Schematic representation of the pressure influence ($P_2>P_1$) on the LS and HS potential wells of Fe(II) SCO complexes.* [Ksenofontov 04]

It should be noted also that the application of pressure could in fact induce a transition in a *HS* system for which a thermal transition does not occur. Pressure effects on the molecules have been found to be relatively complex. For example, pressure was often found to induce changes in the crystal structure [Boillot 02, Guionneau 96, Ksenofontov 98]. In our group, a pressure-induced hysteresis [Molnár 03] as well as pressure pulse induced spin state switching [Bousseksou 03] has also been observed.

I.1.3 Magnetic-field induced spin crossover

Application of a high magnetic field acts also as an external perturbation on the spin crossover phenomenon. Application of a static magnetic field stabilizes the HS state, with a downward shift of the transition temperature $T_{1/2}$, due to Zeeman effect. In a first order approximation [Qi 83], $T_{1/2}$ changes because of the decrease in energy of the molecules in the HS state (the contribution of the diamagnetic LS state can be neglected in Fe^{II} complexes). Hence, the

magnetic energy shift $E_{HS}^m - E_{LS}^m = -\dfrac{\chi B^2}{2}$ is added to the free energy and the displacement of

the transition temperature $\Delta T_{1/2}$ can be calculated as:

$$\Delta T_{1/2} = -\frac{\chi B^2}{2\mu_0 \Delta S(T_{1/2})} \qquad \textbf{(I.5)}$$

where $\Delta S_{T1/2}$ represents the entropy difference between the HS and LS states at the transition

temperature ($T_{1/2}$). *Qi et al.* [Qi 83] were the first to investigate the shift of the transition curve

for the [Fe(phen)$_2$(NCS)$_2$] spin crosover complex ($\Delta S_{T1/2}$ = ca. *50 JK^{-1}mol^{-1}*) in a field of *5.5*

Tesla and they observed a diminution of $\Delta T_{1/2}$ = *0.1 K*.
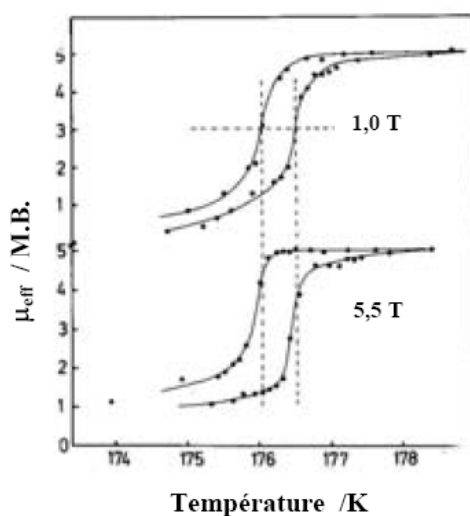
Fig.I.8: Application of a static magnetic field (5.5 Tesla) on the [Fe(phen)$_2$(NCS)$_2$] SCO compound. [Qi 83]

This is a very small value and somewhat difficult to verify experimentally, due essentially to

the limited intensity of the available magnetic field, which was relatively weak (*5-6* Tesla) at

that time. Later, J. Lejay et al. [Lejay 91] could apply a **static magnetic field** of *22 Tesla* on

Co(III) compounds, and observed a shift of the spin transition temperature of about *0.6 K*.

More recently, Bousseksou et al. [Bousseksou 00] have studied experimentally and theoretically the

effects of an intense **pulsed magnetic field** of 32 Tesla on the [Fe(phen)$_2$(NCS)$_2$] compound.

This magnetic field corresponds to an expected temperature shift of 2.0 K. Applying the

pulsed magnetic field in the thermal hysteresis loop on the ascending branch induced indeed

an irreversible, though incomplete LS→HS conversion (Fig.19). [Bousseksou 02] The effects on

the descending branch were found reversible. These observations were confirmed on several

other complexes and even a quasi-complete switch could be obtained for a Co(II) complex

(figure I.9). [Bousseksou02, Bousseksou04] In addition, the same authors have reported the effect of a pressure pulse on the HS fraction within the hysteresis loop of the compound [Fe(phen)$_2$(NCS)$_2$] and this had the expected opposite effect ("mirror effect") when compared to a magnetic field. [Bousseksou 03, Bonhommeau06]
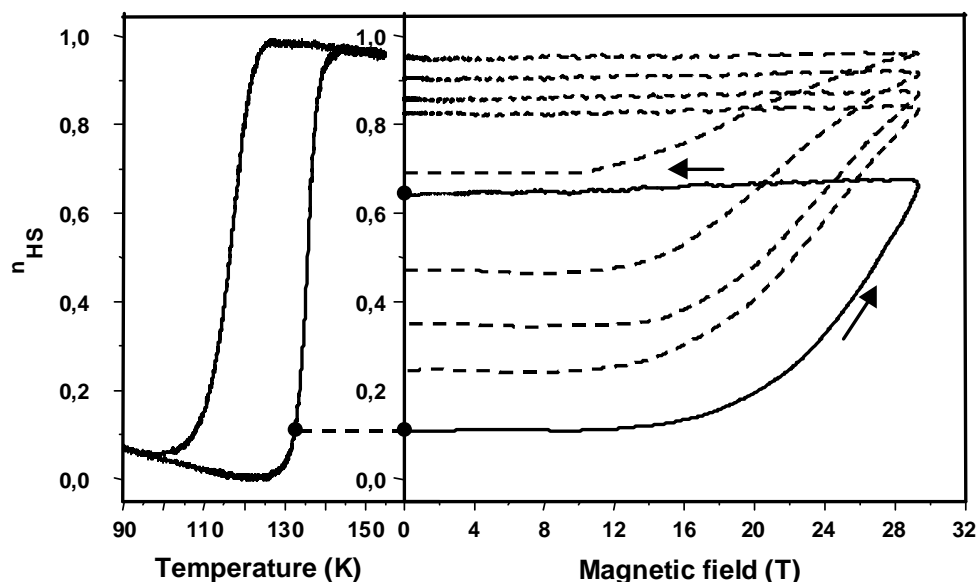
Fig.I.9: *Set of isotherms n$_{HS}$(B) showing the irreversible (and quasi-total) triggering effect on the HS fraction in Co(H$_2$(fsa)$_2$en)(py)$_2$ for an applied pulsed magnetic field in the metastable LS state.* [Bousseksou 02]

I.1.4 Light induced spin state change

In 1982, the discovery of a light-induced spin crossover in a series of iron(II) spin-crossover compounds by McGarvey and Lawthers, [McGarvey 82] had great impact on spin-crossover research. McGarvey *et al.* described in their paper the use of a pulsed laser to perturb the equilibrium between the singlet (^{1}A) and quintet (^{5}T) states in several Fe(II) complexes in solution. Two years later, Decurtins et al. [Decurtins 84] discovered a surprising effect by irradiating a solid Fe(II) SCO sample with green Ar^+ laser (514.5 *nm*) in the singlet absorption band at liquid helium temperatures. The ground low spin state was excited and the metastable high spin state was gradually populated until a complete conversion. The metastable high spin state had a very long lifetime at sufficiently low temperature: more than 10^6 s for [Fe(ptz)$_6$](BF$_4$)$_2$] at 20 K. Therefore this solid-state effect was named "**Light Induced Excited Spin State Trappin*g* (*LIESST*)**". Very soon, Decurtins et al. [Decurtins 85] were able to establish the mechanism for the *LIESST* effect in this system. Later on, Hauser reported the reverse-LIESST effect [Hauser 86], wherein red light was used to pump the

metastable high spin molecules and to convert the compound back to the thermodynamically stable *LS* state.
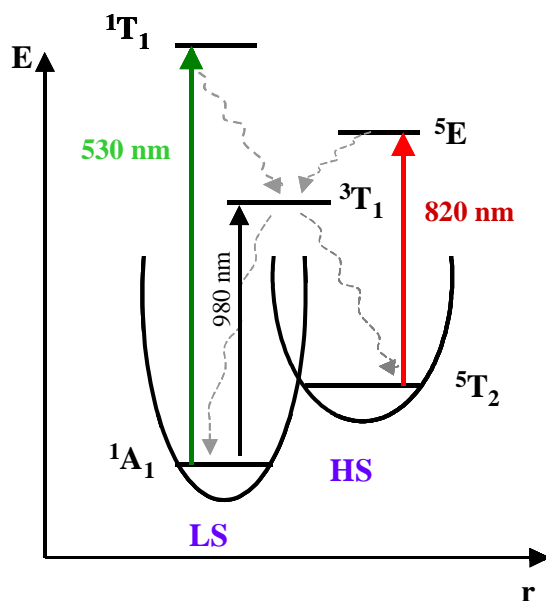
Fig.I.10*: Jablonski diagram illustrates the LIESST and reverse-LIESST effects: straight arrows are the light induced vertical transitions; the undulate arrows represent the relaxation processes. [Hauser 91]*

The exact mechanism of the LIESST phenomenon and the involved intersystem crossing processes is still debated. According to Hauser et al. the LIESST effect occurs in two successive transitions. [Hauser 91] The first relaxation step leads to the $^3T_1$ state (or less frequently to the $^3T_2$, which is not shown in the figure I.10). In the second step, the system can relax into the $^5T_2$ state (a crossing of levels can be observed through a spin-orbital coupling), where it remains trapped (at sufficiently low temperatures) because of the large energy barrier between $^5T_2$ and $^1A_1$ states. This energy barrier is due to the large difference in the metal-ligand bond lengths. The fact that the energy level of the $^3T_1$ state is just below the ^5E state for spin crossover complexes suggests, that the LIESST effect should be a reversible transition. It is indeed possible to pump back the system to the LS state by irradiating the metastable HS state at 820 nm at low temperature (20 K). This irradiation induces the transition $^5T_2 \rightarrow {}^5E$, then the ^5E excited state relaxes to the $^1A_1$ (LS) state via the $^3T_1$ state. [Hauser 91] However, trapping the system in metastable *HS* state is only efficient at cryogenic temperature. This is a serious limitation for the development of optical devices based on spin crossover materials. This problem has recently been overcome using pulsed laser excitation (8 ns pulses) within the thermal hysteresis loop in the [Fe(C$_4$H$_4$N$_2$){Pt(CN)$_4$}] spin crossover complex [Bonhommeau 05] (figure I.11). Our group evidenced in their first observation a partial and irreversible LS to

HS conversion. Later we showed a complete bidirectional (complete HS to LS as well as LS to HS) **photoconversion following a short one-shot laser irradiation** of {Fe^{II}(pyrazine)[Pt(CN)$_4$]} single crystals at room temperature [Cobo 08]. This last observation is promising and opens up an interesting possibility for new generation of data storage devices.
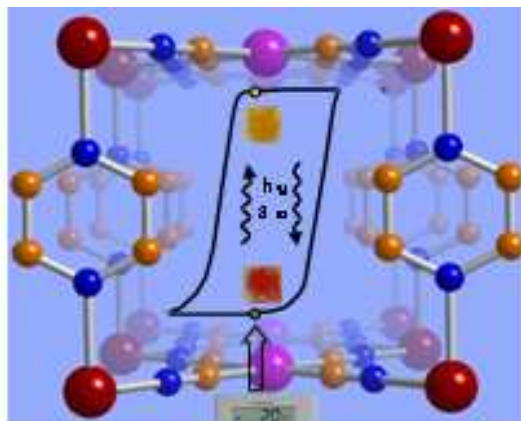
Fig.I.11: *Light-pulse-induced switching between two spin states at room temperature.*
[Bonhomeau 05, Cobo 08]

I.1.5 Guest adsorption/desorption-introduced spin state change

Very recently, Real et al. has demonstrated the chemoresponsive behavior of the Hofmann clathrate porous coordination polymers {Fe(pz)[M^{II}(CN)$_4$]} (pz = pyrazine; M^{II} = Ni, Pd, Pt) based on the spin-crossover properties of the iron(II), and the cooperative response generated by the components of the framework, conferring to the solid a bistable behavior at ordinary temperatures. A reversible change of spin state at the iron(II) sites was observed cooperatively with the uptake of guest molecules. The high-spin state (HS, yellow) is stabilized by hydroxilic solvents, five- and six-membered aromatic molecules, while the low spin state (LS, red-brown) can be stabilized by CS$_2$ at 298 K (see figure. I.12) [Ohba 09]. Furthermore, the occurrence of coordinatively unsaturated metal centers M(II) enhance adsorptive selectivity for specific guest substances (halogene molecules). In the same year and on the same compound, Kepert *et al*. reported also the guest-dependent SCO properties and spin-state-dependent host/guest properties. The adsorption of a wide range of small molecular guests, both gases (N$_2$, O$_2$, CO$_2$) and vapors (methanol, ethanol, acetone, acetonitrile, and toluene) in the {Fe(pz)[Ni(CN)$_4$]} Hofmann-type system occurs with sufficient energy to significantly

perturb the energetics of SCO, thereby yielding dramatic changes to the SCO properties [Southon 09].

Based on these pioneer investigations, the guest adsorption/desorption can join the well established quartet of temperature, pressure, magnetic field, and light irradiation as SCO stimuli. Such a property, which is highly specific for each of the guests studied, points to possible molecular sensing applications for systems of this type.
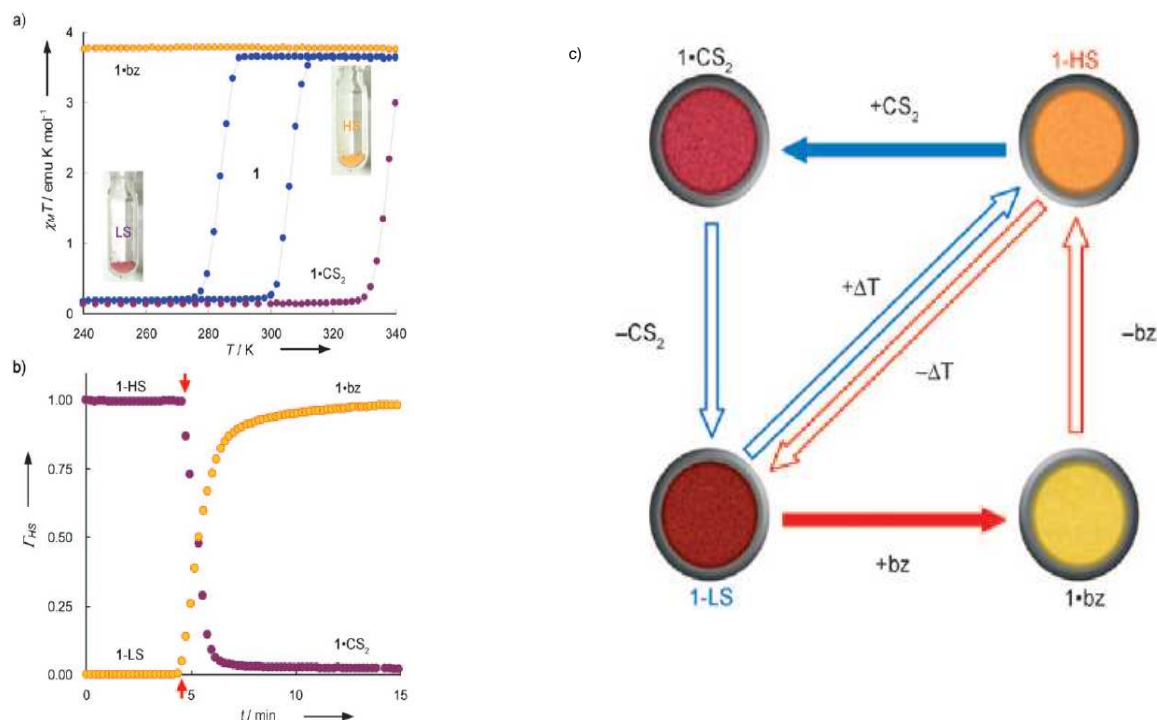
Fig.I.12: *Magnetic behavior of {Fe(pz)[Pt(CN)$_4$]} powder and its clathrates a) Temperature dependences of $\chi_M T$ for guest-free **1** (blue), benzene (Bz) clathrate (**1·bz** : yellow), and CS$_2$ clathrate (**1·CS$_2$** : purple); b) Time dependence of the fraction of the HS state (G) under a benzene (yellow) and CS$_2$ (purple) atmosphere at 293 K; and c) Schematic chemical and thermal memory process. The color circles are real photos of powder samples.* [Ohba 2009]

I.1.6 Detection of spin crossover

Whatever is the external stimuli (heat, magnetic field, pressure, light, or chemical stimuli), Fe(II) SCO complexes undergo drastic variation of the metal-ligand bond lengths (≈ 0.2 Å, i.e., $\approx 10\%$) and ligand-metal-ligand bond angles ($0.5°–8°$) [Gütlich 94], accompanied by magnetic and optical property changes arising from a change in relative occupancies of the t_{2g} and e_g orbitals. Consequently, magnetic and optical measurements [König 84, Bousseksou 03] are the major experimental techniques used for quantitative investigations of the spin transitions.

Detection of spin crossover can be implemented in a simple way, by measuring the mole fraction of the HS state (or LS state), γ_{HS} , as a function of different parameters (T, B, P..). This mole fraction can be measured by several methods:

- **Measurement of magnetic susceptibility** as a function of temperature, χ (T), has always been the principal technique for characterization of SCO compounds. [König 91, Gütlich 94] For measurements on solid samples, a superconducting quantum interference device magnetometer (SQUID) and the traditional balance methods (Faraday) can be used. The product χT for a SCO material is determined by the temperature dependent contributions γ_{HS} and γ_{LS} according to χ (T) = γ_{HS} χ_{HS} + (1-γ_{HS}) χ_{LS}. With the known susceptibilities of the pure HS and LS states, the mole fraction of the HS state γ_{HS} at any temperature is easily derived and is plotted to produce the spin transition curve. Expression of the spin transition curve in terms of the effective magnetic moment μ_{eff} = (8 χ T)$^{1/2}$ as a function of temperature has been widely used, but is now less common.

- **^{57}Fe Mössbauer Spectroscopy** is a standard method for the characterization of SCO compounds of iron, based on the recoilless nuclear resonance absorption of γ radiation. The isomer shift δ and the quadrupole splitting ΔE_Q, two of the most important parameters derived from a Mössbauer spectrum [Greenwood 71], differ significantly for the HS and LS states of both Fe(II) and Fe(III). The two spin states are discernible by their characteristic subspectra. The area fractions of the resonance lines can be determined with the help of specially developed data fitting computer programs. These area fractions t_{HS} and t_{LS} are proportional to the products $f_{HS}\gamma_{HS}$ and $f_{LS}\gamma_{LS}$, respectively, where f_{HS} and f_{LS} are the so-called Lamb-Mössbauer factors of the HS and LS states. Only for $f_{HS} = f_{LS}$, the area fractions are a direct measure of the respective mole fractions of the complex molecules in the different spin states, i.e. $t_{HS}/(t_{HS}+t_{LS}) = \gamma_{HS}$. In most cases, however, the approximation of $f_{HS} \approx f_{LS}$ is made.

- **Heat capacity measurements**

Calorimetric measurements on SCO compounds (treated in detail by Sorai et al. [Sorai 74]) provide important thermodynamic quantities such as enthalpy and entropy changes accompanying a spin transition (ST).

- **Measurement of vibrational spectra**

In an infrared or Raman spectra measured as a function of temperature, [Takemoto 72,Takemoto 73, Bousseksou 00, Tuchagues 04] the vibrational modes belonging to the HS and the LS species can be readily recognized as those decreasing and increasing in intensity, respectively, as the temperature is lowered. The majority of the low-frequency modes suffer dramatic changes upon spin transition. The general trend is a large decrease of the frequencies when going from the LS to the HS state reflecting the weaker metal-ligand bonds in the HS state. In several instances a spin transition curve, $\gamma_{HS}(T)$, has been derived from the normalized area fractions of characteristic HS or LS bands.

- **X-ray structural studies**

As discussed earlier in this chapter, thermal SCO in solid transition metal compounds is always accompanied by significant changes in the metal-donor atom bond lengths (10%), which may cause typically a 1–15% change in elementary cell volumes [König 91].Thus single crystal structure determination at variable temperatures above and below the transition temperature is very informative of the nature of SCO phenomena in solids. The temperature dependence of X-ray powder diffraction data can be a suitable diagnostic of the nature of the SCO and of changes in the lattice parameters.

- **UV-vis absorption measurements**

The thermal SCO is always accompanied by a color change (thermochromism). This offers a very convenient and quick means of detecting the occurrence of a transition by simple observation of the color at different temperatures [Descurtins 84, Bousseksou 03], but also a quantitative tool to determine the HS fraction as a function of an external perturbation. The knowledge of positions and intensities of electronic transitions is also desirable and UV-vis absorption spectroscopy is frequently employed to obtain the electronic spectrum of SCO compounds at different temperatures.

- **Other techniques:**

It was recently shown that the spin state change is also accompanied by an important variation in the dielectric constant in a wide frequency range (kHz-THz-vis) and even hysteresis loops of ε have been observed around room temperature (dielectric spectroscopy) [Bousseksou 03]. Proton NMR measurements, Positron annihilation spectroscopy (PAS), RPE, X-ray spectroscopies (XANES, XES) … have been also applied to the detection and characterization of transitions.

I.1.6 Spin crossover thin films and nanoparticles

The interest in molecular materials possessing properties relevant for practical applications has considerably increased. This interest mainly comes from the need of the development of new smart nanomaterials and new products for potential applications, such as memories, switching devices and sensors. The characteristic that defines a molecular switch is the bistability domain with an "ON" and an "OFF" position. The two states can be isomers, an acide and its conjugate base, the oxidized and reduced forms of a redox acive molecule, or even the complexed and uncomplexed form of a receptor [Fabbrizzi 1999, Diederich 2001]. In such a context, the molecular bistability associated with the SCO phenomenon is very relevant. The main advantage of using SCO materials is that: 1) transition can occur even at nanometer scales, 2) they involve a change of electronic states, resulting in very fast and sharp transitions between the metastable states, and 3) these molecular materials provide a wide range of flexibility in the design of material with tunable optical, electric and magnetic properties.
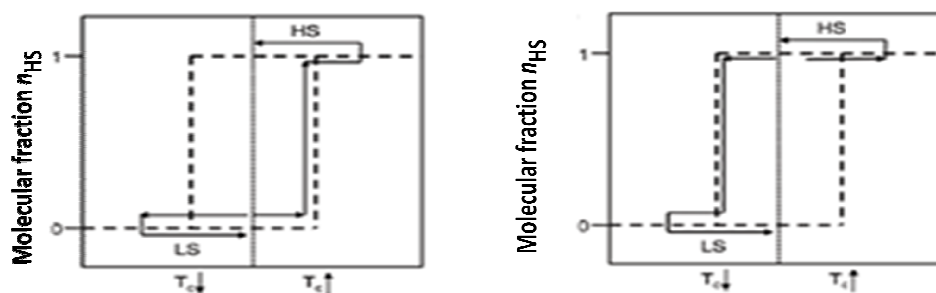
Fig.I.13: *Schematic representation of the memory effect in spin crossover systems.*

These appealing properties cannot be exploited in bulk materials, but only if thin films or nanoparicles of the compounds are prepared and deposited or patterned (spin coating, nano-patterning or nano-scale organization) on surfaces. The high versatility and possibility to tune properties of switchable coordination compound thin films and nanoparticales confers a promising market potential on those products in the highly competitive fields of microelectronics and photonics. Besides that, studies on nano-objects of molecule-based materials can be helpful to generate new fundamental knowledge on size-reduction effects and the dynamics of the spin crossover phenomenon. These studies bridge gaps between our understanding of single molecules and bulk macroscopic materials.

The first demonstration of SCO materials in a display device were reported by Kahn et al. [Kahn 98].
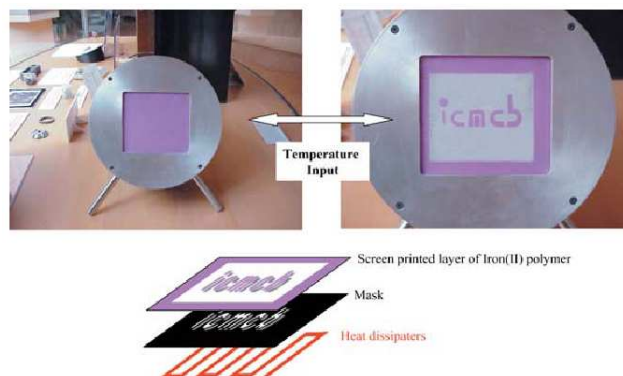
Fig.I.14: *Laboratory scale display. SCO screen-printed layer before writing (left) and after thermal writing (right). Schematic illustration of the display device involving the SCO layer, the aluminum plate containing the message and the heat dissipater resistance (bottom). When the temperature exceeds the critical "up temperature" the material transits from purple to white and the information is displayed.* [Kahn 98]

The substrate consists of an aluminum plate on which resistive dots and connecting electrodes were previously screen printed. The dots are addressed through columns and rows. The dots, when electrically addressed, act as heat dissipaters. When the temperature is above $T_{1/2} \downarrow$, the material passes from violet to white. The information is stored as long as the system remains at a temperature within the hysteresis loop. To erase the information the temperature has to be lowered below $T_{1/2}\downarrow$ using a Peltier element.

The pioneering approaches to obtain SCO thin films employed the Langmuir–Blodgett technique, [Soyer 98] or a simple mixing of the complexes with polymers or other materials, which can be spin coated on surfaces. [Matsuda 07] Matsuda and Tajima obtained 30 nm of [Fe(dpp)$_2$](BF$_4$)$_2$ SCO thin film, which transits around 360 K.

In 1999 Létard et al. [létard 99] reported a LIESST effect on a [Fe(Bi-DFOD)$_2$(NCS)$_2$)] thin film obtained by the Langmuir-Blodgett technique. Recently a layer-by-layer assembly technique was also proposed to deposit alternating layers of SCO cations and polyanions. [Jaiswal 02] Unfortunately the resulting films were not purely composed of the spin-crossover complex, but consisted of a mixture of the complex and a polymer or a surfactant, which alter strongly the spin crossover as well as dielectric and optical properties of the films. Later on, Gütlich *et al.* proposed another approach to the synthesis of thin films in the form of liquid-crystals (figure I.15) [Seredyuk 06].
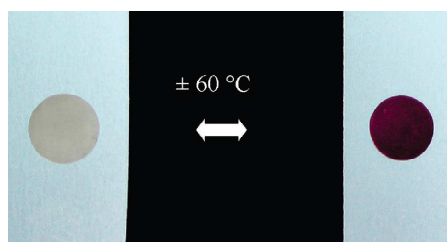
Fig.I.15: *Thermochromic effect in liquid-crystal SCO films* [Seredyuk 06]

Recently, interesting progress has been made in the area of spin crossover complexes with infinite one-, two- or three-dimensional (1D, 2D, 3D) networks, the so-called coordination polymers [Cobo 06]. The main objective of this approach was the enhancement and fine-tuning of cooperative properties by the strong covalent links between the metallic cores in the polymers. Indeed, a number of highly cooperative polymer systems have been reported in recent literature displaying hysteretic behaviour (thermal and piezo) even at room temperature, in some cases. In addition to this, it was recently demonstrated that 3D coordination polymers represent also an attractive platform for growth of surface thin films with spin crossover properties. In fact, the 3D network structure allows assembling, via stepwise adsorption reactions, multilayer films based entirely on intra- and interlayer coordination bonds. Thin films of the 3D SCO compounds $Fe(pyrazine)[M(CN)_4](M = Ni, Pd$ or Pt) were grown by Cobo *et al.* [Cobo 06] via a sequential assembly method using coordination reactions as shown in figure I.16.
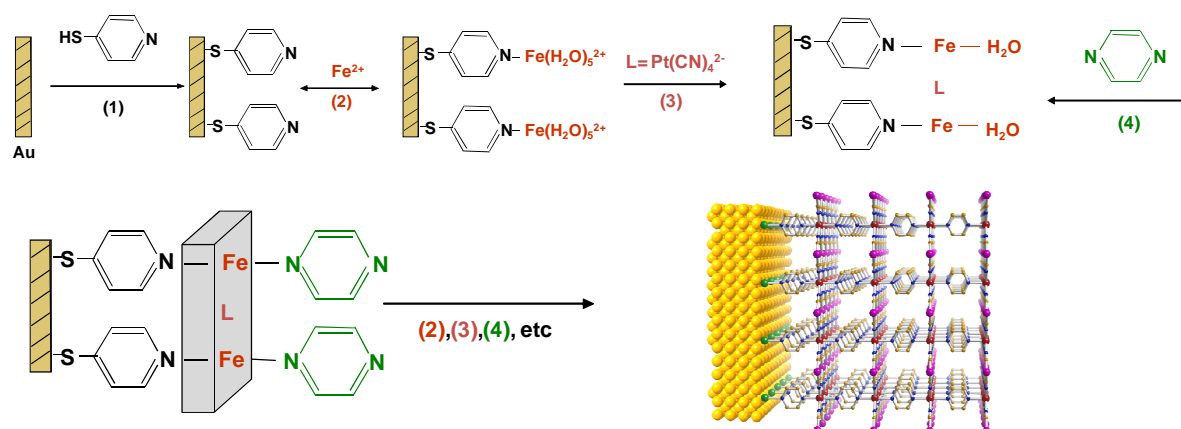
Fig.I.16: *Schematic procedure of the sequential assembly of $Fe(pyrazine)[M(CN)_4](M = Ni, Pd$ or Pt) thin films displaying room temperature spin crossover and host-guest properties.*

A Raman microscopy investigation revealed that these thin films displayed room temperature SCO with a wide hysteresis loop. In this thesis (chapter III), we will investigate the properties of this type of thin films (thickness, refractive index …) using AFM microscopy and surface plasmon resonance.

The first results concerning the synthesis of SCO nanoparticles were reported by Létard *et al.*[Létard 04] These authors reported the observation of a thermal hysteresis loop in the nanoparticles of the compound $[Fe(NH_2trz)_3]Br_2$ of *ca.* 70 nm size obtained by the reverse micelle technique (also called water-in-oil microemulsions). The reverse micelles consist of a dispersion of polar liquid droplets stabilized by a surfactant which contains both hydrophobic tail-groups and hydrophilic head-groups in an oil phase. The above mentioned nanoparticles maintained the sharp spin transition measured for the bulk powder.

In 2007 Coronado *et al.*[Coronado 07] using a similar approach have succeeded in synthesizing nanoparticles of the $[Fe(Htrz)_2(trz)](BF_4)$ complex with a medium statistical size of *ca.* 15 nm, which exhibited a 43 K wide hysteresis loop. Recently our group and two other groups have reported the elaboration of Hofmann clathrate like 3D network $[Fe(pz)\{M(CN)_4\}]$ (pz = pyrazine, M = Pt or Ni) nanoparticles using different approaches. The water in oil microemulsion technique has been used by both, the Real [Boldog 08] and Mallah [Volatron 08] group to prepare various sized nanocrystals of the $[Fe(pz)\{Pt(CN)_4\}]$ compound. The control of the size was achieved by modifying the concentration of the precursors. The study of the magnetic properties revealed that the particles have a behavior different from that of the bulk. The observed modification of the transition temperature, the hysteresis loop width, the abruptness of the transition and the residual fractions were related to the particle size reduction (figure I.17).

Fig.I.17: *Magnetic properties in the form of $\chi_M T$ vs T plots for the bulk and nanocrystals of the $[Fe(pz)\{Pt(CN)_4\}]$ compound.* [Real08]
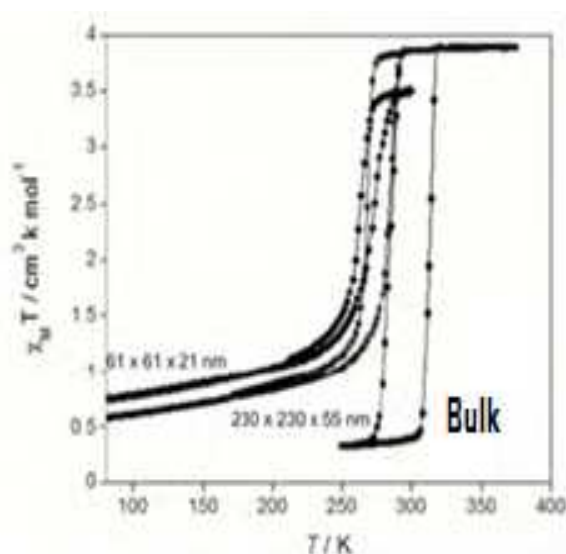
The particle size effect on the spin crossover properties of [Fe(NH$_2$trz)](Br)$_2$ was reported by the group of Létard [Arnaud 09]. For particle sizes of 50 and 30 nm a relatively gradual thermal spin crossover occurs without existence of thermal hysteresis although the equilibrium temperature of the transition is almost not affected by the decrease of the size. The same group used a Differential Interference Microscope (DIC) set-up operating in transmission to conclude that the gradual spin transition recorded for the bulk could be due to the compilation of individual abrupt transitions on the warming branch or to the compilation of already individual smooth transitions on the cooling branch.

Our group have succeeded in the synthesis of ultra-small nanoparticles of the spin crossover coordination polymer Fe(pz)[Ni(CN)$_4$] [Larionova 08] obtained by using the biopolymer chitosan as matrix. The porous chitosan beads containing amino functionalities allow the growth of 4 nm nanoparticles with a narrow size distribution. Mössbauer spectroscopy revealed that only *ca.* 1/3 of the iron (II) ions of the nanoparticles undergo a cooperative thermal spin transition with a hysteresis loop (figure I.18).
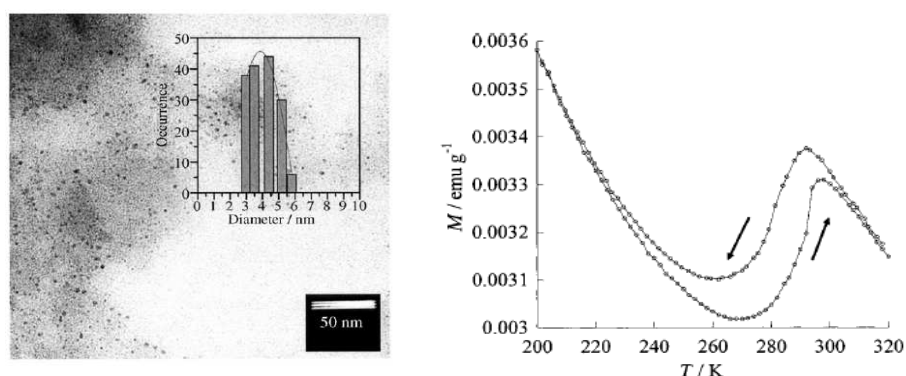
Fig.I.18: TEM image and magnetic study of 4nm Fe(pz)[Ni(CN)$_4$] nanoparticles

In order to develop applications in thermometry and thermal imaging, our group designed a two-component system comprised of ultra-small SCO nanoparticles (10 nm) and an appropriate fluorescent agent (rhodamine-110) displaying negligible thermal quenching and a good overlap between the fluorescence band of Rhodamine and the absorption of the nanoparticles (in the LS state). It is shown that the luminescence can probe the spin state of the system [Salmon 10].
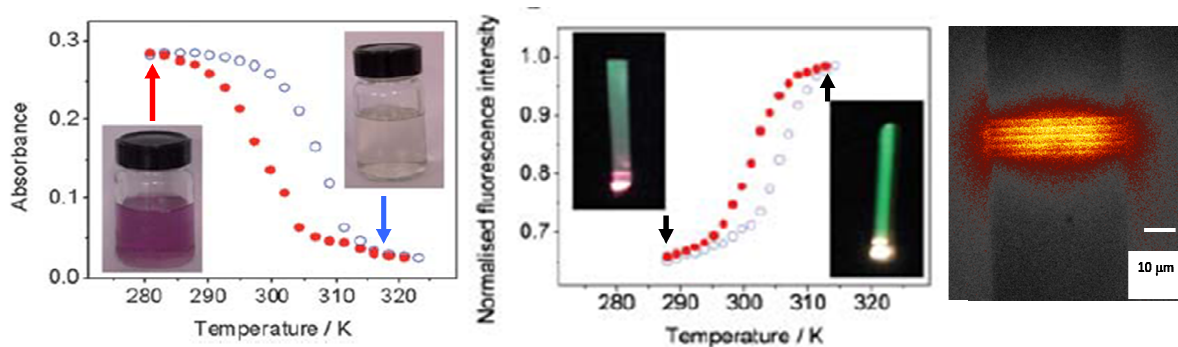
Fig.I.19: *(**Left**) Temperature dependence of the optical absorbance of a spin crossover nanoparticle (10 nm) suspension, (**Middle**) Temperature dependence of the fluorescence intensity of the system doped by rhodamine, (**Right**) Fluoresce microscopy images of Ni nanowires covered by the nanoparticles. Thermal imaging of nanowires resistance heated by Joule effect.* [Salmon 10].

The development of methods giving access to nanostructures that preserve the integrity of the material is technologically of utmost importance for the application of SCO compounds. For example, as it was shown by Molnar *et al.* [Molnar 07], micro- and nanometric patterns of the Fe(pyrazine)[M(CN)$_4$] SCO compound can be elaborated using an electron-beam lithographic approach and lift-off . Very recently Thibault et al. [Thibault 10] have shown that micro-transfer molding (μTM) and micro-contact (μCP) printing techniques can be used to fabricate homogenous micro- and nano-patterns of spin crossover nanoparticles over large area (figure I.20). It was shown that the nanoparticles keep their spin crossover properties (with a transition around room T) after the soft lithography step. Therefore these low-cost patterning techniques provide interesting perspectives for the integration of spin crossover materials in micro- and nanoscaled devices.
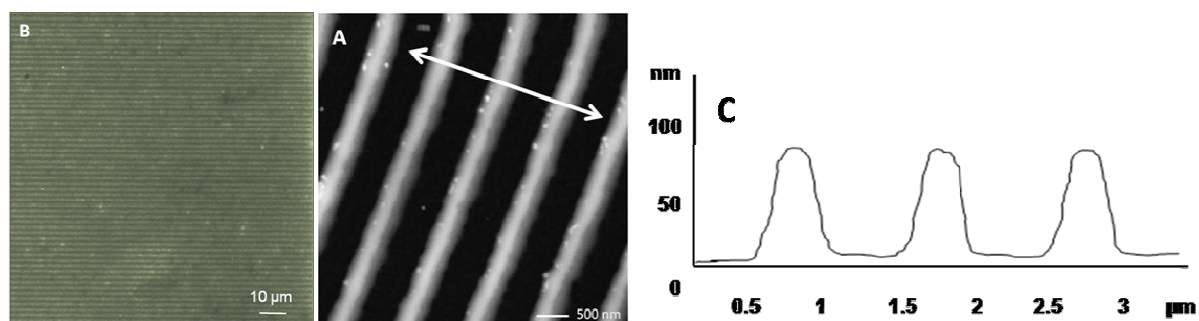
Fig.I.20: *AFM topographic images of line gratings with spin crossover nanoparticles fabricated by* μ*TM.* [Thibault 10]

I.2 Valence Tautomeric Transition Metal Complexes

Tautomerism by definition concerns all molecules which can readily interconvert into isomers by transfer of a chemical group. Valence tautomers (VTs) are a family of molecules capable of reversible interconversion between redox isomers.

In general, valence tautomerism (VT) has been associated with compounds that have the following properties:

- o A compound must contain intermolecularly–linked donor and acceptor centers that have valence electronic levels, and associated redox properties, of similar energy.
- o Electronic coupling between the donor and acceptor must be of sufficient strength to facilitate electron transfer, but not so strong that the discrete electronic structures are lost through molecular-orbital mixing.
- o The electron transfer process must have accompanying structural changes that contribute to changes in enthalpy and entropy that are of the same sign.

In general the tools used for the investigation of SCO complexes are applicable for VT complexes as well.

I.2.1 Different classes of Valence Tautomeric complexes

Most compounds that have been found to exhibit properties associated with VT consist either of a **redox active metal ion coordinated by redox active organic ligands** [Hendrickson 04] **or two redox active metal ions**, which have the potential to exhibit a charge-transfer [Mathonière 08, Bleuzen 09].

As the coordination chemistry of o-quinone ligands has developed over the past 30 years it has been found that the energy of the redox-active quinone p-orbital is quite close to the energies of transition metal d-orbitals [Hendrickson 04]. Quinone ligands coordinated as either partially reduced semiquinonates (SQ) or fully reduced catecholates (Cat) have been used most commonly (Figure.I.21).
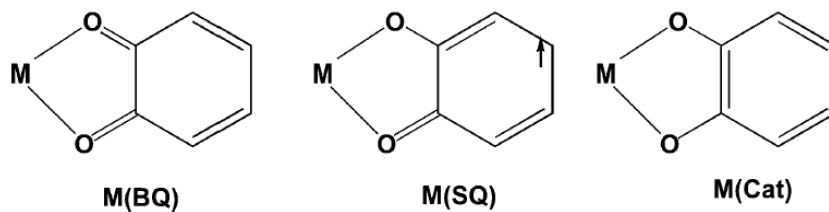
Fig.I.21: *Schematic representation of the quinone ligand, partially reduced semiquinonates (SQ) and fully reduced catecholates (Cat).* [Hendrickson 04]

Initial observations on VT were described for a complex of cobalt where the metal ion can be switched between HS-Co(II) and LS-Co(III) with electron transfer to an SQ ligand (figure I.22) [Hendrickson 04, Shultz 01]. Details of the characterization on the complexes of the Co(N-N)(SQ)(Cat) series have been described in several reviews [Hendrickson 04]. The spin state change for the metal ion that accompanies the shift in charge distribution results in a large change in magnetism for the complex, providing a convenient probe that may be used to follow changes in the concentration of redox isomers. The large changes in optical, structural and magnetic properties that accompany the valence tautomeric interconversion have potential applications in bistable molecular materials.

Fig.I.22: *Possible intramolecular electron transfer processes for a valence tautomeric cobalt complex.* [Hendrickson 04]
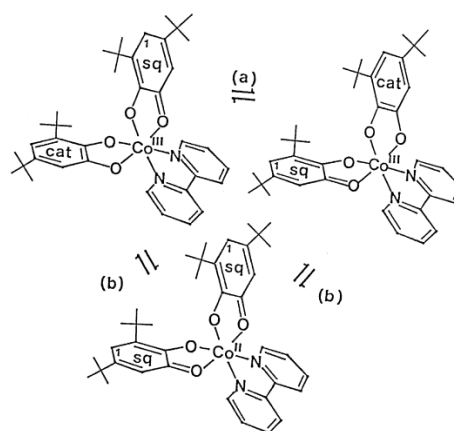
Prussian blue analogue complexes are mixed-valence compounds, which have the potential to exhibit a charge-transfer phase transition between two redox active metal ions and represented by two parabolic potential-energy curves due to valence isomers in the nuclear coordinate of the coupled vibrational mode. [Launay 82, Brown 80]

The $Na_xCo_yFe(CN)_6.zH_2O$ Prussian blue analogue is one of the best examples of compounds that can show the bistability between two phases under external stimuli, e.g. one is the phase

consisting mainly of the $Fe^{III}(t_{2g}^5 e_g^0$, LS, S=1/2)-CN-$Co^{II}(t_{2g}^5 e_g^2$, HS, S = 3/2) form (high temperature phase) and the other consisting mainly of the $Fe^{II}(t_{2g}^6 e_g^0$, LS, S = 0)-CN-$Co^{III}(t_{2g}^6 e_g^0$, LS, S = 0) form (low temperature phase). [Shimamoto 02]
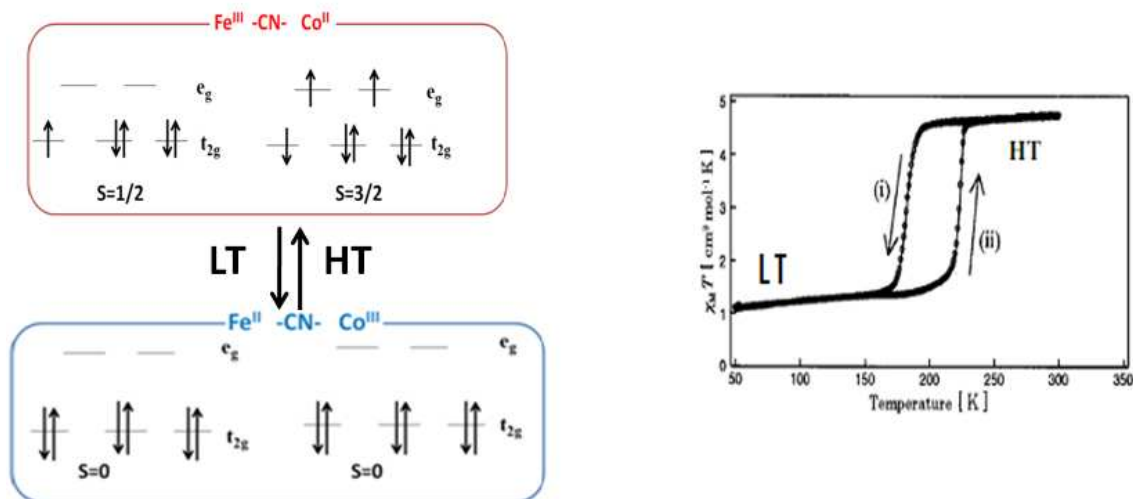
Fig.I.23: *The left part of the figure depicts the charge transfer responsible of the change of magnetization (right part of the figure) during the cooling (i) and warming (ii) process in* $Na_xCo_yFe(CN)_6.zH_2O$. [Hashimoto 02]

Another example for a CoFe system, which is also shown to possess electron transfer capability is the molecular complex $\{[pzTp)Fe^{III}(CN)_3]_4[Co^{II}(pz)_3-CCH_2OH]_4[ClO_4]_4\}\cdot 4H_2O$. In this later octanuclear complex it was found that the diamagnetic $\{Fe^{II}_4Co^{III}_4\}$ cages convert to paramagnetic $\{Fe^{III}_4Co^{II}_4\}$ ones reversibly under the influence of temperature and light. [Li 08]

I.2.2 Structure and properties of Prussian Blue Analogues

Around 1700 Prussian Blue (PB) was accidentally discovered by Diesbach, a painter from Berlin who actually tried to create a red colored paint. [Ludi 81] PB with the formula $Fe^{III}_4[Fe^{II}(CN)_6]_3 \cdot 14H_2O$ consists of $[Fe(CN)_6]$ units linked to Fe^{II} via bridging cyano ligands. Both iron ions are octahedrally surrounded (figure I.24).

The intense blue color of PB is associated with the transfer of electrons from Fe(II) to Fe(III). In other words, this mixed valence compound absorbs certain wavelengths of visible light resulting from intervalence charge transfer. In this case, light around 680 nanometers in wavelength is absorbed (E= 14100 cm^{-1}, ε = 9800 L mol^{-1} cm^{-1}) [Robin 62] and the transmitted light appears blue as a result.

The stoichiometry of prussian blue analogues (PBAs) is represented by the formula $A_xM[M'(CN)_6]y.zH_2O$ with A = {alkali} cation. In the case that M is a divalent metallic (d-block) ion and M' a trivalent metallic ion, two extreme stoichiometries exist: $AM[M'(CN)_6]\cdot H_2O$ (stoichiometric) and $M_3[M'(CN)_6]_2\cdot zH_2O$ (i.e. no alkali cation). Usually, the actual stoichiometry lies between these two extremes.
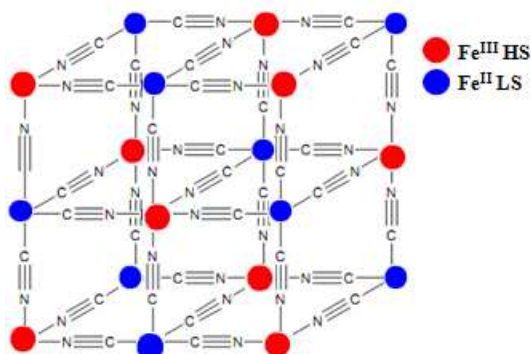
Fig.I.24: *Part of the structure of Prussian Blue (alkali ions and water molecules in the interstitial sites are omitted for clarity).*

Generally, the structure of PBAs shows a cubic lattice similar to the lattice of PB itself where either the C bound Fe ion or the N bound Fe ion or both have been replaced by a different metal ions [Ludi 70]. The space group is Fm$\overline{3}$m or F$\overline{4}$3m, but the difference lies in the precise distribution of the interstitial ions: in Fm$\overline{3}$m the ions are equally and randomly distributed over the interstitials sites, whereas in F$\overline{4}$3m two different interstitial sites exist (see Figure I.25). In the latter case, the cation has a preference for one of these sites.
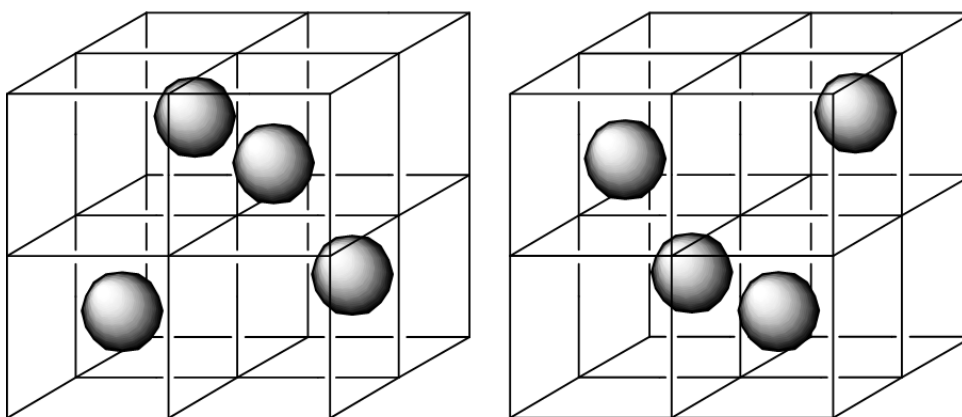
Fig.I.25: *The two different interstitial sites present (grey spheres) in a unit cell with space group F$\overline{4}$3m. Solid lines indicate the (200), (020) and (002) planes and do not represent a chemical bond.* [vertelman 09]

Occasionally, a tetragonal space group is found for PBAs, in which one of the axes of the cubic space group is elongated with respect to the other two axes [Ohkoshi 05]. This occurs mostly when a larger cation such as $N(CH_3)_4^+$ [Witzel 00] is incorporated or when a Jahn-Teller active metal ion such as Mn^{III} [Tokoro 04] is present. In special cases, when the C-M'-C or N-M-N angles are not right angles, a hexagonal space group is found [Zhang 07].

Basically in PBAs two different transition metal ions can be present. Alternatively, each of these metals can have unpaired electrons and thus give rise to a magnetic moment when placed in a magnetic field. In this way, it is possible to tune the magnetic properties of PBAs by selectively choosing the specific metal ions involved without altering the structure too much.

The group of Verdaguer et al. [Verdaguer 99] has explained how magnetic interactions in PBAs take place in a $A_xM[M'(CN)_6]_y \cdot zH_2O$ system. It is also possible to have changes in the magnetization when applying pressure [Coronado 05]. In 1996 Sato *et al.* noticed that when irradiating $K_{0.2}Co_{1.4}[Fe(CN)_6]_{6.9}H_2O$ with red light (660 nm) the magnetization below the Curie temperature was increased and the Curie temperature increased as well (Figure I.26). Conversely, when irradiating with blue light (450 nm) the reverse process took place [Sato 96]. The process could be repeated several times.
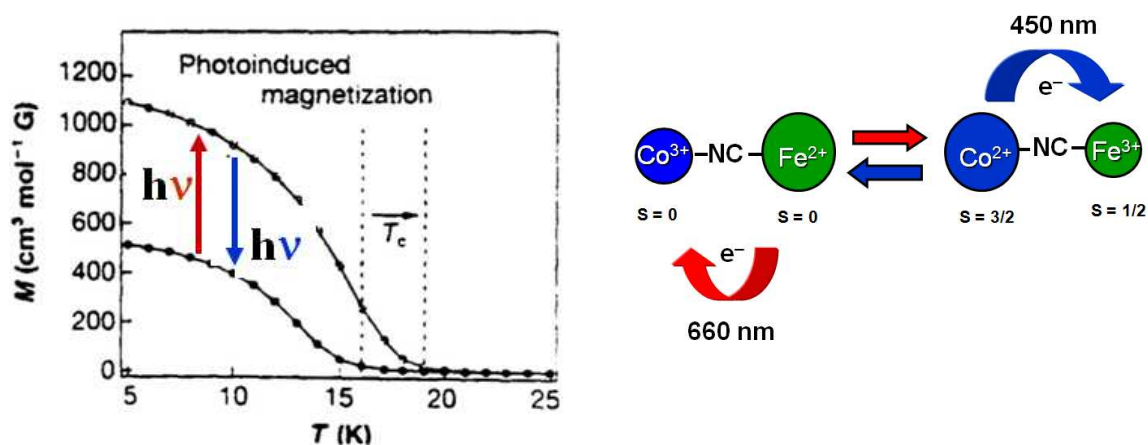
Fig.I.26: *Difference in field cooled magnetization of $K_{0.2}Co_{1.4}[Fe(CN)_6]6.9.H_2O$ before and after irradiation with 660 nm light* [Sato 99]. *The right part of the figure depicts the charge transfer responsible for the change of magnetization.*

It was found that the process involved a reversible charge transfer combined with low spin to high spin conversion from low spin Fe^{III} and high spin Co^{II} (the high temperature, HT phase) to low spin Fe^{II} and low spin Co^{III} (the low temperature, LT phase).

Soon it was discovered that also the CoFe PBAs with Na+, Rb+ and Cs+ as inserted alkali cation showed this phenomenon. [Varret 98, Escax 01, Yokoyama 98]. However, when no alkali cation was present no electron transfer takes place [Sato 99], nor when too much alkali cation was present in the network. [Bleuzen 00]

Later it was found that a similar charge transfer process takes place under the influence of temperature: [Goujon 01] when heating the magnetic susceptibility increases abruptly around a temperature ranging from 225 to 300 K. Conversely, when cooling down, the reverse process takes place, giving the entire process a broad hysteresis width. The precise transition temperatures depend strongly on the specific stoichiometry of the compound. In 2002 Shimamoto et al. [Shimamoto02] found out that within the hysteresis loop the $A_xCo[Fe(CN)_6]_y \cdot zH_2O$ system could be transformed from the LT to the HT phase with a one-shot laser pulse (6 ns) of 532 nm. Few years after the discovery of the charge transfer in Co – Fe PBA Ohkoshi *et al.* found another material displaying a temperature induced change in magnetisation: **RbMn[Fe(CN)$_6$]**. [Ohkoshi 02] On heating, the magnetic susceptibility changes abruptly from 3.16 cm^{3}K mol^{-1} at 285 K to 4.65 cm^3 K mol^{-1} at 320 K. On cooling, the reverse process takes place between 245 K and 200 K. The entire process had an unusual hysteresis width of 73 K (Figure I.27).
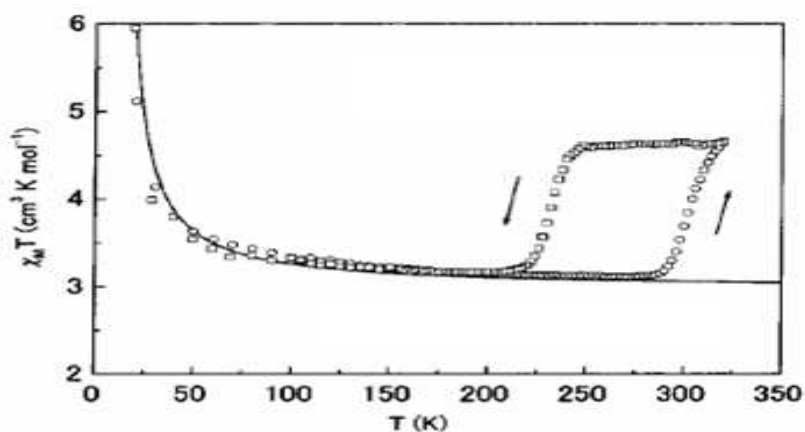
Fig.I.27: *The variation of the magnetic susceptibility with temperature for the complex RbMn[Fe(CN)$_6$].*[Ohkoshi 02]

At first it was believed that the process was due to a spin crossover of the Mn ion from intermediate spin at low temperatures to high spin at high temperatures. [Ohkoshi 02]

Later, however, Fe-C and Mn-N distances found by refining X-ray powder diffraction profiles and X-ray absorption fine structure experiments indicated that the behavior was due to a charge transfer between Mn and Fe ions. [Moritomo 02, Yokoyama 02] **At low temperatures the system consists of low spin Fe^{II} and high spin Mn^{III} (LT phase)**, whereas at high temperatures low spin Fe^{III} and high spin Mn^{II} are present (HT phase). Furthermore, the transition is accompanied by a structural phase change from cubic in the HT phase (F$\bar{4}$3m) to tetragonal (I$\bar{4}$m2) in the LT phase, due to a Jahn-Teller distortion of the Mn^{III} ion. The LT phase orders ferromagnetically below 12 K. [Ohkoshi 05, Tokoro 03] It was observed also that the broadness of the hysteresis and the specific temperatures at which the temperature induced phase transitions take place is dependent on the specific stoichiometry. [Cobo 05] In this case though, the most complete charge transfer takes place when the ratio is close to Rb:Mn:Fe = 1:1:1. As already mentioned, the valence-tautomeric thermal phase transition is entropy driven. Cobo *et al.* [Cobo 07] claimed that the phase transition is accompanied by an important change in the entropy of mainly vibrational origin, which is reflected in the clear changes observed in low frequency Raman spectra. The electronic contribution to the change in entropy is about 7.3 J K^{-1}mol^{-1} (ΔS_{el} = Rln (12/5)) [Cobo 07].
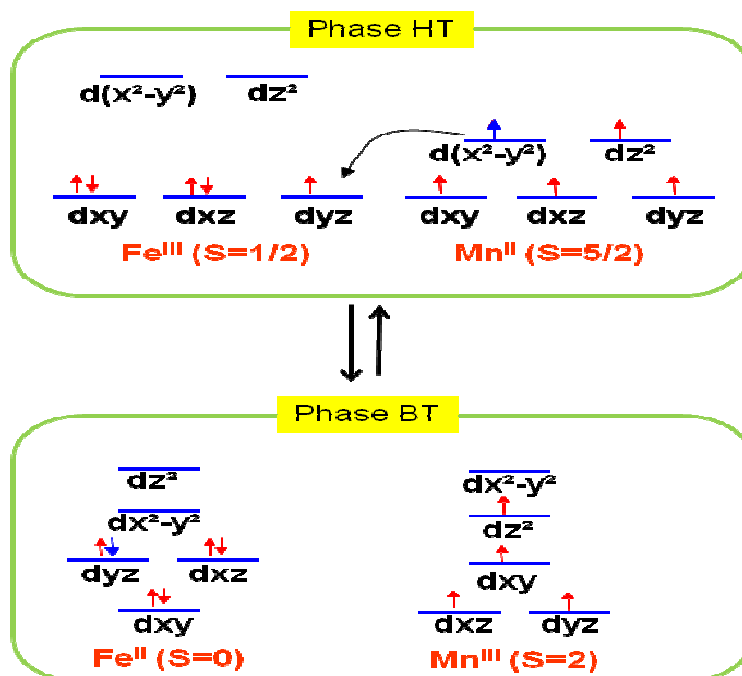
Fig.I.28: *Charge transfer process in Rb$_x$Mn[Fe(CN)$_6$]$_y$.zH$_2$O.*

Soon after the observation of temperature induced changes also a photo-induced phase transition from the LT to the HT phase were realized. This transition was induced at 3 K using a one-shot-laser-pulse of 532 nm. [Tokoro 03-05] The discovery of the reverse transition from this photo-induced HT phase back to the LT phase took quite some time: only very recently it was found that irradiation with 410 nm light gives the reverse phase transition.[Tokoro08]

Rapidly cooling the HT phase leads to 'trapping' of the HT phase at very low temperatures. [Tokoro 55] The trapped phase is slightly different from the photo-induced HT phase at low temperatures in that it has a somewhat larger unit cell, but the space group is still F-43m. When $RbMn[Fe(CN)_6]$ is irradiated with laser light (λ = 1064 nm) the evolving of 532 nm light is observed, indicating second harmonic generation by the material. [Ohkoshi 05]

In $Rb_{0.82}Mn[Fe(CN)_6]_{0.94}.H_2O$ Ohkoshi et al.[Ohkochi07] found a hysteresis loop in the polarization with electric field, which according to the authors indicates that ferroelectricity is present. Because $Rb_{0.94}Mn[Fe(CN)_6]_{0.98}.0.4H_2O$ does not show this hysteresis loop, the authors related the observed ferroelectricity in the previous compound to mixing of Fe^{II}, Fe^{III}, Fe vacancies, Mn^{II} and Jahn-Teller distorted Mn^{III}.

II.1.5 References

C. Arnaud, T. Forestier, N. Daro, E. Freysz, J.- F. Letard, G. Pauliat, G. Roosen, *Chem. Phys. Lett*. 470, **2009**, 131 – 135.

V. Balzani, A. Credi, FM. Raymo, JF. Stoddart Angew Chem Int Ed 39, **2000**, 3348.

W. A. Baker, H. M. Bobonich, *Inorg. Chem*. 3, **1964**, 1184.

C. M. Bell, M. F. Arendt, L. Gomez, R. H. Schmeh, T. E. Mallouk, *J. Am. Chem. Soc*.116, **1994**, 8374.

A. Bleuzen, C. Lomenech, V. Escax, F.Villain, F.Varret, C.Cartier dit Moulin,; M.Verdaguer, *J.Am.Chem.Soc*, 122, **2000**, 6648.

A. Bleuzen, V. Marvaud, C. Mathoniere, B. Sieklucka, M. Verdaguer, *Inorg. Chem*, 48, **2009**, 3453.

M. L. Boillot, J. Zarembowitch, J. P. Itié, A. Polian, E. Bourdet, J. Haasnot, *New J. Chem. Solids* 26, **2002**, 313.

I. Boldog, A. B. Gaspar, V. Martnez, P. Pardo-Ibanez, V. Ksenofontov, A. Battacharjee, P. Gutlich, J. A. Real, Angew. Chem. Int. Ed. 47, **2008**, 6433 – 6437.

S. Bonhommeau, G. Molnár, A. Galet, A. Zwick, J.A. Real, J.J. McGarvey, A. Bousseksou, *Angew. Chem. Int. Ed*. 44, **2005**, 4069.

S. Bonhommeau, G. Molnár, M. Goiran, K. Boukheddaden, A. Bousseksou, *Phys. Rev. B*, 74, **2006**, 064424.

A. Bousseksou, G. Molnár, P. Demont, J. Menegotto, *J. Mater. Chem. 13*, **2003**, 2069.

A. Bousseksou, G. Molnár, J. P. Tuchagues, N. Menendez, E. Codjovi, F. Varret, *C. R. Chim,* 6, **2003**, 329.

A. Bousseksou, J. McGarvey, F. Varret, J.A. Real, J.-P. Tuchagues, A.C. Dennis , M.L. Boillot, *Chem. Phys. Lett*, **2000**, *318*, 409.

A. Bousseksou, N. Nègre, M. Goiran, L. Salmon, J.-P. Tuchagues, M. Boillot, K. Boukheddaden, F. Varret, *Eur. Phys. J. B*, **2000**, *13*, 451.

A. Bousseksou, K. Boukheddaden, M. Goiran, C. Consejo, M-L. Boillot, J-P. Tuchagues, *Phys. Rev. B* 65, **2002**, 172412.

A. Bousseksou, G. Molnár, J. P. Tuchagues, N. Menendez, E. Codjovi, F. Varret, *C. R. Chim,* 6, **2003**, 385.

A. Bousseksou, F. Varret, M. Goiran,K. Boukheddaden, J. –P. Tuchagues, *Top. Curr. Chem,* 235, **2004**, 65.

D.B. Brown, Mixed Valence compounds; NATO ASI; Reidel: Dordrecht, **1980.**

L. Cambi, A. Cagnasso, Atti. Accad. Naz. Lincei, 13,**1931**, 809.

L. Cambi, L. Malatesta, Ber. Dtsch. Chem. Ges, 70, **1937**, 2067.

S. Cobo, G. Molnár, J. A. Real, A. Bousseksou, *Angew. Chem. Int. Ed., 45,* **2006**, 5786.

S. Cobo, R. Fernandez, L.Salmon, G. Molnar, A. Bousseksou, Eur. J. Inorg.Chem, **2007**, 1549.

S.Cobo, D. Ostrovskii, S. Bonhommeau, L. Vendieer, G. Molnar, L . Salmon, Koichiro Tanaka, A. Bousseksou,, J. Am. Chem. Soc, 130 **2008**, 9019.

E. Coronado, M. C. Gimenez-Lopez, G. Levchenko, F. M. Romero, V. Garcia-Baonza, A. Milner, M. Paz-Pasternak, J. Am. Chem.Soc, 127, **2005**, 4580.

E. Coronado, J. R. Galán-Mascarós, M. Monrabal-Capilla, J. Garciía-Martínez, P. Pardo -Ibánez, *Adv. Mater, 19*, **2007**, 1359–1361.

S. Decurtins, P. Gütlich, C. P. Köhler, H. Spiering, A. Hauser, *Chem. Phys. Lett. 105*, **1984**,1.

S. Decurtins, P. Gütlich, K.M. Hasselbach, A. Hauser, H. Spiering, *Inorg. Chem*, 24, **1985**, 2174.

F. Diederich, Chem. Commun, 219, **2001**.

V. Escax, A. Bleuzen, C. Cartier dit Moulin, F. Villain, A. Goujon, F.Varret, M. Verdaguer, J. Am. Chem. Soc, 123, **2001**, 12536.

M. N. Greenwood, T. G. Gibb, *Mössbauer Spectroscopy*, **1971**, Chapman and Hall Ltd, London.

A. Goujon, F.Varret, V.Escax, A.Bleuzen, M. Verdaguer, Polyhedron, 20, **2001**, 1339.

P. Guionneau, J. Gaultier, D. Chasseau, G. Bravic, Y. Barrans, L. Ducasse, D. Kanazawa , P. Day, M. Kurmoo, *J. Phys. I France,* 6,**1996**, 1581.

P. Gütlich, A. Hauser, and H. Spiering, Angew. Chem., Int. Ed. Engl., 33, **1994**, 2024.

P. Gütlich, H. A. Goodwin, *Top. Curr. Chem.* 233, **2004**, 1.; P. Gütlich, A. B. Gaspar, V. Ksenofontov, Y. Garcia, *J. Phys. Condens. Matter*. 16, **2004**, 1087.

A. Hauser, *Chem. Phys. Lett*, 124, **1986**, 543.

A. Hauser, *J. Chem. Phys*, 94, **1991**, 2741.

A. Hauser, *"Ligand field theoretical considerations"*, in *Top. Curr. Chem., Spin Crossover in Transition Metal Compounds I*, *233*, **2004**, 49.

A. Hauser, *"Light-Induced Spin Crossover and the High-Spin$\rightarrow$ Low-Spin Relaxation"*, in *Top. Curr. Chem., Spin Crossover in Transition Metal Compounds II*, *234*, **2004**, 155.

David N. Hendrickson. Cortlandt G. Pierpont," Valence Tautomeric Transition Metal Complexes", *Top Curr Chem* 234, **2004**, 63.

A. Jaiswal, S. Floquet, M. L. Boillot, P. Delhaès, *Chem. Phys. Chem*, 12, **2002**, 1045.

O. Kahn, C. Jay-Martinez, *Science* 279, **1998**, 44.

E. König, G. Ritter, S. K. Kulshreshtha, J. Waigel, and H. A. Goodwin, *Inorg. Chem.*, 23, **1984**, 1896.

E. König, "Nature and dynamics of the spin-state interconversion in metal complexes", in Struct. Bonding, Springer-Verlag, Berlin Heidelberg New York, 76,**1991**, 51.

V. Ksenofontov, G. Levchenko, H. Spiering, P. Gütlich, J. -F. Létard, Y. Bouhedja , O. Kahn, *Chem Phys. Lett*. 294, **1998**, 545.

V. Ksenofontov, A. B. Gaspar, P. Gütlich, *Top. Curr. Chem* 235, **2004**, 23.

W. Kosaka, T. Ishihara, H. Yashiro, Y.Taniguchi, K. Hashimoto, S.-I. Ohkoshi, Chem. Lett., 34, **2005**, 1278.

J. Larionova, L. Salmon, Y. Guari, A. Tokarev, K. Molvinger, G. Molnár, A. Bousseksou, *Angew. Chem. Intl. Ed.*, *47*, **2008**, 8236.

J. P. Launay, F. Babonneau, *Chem. Phys*. 67, **1982**, 295.

J. Lejay, A.G.M. Jansen, P. Wyder, *Phys. Rev. B,* 43, **1991**, 8196.

J.-F. Léard, O. Nguyen, H. Soyer, C. Mingotaud, P. Delhaes, O. Kahn, *Inorg. Chem*. 38, **1999**, 3020.

J.-F. Létard, P. Guionneau, L. Goux-Capes, *Top. Curr. Chem*. 235, **2004**, 221–249.

D. Li, R. Clérac, O. Roubeau, E. Harté, C. Mathoniere, R, Le Bris, SM. Holmes, *J. Am. Chem. Soc*, 130, **2008**, 252.

A. Ludi, H.-U. Gudel, M. Ruegg, Inorg. Chem., 9, **1970**, 2224.

A. Ludi, J. *Chem. Edu*., 58, **1981**, 1013.

C. Mathonière, H. Kobayashi, R. Le Bris, A. Kaiba, I. Bord, *C. R. Chimie*, 11, **2008**, 665.

M. Matsuda, H. Tajima, *Chem. Lett.*, *36*, **2007**, 700.

J. J. McGarvey, I. Lawthers, *J. Chem. Soc., Chem. Comm*, **1982**, 906.

A. Milner, M. Paz-Pasternak, *J. Am. Chem. Soc*., 127, **2005**, 4580.

G. Molnár, V. Niel, J-A. Real, L. Dubrovinsky, A. Bousseksou, J. J. McGarvey, *J. Phys. Chem. B*, 107, **2003**, 3149.

G. Molnár, S. Cobo, J. A. Real, F. Carcenac, E. Daran, C. Vieu, A. Bousseksou, *Adv. Mater*., *19*, **2007**, 2163.

Y. Moritomo, K. Kato, A. Kuriki, M. Takata, M. Sakata, H. Tokoro, S.-I. Ohkoshi, K. Hashimoto, *J. Phys. Soc. Jpn*., 71, **2002**, 2078.

Y. Moritomo, M. Hanawa, Y. Ohishi, K. Kato, M. Takata, A. Kuriki, E. Nishibori, M. Sakata, S.-I. Ohkoshi, H. Tokoro, K. Hashimoto, *Phys. Rev. B*, 68, **2003**,144106.

T. Nuida, T. Matsuda, H. Tokoro, S. Sakurai, K. Hashimoto, S.-I. Ohkoshi, *J. Am. Chem. Soc*, 127, **2005**, 11604.

Masaaki Ohba, Ko Yoneda, Gloria Agusti, M. Carmen Muñoz, Ana B. Gaspar, José A. Real, Mikio Yamasaki, Hideo Ando, Yoshihide Nakao, Shigeyoshi Sakaki, and Susumu Kitagawa *Angew. Chem. Int. Ed*. 48, **2009**, 4767.

S.-I. Ohkoshi, H. Tokoro, M. Utsunomiya, M. Mizuno, M. Abe, K. Hashimoto, *J. Phys. Chem. B*, 106, **2002**, 2423.

S.-I. Ohkoshi, H. Tokoro, K. Hashimoto, *Coord. Chem. Rev*., 249, 2005, 1830.

S.-I. Ohkoshi, H. Tokoro, T. Matsuda, H.Takahashi, H. Irie, K. Hashimoto, *Angew. Chem. Int. Ed*., 46, **2007**, 3238.

Y. Qi, E. W. Muller, H. Spiering, P. Gütlich, *Chem. Phys. Lett*, 101, **1983**, 503.

M. B. Robin, *Inorg. Chem*. 1, **1962**, 337.

M. B. Robin, P. Day, Adv. *Inorg. Chem. RADIOCHEM*, 10, **1967**, 247.

L. Salmon, G. Molnár, D. Zitouni, C. Quintero, C. Bergaud, J.- C. Micheau A. Bousseksou, *J. Mater. Chem*. 20, **2010**, 5499.

N. Sasaki, T. Kambara, *J. Phys. C: Sol. State. Phys*, 15, **1982**, 1035.

O. Sato, T. Iyoda, A. Fujishima, K. Hashimoto, *Science*, 272, **1996**, 704.

O. Sato, Y. Einaga, A. Fujishima, K. Hashimoto, *Inorg. Chem*., 38, **1999**, 4405.

A. Scuiller, C. Train, R. Garde, G. Gelly, C. Lomenech, I. Rosenman, P.Veillet, C. Cartier, F. Villain, *Coord. Chem. Rev*. 190-192, **1999**, 1023.

M. Seredyuk, Ana B. Gaspar, V. Ksenofontov, S. Reiman, Y. Galyametdinov, W. Haase, E. Rentschler, P. Gütlich., *Chem. Mat*., 18, **2006**, 2513.

N. Shimamoto, S.-I. Ohkoshi, O. Sato, K. Hashimoto, *Chem. Lett*., **2002**, 486.

N. Shimamoto, S-I. Ohkoshi, O. Sato, K. Hashimoto, *Inorg. Chem*. 41, **2002,** 678-684.

D. N. Shultz, In Magnetism-From Molecules to Materials; Miller, J.S.;Drillon, M. *Eds.,wiley, VCH: Weinheim-New york*, **2001**.

C.P. Slichter, H.G. Drickamer, *J. Chem. Phys*., 52, **1972**, 2142.

M. Sorai, S. Seki, *J. Phys. Chem. Solids*, 35, **1974**, 555.

P D. Southon, L Liu, E A. Fellows, DJ. Price, GJ. Halder, KW. Chapman, B Moubaraki, KS. Murray, JF. Létard, CJ. Kepert, *J. Am. Chem. Soc*, 131, **2009**, 8025.

H. Soyer, C. Mingotaud, M. L. Boillot, P. Delhaès, *Langmuir*, 14, **1998**, 5890.

S. Sugano, Y. Tanabe, H. Kamimura, *Pure. Appl. Phys*, **1970**, 33.

J. H. Takemoto, B. Hutchinson, *Inorg. Nucl. Chem. Lett. 8*, **1972**, 769.

J. H. Takemoto , B. Hutchinson, *Inorg. Chem. 12*, **1973**, 705.

C. Thibault, G. Molnar, L. Salmon, A. Bousseksou, C. Vieu, *Langmuir*, 26, **2010**, 1557.

H. Tokoro, S.-I. Ohkoshi, K. Hashimoto, *Appl. Phys. Lett.*, 82, **2003**, 1245.

H. Tokoro, T. Matsuda, K. Hashimoto, S.-I. Ohkoshi, *J. Appl. Phys.*, 97, **2005**, 10M508.

H. Tokoro, S. Miyashita, K. Hashimoto, S.-I. Ohkoshi, *Phys. Rev. B*, 73, **2006**, 172415.

H. Tokoro, T. Matsuda, S.Miyashita, K. Hashimoto, S.-I. Ohkoshi, *J. Phys. Soc. Jpn*., 75, **2006**, 085004.

H. Tokoro, T. Matsuda, T. Nuida, Y. Moritomo, K. Ohoyama, E. D. Loutete Dangui, K. Boukheddaden, S.-I. Ohkoshi, *Chem. Mater.*, 20, **2008**, 423.

J.-P. Tuchagues, A. Bousseksou, G. Molnar, J.J. Mc Garvey , F.Varret, "Isokinetic and Isoequilibrium Relationships in Spin Crossover Systems", *in Top. Curr. Chem., Spin Crossover in Transition Metal Compounds III*, 235, **2004**, 85.

F. Varret, H. Constant-Machado, J. L. Dormann, A. Goujon, J. Jeftic, M. Nogues, A. Bousseksou, S. I. Klokishner, A. Dolbecq, M. Verdaguer, *Hyperfine Inter.*, 113, **1998**, 37.

F. Varret, *C.R. Chimie* **2003**, *6*, 329.

F. Varret, A. Bleuzen, K. Boukheddaden, A. Bousseksou, E. Codjovi, C. Enachescu, A. Goujon, J. Linares, N. Menendez, M. Verdaguer, *Pure. Appl. Chem*, 74-11, **2002**, 2159.

M. Verdaguer, A. Bleuzen, V. Marvaud, J. Vaissermann, M. Seuleiman, C. Desplanches, A. Scuiller, C. Train, R. Garde, G. Gelly, C. Lomenech, I. Rosenman, P.Veillet, C. Cartier, F. Villain, *Coord. Chem. Rev*. 190-192, **1999**, 1023.

E. J. M. Vertelman, E. Maccallini, D. Gournis, P. Rudolf, T. Bakas, J. Luzon, R. Broer, A. Pugzlys, T. T. A. Lummen, P. H. M. van Loosdrecht, P. J. van Koningsbruggen, *Chem. Mater.* 18, **2006**, 1951.

E, J, M Vertelman, *Ph.D. thesis*, **2009**, University of Groningen, Zenike Insitute for Advanced Materials, Netherland.

F. Volatron, L. Catala, E. Rivière, A. Gloter, O. St_phan, T. Mallah, *Inorg. Chem.* 47, **2008**, 6584 – 6586.
P. A. Wicklund, L. S . Becckmann, D. G. Brown, *inorg. Chem.* 15, **1976**, 1996.

M. Witzel, B. Ziegler, D. Babel, Z. Anorg. Allg.Chem.*, 626, **2000**, 471.

T. Yokoyama, T. Ohta, O. Sato, K. Hashimoto, *Phys. Rev. B*, 58, **1998**, 8257.

T. Yokoyama, M. Kigushi, T. Ohta, O. Sato, Y. Einaga, K. Hashimoto, *Phys. Rev. B*, 60, **1999**, 9340.

T. Yokoyama, H. Tokoro, S.-I. Ohkoshi, K. Hashimoto, K. Okamoto, T. Ohta, *Phys. Rev. B*, 66**, 2002**, 184111.

L.-P. Zhang, X.-J. Zhou, T. C. W. Mak, P. A. Tanner, *Polyhedron*, 26, **2007**, 4019.

Chapter II: Electrical investigation of switchable molecular compounds

Altering the properties of materials by an external perturbation is highly attractive for the construction of switches and memory devices. Indeed much research has been directed towards the development of electrically switchable optical materials for applications in memory and display devices as well as for smart mirrors and windows to control the flow of light and heat into and out of glazing. [Lamber 98, Waser 03] Research is now focusing on investigating other novel switching mechanisms that can be induced by an electric field such as metal-insulator transitions [Kanki 03] or exotic electric – field - induced phenomena – nonlinear resistance effects.

Here we present the observation of an electric field-induced charge transfer phase transition in cyanometallate complexes, involving changes in their magnetic, optical and electronic properties as well. The idea comes from the fact that cyano – bridged metallocomplexes can exhibit intervalence charge transfers, in which an electron transfer occurs between two metal ions, which can be induced by an external stimulus (T, P, B, hυ). This means that, using an external electric field as stimulus within the hysteresis loop could therefore be expected to induce the interconversion between the two states, triggering a nonlinear change in the material's properties.

In the first part of this chapter we report on the charge transport and dielectric properties of the bistable valence tautomeric complexes in a broad frequency range (10^{-2} – 10^6 Hz) including RbMnFe and NaCoFe type Prussian blue analogues as well as a Co –W bimetallic complex. Then we will discuss the first experimental observation of an electric field induced switching on these compounds and we propose a mechanism to explain the observed phenomena. In the last part of the chapter, we will report on the hysteretic bistability in the electrical properties of the bulk {Fe(HB(pz)$_3$)$_2$} spin crossover complex. Synthesis, characterization and dielectric properties of {Fe(HB(pz)$_3$)$_2$}thin films will be also reported. This work will be summarized by building a prototype of a read-only memory (ROM) device based on {Fe(HB(pz)$_3$)$_2$} SCO thin films, thanks to the significant switch of the conductivity in the two spin states, which suggests that I – V measurements can be used to read the information stored in the bistable system.

II.1 Charge transport and dielectric properties of valence tautomeric complexes

A few investigations have already considered the electrical conductivity of valence tautomeric complexes in the solid state, namely Prussian blue and its analogues.[Tennakone 83, Xidis 91] Similar to other low-mobility, disordered solids the charge transport is thought to take place in these materials due to hopping conduction. In general, a nearest neighbor electron transfer is considered as the predominant process, but ionic conductivity may also occur to some extent, especially in wet samples. In this latter case, apparently, alkali metal ions are transported in their hydrated forms and the water molecules present in the interstices lower significantly the barriers to the movement of these ions. In any case, the charge transport is accompanied by dipole relaxation phenomena. In samples with low water content, the dipole motion corresponds to the intervalence charge transfer between the two transition metal sites (M_A^{2+}-CN - M_B^{3+} $\leftrightarrow$ M_A^{3+}- CN - M_B^{2+}). By determining the rate at which these dipole moments are oscillating, one can determine thus the rate of the intervalence electron transfer. Unfortunately, the comparison of data obtained on different samples is not straightforward owing to their non-stoichiometric, disordered nature and the presence of water in the interstices of the lattice, which are difficult to control in the experiments. For this reason, **the possibility to investigate the same sample in the same conditions (T, P, etc.), but in two different electronic states (co-existing within a large thermal hysteresis region) offers a unique opportunity to investigate the mechanism of the charge transport in this family of compounds** and in particular the influence of the electronic and crystallographic structure on the site-to-site electron hopping process and associated dipole relaxation phenomena. **Besides these fundamental aspects it is also of interest to see if the conductivity changes accompanying the phase transition in this type of compounds can be sufficiently important to be eventually used in practical applications**, such as memory or switching devices.

II.1.1 Experimental setup

Dielectric spectroscopy measures the dielectric permittivity as a function of frequency and temperature. Thus it is an informative technique used to determine the molecular motions and structural relaxations present in polymeric materials possessing permanent dipole moments. In general, to carry out dielectric measurements, the material is submitted to a sinusoidal voltage; this process causes alignment of dipoles in the materials, which results in polarization. The polarization will cause the output current ($I(t) = I_m \sin(\omega t + \varphi) = Re\{I^*_m e^{i(\omega t + \varphi)}\}$) to lag behind the applied electric voltage ($U(t) = U_m \sin(\omega t) = Re\{U^*_m e^{i(\omega t)}\}$) by a phase shift angle, φ. The magnitude of the phase shift angle is determined via measuring the resulting current. The complex capacitance $C^*(\omega)$, the admittance $Y^*(\omega) = i\omega C^*(\omega)$, and its reciprocal value $Z^*(\omega) = 1/Y^*(\omega)$, the impedance, are measured over a range of temperature and frequency, and are related to the dielectric permittivity, ε', and the dielectric loss factor, ε'' by a useful quantity called the loss:

$$\tan \delta = C''/C' = \varepsilon''/\varepsilon' = Z'/Z'' = Y''/Y'$$

where $\delta = \pi/2 - \varphi$ is the loss angle. The permittivity, ε', represents the amount of dipole alignment (the energy stored) and the loss factor, ε'', measures the energy required to align dipoles or move ions. The basic principle of the measurement is shown in Fig II.1. Typically a sinusoidal voltage $U_1(t)$ with frequency $\omega/2\pi$ is applied to the sample by a generator, covering the frequency range from 10^{-2} to 10^6 Hz. The resistor R converts the sample currents $I_s(t)$ into a voltage $U_2(t)$. The complex sample impedance Z^*_s is calculated from the measured data by:

$$Z^*_s = U^*_s(\omega) / I^*_s(\omega) = R (U^*_1(\omega) / U^*_2(\omega) - 1)$$

The complex conductivity $\sigma^*(\omega)$ was determined from the complex impedance $Z^*_s(\omega)$ and the sample geometry:

$$\sigma^*(\omega) = 1/Z^*_s(\omega) \, e/S$$

where e is the sample thickness and the S the sample surface.

In collaboration with Philippe Demont at the "CIRIMAT" in Toulouse, the dc and ac conductivity measurements have been carried out in a two-probe geometry either on powder samples (diameter 10 mm, thickness ca. 0.1 mm) contained in a Teflon sample holder between two stainless steel electrodes or on pellets (diameter 3.3 mm, thickness 0.4 mm) compacted at a pressure of 70 bars for 5 min. There were no significant differences in conductivities or magnetic susceptibilities between the powder samples and pellets, though the latter gave, in general, somewhat better results in terms of standard deviation of the measured conductivity values. In the case of single crystals (ca. 1 mm size) electrical contacts were fixed using a silver paste. Direct current as a function of applied dc voltage (0.05 - 20 V) and temperature (160-350 K) were measured using a Keithley 617 electrometer and a home-built, electrically shielded, He exchange gas cryostat. The temperature was varied at a rate of 1 $Kmin^{-1}$. AC conductivity measurements were carried out as a function of frequency (10^{-2} – 10^6 Hz) and temperature (100 - 350 K) by means of a broadband dielectric spectrometer (Novocontrol BDS 4000 coupled to a Quatro Cryosystem) at an applied ac voltage ranging from 50 mV to 3 V rms. Frequency sweeps were carried out isothermally. Variable-temperature dc magnetic susceptibility measurements were carried out on powder, pellet and single crystal samples at heating and cooling rates of 1 $Kmin^{-1}$ using a Quantum Design MPMS2 SQUID magnetometer operated at 2 T magnetic field. The magnetic properties of the samples have been checked several times during the experiments and no significant evolution has been observed.
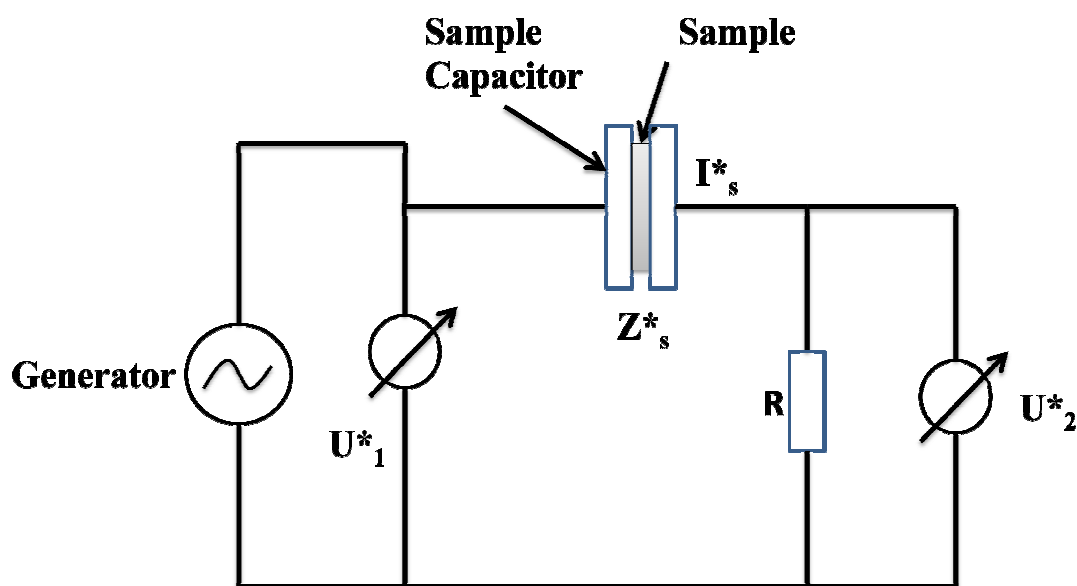

Fig.II.1: *Simplified scheme of the dielectric spectroscopy setup.*

II.1.2 $Rb_xMn[Fe(CN)_6]_y \cdot zH_2O$

We have studied the charge transport in valence-tautomeric $Rb_xMn[Fe(CN)_6]_y.zH_2O$ samples with different stoichiometries, which have been synthesized following the "method 2" described in Ref. [Vertelman 06]. The precipitates were filtered, washed with water, dried at 90 °C and kept in a desiccator at room temperature between the different measurements. The composition of the obtained brown powders was established from elemental analysis as $Rb_{0.76}Mn[Fe(CN)_6]_{0.91}.1.6H_2O$ (**1**), $Rb_{0.82}Mn[Fe(CN)_6]_{0.96}.0.7H_2O$ (**2**), $Rb_{0.96}Mn[Fe(CN)_6]_{0.98}\bullet0.75H_2O$ (**3**), and $Rb_{0.38}Mn[Fe(CN)_6]_{0.82}.4.5H_2O$ (**4**). Single crystals of $RbMn[Fe(CN)_6].H_2O$ (**5**) were grown by the method described in Ref. [Vertelman 08].

The temperature dependence of the effective magnetic moment (μ_{eff}) and the temperature dependence of the dc conductivity, σ_{dc}, (measured at 2 V and 20 V) of sample (**1**) are shown in Figure II.2.
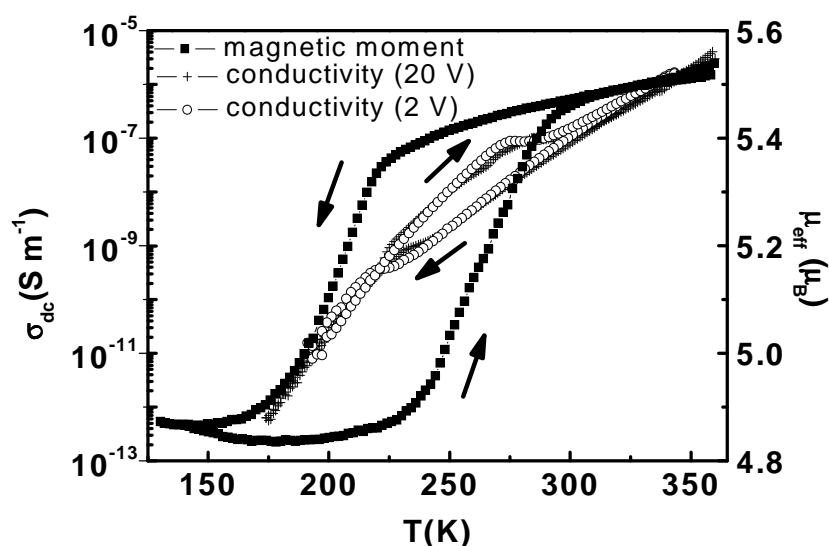
Fig.II.2: *Temperature dependences of the dc conductivity (measured at 2 and 20 V bias) and the effective magnetic moment for sample* ***1***.

The μ_{eff} value at 300 K (HT phase) is 5.5 μ_B. When decreasing the temperature μ_{eff} decreases slowly and drops more abruptly between *ca.* 210 and 190 K. At 150 K it reaches the value of 4.9 μ_B. When heating the sample the reverse transition occurs in the 235 – 295 K temperature range. It should be noticed that the HT value of the magnetic moment differs significantly from the expected spin-only value of 6.1 μ_B. Such differences have been observed previously [Vertelman 06] and can be attributed to the incomplete nature of the phase transition. However at 300 K the electrical conductivity is *ca.* 10^{-7} S.m^{-1}, which is two orders of magnitude higher

than that reported for vacuum-dried Prussian blue.[Tennakone 83] σ_{dc} is strongly thermally activated in the investigated temperature range and drops to 10^{-12} S.m^{-1} at 180 K. The conductivity displays a large thermal hysteresis loop between *ca.* 220 and 300 K. The hysteresis region on the high temperature side corresponds well to the magnetic data, but a significant difference is observed on the low temperature side. Between 210 and 170 K, where the HT phase transforms to the LT phase, the conductivity has a similar value independently if it is recorded in the heating or cooling cycles. In a first instance one may suppose therefore that there is **a crossover in the conduction mechanism around 220 K** and the conductivity becomes rather insensitive to the actual electronic and crystallographic form below the crossover point.

In order to better understand the possible origin of this crossover point and the effects of the valence-tautomeric phase transition we have investigated the frequency as well as temperature dependent behavior of the complex conductance. The temperature dependence of the real part $\sigma'(\omega)$ of the ac conductivity is shown in Figure II.3 for the different samples.

In sample **1**, at 125 kHz the conductivity exhibits very weak temperature dependence and no hysteresis is observed (Figure II.3 a). At 10 mHz the temperature dependence of the ac conductivity is the same, within the measurement errors, as that of σ_{dc} (σ' (300K) = 9.6x10^{-8} S.m^{-1} and σ'(180K) = 1.3x10^{-12} S.m^{-1}). At this frequency σ' exhibits a hysteresis, which corresponds well to the hysteresis region detected by magnetic measurements, but a crossing of the heating and cooling curves occurs in the hysteresis region around 230 K – very close to the crossing observed in the dc measurement. The conductivity behavior at 30 Hz appears to be intermediate between the high- and low-frequency cases. Samples **2** and **3** exhibit somewhat different phase transition temperatures and thus the thermal hysteresis of the magnetic moment differs to some extent. For sample **2** we observed σ' (300K, 10mHz) = 5x10^{-8} S.m^{-1} and σ' (180K, 10mHz) = 1.2x10^{-12} S.m^{-1} and a conductivity hysteresis loop between 170 and 305 K with a crossover point close to 220 K (Figure II.3 b).

In the case of sample **3** the measured values - σ' (300K, 10mHz) = 1.6x10^{-8} S.m^{-1} and σ' (180K, 10mHz) = 4.2x10^{-13} S.m^{-1} – are close to those of the two other compounds. On the other hand, in this sample the phase transition is practically complete at 220 K, which explains why one cannot observe the crossover in the conductivity hysteresis (Figure II.3 c).

Similar results were obtained on the single crystal sample **5** as well (Figure II.3 e), but the ill-defined electrode geometry makes the data analysis more difficult (*vide infra*). We have also measured the ac conductivity in sample **4**, which does not exhibit charge transfer phase transition and remains in the HT phase in the whole temperature range. The conductivity of this sample was found somewhat higher than the two others (σ' (300K, 10mHz) = 7.0×10^{-7} S.m^{-1} and σ' (180K, 10mHz) = 3.2×10^{-11} S.m^{-1}) and no hysteresis of σ occurs (Figure II.3 d).
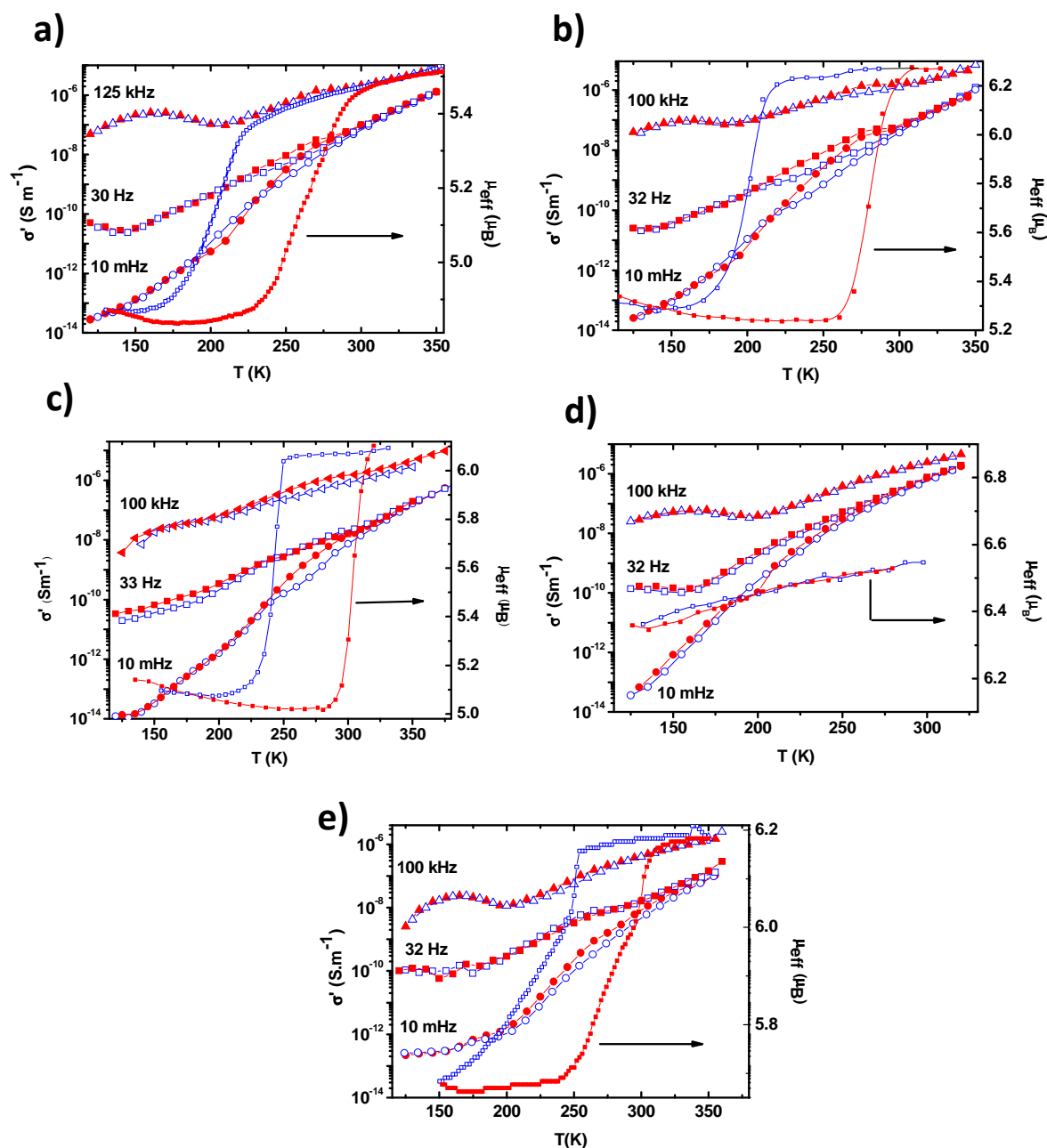

Fig.II.3: *Temperature dependence of the ac conductivity at different frequencies and the effective magnetic moment for samples **1** (a), **2** (b), **3** (c), **4** (d) and **5** (e). Closed and open symbols correspond to the heating and cooling cycles, respectively. Data points are connected to guide the eye.*

The temperature dependence of the ac conductivity can be better understood from Figure II.4 which displays the frequency dependence of σ' at different temperatures for sample **2** in the heating and cooling modes. (Analogous behaviours were observed in each sample, which are omitted therefore.)
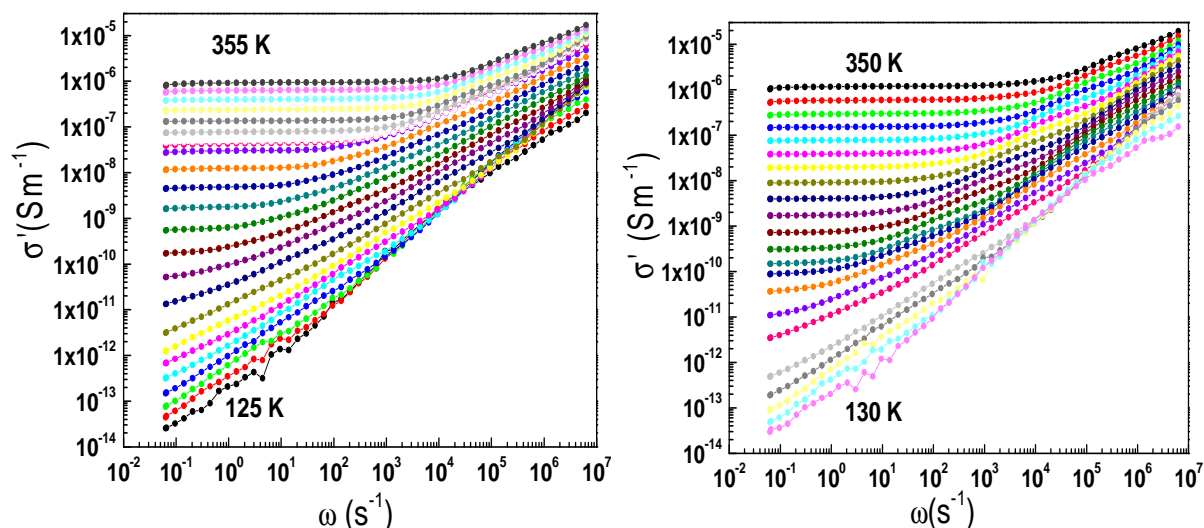
Fig.II.4: *Frequency dependence of the ac conductivity for sample **2** at fixed temperatures in the heating (left) and the cooling (right) cycles. Curves are displayed by steps of 10 K. Data points are connected to guide the eye.*

At high temperatures and low frequencies σ' is constant and equals closely the dc values. As the frequency increases a gradual dispersion sets in resulting in an apparent **power law** dependence ($\sigma' \sim \omega^n$) with an exponent $n \cong 0.6$ at high temperatures. The **crossover frequency** (ω_c) which separates the power-law and the frequency-independent (dc) regimes decreases continuously with decreasing temperature from *ca.* 0.5 kHz to 10 mHz between 345 K and 225 K. This behavior is typical to disordered solids consisting of regions with different conductivities.[Dyre 00] At high frequencies the carrier motion is localized, but as the frequency decreases charge transport must extend over longer distances and will be increasingly limited by bottlenecks of poorly conducting regions, therefore the conductivity decreases as well. The fact that the temperature dependence of σ' in the power-law regime is less pronounced is consistent with the observation that the thermal hysteresis becomes less detectable at high frequencies and low temperatures.

The measurement of the impedance allows one to determine both the complex conductivity and the complex dielectric function which are related to each other by $\sigma^* = i\omega\varepsilon_0\varepsilon^*$ (ε_0 being the permittivity of the free space).

The motion of the charge carriers in low-mobility solids is accompanied by an electrical relaxation, therefore the analysis of ε' (or σ'') can contribute to the understanding of the charge transport mechanisms. In Prussian blue analogues the electron transfer between the metallic sites is accompanied by a change in the direction of the dipole moments in the sample (for example $Mn^{II} \rightarrow Fe^{III}$ vs. $Mn^{III} \leftarrow Fe^{II}$). Therefore one can expect a significant difference in ε' with the phase transition between the HT and LT forms of $Rb_xMn[Fe(CN)_6]_y.zH_2O$. Ohkoshi *et al.* [Ohkoshi 05] reported dielectric constant measurements on this compound both in the radio-frequency (1-100 kHz) and optical (300-1000 THz) regions. Though reflecting different processes (dipolar and electronic) ε' was found to change significantly upon the phase transition in both frequency domains and the observed hysteresis loop was comparable with the magnetic susceptibility data. In our case we investigated ε' in the 10 mHz - 1 MHz frequency domain. As an example, Figure II.5 shows the thermal variations of ε' measured at 2 kHz for the different samples (with and without thermal hysteresis of the magnetic moment).

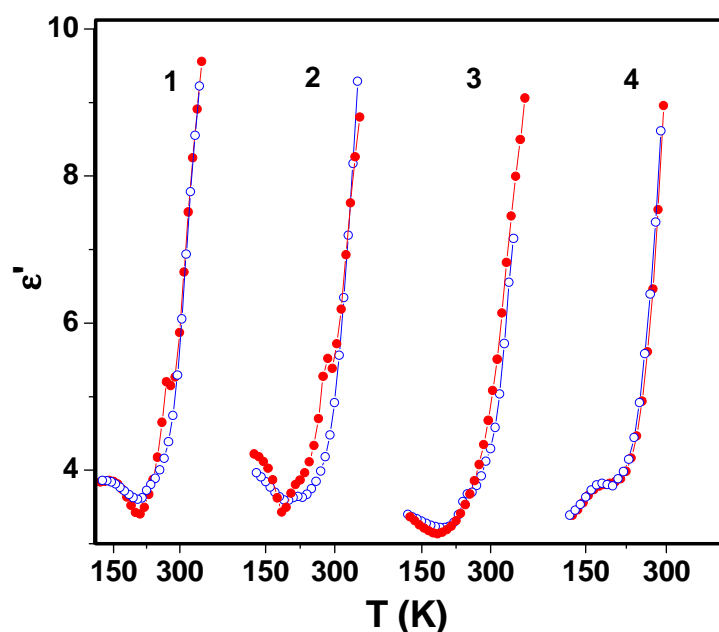***Fig.II.5:*** *Temperature dependence of the dielectric constant (ε') at 2 kHz for samples **1** - **4**. Closed and open symbols correspond to the heating and cooling cycles, respectively. Data points are connected to guide the eye.*

The main observation here is that the temperature dependence of the dielectric constant corresponds also to the hysteresis of the magnetic moment. Alike in the conductivity data, a crossing of cooling and heating curves appears in the hysteresis region close to 220 K.

Unfortunately, the frequency and temperature dependences of the dielectric permittivity are difficult to analyze, by means of the conventional Cole-Cole representation, because a strong low-frequency dispersion of ε' and ε'' appears when the temperature increases. This behavior is characteristic of charged carrier systems.[Jonscher 83] By using the electric **modulus formalism** for the treatment of dielectric data, an enhancement of the contribution of conductivity effects can be obtained.[Macedo 72] The conductivity relaxation model, in which the dielectric modulus is defined by $M^*(\omega) = 1/\varepsilon^*(\omega)$, can be used to get information about the relaxation mechanism in the absence of a well-defined dielectric loss peak. As far as conductive effects are concerned, the **electric loss moduli $M''(\omega)$** exhibit relaxation maxima in contrast to the relatively smooth patterns of $\varepsilon''(\omega)$ plots. Another advantage arises from the fact that the contribution of electrode screening effect in the low-frequency spectrum tail can be eliminated. To estimate the dielectric relaxation in $Rb_xMn[Fe(CN)_6]_y.zH_2O$ samples, the complex permittivity is converted to the complex electric modulus. As an example, Figure II.6 displays the imaginary part of the electric modulus (scaled by M''_{max}) as a function of the frequency of the electrical field (scaled by ω_{max}) at different temperatures in the heating and cooling cycles for sample **2**. (Analogous behaviours were observed for all other samples.)
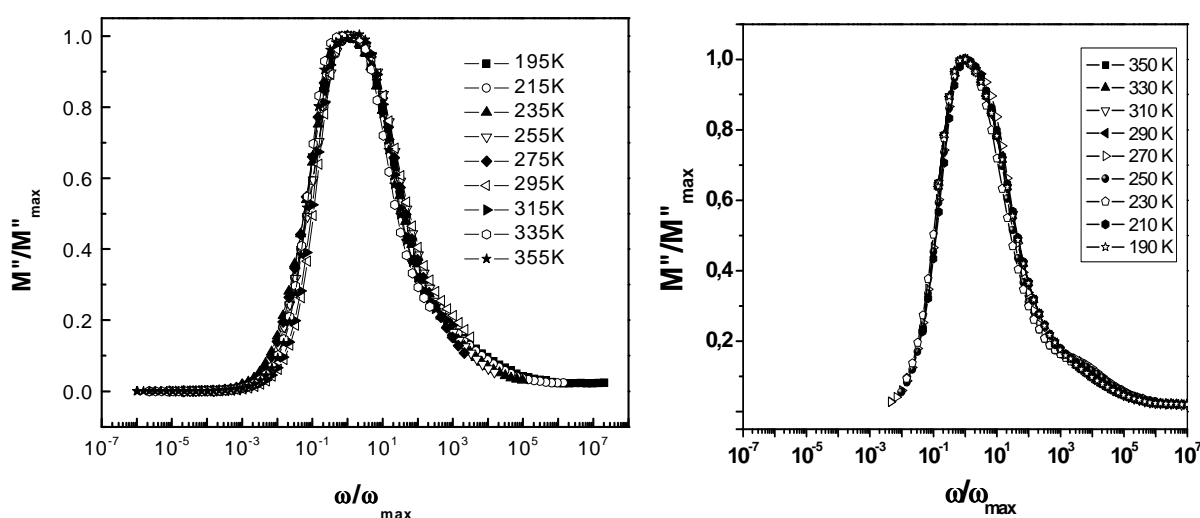

Fig.II.6: *Plot of normalized loss electric modulus (M''/M''_{max}) vs. reduced frequency (ω/ω_{max}) at various temperatures in the heating (left) and cooling (right) cycles for sample 2. Curves are displayed by steps of 20 K. Data points are connected to guide the eye.*

The perfect overlap of the curves for the investigated temperatures leads to a master curve. This means that all dynamic processes occurring at different temperatures exhibit the similar activation energy and that the distribution of relaxation time is independent of temperature. The frequency of the *M''* peak maximum is defined as **the dielectric relaxation frequency** (ω_p) and it was found to increase with increasing temperature.

II.1.2.1 Charge transport and dielectric relaxation in $Rb_xMn[Fe(CN)_6]_y \cdot zH_2O$

The temperature dependence of the dc conductivity of each $Rb_xMn[Fe(CN)_6]_y.zH_2O$ sample exhibits two regions – independently if they exhibit charge transfer phase transition or not. Above *ca.* 220 K the temperature dependence of the dc conductivity is described – as expected for a small polaron hopping mechanism - by an Arrhenius equation:

$$\sigma_{dc}(T) = (B/T) \exp(-E_{dc}/k_BT) \qquad (1)$$

The activation energy of the dc conductivity (E_{dc}) was found 0.57(1), 0.56(2), 0.51(1) and 0.43(1) eV for samples **1**, **2, 3** and **4** respectively (table 1).

The activation energies were found the same within the experimental incertitude in the HT and LT phases. (We shall note here that the E_{dc} values have been extracted actually from the frequency-independent part of the ac conductivity data – displayed in Figure II.2.) One may speculate that the smaller activation energy obtained in the case of sample **4** is due to its significantly higher water content and associated higher dielectric constant.[Tennakone 83] When the temperature decreases below *ca.* 220 K deviations from *eq. (1)* indicate the presence of a change in the conduction mechanism. In fact, the observation of a variable activation energy (*i.e.* non-Arrhenius) conduction mechanism at low temperatures is a quite general feature of small polaron hopping. [Sayer 72] As it has been discussed by Austin and Mott, at relatively low temperatures the zero-point vibrational energy allows polaron hopping to occur without any thermal activation. [Austin 69] These authors predicted a departure from the linear *ln(σ_{dc}T) vs. T^{-1}* behavior for temperatures below *T=θ_D/2*, where θ_D is defined by:

$$k_B\theta_D = \hbar\omega_{ph} \qquad (2)$$

with ω_{ph} being the average (or predominant) phonon frequency. In our case, this phonon frequency ω_{ph} can be calculated as 5.8×10^{13} s^{-1} (*ca.* 310 cm^{-1}), which falls in the range of typical frequencies of breathing modes of the metal-coordination polyhedra in Prussian blue analogues.[Cobo 07]

	LT		HT		LT		HT	
	E_{dc} (eV)	B (Scm^{-1}K)	E_{dc} (eV)	B (Scm^{-1}K)	E_p (eV)	ω_{0p} (s^{-1})	E_p (eV)	ω_{0p} (s^{-1})
1	0.57 ± 0.01	9200 ± 300	0.57 ± 0.01	1120 ± 110	no reliable data			
2	0.54 ± 0.01	670 ± 130	0.57 ± 0.01	450 ± 130	0.55 ± 0.01	3.2×10^{13} ± 1.6×10^{13}	0.53 ± 0.01	1.4×10^{12} ± 0.6×10^{12}
3	0.50 ± 0.01	820 ± 130	0.51 ± 0.01	770 ± 160	0.56 ± 0.01	8.0×10^{12} ± 1.6×10^{12}	0.57 ± 0.01	1.9×10^{12} ± 1.9×10^{12}
4	no phase transition		0.44 ± 0.01	45 ± 4	no phase transition		0.42 ± 0.02	4.8×10^{11} ± 0.2×10^{11}
5	no reliable data		0.52 ± 0.01	810 ± 80	no reliable data		0.50 ± 0.01	9×10^{9} ± 3×10^{9}

Table.II.1: *DC conductivity and dielectric relaxation activation parameters for the different samples of Rb$_x$Mn[Fe(CN)$_6$]$_y$.zH$_2$O in the LT and HT phases derived using equations (1) and (4) respectively.*

As mentioned before, the conduction due to a process of site-to-site charge transfer must involve a dielectric relaxation. This is because a hop to a new site can lead to successful charge transport only if the polarization cloud follows. This electric relaxation requires a relaxation time, τ. With increasing frequency the polarization (or dielectric constant) will monotonically decrease because the relaxation cannot follow the electrical field beyond a certain frequency. Indeed, this has been observed in our samples as well. On the low frequency side the dispersion of ε' has its physical origin in electrode polarization effects. On the other hand, at higher frequencies the analysis of the electrical modulus reveals a dipole relaxation process, which is thermally activated. To determine with more precision the frequency of the dielectric relaxation peaks, the experimental data of the dielectric loss

modulus $M''(\omega)$ can be conveniently fitted by a superposition of two or three Havriliak-Negami functions[Havriliak 67]:

$$M''(\omega) = \sum_{j=1} \frac{\Delta M_j}{[1+(i\omega\tau_j^{HN})^{\alpha_j}]^{\beta_j}} \qquad (3)$$

where $\tau^{HN} = \frac{1}{\omega_p}[\sin\frac{\alpha\pi}{2(1+\beta)}]^{\frac{1}{\alpha}}[\sin\frac{\alpha\beta}{2(1+\beta)}]^{-\frac{1}{\alpha}}$ and ΔM are the mean relaxation time of the

relaxation time distribution and the relaxation strength, respectively. The two shape parameters α and β determine the logarithmic slope of the low frequency loss tail α and the high frequency loss tail $-(\alpha\beta)$. In both samples ω_p exhibit a thermally activated dependence, *i.e.* it obeys the Arrhenius equation:

$$\omega_p(T) = \omega_{0p} \exp(-E_p/k_B T) \qquad (4)$$

Figure II.7 shows the Arrhenius plot of the two main relaxation frequencies for sample **2** (in the heating cycle).

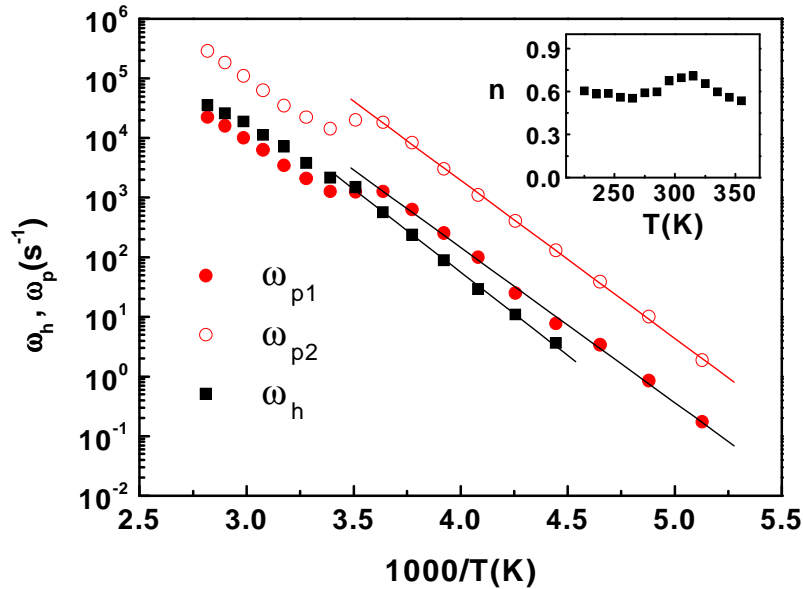***Fig.II.7:*** *Arrhenius plot of the relaxation frequencies ω_p, obtained from the maximum in $M''(\omega)$ and ω_h, obtained from the non-linear least-squares fitting of $\sigma'(\omega)$ to equation (5) (sample **2**, heating cycle). The solid lines are the least-squares linear fits to equations (4) and (6). The insert shows the thermal variation of the power exponent n in equation (5).*

The two main relaxation processes show very similar temperature dependences, though the values of the pre-exponential factor ω_{0p} are somewhat different. Figure II.7 displays also the temperature dependence of the crossover frequency ω_c determined from the ac conductivity data of the same sample. Indeed, the frequency dependence of σ' is usually well described by using **Jonscher's "universal dielectric response"** (UDR). [Jonscher 83]

$$\sigma'(\omega) = \sigma_{dc} + A\omega^n = \sigma_{dc}[1+(\omega/\omega_c)^n] \tag{5}$$

where the characteristic frequency ω_c corresponds to the onset of the conductivity dispersion and n is the frequency exponent, which has a value around 0.6 ($\pm$0.05) in the high temperature range (see the inset of Figure II.7). **The crossover frequency corresponds to the hopping frequency ω_h of the charge carriers** and shows a thermal variation similar to the dielectric modulus loss peak maximum. Indeed, as seen in Figure II.6, the hopping frequency is also thermally activated for sample **2** and it is fitted to the Arrhenius equation:

$$\omega_h(T) = \omega_{0h}\exp(-E_h/k_B T) \tag{6}$$

where E_h is the activation energy for hopping and ω_{0h} is the attempt frequency (i.e. the phonon frequency). Upon comparing the values of E_p (0.55(1) eV) and the activation energy of hopping (E_h = 0.53(2) eV) in the LT phase (heating mode), it can be assumed that these two representations are completely equivalent even if they emphasize different aspects of the underlying mechanisms of charge transport.

In Figure II.8, the temperature dependence of direct current conductivity, using equation *(1)*, is compared to the temperature behavior of the main relaxation frequency ω_p (see equation 4) for sample **2**.
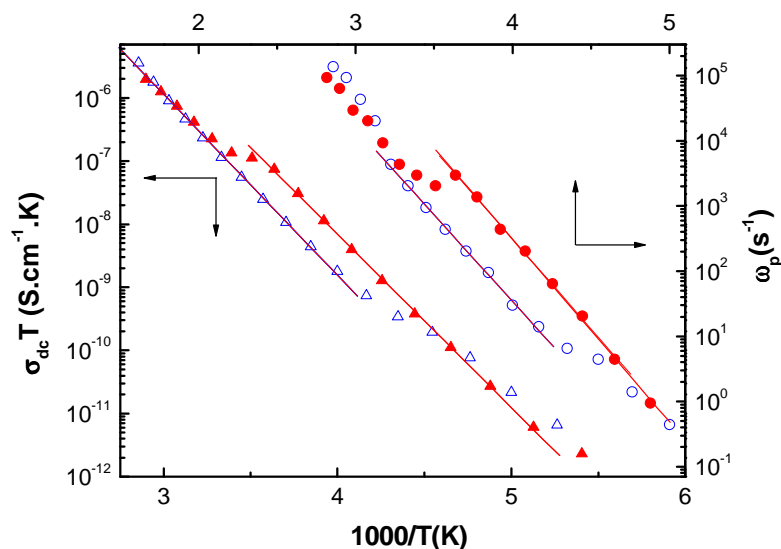
Fig.II.8: *Temperature dependence of the dc conductivity (triangles) and the conductivity relaxation frequency (circles) for sample **2**. Closed and open symbols correspond to the heating and cooling cycles, respectively. The solid lines are the least-squares linear fits to equations (1) and (4).*

Table II.1 summarizes the fitting results for each sample. The activation energy of the relaxation frequency (E_p) was evaluated as *ca.* 0.54(1), 0.56(1) and 0.42(2) eV for samples **2, 3** and **4**. **The fact that $E_{dc} \cong E_p$ implies that the charge carrier has to overcome the same energy barrier while conducting as well as relaxing**. **The observed dielectric relaxation is therefore due to the electrical conduction.** This means also that ω_p and σ_{dc} are proportional and the constant of proportionality is universal, varying only weakly with the temperature. This finding is known as the Barton-Nakajima-Namikawa relationship and indicates that the dc and ac conductivities are closely related to each other and based on the same mechanism of charge transport. Indeed, the frequency dependent conductivity of many disordered materials (inorganic glasses, polymers, doped semiconductors, and ionic conductors) is known to exhibit such universality and their behavior can be scaled to a master curve (*i.e.*, the conductivity data follow the time–temperature superposition). [Jonscher 83] The above discussion was restricted to compacted powder samples because they provided the highest quality complex conductivity data (due to their favorable electrode geometry). However, in polycrystalline materials in addition to bulk conductivity, grain boundary resistance and polarization have to be considered as well, especially in the low-frequency range. Under the action of an electric field, the grains are polarized by the accumulation of charge carriers on their boundaries, leading to an additional relaxation component in the dielectric spectrum of

the material. In many cases, separation of the bulk and grain boundary effects is straightforward by means of Cole-Cole type plots of the complex impedance (or permittivity) data. In our case, Cole-Cole arcs did not apply and only a continuous increase of ε'' with ε' was observed. For this reason we used the modulus formalism for separating interfacial phenomena from dipole relaxation due to charge hopping. For further investigation of eventual grain boundary effects on the complex conductivity of this material, we have investigated a single crystal sample of $RbMn[Fe(CN)_6].H_2O$ as well (sample **5**).[vertelman 08] Due to the small size (*ca.* 1 mm^3) and non-geometrical shape of the available crystals the electrode geometry is ill-determined and this leads to high uncertainty in the absolute value of the conductivity and also to higher standard deviation of the data, especially at low temperatures. Nevertheless, the conductivity data on single crystals resembles closely to those obtained on polycrystalline samples (Figure II.3 e). Notably, we noticed a marked deviation from an Arrhenius-type behavior below 220 K. Between 350 and 220 K the conductivity falls four orders of magnitude, similar to the polycrystalline case, which corresponds to a thermal activation energy of *ca.* 0.52 eV (table 1). Note here that in the single crystals the phase transition takes place rather gradualy between the pure HT phase and a mixed (1:1) HT+LT form and therefore fitting cannot be carried out in the LT phase. However, it appears clearly that both the relaxation frequency and the conductivity of the LT form are higher when compared to the pure HT phase (at a given temperature). The frequency dependence of the conductivity follows a power law and, as a consequence, the hysteresis of the conductivity disappears at higher frequencies. The electric loss moduli $M''(\omega)$ exhibit temperature dependent relaxation maxima and the $M''(\omega)$ curves at different temperatures can be scaled to a master curve similar to the powder samples. The activation energy of the relaxation is *ca.* 0.50 eV. This means that in the crystals as well the relationship $E_{dc} \cong E_p$ is confirmed. The main difference between the single crystal and polycrystalline samples is observed below *ca.* 200 K in the low-frequency region, where the crystals show significantly less temperature dependent (virtually activationless) conductivity. Since there is no single straightforward theory that may allow us to discuss the mechanism of this low temperature conductivity process and the quality of the data is also rather poor at low temperatures, the discussion of the interplay between the charge transport and the charge transfer phase transition will be confined to the high temperature region (> 220 K).

II.1.2.2 Charge transport and the charge transfer phase transition in $Rb_xMn[Fe(CN)_6]_y \cdot zH_2O$

As shown in Figures II.2, II.3 and II.5 the thermal hysteresis of the magnetic susceptibility can be clearly correlated with a hysteresis of the dc conductivity as well as the dielectric permittivity. However, inside the hysteresis region a crossing point appears in $\sigma_{dc}(T)$ as well as in $\varepsilon'(T)$ around 210-230 K, leading to a strange "double-loop" curve, which is not observed in the magnetic measurements. Clearly, this crossing point is not related to the charge transfer phase transition, since it is observed in sample **4**, neither to another structural modification since powder X-ray diffraction, Raman spectroscopic and differential scanning calorimetric measurements revealed no singularity around 220 K. Therefore, we believe that this crossing point is not related to any structural change in the sample and should be associated with a departure from an Arrhenius-like hopping process towards an activationless, **tunneling** conduction mechanism (as described above).

In the high temperature range our observations point clearly to a conduction mechanism by **small polaron hopping**. Given that the water content of our samples was kept as low as possible we adopt the hypothesis of Rosseinsky *et al.* [Rosseinsky 87] and we assign this hopping process to an intervalence electron transfer Mn^{2+}-NC-$Fe^{3+} \leftrightarrow Mn^{3+}$-NC-$Fe^{2+}$. This assignment is corroborated by our thermopower measurements as the sign of the Seebeck coefficient was found negative in each sample. (Typically S exhibits values of *ca.* $-120(\pm 20)$ µV/K between 300 and 350 K.). Bearing in mind that this assignment concerns only the high temperature region, the possible effects of the phase transition on the charge transport will now be considered. In the case of hopping transport we can use the well-established relationship, using the **Einstein diffusion equation**, between the dc conductivity and the hopping frequency[Mott 79]:

$$\sigma_{dc} = (n_c e^2 a^2 / 6k_B T)\nu_p = (n_c e^2 a^2 / 6k_B T)\nu_{0p}[\exp(-E_p/k_B T)] \qquad (7)$$

where $\nu_p = \omega_p/2\pi$, a is the hopping distance (*i.e.* the Fe-Mn distance), n_c is the carrier density (*i.e.* the density of Fe-Mn pairs) and E_p is the activation energy for the hopping process. This equation implies that the activation energy for ω_p and σ_{dc} is the same ($E_p = E_{dc}$), which we have already demonstrated above. A further proof for the applicability of *eq. (7)* in the present case comes from the evaluation of n_c, which appears to be of the order of 3 ($\pm$ 2) x10^{26} m^{-3}

and nearly independent of the temperature. This value is reasonably close to the theoretical number density of Fe-Mn pairs of 3.4×10^{27} m^{-3} in RbMn[Fe(CN)$_6$].H$_2$O if one takes into account that the hopping probability will be necessarily reduced to some extent in the real material due to the vacant metallic sites, charge disorder and interactions between the polarons.[Sayer 72]

Figures II.2 and II.3 reveal clearly that the dc conductivity is higher in the LT phase. Let us note that the same observation was made by Sato *et al.* in the case of the compound Na$_x$Co[Fe(CN)$_6$]$_y$.zH$_2$O.[Sato 04]

In the case of Rb$_x$Mn[Fe(CN)$_6$]$_y$.zH$_2$O the higher conductance (σ_{dc}) of the LT phase parallels the higher hopping frequencies (ω_p) (Figure II.8), which can be explained either by a lower activation barrier (E$_p$) or by a higher value of the pre-exponential factor (ω_0). In our samples **1** and **2** the activation energy in the HT and LT phases was found very similar (0.54 ± 0.03 eV) (table 1), while in the sample investigated by Sato *et al* [Sato 04] the activation energy of the dc conductivity was even smaller in the HT phase (0.34 eV) when compared to the LT phase (0.54 eV). This points to the important role of the pre-exponential factor, which increases in the case of sample **2** (for example) from $(1.5 \pm 0.6) \times 10^{12}$ s^{-1} to $(3.8 \pm 2.6) \times 10^{13}$ s^{-1} when going from the HT to the LT phase. These values of ω_0 are of the order of the lattice phonon frequencies to which carriers can be coupled. This **central role of the phonons** would not be surprising since strong electron-phonon interaction is a prerequisite for small polaron formation and the charge transfer phase transition involves also a strong modification of the lattice dynamics. Indeed the LT phase is much stiffer due to its reduced volume and the Jahn-Teller distortion in the LT phase alters also the electron-phonon coupling scheme. Even if the uncertainty of the absolute values of ω_0 are relatively high, we stress that we observed an increase of the pre-exponential factor upon the HT→LT transition for each sample, both in the dc conductivity and, independently, in the dielectric relaxation data while the activation energy remained closely constant. One should also note that the value of ω_0 cannot be directly associated with a particular phonon frequency, but it is better described as an "effective attempt frequency" not only because the charge carrier may be coupled to different (and multiple!) phonon modes in the HT and LT phases, but also because of the possibility of non-adiabatic processes, which decrease the probability of successful hopping events. [Havriliak 67]

In summary we can say that the conductivity change upon the charge transfer phase transition in $Rb_xMn[Fe(CN)_6]_y.zH_2O$ is mainly determined by the variation of the pre-exponential factor. Since the constants involved in σ_0 (*i.e.* the hopping distance, the phonon frequency and density of donor-acceptor pairs) change little from one phase to another or from one stoichiometry to another, **the value of σ_0 is expected to vary less than an order of magnitude upon the phase transition, which has been confirmed here experimentally**. We believe that the comparable activation energy values in the HT and LT phases occur only fortuitously. For example, one may speculate that the shorter distances in the LT phase imply higher force constants. Assuming parabolic potential energy curves the former will lead to smaller activation energy due to the proximity of the potential wells, while the later will increase the barrier due to the higher curvature of the wells. In certain circumstances the two effects might thus just cancel each other.

II.1.3 $Na_xCo[Fe(CN)_6]_y.zH_2O$ and $Co_3[W(CN)_8]_2(pyrimidine)_4 \cdot 6H_2O$

In order to confirm the universality of the charge transport properties observed and discussed for $Rb_xMn[Fe(CN)_6]_y \cdot zH_2O$, we have investigated two more compounds that exhibit a charge transfer phase transition; $Na_xCo[Fe(CN)_6]_y \cdot zH_2O$ in two different stoichiometries, $Na_{0.2}Co[Fe(CN)_6]_{0.73} \cdot 4.13H_2O$ (**6**) [Vertelman 09], $Na_{2.2}Co_4[Fe(CN)_6]_{3.3} \cdot 15H_2O$ (**7**) [Bleuzen 03] and **$Co_3[W(CN)_8]_2(pyrimidine)_4 \cdot 6H_2O$** (**8**) [Ohkoshi 06, Ohkoshi 08]. The $Na_xCo[Fe(CN)_6]_y \cdot zH_2O$ compound has a typical cubic structure of the Prussian-blue type complexes. This compound exhibits a CT phase transition between the high-temperature (HT) $Fe^{III}(t_{2g}^5 e_g^0$, LS, S=1/2)-CN-$Co^{II}(t_{2g}^5 e_g^2$, HS, S=3/2) and the low-temperature (LT) $Fe^{II}(t_{2g}^6 e_g^0$, LS, S=0)-CN - $Co^{III}(t_{2g}^6 e_g^0$, LS, S=0) phases accompanied by a thermal hysteresis loop. On the other hand, the complex $Co_3[W(CN)_8]_2(pyrimidine)_4 \cdot 6H_2O$ is based on octacyanometalate building blocks and it was shown to display a CT phase transition between the HT $Co_{HS}^{II}(S = 3/2) - NC - W^V(S = 1/2)$ and the LT $Co_{LS}^{III}(S = 0) - NC - W^{IV}(S = 0)$ electronic configurations (HS and LS stand for high-spin and low-spin respectively) [Ohkoshi 06, Ohkoshi 08].

In the same way as we presented the results for the complex $Rb_xMn[Fe(CN)_6]_y \cdot zH_2O$, we will discuss the dielectric properties of the other compounds. We will start by the $Na_xCo[Fe(CN)_6]_y.zH_2O$ which is also a Prussian blue analogue compound. In the

$Na_{0.2}Co[Fe(CN)_6]_{0.73}.4.13H_2O$ compound, the product of the molar magnetic susceptibility and the temperature displays a thermal hysteresis loop (figure II.9). The molar magnetic susceptibility, falls from 3.65 cm^3 K mol^{-1} to 3.22 cm^3 K mol^{-1} on going from the HT to the LT phase. The phase transition temperatures in the cooling (heating) modes are 170 K (180), yielding 10 K as hysteresis loop width. On the other hand the temperature as well as frequency dependence of the real part σ' (ω) of the ac conductivity exhibits a small hysteresis, which roughly corresponds to the hysteresis region detected by magnetic measurements. We observed σ' (310 K, 10 mHz, 33 Hz, and 100 kHz) = $3.4x10^{-7}$ $S.cm^{-1}$, σ' (190 K, 10 mHz) = $8x10^{-12}$ $S.cm^{-1}$, σ' (190 K, 33 Hz) = $4.6x10^{-11}$ $S.cm^{-1}$, and σ' (190 K, 100 kHz) = $5.8x10^{-9}$ $S.cm^{-1}$. Moreover we observed the same crossing behavior of the heating and cooling curves that occurs in the hysteresis region close to the phase transition temperatures around 190 K (No crossing point observed at 100 kHz).
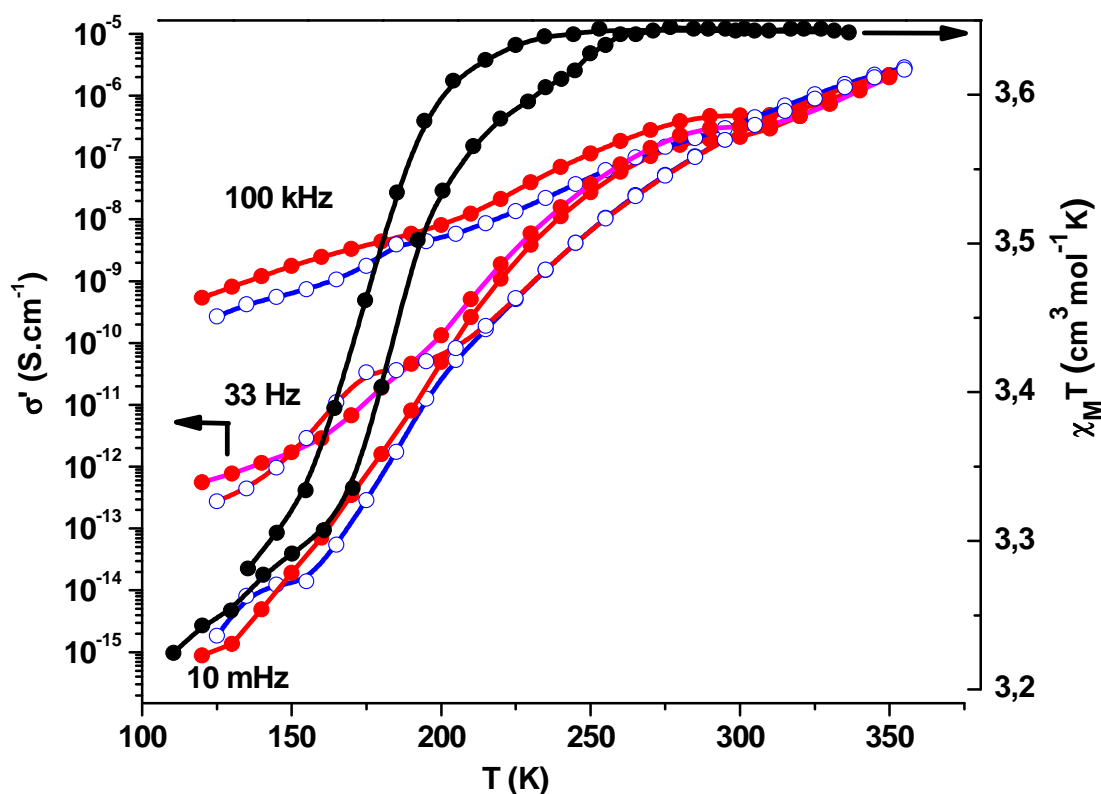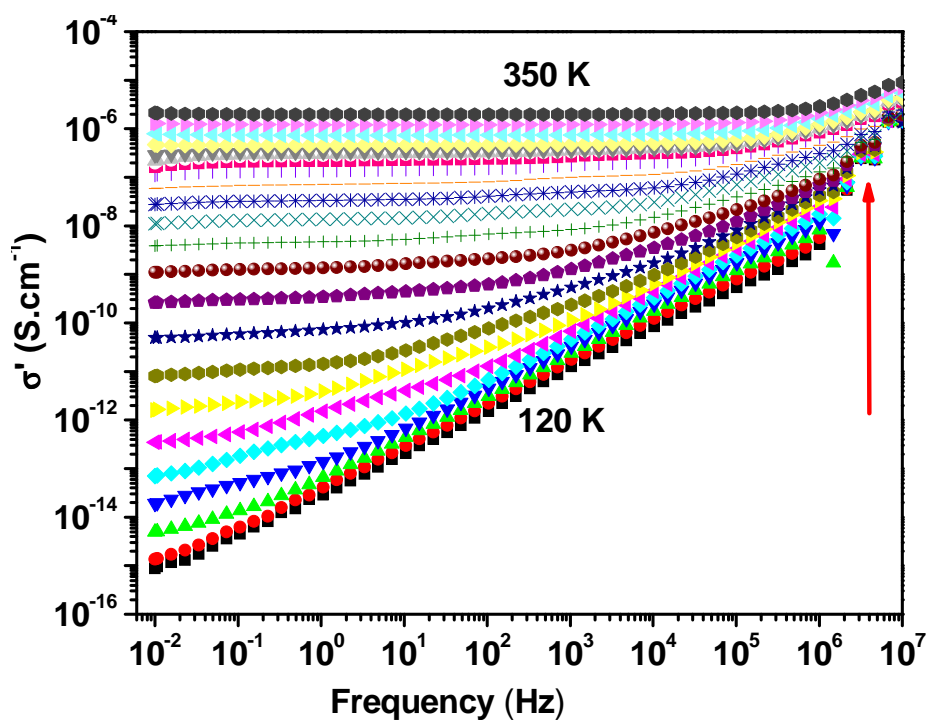

Fig.II.9: *Temperature dependence of the ac conductivity (real part) at different frequencies and that of the $\chi_M T$ product for sample **6**. Closed and open symbols correspond to the heating and cooling cycles, respectively. Data points are connected to guide the eye.*

Figure II.10 displays the frequency dependence of σ' at different temperatures in the heating (fig.II.10 a) and cooling ((fig.II.10 b) modes.
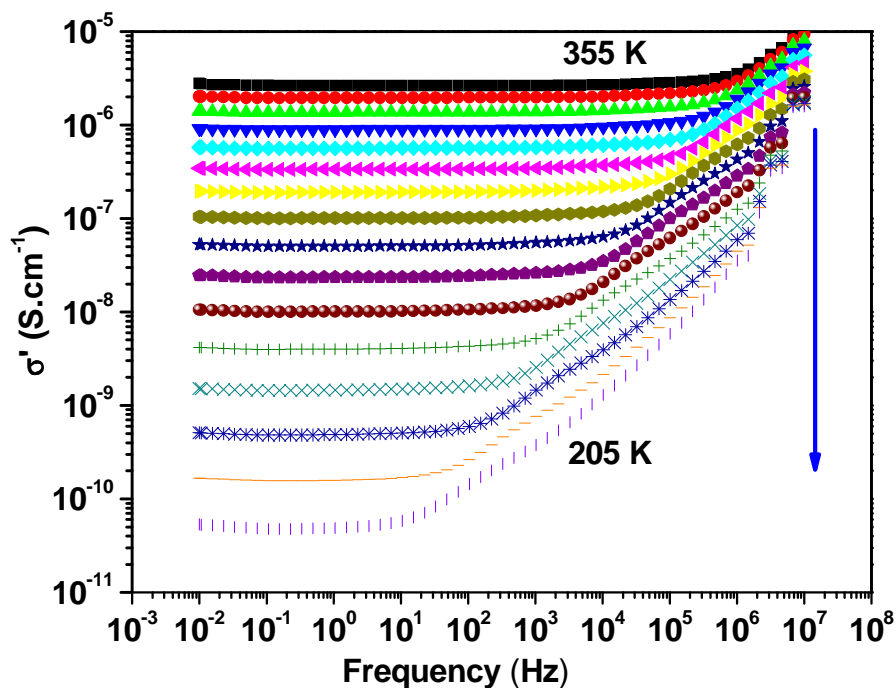
a)

b)

Fig.II.10: *Frequency dependence of the ac conductivity at fixed temperatures ranging from 120 to 350 K in the heating (a) and from 355 to 205 in the cooling (b) cycles for sample **6**. Curves are displayed by steps of 10 K.*

At high temperatures and low frequencies σ' is constant in the heating and cooling modes. As the frequency increases a gradual dispersion sets in resulting in apparent power law

dependence ($\sigma' \sim \omega^n$) at high temperatures. The crossover frequency (ω_c) which separates the power-law and the frequency-independent (dc) regimes decreases continuously with decreasing temperature from *ca.* 3.10^5 Hz to 10 mHz between 350 K and 120 K in the heating mode and 3.10^5 Hz to 4 Hz between 355 K and 205 K in the cooling mode. This behavior is similar to what already observed for the RbMnFe samples. To estimate the dielectric relaxation of this sample in the heating and cooling modes, we plotted the imaginary part of the complex modulus (fig.II.11).
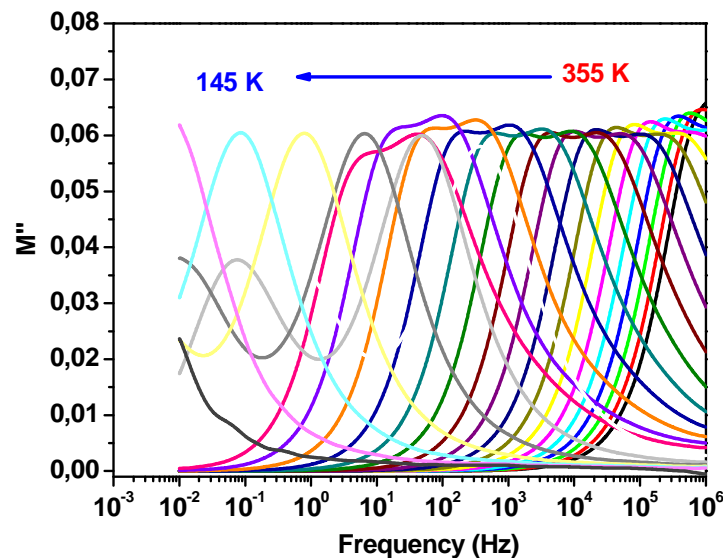
a)
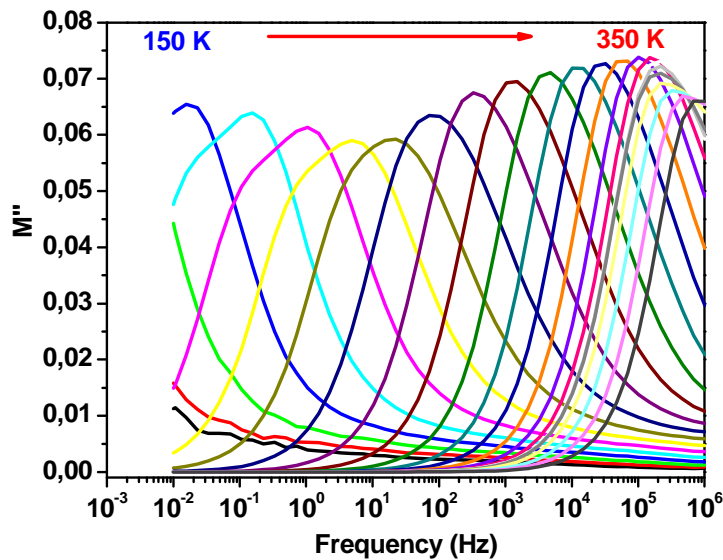
b)

Fig.II.11: *Plot of the loss electric modulus (M") vs. the frequency at various temperatures ranging from 150 to 350 K in the heating (a) and cooling cycles for sample (6). Curves are displayed by steps of 10 K. Data points are connected to guide the eye.*

Similar to the case of the $Rb_xMn[Fe(CN)_6]_y.zH_2O$ analogues, the analysis of the electrical modulus reveals a dipole relaxation process of site-to-site charge transfer, which is thermally activated. To determine the activation energy in this sample, the temperature dependence of direct current conductivity, using equation *(1)*, is compared to the temperature behavior of the main relaxation frequency ω_p (see equation 4) for the same sample.
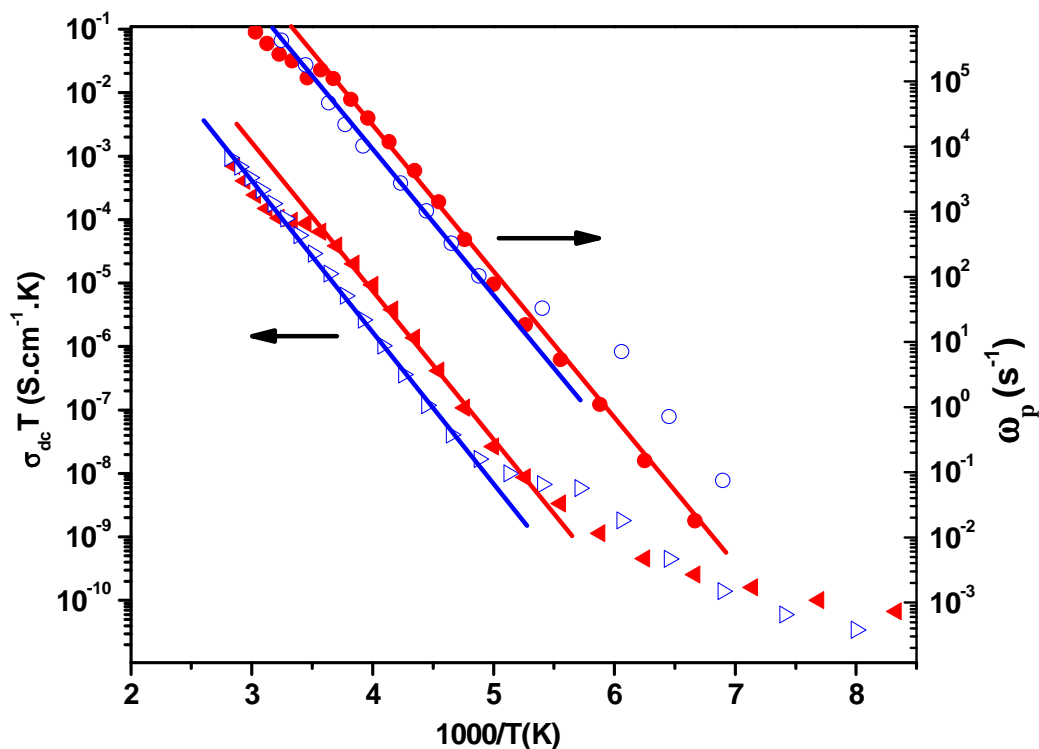

Fig.II.12: Temperature dependence of the dc conductivity (triangles) and the conductivity relaxation frequency (circles) for sample 6. Closed and open symbols correspond to the heating and cooling cycles, respectively. The solid lines are the linear fits.

 The activation energy of the relaxation frequency (E_p) was evaluated as *ca.* 0.50 ±0.01 and 0.49 ±0.01 eV in the heating and the cooling modes, respectively, whereas the activation energy of the charge transport were found about 0.52 ±0.01 and 0.49 ±0.01eV in the heating and the cooling modes, respectively.

The fact that $E_{dc} \cong E_p$ implies that the charge carrier has to overcome the same energy barrier while conducting as well as relaxing in the heating and cooling mode. It appears therefore that the charge transport properties discussed above are general for this family of compounds.

We have also investigated the $Na_{2.2}Co_4[Fe(CN)_6]_{3.3}.15H_2O$ and $Co_3[W(CN)_8]_2(pyrimidine)_4 \cdot 6H_2O$ compounds, which will be used later for further investigation (see II.2). In these compounds also, the product of molar magnetic susceptibility and the temperature displays a thermal hysteresis loop due to the CT phase transition (figure II.13). The molar magnetic susceptibility and the conductivity values characterizing the two compounds are as follows:

- For the $Na_{2.2}Co_4[Fe(CN)_6]_{3.3}.15H_2O$ sample (fig.II.13 a), the molar magnetic susceptibility falls from 14.5 cm^3 K mol^{-1} to 2.4 cm^3 K mol^{-1} on going from the HT to the LT phase. The phase transition temperatures in the cooling (heating) modes are 218 K (238), yielding 20 K wide hysteresis loop, whereas σ' (350 K, 10 mHz, 100 kHz) = $2.5x10^{-6}$ S.m^{-1}, σ' (205 K, 100 kHz) = $6.5x10^{-9}$ S.cm^{-1}, and σ' (205 K, 10 mHz) = $3.2x10^{-11}$ S.cm^{-1}.

- For the $Co_3[W(CN)_8]_2(pyrimidine)_4 \cdot 6H_2O$ sample (fig.II.13 b), the molar magnetic susceptibility falls from 14.3 cm^3 K mol^{-1} to 2.8 cm^3 K mol^{-1} on going from the HT to the LT phase. The phase transition temperatures in the cooling (heating) modes are 216 K (296), yielding 80 K wide hysteresis loop, whereas σ' (350 K, 10 mHz, 33 Hz) = $4.2x10^{-9}$ S.cm^{-1}, σ' (260K, 33 Hz) = $4.6x10^{-11}$ S.cm^{-1}, and σ' (260 K, 10 mHz) = $1.5x10^{-11}$ S.cm^{-1}.

a)
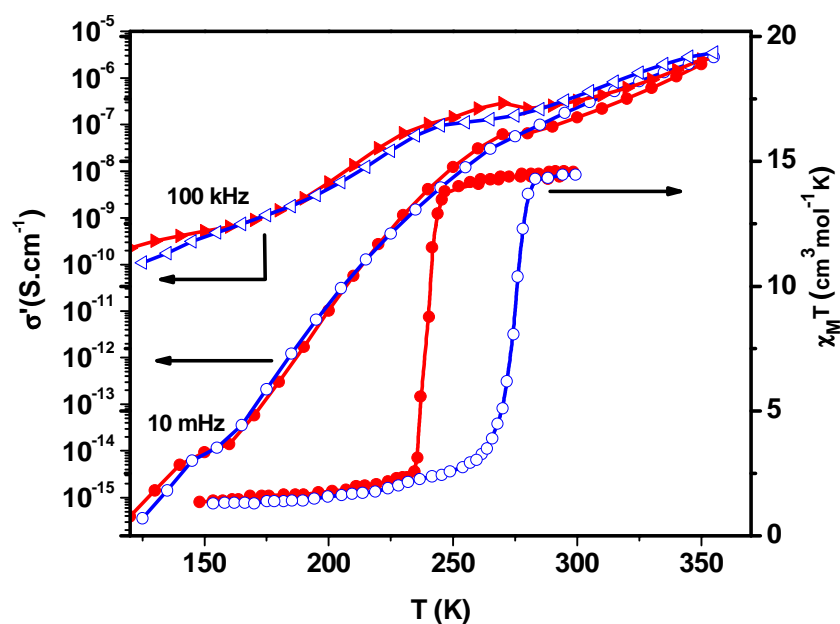
b)
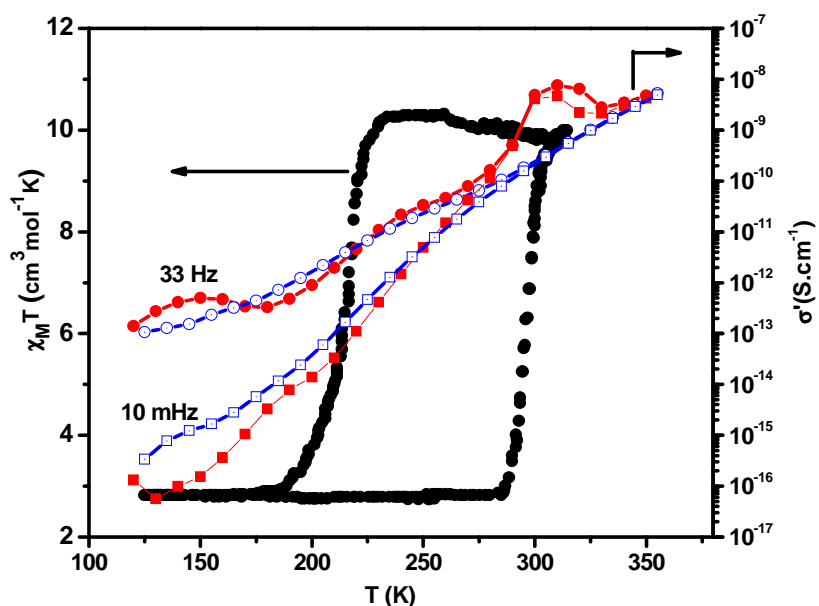
Fig.II.13: *Temperature dependence of the ac conductivity at 10 mHz and 100 kHz for the Na$_{2.2}$Co$_4$[Fe(CN)$_6$]$_{3.3}$.15H$_2$O sample (a) and at 33 Hz and 10 mHz for the Co$_3$[W(CN)$_8$]$_2$(pyrimidine)$_4$·6H$_2$O sample (b). Closed and open symbols correspond to the heating and cooling cycles, respectively. Product of molar magnetic susceptibility is depicted for each sample in, (a) for the Na$_{2.2}$Co$_4$[Fe(CN)$_6$]$_{3.3}$.15H$_2$O sample, and in (b) for the Co$_3$[W(CN)$_8$]$_2$(pyrimidine)$_4$·6H$_2$O sample.*

In both samples, the conductivity exhibits very small changes between the HT and LT phases when compared to what observed in the RbMnFe samples and the electrical properties do not allow to follow the phase changes (within our experimental precision). On the other hand, the

conductivity mechanism appears very similar again. In particular, a crossover frequency (ω_c) which separates the power-law and the frequency – independent (dc) regimes were observed in these two compounds as well (fig.II.14).

a)

b)

c)

d)
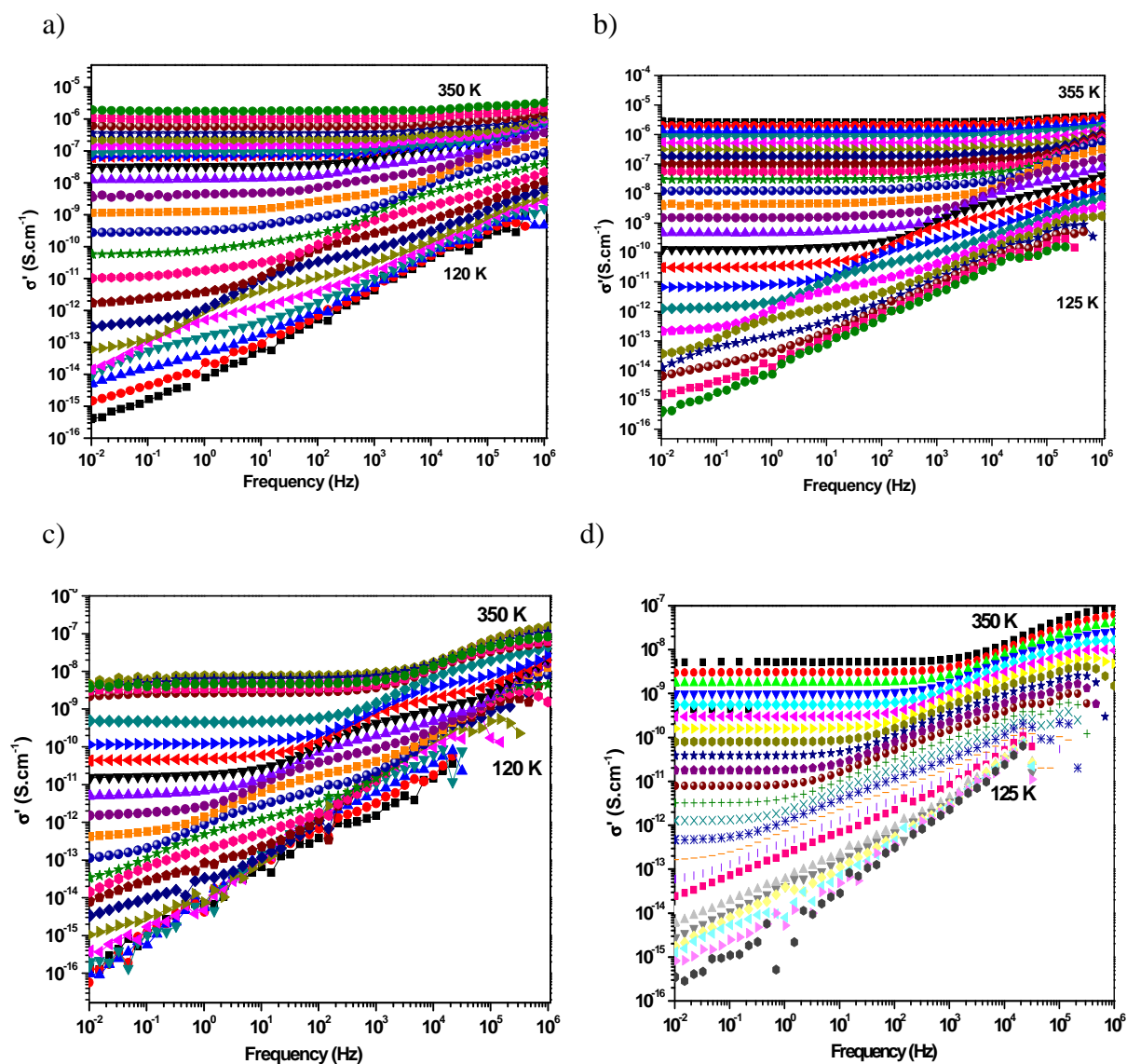
Fig.II.14: *Frequency dependence of the ac conductivity at fixed temperatures ranging from 120 to 350 K; in the heating (a) and the cooling (b) cycle for the $Na_{2.2}Co_4[Fe(CN)_6]_{3.3}.15H_2O$ sample and in the heating (c) and the cooling (d) cycle for the $Co_3[W(CN)_8]_2(pyrimidine)_4 \cdot 6H_2O$. Curves are displayed by steps of 10 K.*

The dielectric relaxation of these samples in the heating and cooling modes, are presented in fig.II.15 and II.16. Interestingly, in the $Co_3[W(CN)_8]_2(pyrimidine)_4 \cdot 6H_2O$ sample we observe two relaxation maxima in M''. Moreover in this sample the relaxation frequency is

significantly lower than what was observed in the NaCoFe and RbMnFe samples. This observation is in agreement with the fact that σ' (CoW) << σ'(RbMnFe or NaCoFe).

a)   b)
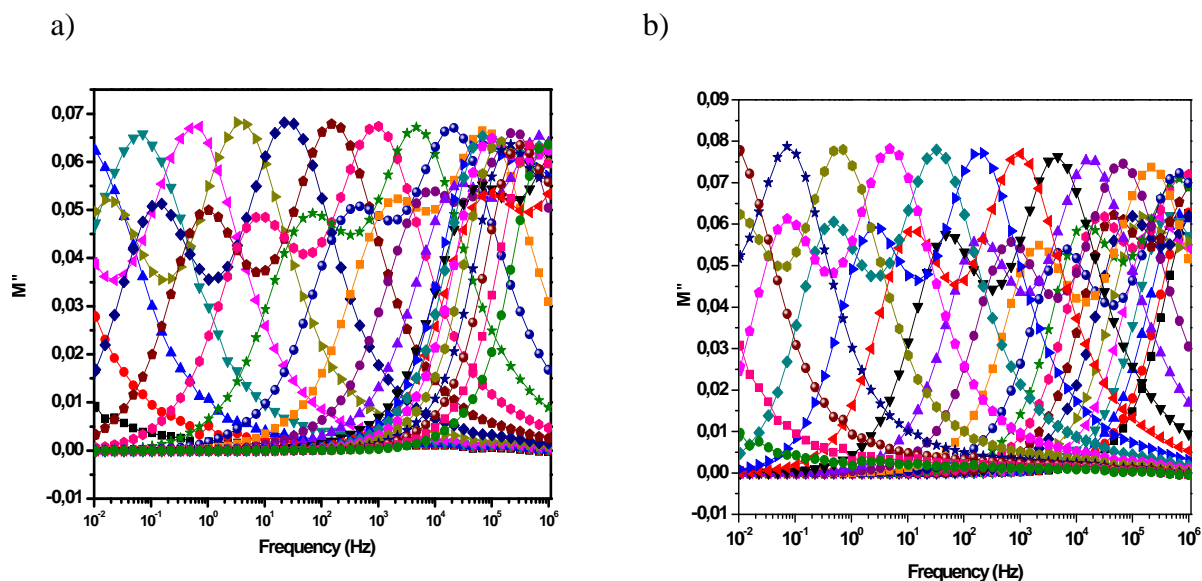
Fig.II.15: *Plot of the loss electric modulus (M") vs. the frequency at various temperatures ranging from 150 to 350 K in the heating (a) and the cooling (b) cycle for the $Na_{2.2}Co_4[Fe(CN)_6]_{3.3}.15H_2O$ sample Curves are displayed by steps of 10 K. Data points are connected to guide the eye.*

a)   b)
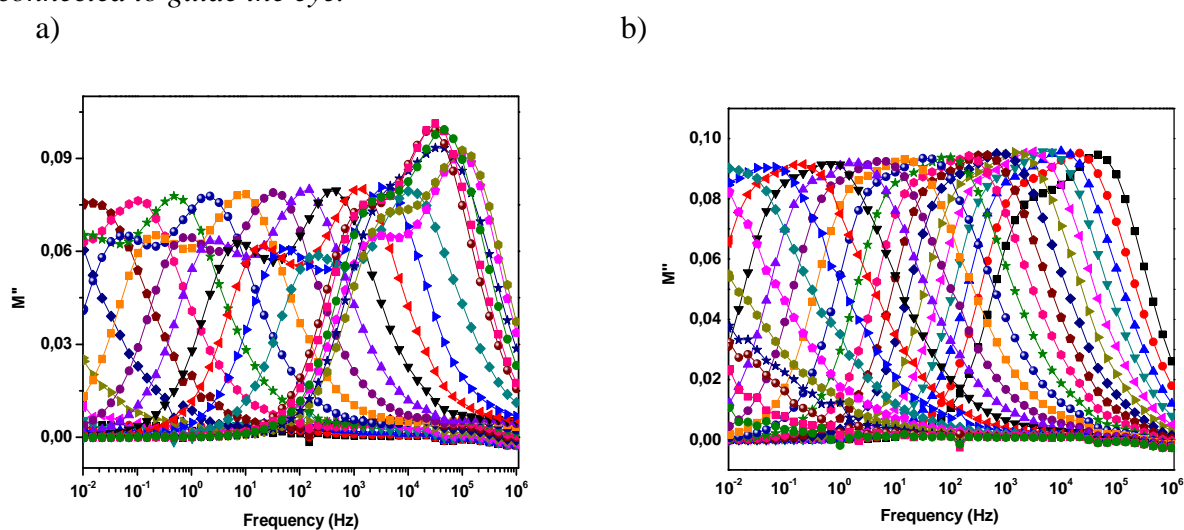
Fig.II.16: *Plot of the loss electric modulus (M") vs. the frequency at various temperatures ranging from 150 to 350 K in the heating (a) and the cooling (b) cycle for the $Co_3[W(CN)_8]_2(pyrimidine)_4·6H_2O$. Curves are displayed by steps of 10 K. Data points are connected to guide the eye.*

II.1.4 Conclusions

We have studied the charge transport in valence-tautomeric **$Rb_xMn[Fe(CN)_6]_y.zH_2O$, $Na_xCo[Fe(CN)_6]_y.zH_2O$** and **$Co_3[W(CN)_8]_2(pyrimidine)_4·6H_2O$** samples with different stoichiometries.

The large bistability domain allowed us to investigate the charge transport in the two valence-tautomeric phases in strictly identical experimental conditions. In each compound, the frequency-dependent conductivity obeys time-temperature superposition (scaling law) typical to disordered solids. The dc conductivity shows Arrhenius behavior at high temperatures. A dipole relaxation process displaying the same thermal activation energy as the conductivity has been also observed. The overall experimental results can be explained by the Mott theory $\sigma_{dc} = (n_c e^2 a^2/6k_B T)\, \nu_p$. These characteristics were found common for each sample and imply a **small polaron hopping** mechanism of the charge transport, which we assigned to the **intervalence electron transfer** in the different compounds.

In the case of $Na_x Co[Fe(CN)_6]_y.zH_2O$ and $Co_3[W(CN)_8]_2(pyrimidine)_4 \cdot 6H_2O$ samples no clear effect of charge transfer phase transition on the conductivity (σ_{dc}) was observed. On the other hand for the RbMnFe samples the valence-tautomeric phase transition is clearly displayed in the thermal hysteresis of the electrical properties. However, **at low temperatures a crossover occurs in the conductivity mechanism from an Arrhenius-type to a variable activation energy behavior leading to a strange "double-loop" shape of the hysteresis loop**. This crossover is typical to small polaron hopping phenomena and from the investigation of samples that do not display phase transition we could unambiguously conclude that the two phenomena (the valence tautomeric phase transition and the crossover in the conductivity mechanism) are independent and occur in the same temperature range in certain samples only by coincidence. On the other hand, the charge transfer phase transition modulates obviously the conductivity and therefore the conductivity data reflects both phenomena. Actually, the phase transition does not lead to a modification of the transport and dielectric relaxation mechanisms, but it does modify the conductivity and the relaxation rate. Surprisingly, the activation energy of the conductivity was found fairly similar in the two phases in the case of $Rb_x Mn[Fe(CN)_6]_y.zH_2O$ samples. On the other hand **the charge transfer rate and, as a consequence, the conductivity as well are higher in the LT phase. This difference is clearly displayed in the pre-exponential factor of the hopping frequency**, which correlates well, at least qualitatively, with the fact that the HT→LT phase transition involves a strong stiffening of the lattice.

II.2 Electric field - induced charge – transfer phase transition in valence tautomeric complexes

Several materials exhibit large and reversible changes in their optical properties (color, refractive index …) under an externally applied electric field. Among these, the most well known are electro-optical materials, electrochromic and liquid crystal systems [Lampert 98, Dalton 99]. However, the performance of the existing materials (cost, lifetime, energy consumption, response time ...) is still limited and a lot of research activity is currently being undertaken in order to improve them. On the other hand, instead of improving the existing technologies, it is important also to explore novel physical mechanisms, which may lead to electric-field-induced (EFI) switching of material properties. For example, bistable organic compounds [Luo 02] or materials exhibiting metal-insulator transitions [Kanki 03] have been reported to display interesting and potentially useful switching properties under external electrical bias.

In this context bistable coordination complexes exhibiting two close-lying electronic states represent an appealing field of investigation. As discussed in the thesis of Thomas GUILLON in our team [Guillon 07], **no spin transition was observed when an external electric field was applied on various spin crossover complexes**. **For this reason, in the present thesis we focus on charge-transfer (CT) complexes**, which can adopt several (meta-) stable charge-localized electronic forms differing in charge distribution [Kato 03]. As we have already seen, within this vast family, a few compounds display first-order thermal phase transitions associated with a metal-to-metal electron transfer in contrast to spin crossover complexes when the electron transfer occurs between the d orbitals of the same metal ion. [Ohkoshi 05, Loutete-Dangui 08] Therefore using an external electric field as stimulus within the hysteresis loop one can expect to induce the interconversion between the two states.

The large thermal hysteresis loop, which accompanies in most cases these phase transitions confers a memory effect to these systems creating a fundamentally new scope for electric-field-driven switching and memory devices when the field is applied within the hysteresis region. It should be noted that somewhat similar experiments have already been carried out on a NaCoFe-type Prussian blue analogue compound by Sato *et al* [Sato 04] but only a reversible current switching was reported by these authors - outside the hysteresis loop.

II.2.1 Experimental set up

Sample synthesis and characterization. The microcrystalline powder of $Rb_{0.8}Mn[Fe(CN)_6]_{0.93} \cdot 1.62H_2O$ (**9**) was prepared in our team with the help of Saioa COBO and Lionel SALMON by slowly adding an aqueous solution (50 ml) of $MnCl_2 \cdot 4H_2O$ (2.5 mmol) to an aqueous solution (50 ml) of $K_3[Fe(CN)_6]$ (2.5 mmol) and RbCl (25 mmol). The solution was stirred mechanically and kept at a temperature of 50°C during the addition procedure and over a successive hour. The brown powder precipitate was filtered, washed with Millipore H_2O and dried in air at room temperature. Elemental analysis calculated for $Rb_{0.8}Mn[Fe(CN)_6]_{0.93} \cdot 1.62H_2O$ (358.10 g/mol): calcd. Rb 19.12, Mn 15.55, Fe 14.69, C 18.95, N 22.11; found Rb 19.12, Mn 15.55, Fe 14.13, C 19.70, N 23.11, H_2O 8.18. All chemicals were purchased from Sigma-Aldrich and used without purification. The powder of $Co_3[W(CN)_8]_2(pyrimidine)_4 \cdot 6H_2O$ (**2**) has been synthesized as described in ref. [Ohkoshi 08]. The synthesis procedure and characterization of $Na_2Co_4[Fe(CN)_6]_{3.3} \cdot 15H_2O$ (**3**) sample studied in this work are detailed in ref.[Bleuzen 03].

The charge transfer phase transition was confirmed in each sample by magnetic susceptibility measurements, which were carried out by means of a Quantum Design MPMS magnetometer at heating and cooling rates of 1 $Kmin^{-1}$.

Raman spectroscopy under electrical bias. The fine powder samples (*ca.* 3 mg with an effective diameter of 3 mm) were pressed between two electrodes, a metallic one and an ITO (indium-tin oxide) deposited on a transparent glass plate. This "cell" was attached to the cold finger of an Optistat-CF Oxford Instruments He exchange gas cryostat. Raman spectra were collected between 320 and 80 K using a LabRAM-HR (Jobin-Yvon) Raman spectrometer (600 grooves/mm grating, 100 μm entrance slit, ~3 cm^{-1} spectral resolution) coupled to a CCD detector (Andor DU420) and an Olympus BXFM optical microscope. Raman scattering was excited at 632.8 nm by means of a HeNe laser with 0.07 mW excitation power on the sample (see figure II.17).
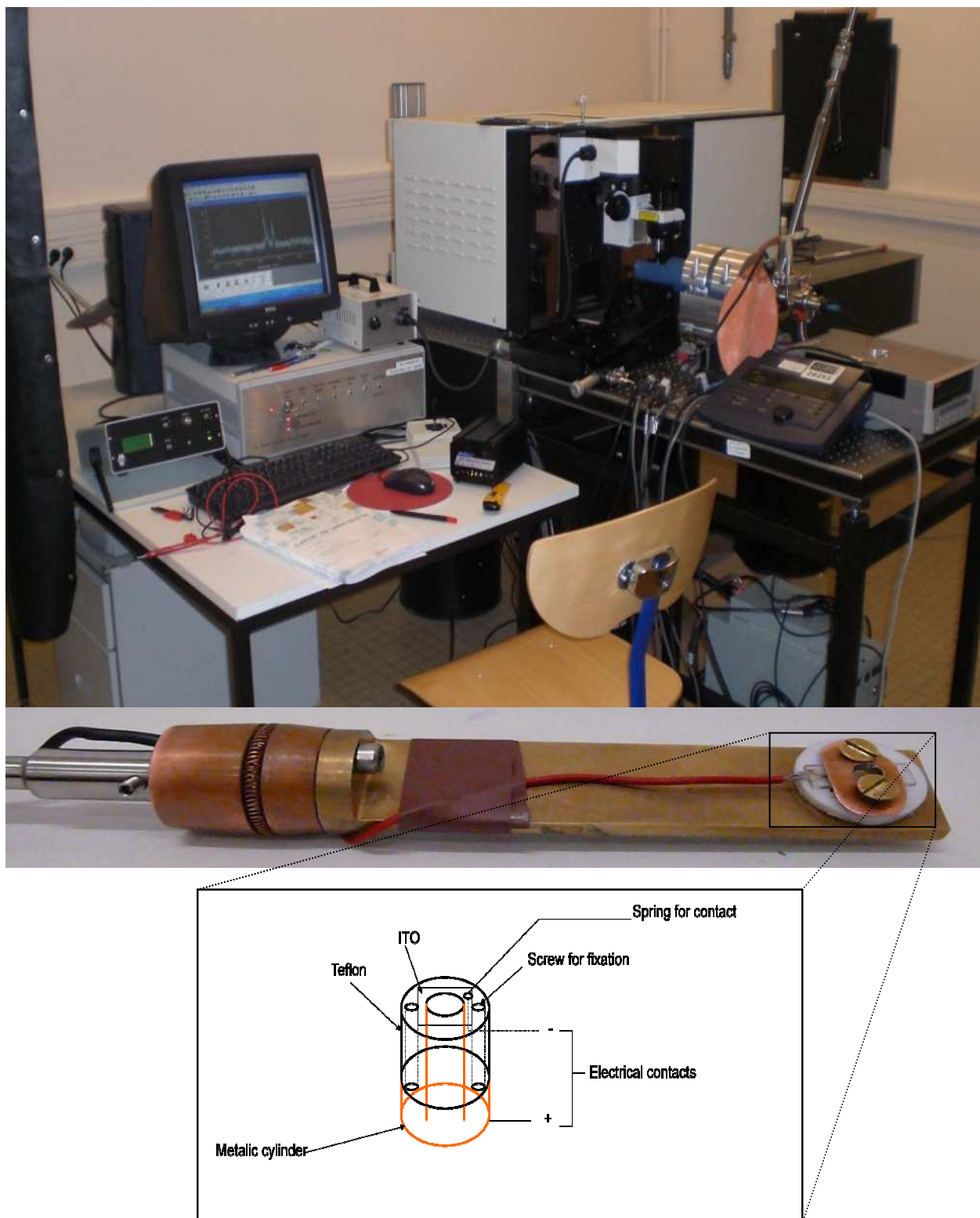
Fig.II.17 *Photo of the experimental setup (variable temperature Raman microscopy under external bias) used to investigate the electric field-induced charge-transfer phase transition. The bottom photograph shows the cold finger of the cryostat with the electrical cell. The scheme of the cell is also shown.*

The laser beam was focused on the sample via a long-working-distance X50 microscope objective, which served also to collect the scattered photons. The Rayleigh scattering was removed by a holographic notch filter and the Raman spectra were recorded between 1800 and 2400 cm^{-1} with typical acquisition times between 2 – 5 min. We used a Keithley model 6430 source-meter to apply voltages up to 210 V on our sample and to control its resistivity during the experiments. Electric field values indicated in the text are deduced from voltages applied according to the source-meter and not the genuine values at the sample because losses, due to the geometry of the electrodes and to the sample heterogeneity notably, could not be assessed reliably. In most cases, at the interface with the ITO electrode (cathode) the powder sample was not homogenously converted by the electric excitation probably due to an imperfect contact with the electrode.

II.2.2 Investigation of Rb$_x$Mn[Fe(CN)$_6$]$_y$·zH$_2$O

In order to test the idea of using an external electric field as a stimulus for charge transfer phase transition, we have decided to investigate the following three-dimensional (3D) coordination network: Rb$_{0.8}$Mn[Fe(CN)$_6$]$_{0.93}$·1.62H$_2$O which exhibits a CT phase transition between the high-temperature (HT) Fe^{III}(S=1/2)–CN–Mn^{II}(S=5/2) and the low-temperature (LT) Fe^{II}(S=0)–CN–Mn^{III}(S=2) states, accompanied by a large thermal hysteresis loop of (mainly) elastic origin[Ohkoshi 05] .It is known from recent literature that the CT phase transition in this family of complexes can be induced by temperature, pressure or light irradiation[Ohkoshi 05, Sato 07]. The two phases display markedly different magnetic, optical and electrical properties in each case, which can not only be used to follow the phase transition, but allows one also to consider them for potential applications in devices. Of particular importance for optical devices is the complex dielectric constant ε* exhibiting drastic variations over the visible spectrum. For example, using the ellipsometry data published in ref. [Loutete-Dangui 08] one can estimate the refractive index and absorbance changes between the two phases at 600 nm as high as Δn=0.16 and Δk=0.5 in compounds analogous to Rb$_{0.8}$Mn[Fe(CN)$_6$]$_{0.93}$·1.62H$_2$O. In addition, the thermal hysteresis loops can be exceptionally large (up to 138 K) and they can encompass the room temperature range in certain cases [Ohkoshi 05, Ohkoshi 08], as for example the Rb$_{0.96}$Mn[Fe(CN)$_6$]$_{0.98}$·0.75H$_2$O compound [L. Salmon, E.J. M. Vertelman et al. 09], which will be studied later in this chapter.

Figure II.18 reports the product of molar magnetic susceptibility and temperature for the microcrystalline samples of $Rb_{0.8}Mn[Fe(CN)_6]_{0.93} \cdot 1.62H_2O$ as a function of the temperature. The $\chi_M T$ value, where χ_M stands for the molar magnetic susceptibility, falls from 4.7 cm^3Kmol^{-1} to 3.4 cm^3Kmol^{-1} on going from the HT to the LT phase. The phase transition temperatures in the cooling (heating) mode are 218 K and 216 K, yielding 73 K hysteresis loop, respectively. The phase transition is accompanied also by a color change from light brown (HT) to dark brown (LT).
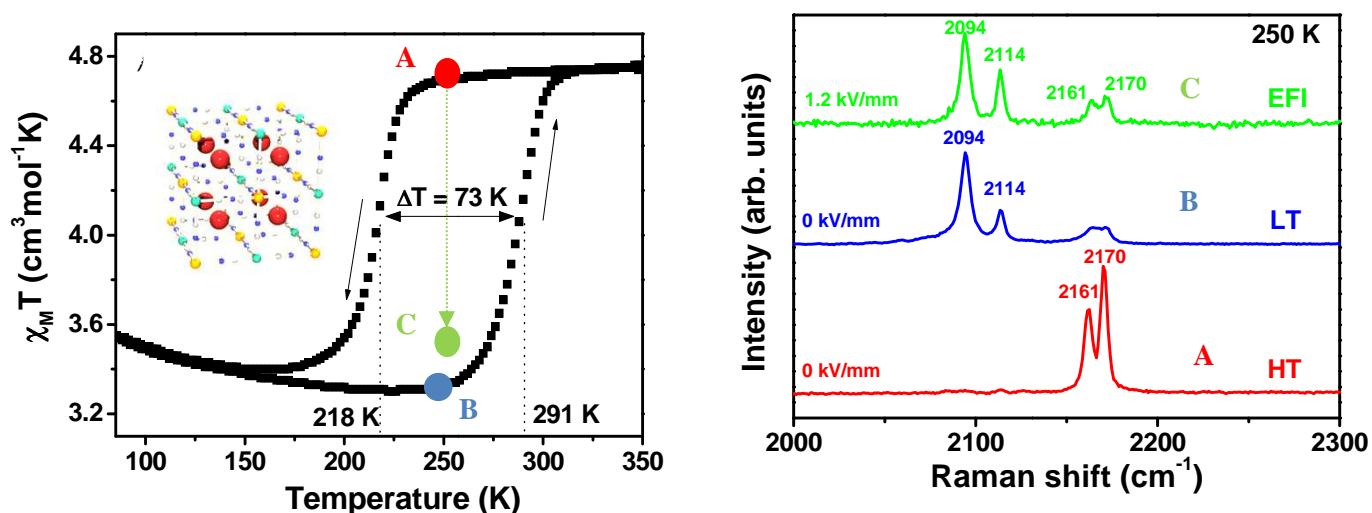
FigII.18: *(left panel) Temperature dependence of $\chi_M T$ of $Rb_{0.8}Mn[Fe(CN)_6]_{0.93} \cdot 1.62H_2O$ (9). The insert shows the room temperature crystal structure of the corresponding compound.* [Vertelman 08, Ohkoshi 08]. *The arrow shows the effect of an electric field of 1.2 kV/m.(Right panel) Raman spectra of $Rb_{0.8}Mn[Fe(CN)_6]_{0.93} \cdot 1.62H_2O$ recorded at 250 K in the high-temperature (HT) and low-temperature (LT) phases without any external electric field as well as under an applied field (EFI) in the cooling mode.*

The CT phase transition can be conveniently followed in this compound by Raman spectroscopy since it exhibits sharp and intense CN stretching modes around 2100-2200 cm^{-1}, which are known to be very sensitive to the oxidation and spin state of the coordinating metal ions[Nakamot 97]. Figure II.18 shows selected Raman spectra of $Rb_{0.8}Mn[Fe(CN)_6]_{0.93} \cdot 1.62H_2O$ excited at 632.8 nm at 250 K in the HT and LT phases before applying an external electric field on the sample. In agreement with previous works [Cobo 07] the HT (Fe^{III}-CN-Mn^{II}) phase of $Rb_{0.8}Mn[Fe(CN)_6]_{0.93} \cdot 1.62H_2O$ reveals two CN stretching modes around 2161 and 2170 cm^{-1}, while the LT phase (Fe^{II}-CN-Mn^{III}) is characterized by two lower frequency modes around 2094 and 2114 cm^{-1}.

One of the most important results of the present thesis is that we were able to observe clear changes in the Raman spectra of these compounds when they were polarized by an external electric field in the HT phase within the thermal hysteresis region. As shown in figure II.18 these spectral changes can be unambiguously assigned to the CT phase transition between the HT and the LT forms of the compounds.

It must be noted that this electric field effect was observed systematically when the transparent electrode (i.e. the surface probed by Raman spectroscopy) was negatively polarized. Furthermore, the electric-field induced CT phase transition is irreversible in the sense that when the field is removed the sample does not return to the initial state. This result can be easily rationalized since the lifetime of the metastable states within the hysteresis region is virtually infinite. Figure II.19 reports the stability of the LT phase in the time. For example at 218 K in the descending branch, the converted LT phase (84%) remains stable for a long time (~27 h), but when the initial temperature is close the phase transition temperature (at 280 K) we have observed a relatively fast relaxation from 36% to 22% in the first 60 min, but after that the complex remains stable.
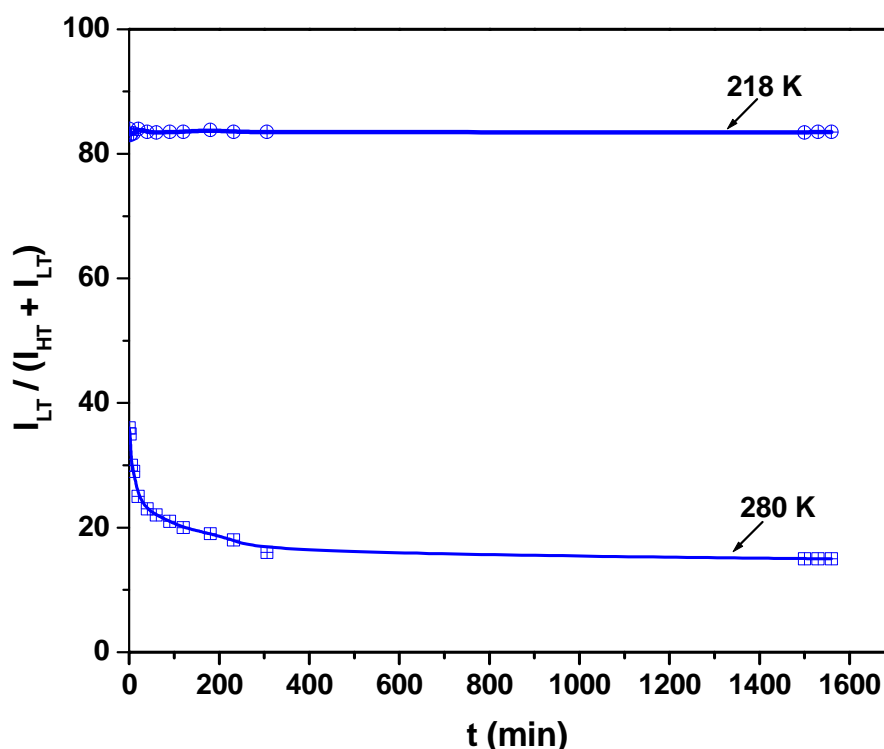

Fig II.19: *Stability in time of the LT phase induced by an external electric field at 218 K and at 280 K. In sample* **9** *the fraction of the LT phase was calculated by integrating the peak surfaces of the Raman spectra.*

Furthermore, we could not induce in any instance the reverse LT→HT phenomenon by an electric field, but the initial HT state of the samples could be restored by heating above their respective thermal transition temperatures (see Fig.II.20). However, we should notice that a proportion of *ca.* 4 % remains as a residual LT fraction even after heating to 60°C.
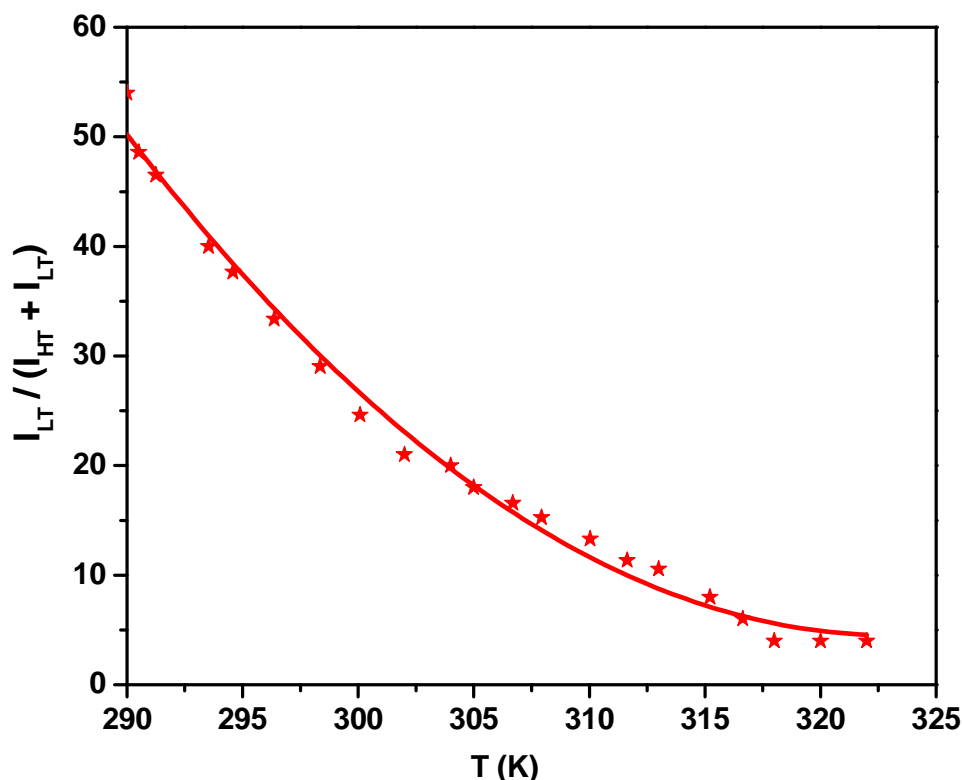
Fig.II.20: *LT fraction as function of the temperature in the heating mode following E-field induced switching of sample **9**. The fraction of the LT phase was calculated by integrating the peak surfaces of the Raman spectra. Data points are connected to guide the eye.*

We have carried out a more detailed investigation of the electric field induced switching phenomenon as a function of the applied electric field and the temperature (Fig.II.21).

The sample was first constrained in a stepwise manner to an increasing applied field at 280 K. Up to *ca.*1.1 kV/mm no significant change was observed in the Raman spectra (Fig.II.21b) and the current flowing through the sample increased monotonically with the increasing bias.
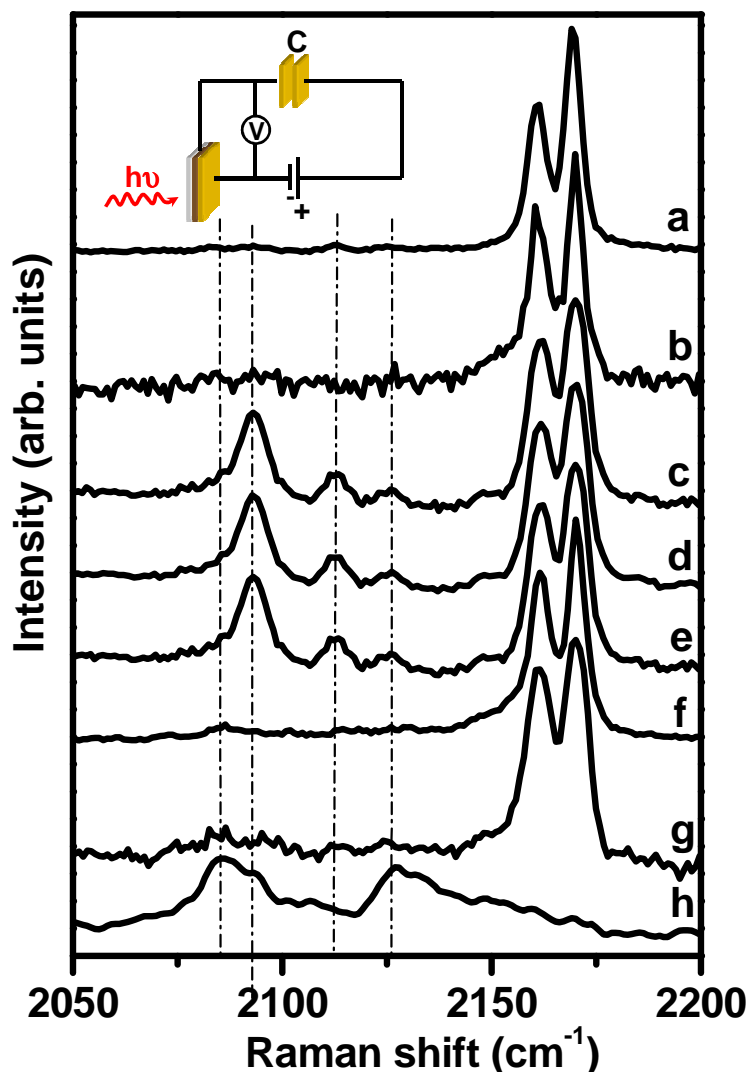
Fig.II.21: *Electric field effect on the Raman spectra of $Rb_{0.8}Mn[Fe(CN)_6]_{0.93} \cdot 1.62H_2O$. Each spectrum was acquired at 280 K successively (a) before the application of any external electric field in the HT phase, (b) after the application of a field of 1.1 kV/mm, (c) after the application of a field of 1.2 kV/mm, (d) after waiting an hour in zero external field, (e) after the application of a field of 1.2 kV/mm in the opposite direction with respect to case (c), (f) after rising the temperature to 330 K, (g) after cooling to 280 K and applying a 1.2 kV/mm field using a capacitor to block the current flow (see insert for the scheme of the circuit) and (h) after the application of a field of 3 kV/mm.*

For a further slight increase of the applied field above a threshold value of *ca.* E=1.2 kV/mm the Raman modes of the LT phase appeared abruptly (fig. 21c) and the current increased also significantly. This may be related to the fact that the LT phase is more conductive. Figure II.22 shows a typical I-V curve on this sample.

Fig.II.22: *Variation of the electric current as function of the electric field applied on a stepwise manner on the compound **9**. The current increases typically from~0.1 to a few mA.*

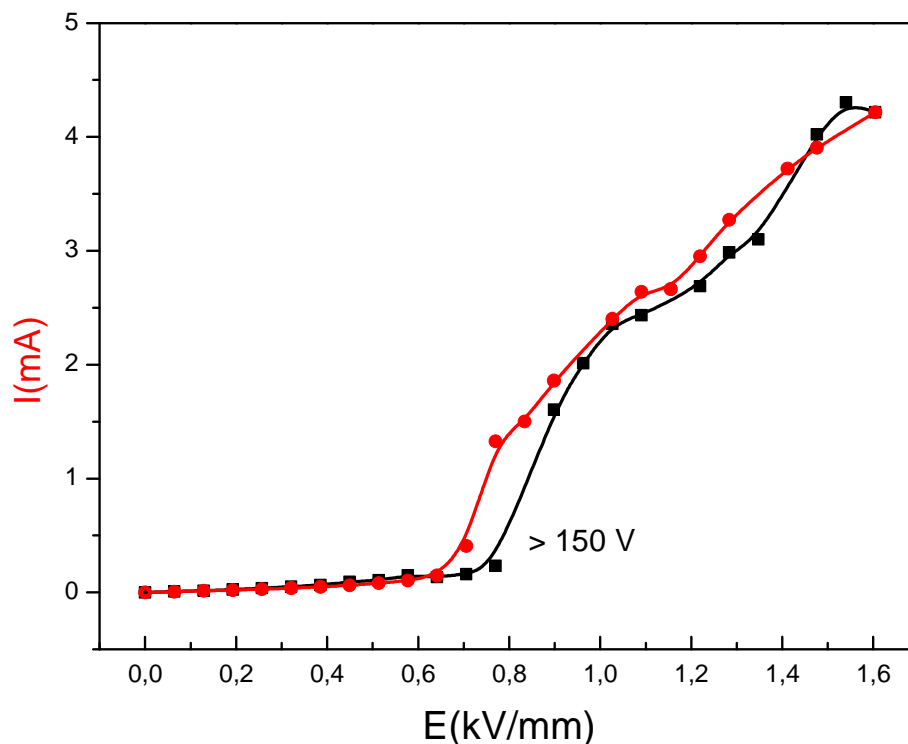The Raman spectrum in Fig.II.21c was recorded immediately following the application of the field, but one should note that the spectrum acquisition takes *ca.* 2 min. We have recorded a few successive Raman spectra under a constant bias and we have observed that the proportion of the signal of the LT phase remains usually stable, albeit a further increase occurred in some cases with the time indicating that the conversion is relatively sluggish. Furthermore, when the field is switched off, the intensity ratio of the LT and HT modes remains constant during (at least) an hour in zero external field (Fig.II.21d). The application of the same field (1.2 kV/mm) but in the opposite direction (*i.e.* positive polarization on the transparent electrode) does not modify either the Raman spectrum (Fig.II.21 e). Finally, when the sample is heated above the phase transition temperature to 320 K it returns to the initial state (Fig.II.21f).

In another experiment, the sample **1** was cooled down to 280 K and was polarized by introducing a capacitor in the circuit to impede the current flow (the scheme of the circuit is shown in the insert of Fig.II.21). No effect could be detected up to applied fields of 3 kV/mm underlying the importance of the charge injection (Fig.II.21g) in the mechanism of the

generated phase transition. After removing the capacitor, we have tried to apply fields higher than 1.2 kV/mm in order to further increase the conversion efficiency. Up to *ca.* 1.8 kV/mm, only the conversion to the LT phase occurs but above ~1.8 kV/mm the irreversible sample reduction starts to compete with the CT phase transition leading to the complete **reduction of the sample** (Mn^{II}-NC-Fe^{II} form) above 2.2 kV/mm, characterised by two Raman modes around 2085 and 2128 cm^{-1} [Bonhommeau 08] (Fig.II.21h).

Electric field effects on Prussian blue, $KFe^{III}[Fe^{II}(CN)_6]$, exhibiting no CT phase transition, have been already studied by Carpenter *et al.*[Carpenter 90] who observed a partial reduction of the compound near the cathode and a partial oxidation near the anode. They explained this phenomenon by the fact that Prussian blue type compounds are mixed conductors in which the alkali cations can move to provide the charge compensation required for the redox reactions. Obviously similar phenomena are expected to occur in other PB analogues as well and can thus rationalize the observed reduction in **9**.

We have also studied the proportion of the HT phase before and after the application of an external electric field (~1.2 kV/mm) at different points of the hysteresis loop (Fig.II.23). For each measurement the sample was first slowly cooled down (warmed up) in the descending (ascending) branch of the hysteresis loop to the desired temperature and it was stabilized during at least half an hour before the Raman spectrum of the initial state of the compound was recorded. Then, another Raman spectrum was recorded immediately after a voltage application on the sample as well as five minutes later to check the stability of the final state. The proportion of the two phases was estimated from the area ratio of the Raman v_{CN} modes ($I_{HT}/I_{HT}+I_{LT}$). In the pure HT phase at 310 K no field effect could be observed. However, Raman spectra collected after the application of the electric field at 280 K (cooling mode) revealed a sample conversion to a state consisting of 36% LT fraction. The same experiment with fresh samples at 250 K and at 210 K led to a quasi-complete HT→LT phase conversion with a final state consisting of 74% and 84% LT fractions, respectively. In a similar manner, we have carried out measurements on the ascending branch as well at 110 and 240 K, but we have observed no field effect on the Raman spectra. However, at 270 K on the ascending branch of the hysteresis loop we could observe a conversion from a 43% LT initial phase to a 68% LT final phase – indicating that the hysteresis loop is modified by the electric field to

some extent. On the whole it appears clearly that the electric field stabilizes the LT phase and the field-induced switch occurs within the hysteresis region.
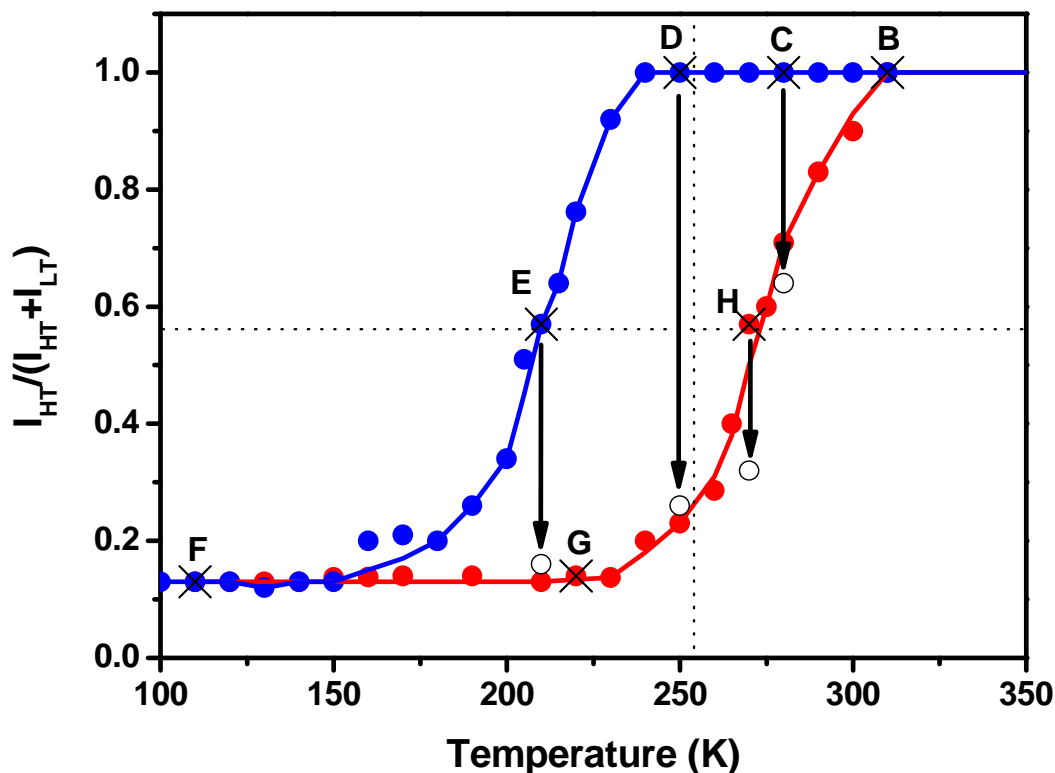

Fig.II.23: *Electric field induced CT transition from different initial states. The closed circles show the temperature dependence of the Raman intensity ratio of the ν_{CN} modes of $Rb_{0.8}Mn[Fe(CN)_6]_{0.93}\cdot1.62H_2O$ in the HT and LT phases in zero applied field ($I_{HT}/(I_{HT}+I_{LT})$). The crosses (open circles) show the proportion of the HT phase before (after) the application of an electrical field of 1.2 kV/mm on different points of the hysteresis loop.*

We have also investigated the electric field effect on two other RbMnFe analogue samples with different stoichiometries:

1) The $Rb_{0.61}Mn[Fe(CN)_6]_{0.86}\cdot2.71H_2O$ [*Molnár, Vertelman et al. 09*] sample (**10**), presents no CT phase transition and we observed only the apparition of the reduced form under an applied electric field. Figure II.24 displays the evolution of the molar magnetic susceptibility of the $Rb_{0.61}Mn[Fe(CN)_6]_{0.86}\cdot2.71H_2O$ sample as a function of temperature. The magnetic behavior clearly shows that the sample does not exhibit an electron transfer. The $\chi_M T$ value at room temperature is 4.75 cm^3 K mol^{-1}. The room temperature Raman spectrum of this sample is characterized by two CN stretching modes around 2159 and 2168 cm^{-1} (HT phase). The

applied electric bias above ~2 kV/mm lead only to the irreversible and complete reduction of the sample (Mn^{II}-NC-Fe^{II} form), characterised by two Raman modes around 2122 and 2082 cm^{-1} [Salmon 09] (Fig.II.21h).
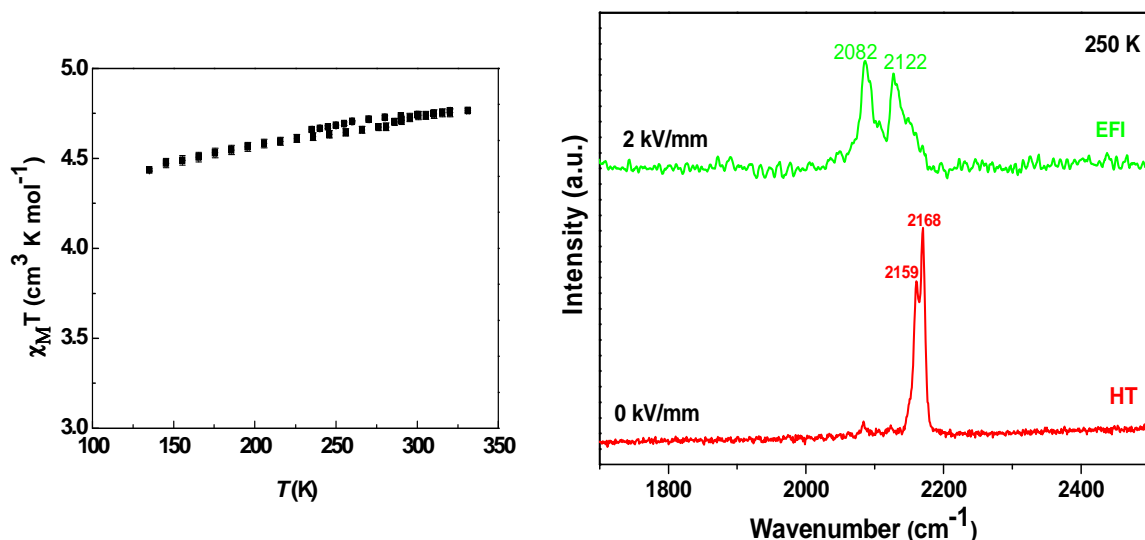
Fig.II.24: *(Left panel) Temperature dependence of $\chi_M T$ of $Rb_{0.61}Mn[Fe(CN)_6]_{0.86}.2.71H_2O$ compound in the cooling and heating modes. (Right panel) Raman spectra of the $Rb_{0.61}Mn[Fe(CN)_6]_{0.86}.2.71H_2O$ compound, recorded at 250 K in the high-temperature (HT) phases without any external electric field as well as under an applied field (EFI).*

2) The $Rb_{0.96}Mn[Fe(CN)_6]_{0.98}.0.75H_2O$ sample [L. Salmon, E.J. M. Vertelman et al. 09], which exhibits a CT phase transition around the room temperature (no need for the cryostat) was also investigated.
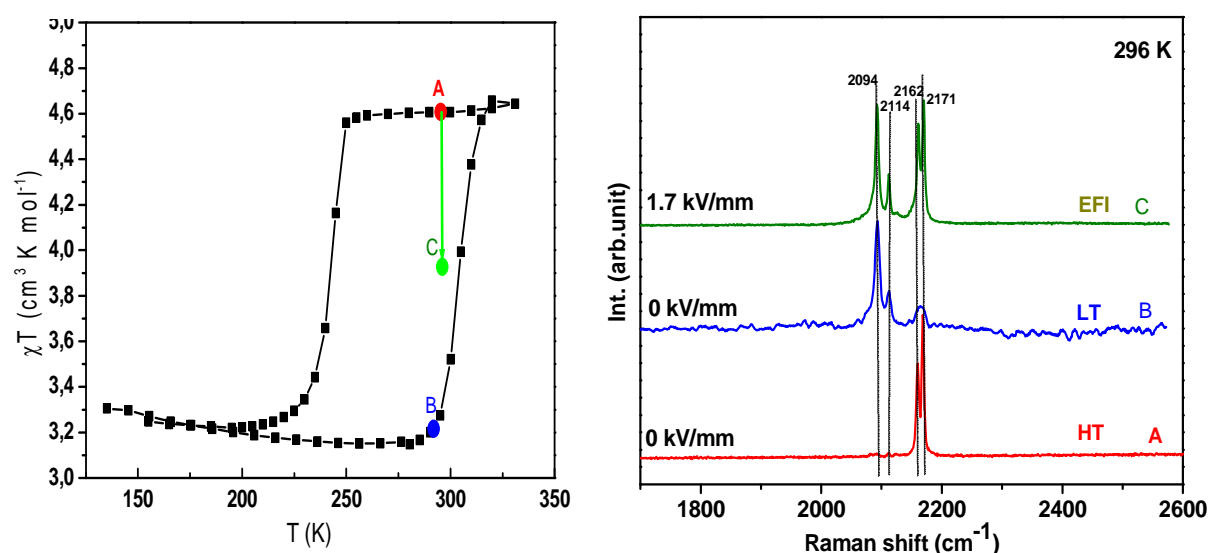
Fig.II.25: *(Left panel) Temperature dependence of $\chi_M T$ of the $Rb_{0.96}Mn[Fe(CN)_6]_{0.98}.0.75H_2O$ sample in the cooling and heating modes. (Right panel) Raman spectra of $Rb_{0.96}Mn[Fe(CN)_6]_{0.98}.0.75H_2O$ recorded at 296 K in the high-temperature (HT) and low-temperature (LT) phases without any external electric field as well as under an applied field (EFI) in the descending branch of the hysteresis.*

Figure II.25 displays the evolution of the molar magnetic susceptibility of the $Rb_{0.96}Mn[Fe(CN)_6]_{0.98}.0.75H_2O$ sample as a function of temperature (left panel). The $\chi_M T$ value decreases abruptly from 4.6 cm^3 K mol^{-1} to 3.2 cm^3 K mol^{-1} around 250 K upon cooling and, conversely, as the sample is warmed up from 130 K, the $\chi_M T$ value increases around 300 K and reaches the initial $\chi_M T$ value. The width of the thermal hysteresis loop (61 K) is defined by $T_{1/2}\downarrow$ = 242 K and $T_{1/2}\uparrow$ = 303 K. The selected Raman spectra of $Rb_{0.96}Mn[Fe(CN)_6]_{0.98}\bullet0.75H_2O$ excited at 632.8 nm and recorded at 296 K in the HT and LT phases before applying an external electric field reveals two CN stretching modes around 2162 and 2171 cm^{-1} in the HT phase, while the LT phase (Fe^{II}-CN-Mn^{III}) is characterized by two lower frequency modes around 2094 and 2114 cm^{-1}.

Clear changes were observed in the Raman spectra of this compound when it was polarized by an external electric field (~1.7 kV/mm) in the HT phase **at room temperature** (no cryostat used at 296 K). The spectrum reveals the CT phase transition between the HT and the LT forms induced by an applied electric field, thereby revealing an interesting and promising approach towards electrically switchable devices working at room temperature.

Conceivable mechanisms for the EFI resistive switching can involve thermal, electronic or electrochemical phenomena. Thermal effects can be easily ruled out here since they cannot explain the HT→LT phase conversion and should facilitate the LT→HT conversion, which was not observed. Ionic transport and electrochemical redox reactions are known to occur in Prussian blue analogues under external electric fields. [Carpenter 90] Indeed, the appearance of the reduced form at fields above 1.8 kV/mm must originate from such a redox phenomenon. The observation of different processes occurring on the cathode and the anode as well as the fact that current flow through the sample is a necessary condition for the EFI HT→LT transition is also in line with an electrochemical phenomenon. However, if the origin of this transition is an electrochemical process one may expect it to occur not only within the hysteresis region but also outside, which is in contradiction with our observations. Another plausible cause for the HT→LT phase transition is **a paraelectric-ferroelectric transition**. Such a transition is known to be triggered by high electric fields and to stabilize the LT phase at the expense of the HT phase by shifting the first-order thermal phase transition towards high temperatures. [Poulsen 08] Indeed, ferroelectricity was reported at cryogenic temperatures in

RbMnFe-type compounds similar to **9.** [Ohkoshi 07] So as to further corroborate this assumption we have carried out dielectric measurements in a wide temperature and frequency range. Figure II.26 displays the temperature dependence of the real part of the dielectric permittivity (ε') at different frequencies.
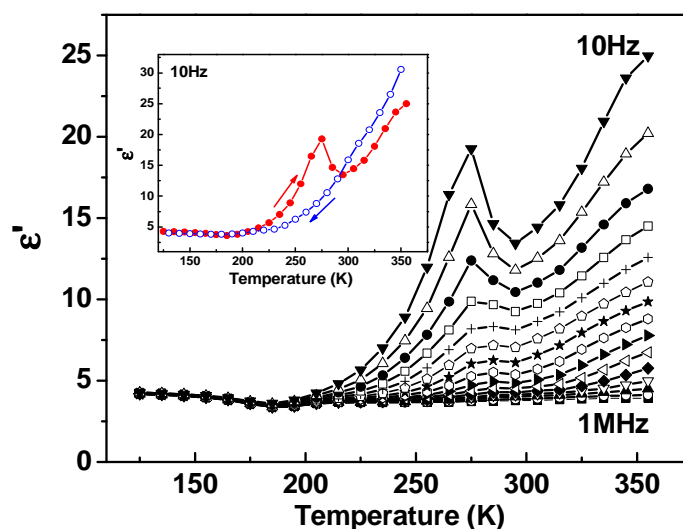
Fig.II.26: *Temperature dependence of the real part of the complex dielectric permittivity of Rb$_{0.8}$Mn[Fe(CN)$_6$]$_{0.93}$·1.62H$_2$O recorded at different frequencies in the heating mode. The hysteresis curve at 10Hz is shown in the insert.*

One can note a dielectric anomaly peak in the ε'(T) curves of the compound **9** close to the phase transition temperatures, the position of which is frequency independent. This suggests the occurrence of a displacive, paraelectric-ferroelectric transition for this compound and we will see later the same anomaly in other compounds as well. For compound **9,** the first-order displacive paraelectric-ferroelectric transition proceeds from the cubic ($F\overline{4}3m$) HT to the tetragonal ($I\overline{4}m2$) LT phase that is from a symmetric to a distorted phase. Considering the sample **1** as a vibronic system, which is the centre of a thermally-induced interplay between ferroelectric and paraelectric phases, we can describe theoretically the potential energy of the system as formed by two types of configurational diagrams: a double well and a simple well (fig. II.27), corresponding respectively to the LT and HT phases.

Fig.II.27: *Effect of the electric field on the temperature dependence of the HT fraction $n_{HT}(T)$ – simulated using the three-states model. The electric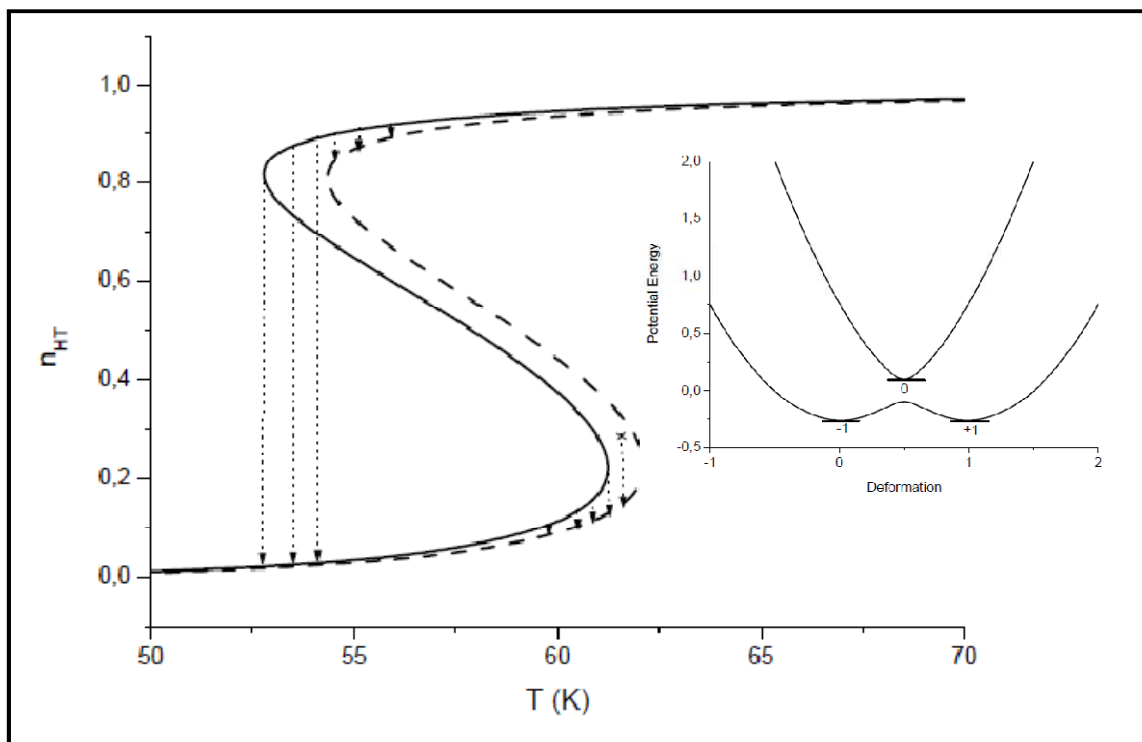 field stabilizes the LT (ferroelectric) phase and polarizes the dielectric system which induces a non-zero electric dipole. The arrows show the direction of the jump of the HT fraction. The insert show the configurational diagram, restricted to one effective distortion mode, showing the potential energy of the system in the LT (double well) and HT (single well) states.*

This situation can be approximated by a three-states system by means of the well-known Blume-Capel model accounting for elastic interactions [Boukheddaden 05]. In collaboration with Kamel Boukheddaden from the University of Versailles, the mechanism was discussed as follows: the electric field effect results from the existence of the ferroelectric-paraelectric transition in this family of compound, which accompanies the cooperative Jahn-Teller transition of sample **9.** We should notice that we have chosen this compound due to the clear indication (dielectric data) of the existence of a ferroelectric (paraelectric) phase in the LT (HT) temperature regime corresponding to the distorted (symmetric) phase.

The deformation represented in the x-axis of fig.II.27 accounts for an effective distortion mode, the average value of which informs on the existence of a dipole moment. By virtue of the intermolecular interactions, the symmetry is broken between the two states of the double well potential and an energy competition takes place between the two phases. While the former originates from dipolar (electrostatic) interactions, the latter is mainly due to the Jahn-Teller coupling which drives the first-order transition.

The application of an external field, $\vec{E}$, introduces the energy contribution $W = -\vec{p}_i.\vec{E}$ (where p_i is the electric dipolar moment) which enhances the "field" breaking the symmetry of the double well. Consequently, the electric field E will be expressed in energy units and the polarization P will be expressed through the molecular distortion <Q>, to which it is related through a monotonic dependence. For simplicity, we neglect the depolarizing field by taking E as a local field. Also, in the present investigation, we disregard electric conductivity, i.e. we deal with an insulating solid and we focus only on the static electric field effect. Moreover, we restrict ourselves to the ferroelastic interaction case between the molecular units, and the electric field $\vec{E}$ is for simplicity taken parallel to the molecular axis. The polarization $\vec{P}$ will be either parallel or antiparallel to $\vec{E}$, and reversing $\vec{E}$ or $\vec{p}$ is equivalent, leading to an electric hysteresis loop with point symmetry in the E-P plane, as observed in recent experiments by Ohkoshi *et al.* [Ohkoshi 07]

The complicated configurational diagram of Fig.II.27 can be simplified as a three states system. The total Hamiltonian accounting for the "elastic" interactions can be written as follows:

$$H = -K \sum_{i \neq j} s_i^2 s_j^2 - \sum_i \Delta_{eff} s_i^2 \quad (1),$$

where $s_i = 0, \pm 1$ is a spin state associated with the paraelectric phase (s=0) and the ferroelectric phase (s=+1, -1). We recognize in Hamiltonian (1) the well known Blume-Capel model,[Boukheddaden 05] where there is no term breaking the symmetry between the states +1 and -1 and in which all the energetic contributions lead to a competition between the LT (s^2=+1) and the HT phases (s^2=0). (In a more realistic model, the parameter K originates from elastic cooperative Jahn-Teller interaction, which couples the local deformations with that of the lattice.) The parameter $\Delta - k_B T \ln g$ is the effective ligand-field energy Δ_{eff} containing a zero temperature energy gap (Δ) between the two phases as well as the effect of the volume increase during the transition, which lowers the phonon field energy resulting in an effective degeneracy g of the state s = 0. The latter is taken here as temperature independent for simplicity. An applied external field stabilizes the LT phase, which has a nonzero dipolar moment. Its energetic contribution can be easily written as $h_i s_i$, where $h_i = -\vec{p}_i.\vec{E}$. The order of magnitude for molecular fields is $E \approx 10^6$ V/m and a typical value for the dipolar moment

is $p \approx 2.0 \times 10^{-28}$ C.m, which yields $h \approx 20K$. In the mean-field approach, the order parameter $q = \langle s^2 \rangle$ which corresponds exactly to the fraction of the LT phase, obeys to the following self-consistent equation

$$k_B T = \frac{\Delta + zKq}{\ln\left(\frac{gq}{(1-q)}\right)} \quad (2).$$

Where z stands for the coordinance of the system, which is taken here equal to 1 for simplicity: i.e. z is absorbed in K. Eq. (2) is the equation of state of the system and it leads to a thermally driven first order transition between the LT (q=1) and the HT (q=0) states. The transition temperature, denoted by T_{eq}, is then given by:

$$k_B Teq = \frac{\Delta + zK/2}{\ln \frac{g}{2}} \quad (3).$$

We have used qualitative values for the model parameters, K=354 K, Δ=200 K and g=1350, leading to the thermal hysteresis depicted in fig.II.27, which contains both stable and metastable states. The latter are identified by the negative slope ($\frac{dn_{HT}}{dt} < 0$) of $n_{HT}(T)$, similarly to the mechanical instability in liquid-gas transition.

As far as $h = 0$, the net polarization, $m = \langle s \rangle$, remains equal to zero in the whole temperature range, due to the absence of the dipolar interactions, which are not considered here for simplicity reasons. Under an electric field, which polarizes and stabilizes the nonsymmetric phase, the equation of state becomes

$$q = \frac{\cosh \beta h}{e^{\beta\left(zKq + \Delta - kT\ln\frac{g}{2}\right)} + \cosh \beta h} \quad (4),$$

and

$$m = q \tanh \beta h \quad (5),$$

while the variational free energy per site is given by

$$F = \frac{1}{2}Kq^2 - k_B T \ln\left[1 + e^{\beta(zKq + \Delta - k_B T \ln g/2)}\right]\cosh(\beta h) \quad (6).$$

In the following, we aim to demonstrate that the electric field stabilizes the LT phase and increases the transition temperature T_{eq} as observed in experiments. Expanding Eq. (4) around the transition temperature, for which q = ½, by considering $\beta h \ll 1$, allows to derive the field dependence of the transition temperature $T_{eq}(h)$:

$$T_{eq}(h) \approx Teq(0) + \frac{h^2}{\Delta + zK/2} \quad (7)$$

Here $T_{eq}(0)$ is the transition temperature of the system under zero applied electric field, given by Eq. (3). It follows that the shift of the transition temperature induced by the electric field writes as:

$$\Delta T_{eq} = \frac{h^2}{k_B T_{eq}(0)\ln\frac{g}{2}} = \frac{p^2 E^2}{\Delta H(0)} \quad (8)$$

ΔT_{eq} depends on the ratio between the square of the electrostatic energy and the enthalpy change at the transition, $\Delta H(0)$. In addition, Eq. (8) shows that the lowering of the transition temperature $T_{eq}(0) = \dfrac{\Delta + zK/2}{k_B \ln\frac{g}{2}}$, by controlling the stoichiometry of the samples, will enhance the electric field effect.

On the hysteresis loop, see fig.II.27, it is found that the electric field shifts the whole hysteresis to the high-temperature side by ~1 K, even if the latter acts differently on the ascending and descending metastable branches. Indeed, denoting by T_h^+ (T_0^+) and T_h^- (T_0^-), the transition temperatures under the "field" h (h=0) at the ascending and descending branches, respectively, one can deduce from Eq. (4) that the associated shifts are given by

$$k_B \Delta T^+ = \frac{h^2}{T_0^+ \ln\frac{g}{2}} \quad \text{and } k_B \Delta T^- = \frac{h^2}{T_0^- \ln\frac{g}{2}} \quad (8).$$

Since $T_0^+ > T_0^-$, it follows that $\Delta T_0^+ < \Delta T_0^-$, which indicates that the electric field causes a nonsymmetric distortion of the hysteresis loop.

It is clear that the proposed model cannot explain all experimental findings. In particular, the absence of EFI HT → LT phase transition upon reversing the sign of the external electric field (*i.e.* no change observed on the anode) is difficult to explain. Furthermore, the necessity of current flow shows also that the observed phenomena are not purely field-induced. It is possible that the migration of charge carriers towards the electrodes under the field facilitates somehow the switching effect, but this explanation remains purely speculative at the present stage. One should note also that in ferroelectric materials, an applied electric field can also induce piezoelectricity in many cases. Taking into account the huge volume contraction when going from the HT to the LT phase (*ca.* 10 % for compound **1**) such electromechanical effects may also contribute to the stabilization of the LT phase under an applied dc bias.

II.2.3 Na$_2$Co$_4$[Fe(CN)$_6$]$_{3.3}$.15H$_2$O and Co$_3$[W(CN)$_8$]$_2$(pyrimidine)$_4$·6H$_2$O

In order to verify if the electric field effect is specific to the RbMnFe complex or it is a more general phenomenon we have investigated two other compounds as well: **Na$_{2.2}$Co$_4$[Fe(CN)$_6$]$_{3.3}$.15H$_2$O**[Bleuzen 03] (**7**) and **Co$_3$[W(CN)$_8$]$_2$(pyrimidine)$_4$·6H$_2$O**[Ohkoshi 06, Ohkoshi 08] (**8**). Compound (**7**) has a typical cubic structure of the Prussian-blue type complex. This compound exhibits a CT phase transition between the high-temperature (HT) Fe^{III}(t$_{2g}^5$e$_g^0$, LS, S=1/2)-CN-Co^{II}(t$_{2g}^5$e$_g^2$, HS, S=3/2) and the low-temperature (LT) Fe^{II}(t$_{2g}^6$e$_g^0$, LS, S=0)-CN-Co^{III}(t$_{2g}^6$e$_g^0$, LS, S=0) accompanied by a thermal hysteresis loop of (mainly) elastic origin[Shimamoto 02]. On the other hand, complex **8** is based on octacyanometalate building blocks (see insert of fig.II.28b) and it was shown to display a CT phase transition between the HT $Co_{HS}^{II}(S = 3/2) - NC - W^V(S = 1/2)$ and the LT $Co_{LS}^{III}(S = 0) - NC - W^{IV}(S = 0)$ electronic configurations (HS and LS stand for high-spin and low-spin respectively) [Ohkoshi 06, Ohkoshi 08]. It is also interesting to notice that, in these two complexes, the CT phase transition is accompanied by a spin state conversion on the cobalt ions as well. In contrast, Rb$_x$Mn[Fe(CN)$_6$]$_y$.zH$_2$O compound does not exhibit any spin state conversion, but a Jahn-Teller distortion occurs in the LT phase on the Mn^{III} ions.
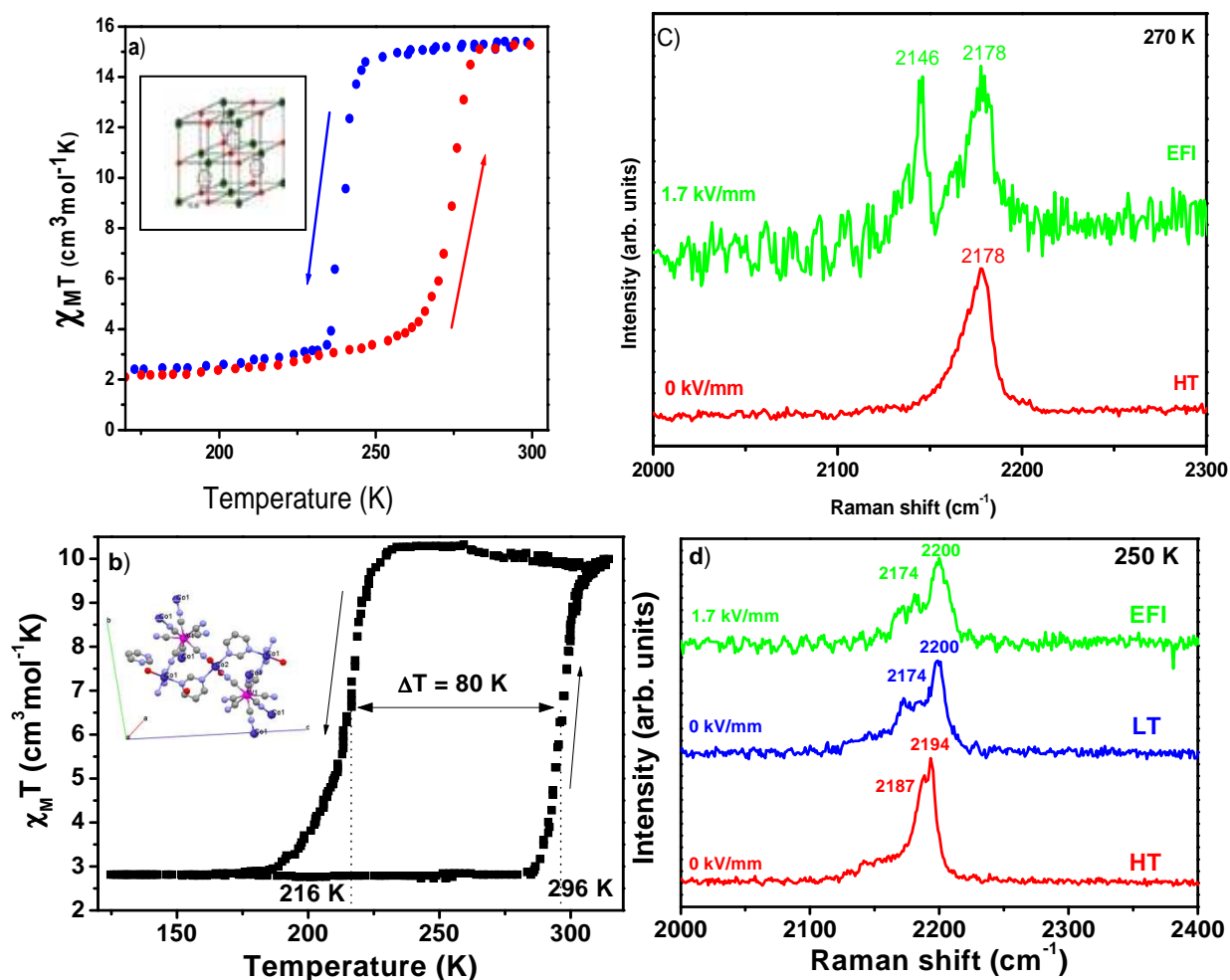
Fig.II.28: *(Left panels) Temperature dependence of $\chi_M T$ of $Na_{2.2}Co_4[Fe(CN)_6]_{3.3}.15H_2O$ (a) and $Co_3[W(CN)_8]_2(pyrimidine)_4 \cdot 6H_2O$ (b) in the cooling and heating modes. (Right panels) Raman spectra of $Na_{2.2}Co_4[Fe(CN)_6]_{3.3}.15H_2O$ (c) recorded at 270 K in the high-temperature (HT) without any external electric field as well as under an applied field (EFI) in the descending branch of the hysteresis and $Co_3[W(CN)_8]_2(pyrimidine)_4 \cdot 6H_2O$ (d) recorded at 250 K in the high-temperature (HT) and low-temperature (LT) phases without any external electric field as well as under an applied field (EFI) in the descending branch of the hysteresis.*

Figures II.28a - II.28b report the product of molar magnetic susceptibility and temperature for the microcrystalline samples **7** and **8** as a function of the temperature. The $\chi_M T$ value, where χ_M stands for the molar magnetic susceptibility, falls from 14.5 cm³K mol⁻¹ to 2.4 cm³Kmol⁻¹ in compound **7** and from 10.3 cm³Kmol⁻¹ to 2.8 cm³Kmol⁻¹ in compound **8** on going from the HT to the LT phase. The phase transition temperatures in the cooling (heating) modes are 218 (238) K and 216 (296) K for compounds **7** and **8**, yielding 20 K and 80 K wide hysteresis loops, respectively. The phase transition is accompanied also by a color change from light

purple (HT) to dark purple (LT) in compound **7** and from red (HT) to blue (LT) in compound **8** [Ohkoshi 06, Ohkoshi 08].

We have found no Raman data in the literature for compound **7** and **8**. However figures II.28c-II.28d show selected Raman spectra of **7** and **8** excited at 632.8 nm, at 250 K in the HT, LT phases for sample **8** and at 270 K in the HT phase for sample **7** before applying an external electric field on the sample. The sample **7** presents a CN stretching mode around 2178 cm^{-1} in the HT phase, whereas the compound **8** presents two CN stretching modes in the HT as well as in the LT phases around 2187, 2194 cm^{-1} and 2174, 2200 cm^{-1}, respectively. Unfortunately we weren't able to get Raman spectra of compound **7** in the thermally induced LT phase. However, and as shown in figures II.28c-II.28d, we were able to observe clear changes in the Raman spectra of these compounds when they were polarized by an external electric field in the HT phase within the thermal hysteresis region. These spectral changes can be unambiguously assigned, to the CT phase transition between the HT and the LT forms of the compound **8**, and we believe that, the CN stretching mode appearing around 2146 cm^{-1} can be assigned to the LT phase of the compound **7.** Furthermore we have tried to apply fields higher than 1.7 kV/mm in order to further increase the conversion efficiency; thereby confirming what already reported for the Rb$_{0.8}$Mn[Fe(CN)$_6$]$_{0.93}$·1.62H$_2$O. Up to *ca.* 1.8 kV/mm, only the conversion to the LT phase occurs but above ~ 2 kV/mm the irreversible sample reduction (Co^{II}-NC-Fe^{II} form), characterized by a single Raman mode around 2100 cm^{-1} starts to compete with the CT phase transition (Fig.II.29). Remarkably, this reduction at higher fields was not observed in sample **3**.
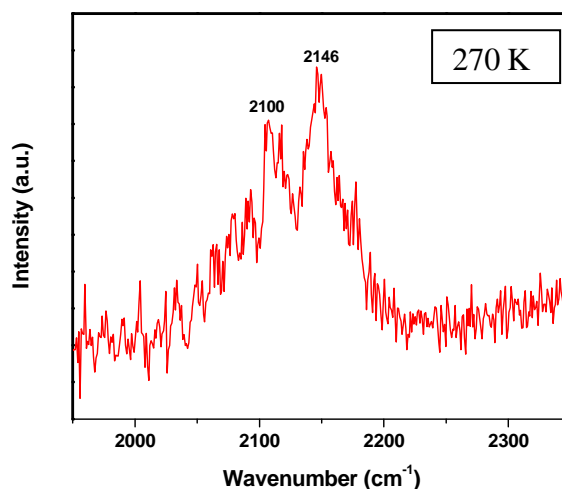

Fig.II.29: *Electric field effect on the Raman spectra of Na$_{2.2}$Co$_4$[Fe(CN)$_6$]$_{3.3}$.15H$_2$O after the application of a field of 3 kV/mm.*

Figure II.30 displays the temperature dependence of the real part of the complex dielectric permittivity (ε') at different frequencies. The occurrence of a peak in ε'(T) for compounds **7** and **8** can lead us also to adopt the paraelectric-ferroelectric transition as a mechanism for the electric field-induced charge-transfer phase transition in these complexes.
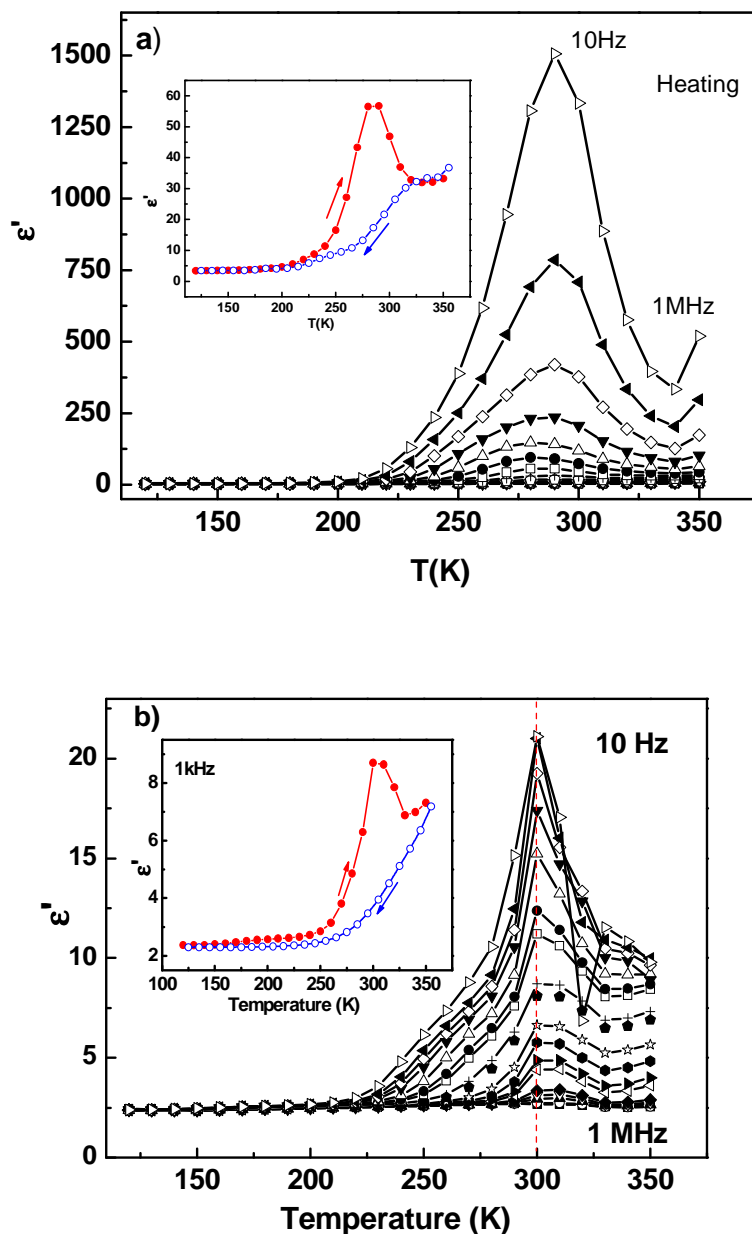

Fig.II.30 *Temperature dependence of the real part of the complex dielectric permittivity of* $Na_{2.2}Co_4[Fe(CN)_6]_{3.3}.15H_2O$ *(a) and* $Co_3[W(CN)_8]_2(pyrimidine)_4·6H_2O$ *(b) recorded at different frequencies in the heating mode. The hysteresis curves at selected frequencies are shown in the inserts.*

We believe that **the application of a static electric field in this family of compounds induces a shift of the transition temperature** $\Delta T_{eq} = \dfrac{p^2 E^2}{\Delta H(0)}$ which depends on the ratio between the square of the electrostatic energy (p is the electric dipole moment and E the external electric field) and the enthalpy change $\Delta H(0)$ at the transition. The concomitant occurrence of the paraelectric-ferroelectric and magnetic transitions entails that magnetic ions (Mn and Fe in **1**, Co and W in **2**) should play an important role in the paraelectric-ferroelectric phase transition albeit vacancies[Ohkoshi 07], alkali-metal ions[Bleuzen 04] and hydrogen bonding between ligand and zeolitic water molecules could also intervene[*Ohkoshi 08*].

II.2.4 Conclusions

We have observed a new type of electric field-induced transition near room temperature within the thermal hysteresis region of transition metal complexes exhibiting charge transfer phase transition phenomena. Of central interest in this family of compounds are the facts that this transition is accompanied by a spectacular change of material properties (magnetic, optical, electrical and mechanical) and also that the material properties can be tuned to a great extent by synthetic chemistry methods. The EFI transition takes place from the high-temperature towards the low-temperature phase, but the inverse switch can easily be achieved as well by thermal-electrical (Joule) effect – leading to an all-electrical device. We believe that the mechanism of this phenomenon is related to a paraelectric-ferro(piezo)electric transition through the field-induced stabilization of the low-temperature phase, but further investigations on the mechanism of this phase transition will be necessary using microscopic and structural probes such as X-ray diffraction and spectroscopy under high electric fields. From the theoretical point of view, this effect can be well described using simple qualitative models, which capture the essential features of the phenomenon. Further advancements in this field – both for the fundamental and applicative aspects – will, however, require the synthesis of thin films of these materials exhibiting thermal hysteresis.

II.3 The spin crossover complex [Fe(HB(pz)₃)₂]

Coordination complexes containing various substituted poly(1-pyrazolyl)borate ligands have been intensively investigated since the pioneering works of Trofimenko.[Trofimenko 99] Iron and cobalt derivatives, among several other possible complexes, have received particular attention because their spin-state equilibrium is highly sensitive to the ligand substitution.[Long 04] The ferrous complex formed with the hydrotris(1-pyrazolyl)borate ligand, [Fe(HB(pz)₃)₂], where pz = pyrazolyl, is one of the most studied complexes of this family (figure II.31). In this thermochromic complex the iron(II) ions undergo a thermally induced spin crossover between their $^1A_1$ low-spin (LS) and $^5T_2$ high-spin (HS) electronic configurations in the 300 - 450 K temperature range. This high temperature spin crossover (SCO) behavior was first revealed by optical spectroscopy[Jesson 68] and confirmed later by magnetic susceptibility, Mössbauer and infrared spectroscopic studies.[Hutchinson 79, Grandjean 89] Interestingly, **the thermal spin transition curve recorded during the first heating differs drastically from the successive thermal cycles**. It reveals an irreversible change in the magnetic and optical properties in the material.[Grandjean 89]

In the course of this study, interesting and unexpected electrical properties of [Fe(HB(pz)₃)₂] have been uncovered with possible relevance for the technological applications of this compound. Moreover, most work on SCO complexes is performed on powder samples, and this is incompatible with industrial needs for thin films with a precise thickness control. So, the irreversible thermal transition in the electric property together with the fact that this compound can be deposited on surfaces by evaporation, suggests that it might be useful as an active element in ROM-type devices for various applications, alongside the initial ideas of Kahn and Martinez. *[Kahn 98]*
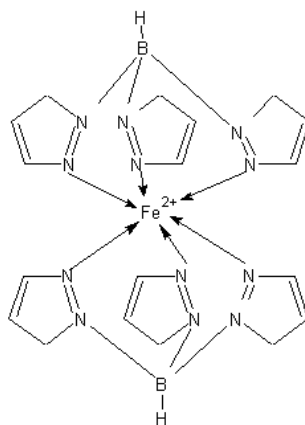

Fig.II.31: *Schematic structure of [Fe(HB(pz)₃)₂].*

II.3.1 Dielectric properties of the bulk [Fe(HB(pz)$_3$)$_2$]

We have decided to re-investigate the remarkable spin crossover properties of the complex [Fe(HB(pz)$_3$)$_2$] in order to confirm the observations previously published in the literature, and then investigate an additional property, which is the electrical conductivity. The hydrotris(1-pyrazolyl)borate ligand,[Trofimenko 67] and the corresponding [Fe(HB(pz)$_3$)$_2$] iron(II) complex[Grandjean 89] used in the following experiments, were synthesized in our team by Lionel SALMON according to experimental procedures reported in the literature. The [Fe(HB(pz)$_3$)$_2$] complex was sublimed at 463 K in vacuum (*ca.* 0.1 Torr) prior to use and either a microcrystalline, clear violet powder or small single crystals (depending on the details of the sublimation conditions) were obtained. Elemental analysis for [Fe(HB(pz)$_3$)$_2$] (481.91 g/mol): calculated. C, 44.86 %; N, 34.88 %; H, 4.18 %; found C, 44.61; N, 34.53; H 4.09. Both magnetic and electric measurements were performed using the same instruments described earlier.

The magnetic properties of Fe[HB(pz)$_3$]$_2$ have been reported earlier in refs. [Hutchinson 79] and [Grandjean 89]. The results that we obtained are quite similar to these reports (Fig.II.32). In our case the $\chi_M T$ product of Fe[HB(pz)$_3$]$_2$ (as prepared) exhibits a gradual increase from 0.07 cm^{3}mol^{-1}K at 300 K to 1.21 cm^{3}mol^{-1}K at 405 K, then an abrupt increase to 2.40 cm^{3}mol^{-1}K at 410 K and finally a gradual increase to 2.80 cm^{3}mol^{-1}K at 450 K. On the contrary, upon cooling, the $\chi_M T$ product gradually decreases to 0.197 cm^{3}mol^{-1}K at 300 K. In agreement with the initial report of Hutchinson *et al.* [Hutchinson 79] the magnetic susceptibility displays an apparent hysteresis only for the first thermal cycle and for all subsequent cooling and heating treatments, the magnetic properties retrace the initial cooling curve, and not the initial heating curve. The temperature at which the sharp and irreversible transition was observed on our sample is different somewhat from previous reports (410 K *vs.* 390 K [Grandjean 89]). One should recognize, however, that the initial state (*i.e.* the freshly sublimated sample) of this sample is thermodynamically unstable and obviously there exist no characteristic transition temperature for such a system since the transformation from the metastable to the stable phase depends not only on the temperature, but also on the time.
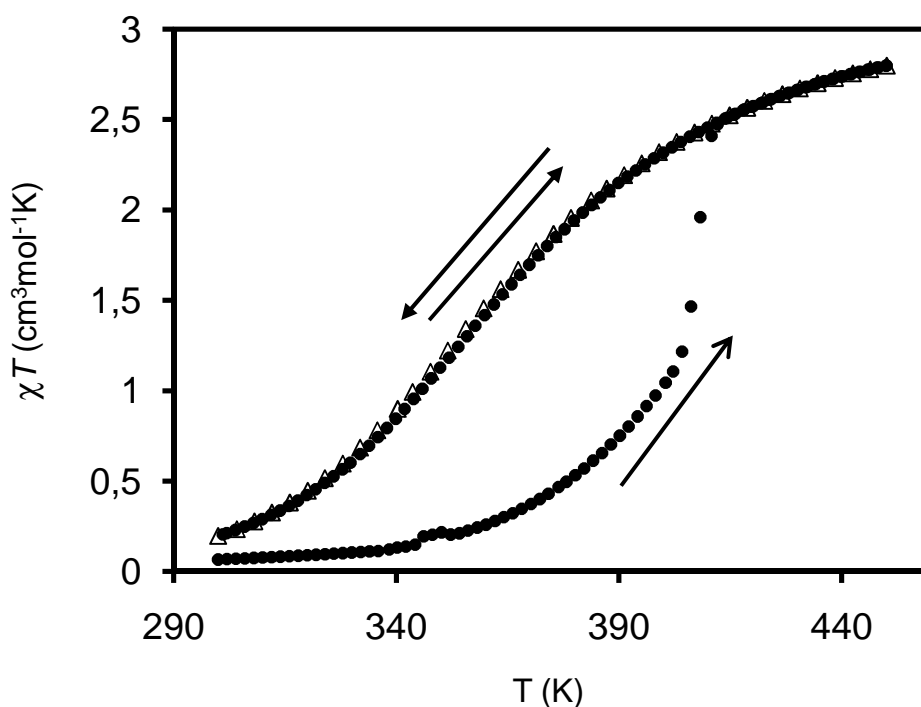
Fig.II.32: *Temperature dependence of the $\chi_M T$ product of Fe[HB(pz)$_3$]$_2$ upon two successive thermal cycles. (First cycle: closed circles, second cycle: open triangles)*

The spin crossover in Fe[HB(pz)$_3$]$_2$ is also accompanied by spectacular color changes. Figure II.33 exhibits digital images of the powder sample recorded at a few representative temperatures. At room temperature the "as-prepared" sample has a violet color (fig.II.33a), which becomes fade when it is heated to 470 K (fig.II.33b). Remarkably, when the sample is cooled back to room temperature its visual aspect appears very different from the initial one. At the end of the first cycle, the initially pale violet, fine microcrystalline powder (fig.II.33a) becomes coarse leading to a deeper color and a more brilliant aspect (fig. II.33c). We have also carried out a microscopic observation of these morphologic changes as shown in figure II.33. The optical microscope shows clearly that the sample is composed of small, needle-like crystallites of a few μm in size before the first thermal cycle (fig.II.33d-e), while it reveals the presence of well-defined single-crystals having various sizes up to a few hundred μm after the first cycle.
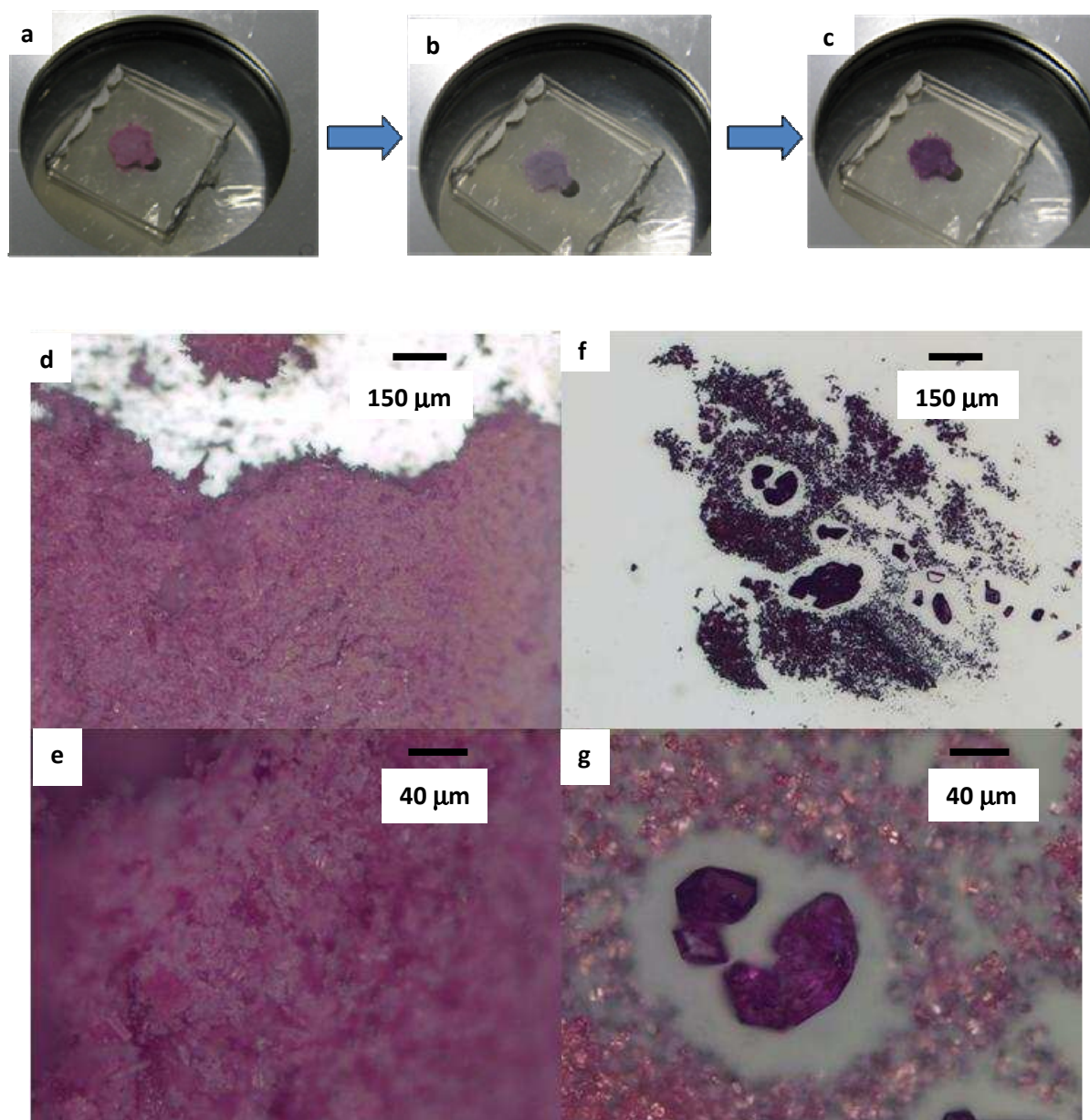
Fig.II.33: *Photographs showing the temperature dependence of the color of the "as prepared" microcystalline sample [Fe(HB(pz)₃)₂] at 295 K (**a**) and at 470 K (**b**) as well as after the first thermal cycle at 295 K (**c**). Microscope images recorded at 295 K displaying the typical aspect of the same sample before (**d**, **e**) and after (**f**, **g**) the first thermal cycle.*

In order to get more quantitative details of the optical changes we have acquired variable temperature diffuse reflectance spectra of Fe[HB(pz)₃]₂ in the 400 – 900 nm range. Figure II.34a displays the reflectivity spectra at different temperatures during the first two thermal cycles. The spectra are plotted as -log(R_{sig}/R_{ref}), where R_{sig}/R_{ref} is the normalized reflectance signal, since this quantity is closely proportional to the absorbance of the sample, provided that the scattering coefficient is wavelength-independent.

a)
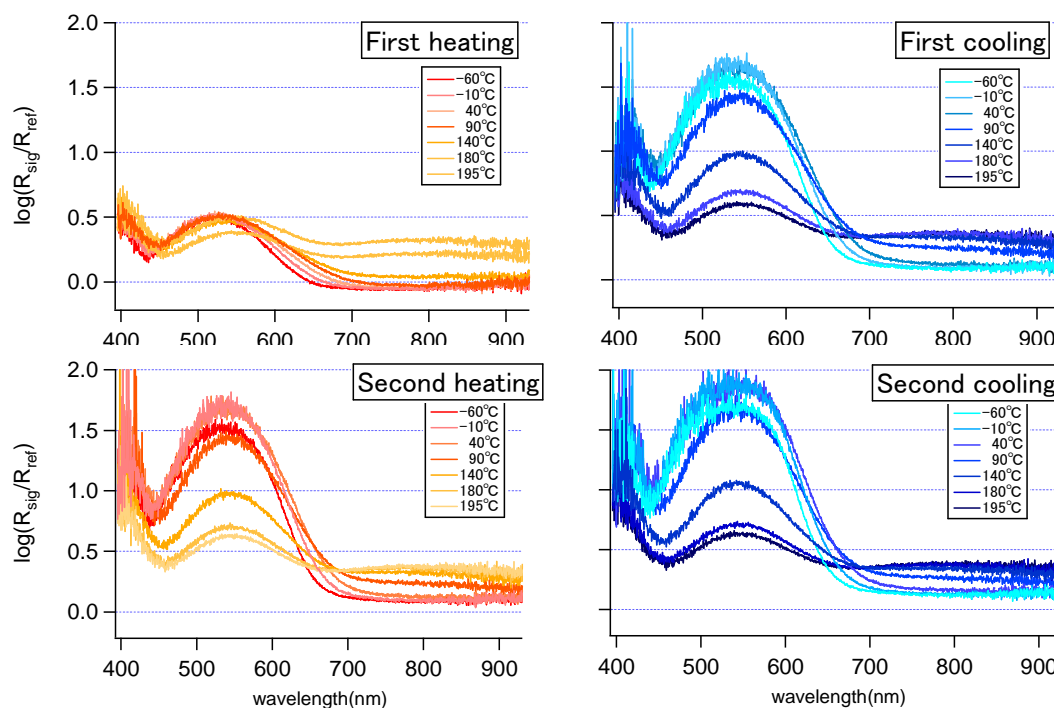
b)

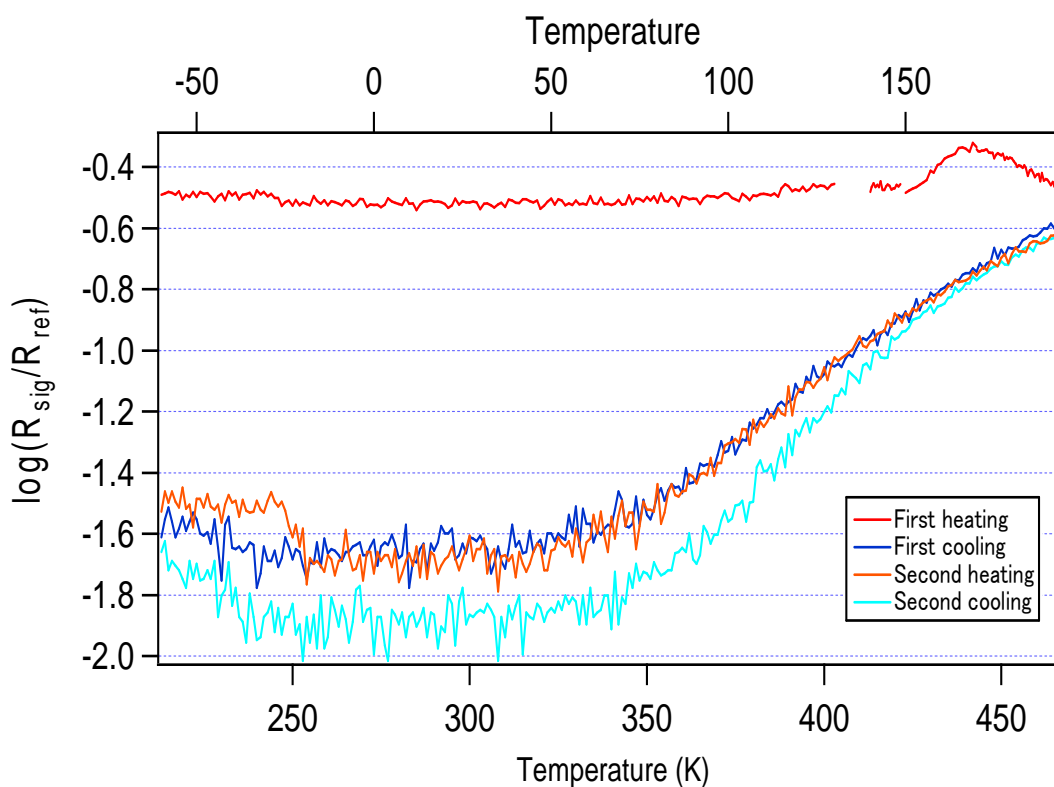***Fig. II.34:*** *(a) Optical reflectivity spectra of Fe[HB(pz)₃]₂ recorded at various temperatures during the first two thermal cycles. (b) Temperature dependence of the reflectivity of* Fe[HB(pz)₃]₂ *(recorded at 530 nm) upon two successive thermal cycles.*

The reflectance spectrum of the sample at room temperature is characterized by an intense absorption band centered around 530 nm - responsible for the violet color of the compound - which have been assigned to the $^1A_{1g} \rightarrow {}^1T_{1g}$ ligand-field absorption of the LS molecules.[Jesson 67] When the temperature increases the intensity of this band decreases due to the transformation of the singlet ground state to the HS quintet state leading to the bleaching of the samples. During the first heating cycle one can also observe a rather abrupt change of the reflectance signal around 430 K (figure II.34b), which can be straightforwardly correlated with the discontinuous change observed in the magnetic measurements. Moreover, the first heating cycle differs significantly from the subsequent cooling and heating cycles, which follow the same trace. These findings are in good agreement with the report of Grandjean *et al.*[Grandjean 89] However, figures II.34a and II.34b reveal also very clearly that the reflectance of the as-prepared sample at 300 K (*i.e.* in the pure LS state) is not the same as that of the thermally cycled sample. The observed enhancement of the singlet absorption band is of course not related to any change of the absorption coefficient, but occurs due to the change of the scattering coefficient (*i.e.* the change of the sample granulometry) in agreement with our visual observations (figure II.33).

Beside the magnetic and optical properties the SCO phenomenon is known to be accompanied by changes of the electrical properties as well. Actually, most SCO complexes are highly insulating and pertinent information can be obtained by determining their (quasi-static) dielectric constant.[Bousseksou 03] We have therefore measured the impedance of a powder sample of Fe[HB(pz)$_3$]$_2$ (sandwiched between two metallic electrode plates) in a large frequency and temperature range. Quite surprisingly we noticed that **the conductivity of the sample is relatively high: *ca.* 6 x10^{-7} S m^{-1} at room temperature**. This observation has been confirmed on two independently synthesized batches proving that it is not due to an accidental contamination, but it is an inherent property of this complex. Figure II.35a displays the frequency dependence of the real part, σ'(f), of the complex conductivity σ*(f), recorded at a few representative temperatures during the first heating cycle. At each temperature one can distinguish low and high frequency regions. In both regions the conductivity exhibits only a slight frequency dependence, but the high frequency part of the spectrum is characterized by a higher conductivity. The critical frequency, f$_c$, which separates the low and high frequency

regions increases continuously with increasing temperature from ca. 1 Hz to 10 kHz between 243 K and 363 K, then decreases to ~ 1 Hz at 433 K.
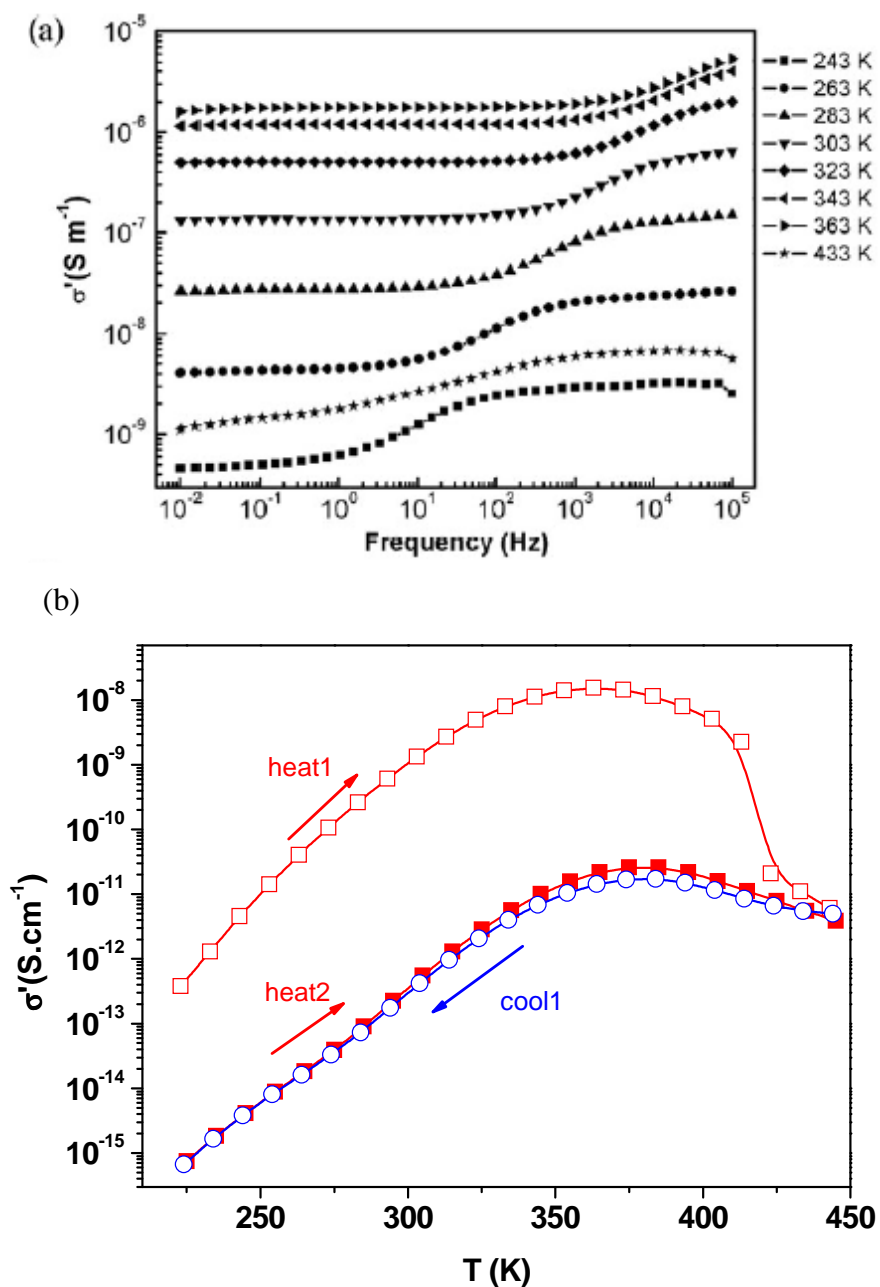

Fig.II.35: (a) Frequency dependence of the ac conductivity of the sample recorded at selected temperatures between 243 and 443 K. (b) Temperature dependence of the ac conductivity of the sample (recorded at 10 mHz) during two successive thermal cycles. (First cycle: open symbols, second cycle: closed symbols)

Figure II.35 exhibits the thermal variation of the real part of the complex conductivity (σ')
extracted from the frequency independent region at 10 mHz. At this frequency, σ' can be
assimilated to the dc conductivity. The dc conductivity is strongly activated up to ca. 360 K,
but then it starts to decrease slowly up to 415 K when it exhibits an abrupt drop. All other
heating and cooling cycles follow a common trace, which differs significantly from the first
heating curve. Notably, **the electrical conductivity (at a given temperature) is smaller by 3
- 4 orders of magnitude when compared to the first heating curve** and displays no
discontinuities. The conductivity data can be clearly correlated with the magnetic and optical
behavior. When the temperature increases, the conductivity of the LS form increases also, but
above ca. 360 K the LS → HS crossover counterbalances the effect of the thermal activation,
which means that the HS form of the compund is more insulating than the LS form. Around
415 K an irreversible transition occurs towards the thermodynamically stable form in
agreement with the magnetic and optical observations. This stable phase is significantly more
insulating than the "as prepared" sample, but in this phase as well the LS form exhibits a
higher conductivity than the HS one (at a given temperature). As far as the charge transport
mechanism is considered, in such a low-mobility solid the conductivity should be associated
by a charge hopping process. These processes can be straightforwardly analyzed within the
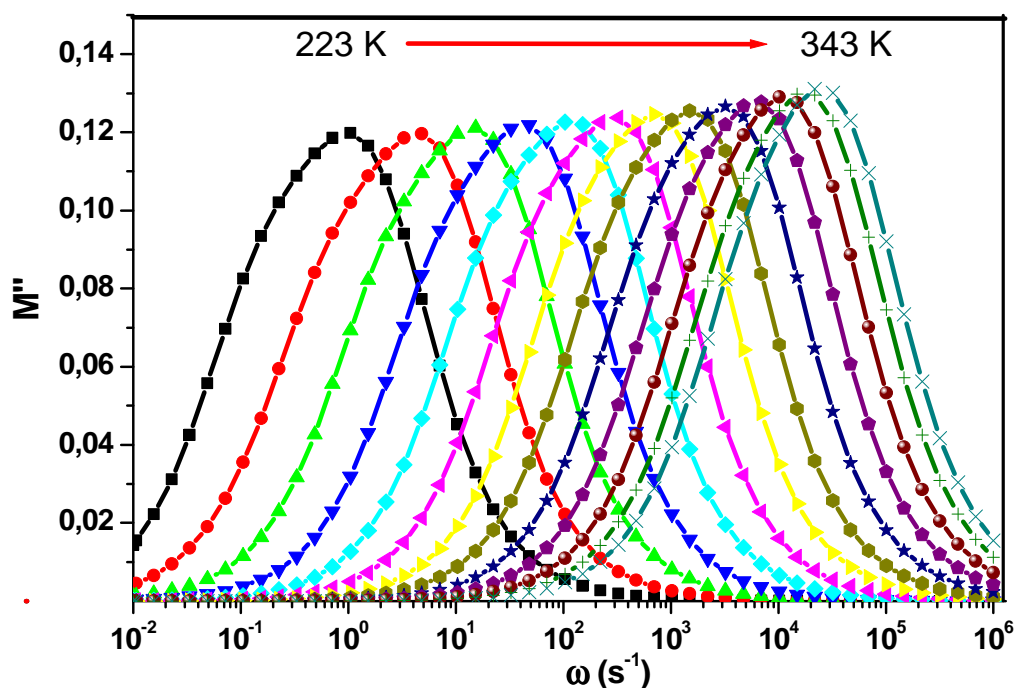Jonscher or the electric modulus formalisms. [Jon83]

Fig.II.36: *The imaginary part of the electric modulus (M") as a function of the frequency of
the electrical field (ω) at different temperatures in the heating mode.*

As seen in Figure. II.36, the hopping frequency (i.e. the frequency for which M" is maximal at a given temperature) is thermally activated. The activation energy of the relaxation frequency (0.52 eV ± 0.01) is roughly equal to the activation energy of the charge transport (0.56 ± 0.01 eV) in the heating mode (Figure II.37).
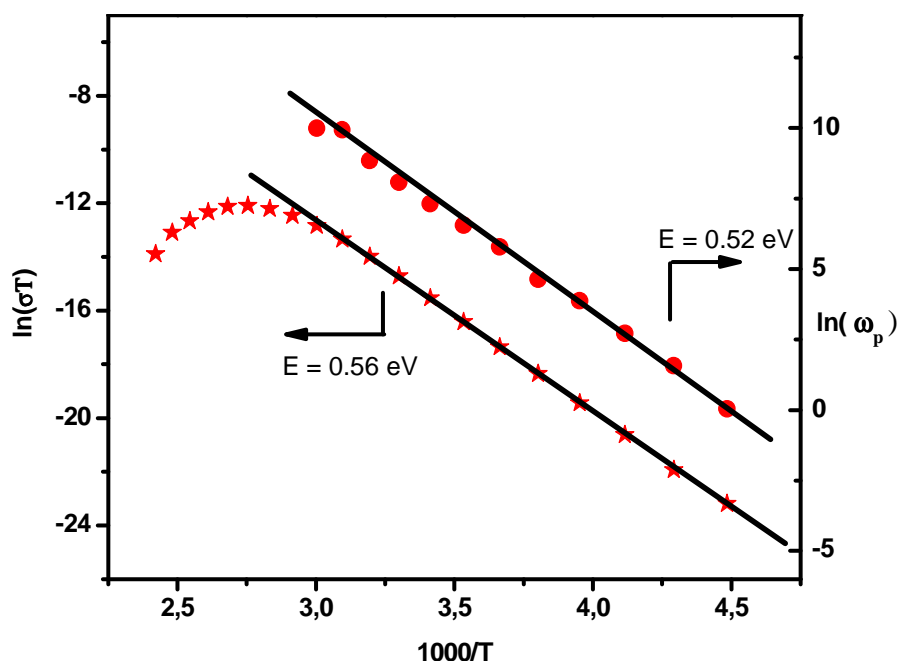

Fig.II.37: Temperature dependence of the dc conductivity (stars) and the hopping frequency (circles) in the heating mode for the compound Fe[HB(pz)$_3$]$_2$. The solid lines are linear fits.

The appealing irreversible thermal transition of the electric properties observed in the bulk Fe[HB(pz)$_3$]$_2$ SCO complex, together with the fact that this compound can be deposited on surface by evaporation, suggests that it might be useful as an active element in ROM-type devices. However, **the obvious question is whether or not the Fe[HB(pz)$_3$]$_2$ SCO thin film retains the same electric properties of those observed in the bulk complex?**

II.3.2 Synthesis, characterization and dielectric properties of [Fe(HB(pz)$_3$)$_2$] thin films

Interdigitated microelectrodes device of 30 μm width have been elaborated using photolithography and lift-off processes. To realize the first photolithographic process, the AZ5214 photoresist was spin coated on a wafer, covering the entire wafer surface. Then the UV (405 nm) light passes though a photomask to expose the photoresist coated wafer. This

first exposure was followed by a second UV irradiation of the whole wafer (without the wash). The photo mask is a glass substrate with clear and opaque regions. After resist development and metal deposition (Ti/Au-10nm/120nm) by evaporation the resist is completely removed, taking the unwanted metal with it (see Fig.II.38). This last operation is called the lift-off process; it was realized in an ultrasonic bath containing acetone. The design of the interdigitated microelectrode devices for photolithography was realized using the CLEWIN software.

In the last step, a thin film of ca. 200 nm of the $[Fe(HB(pz)_3)_2]$ complex was deposited on the TO-8 chips by slow evaporation of the bulk $[Fe(HB(pz)_3)_2]$ complex (fig.II.40). More precisely, a powder of $[Fe(HB(pz)_3)_2]$ complex was placed in the crucible of an Edwards Auto 306 Evaporator under a secondary vacuum of $ca.10^{-5}$ Torr. A tungsten filament is used to heat the crucible (Joule effect) and thus evaporate the sample from the crucible to the TO-8 chips. The film thickness is determined by using a quartz crystal microbalance.
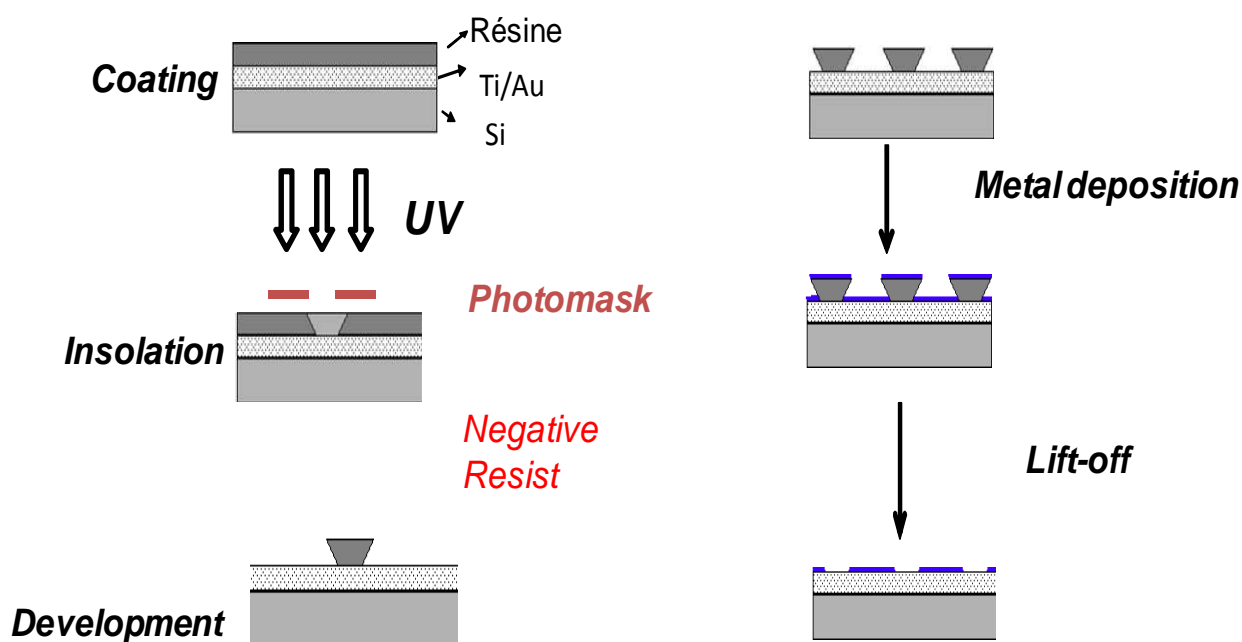
Fig.II.38: *Schematic representation of the photolithographic process*

Finally the fabricated microelectrodes were successfully mounted on a TO-8 support as fig.II.39 illustrates.
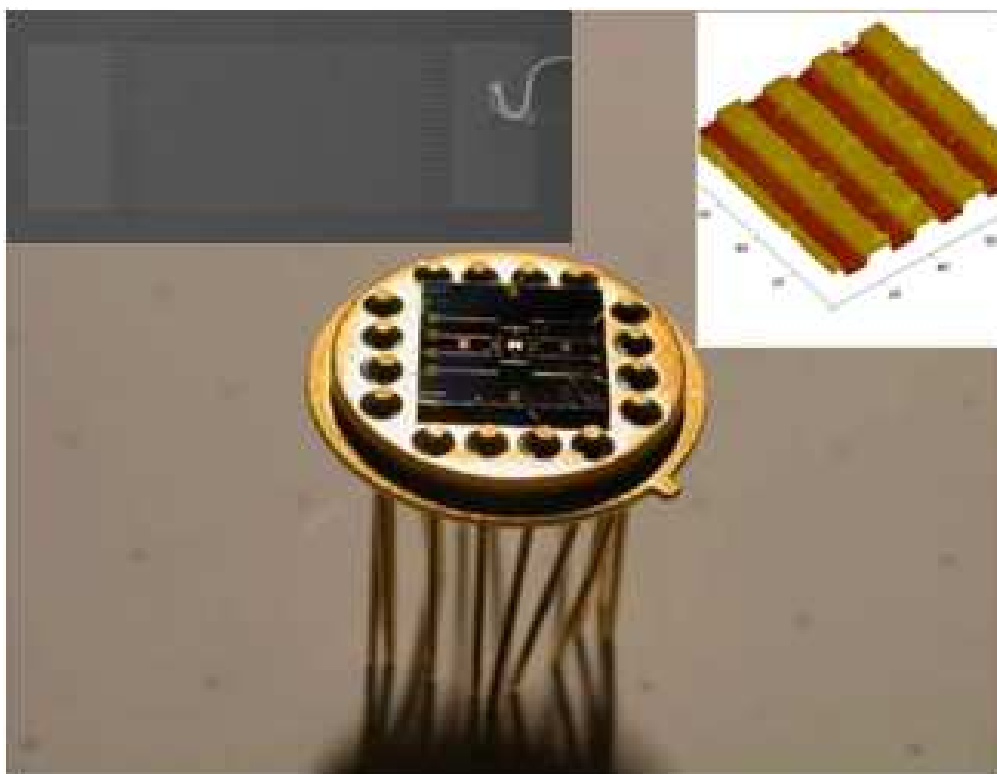
Fig.II.39: *Photo of the microelectrode (the finger length is about 1400 μm) device assembled on TO-8 support. The inserts show SEM (left) and AFM (right) images of the microelectrodes.*

$[Fe(HB(pz)_3)_2]$, 450 K, 10^{-5} Torr

Before

30 μm

After

200 nm

Fig.II.40: *Optical (top) and AFM (down) microscopy images of a thin film of $[Fe(HB(pz)_3)_2]$ deposited on interdigitated microelectrodes by sublimation.*

In order to be sure that we have a [Fe(HB(pz)$_3$)$_2$] thin film and to demonstrate that the molecule remain intact after evaporation, we performed Raman spectroscopy measurements on the thin film (figure II.41).
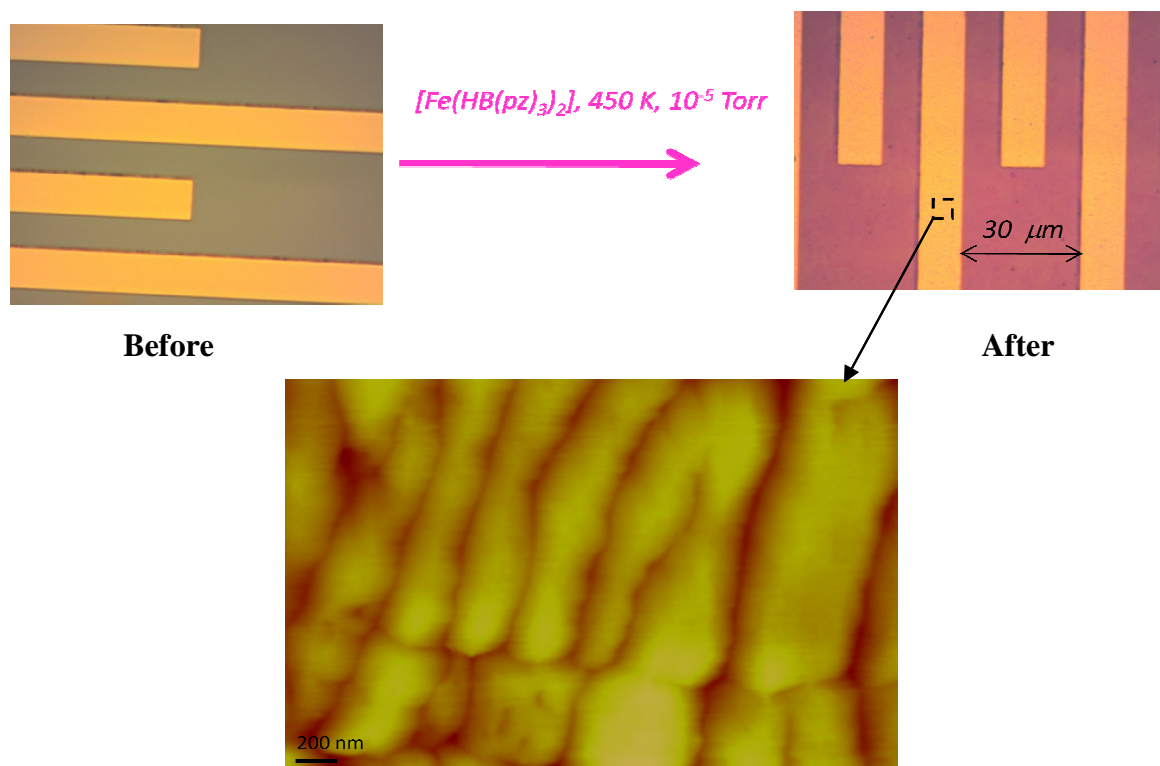
As shown in the figure above, the recorded Raman patterns of [Fe(HB(pz)$_3$)$_2$] in the thin film are almost the same of those obtained with the bulk. The assignment of the bands is relatively easy on the basis of the literature data [During 92, Wootton 97]. In the [1600-660 cm^{-1}] region, we can observe several modes at about, 1500, 1450, 1380, 1350, 1210, 1120, 1050, 980, 780 and 720 cm^{-1} revealing their pyrazolylborate origin. Bands ranging from 980 to 1500 cm^{-1} can be attributed to pyrazolyl ring stretching modes according to the vibrational study of pyrazol by During et al. [During 92]. Bands in the range 780-660 cm^{-1} can be assigned to pyrazolyl bending or twisting vibrations. In this range we should also expect the presence of the B-N strech vibrations. Below 600 cm^{-1}, one can expect to find normal modes corresponding to ring torsions. Between 400 and 200 cm^{-1} bands have been reported involving ν(Fe-N) and δ(N-B-N) vibration. The δ(NFeN) vibration should be located below 200 cm^{-1}.

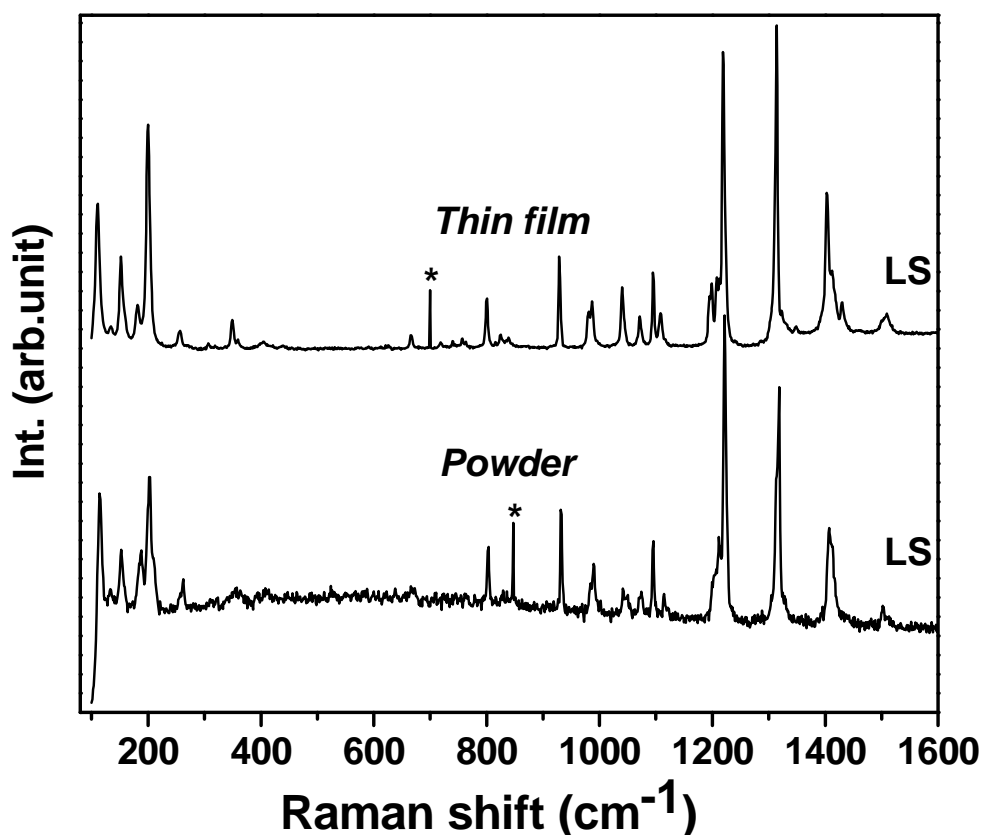**Fig.II.41:** *Raman spectra of the bulk [Fe(HB(pz)$_3$)$_2$]complex and the thin film recorded at room temperature (LS state).*: CCD artifacts.*

AFM, optical microscopy and Raman spectroscopy investigations demonstrate that it is possible to synthesize $[Fe(HB(pz)_3)_2]$ thin films by thermal evaporation. **The films are of good quality and their structure corresponds to the bulk material**.

These results motivated us to investigate the electrical properties of the films as we did for the bulk complex. Therefore we carried out AC conductivity measurements as a function of frequency ($10^{-2} - 10^6$ Hz) and temperature (200 - 450 K) by means of a broadband dielectric spectrometer (Novocontrol BDS 4000 coupled to a Quatro Cryosystem) at an applied ac voltage of 1V (fig.II.42). Frequency sweeps were carried out isothermally. The computed conductivity can be defined as

$$\sigma = K.Y$$

where Y is the admittance and K is the cell constant defined by :

$$K = Le.(N-1)/d$$

where e, N, L, d are, the microelectrode thickness, the number of pair of fingers of interdigitated electrodes, the finger length, and the interelectrode gap, respectively. We should notice that the sample preparation was accomplished by depositing an insulating silicon thin film on top of the $[Fe(HB(pz)_3)_2]$ film **to avoid the evaporation of the complex** at high temperatures during the experiment.

As can be seen from the figure II.42 the thin film displays similar electrical properties that has already observed for the bulk complex. In particular, the powder and film samples resemble closely in that all successive heating and cooling cycles follow a common trace, which differs significantly from the first heating curve, i.e. in both samples there is an irreversible phase change during the first heating. The electrical conductivity (at a given temperature) is always smaller by several orders of magnitude when compared to the first heating curve. On the other hand, the abrupt drop of σ' at 415 K was not observed for the film sample. Furthermore the conductivity of the as-prepared film sample is significantly lower than that of the freshly sublimated powder. These differences between the film and the powder should certainly be traced back to the different electrode configurations.
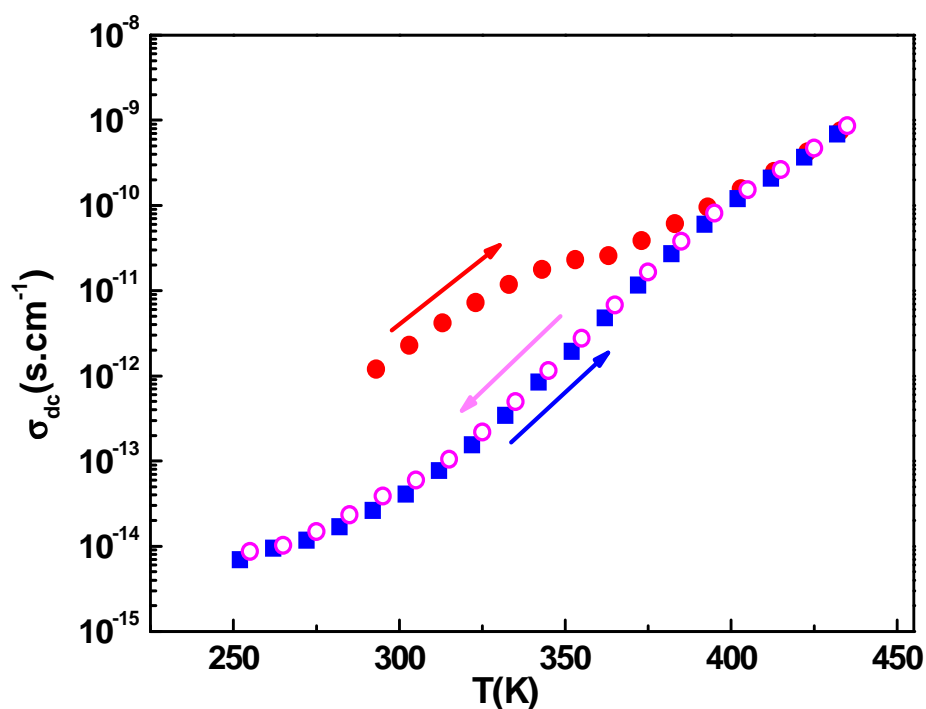
Fig.II.42: *Temperature dependence of the ac conductivity of the [Fe(HB(pz)₃)₂] thin film sample recorded at 10 mHz during two successive thermal cycles. (First cycle: closed symbols; second cycle: open symbols).*
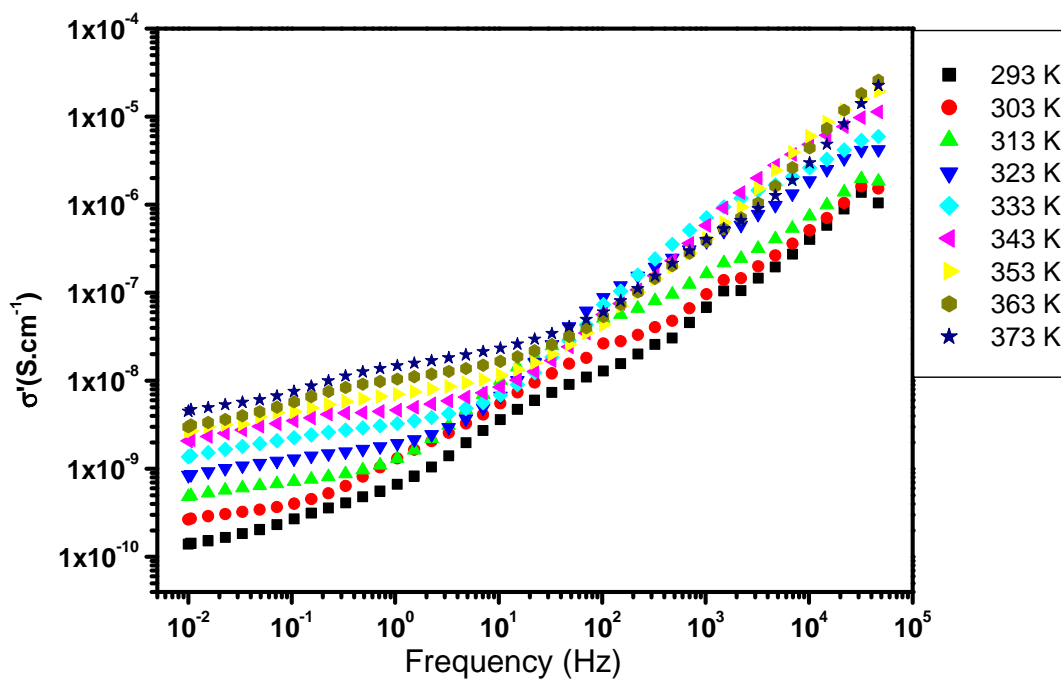
Fig.II.43: *Frequency dependence of the ac conductivity of the [Fe(HB(pz)₃)₂] thin film recorded at selected temperatures between 293 and 373 K in the heating mode.*

II.3.3 Development of a ROM device based on [Fe(HB(pz)$_3$)$_2$] SCO thin films

The irreversible thermal transition in the electric property observed in the [Fe(HB(pz)$_3$)$_2$] SCO thin films motivated us to test the idea of building a **read-only memory** (ROM) prototype. The information storage process consists of the switch of the compound from the LS to HS state by heating, either by increasing the temperature of the whole device or by passing a current through the sample (Joule effect). The read operation can be performed by sensing the device resistivity (Figure.II.44).

Fig.II.44: *Experimental setup used for ROM device tests. The image below shows the connected device to the head of a custom-modified Optistat-DN cryostat (80 - 450 K).*

In this experiment, direct current as a function of sweep applied dc voltage [-3V,3 V] and temperature (298 - 410 K) were measured using a Keithley 6430 Sub - Femtoamp Remote Source Meter and a custom-modified, electrically shielded, variable temperature liquid nitrogen cryostat. The electrometer used in the experiment, measures current with noise smaller than 10 fA, therefore, low current measurements are possible with high accuracy.
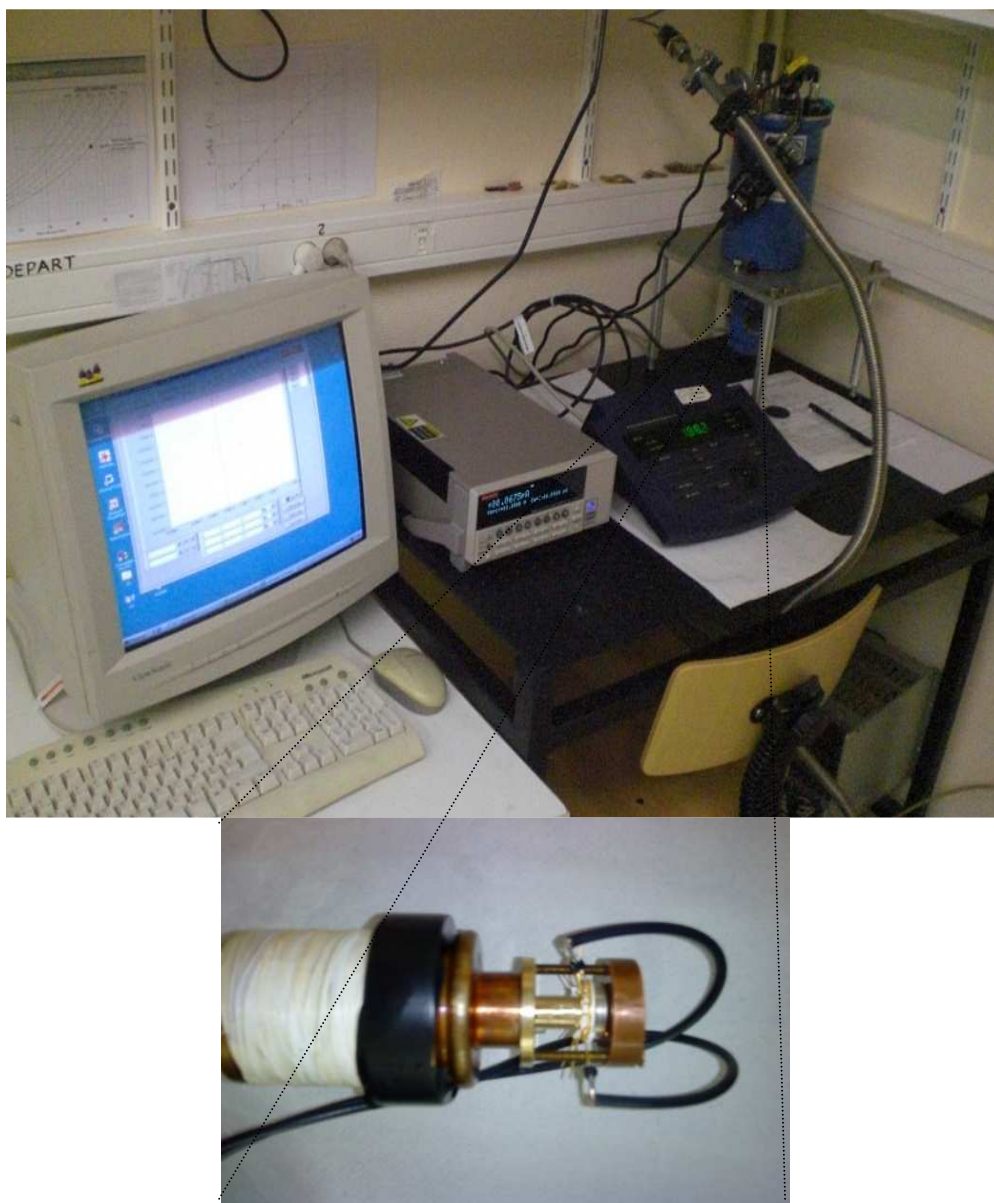
For applied voltages up to 1V, the electric current measurement as function of temperature shows a linear response (Ohmic characteristics) up to ca. 378 K when the electric current reaches 120 nA, but then it drops to 80 nA indicating the transition to the HS state (lower conductivity). The ROM-type behavior during the first thermal cycle has been confirmed (Fig.II.45).
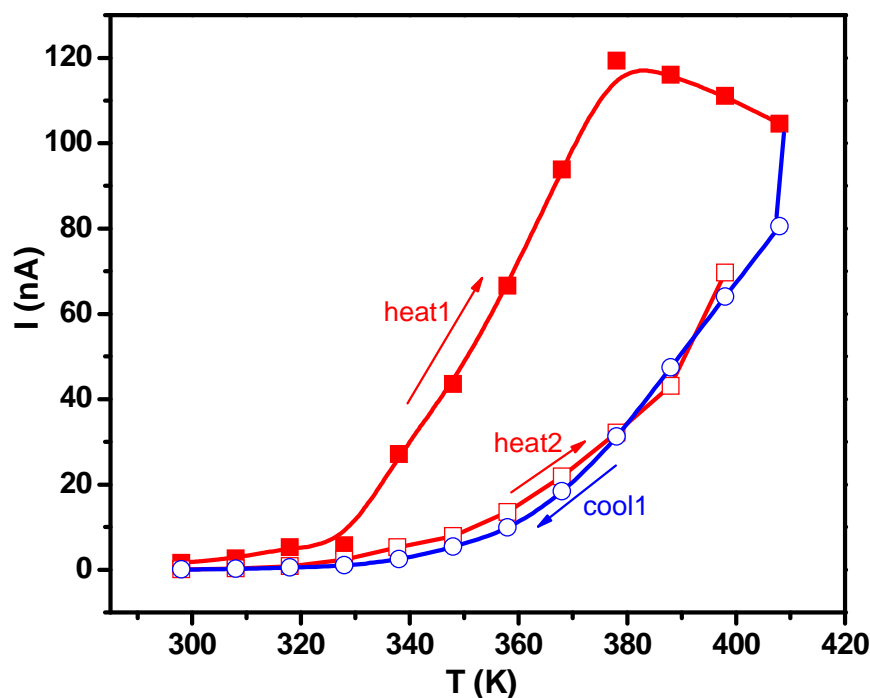
Fig.II.45: *Electric current as function of the temperature at 1V bias in a [Fe(HB(pz)₃)₂] thin film deposited on interdigated microelectrodes.*

We carried out another experiment where the electric current can be an indirect trigger for the spin transition (heating by Joule effect). In this experiment we fixed the device temperature at 370 K. Then we increased the electric field bias from 1 to 10 V (fig.II.46).

From the measurements plotted in the figure II.46 we can say that at a constant operation temperature of 370 K it is possible to switch the device from the high to the low conductivity

state by increasing the bias to 2 V. At 1 V the measured current is about 13 nA. At 2 V the current was relatively high (ca.40 nA) at the beginning of the experiment but then it starts to decrease slowly up to 40 s when it exhibits an abrupt drop to the low conductivity region. Further increase of the voltage above 2 V is accompanied by a small increase of the electric current but remarkably, the current remains at the low conductivity region. This can be interpreted as follow: under a bias of 2 V, the $[Fe(HB(pz)_3)_2]$ thin film sample is Joule-heated from 370 to 378 K (transition temperature). Therefore it was switched from the metastable high conductance form to the stable low conductance form in an irreversible way. We can thus operate the device using a small read voltage (< 1 V) and a somewhat higher write voltage (> 2 V). Of course the actual value of the "switching bias" depends on the device temperature and the time, i.e. at lower temperatures one has to apply either higher bias or wait longer (and vice-versa). On the other hand, the readout is possible at room temperature.

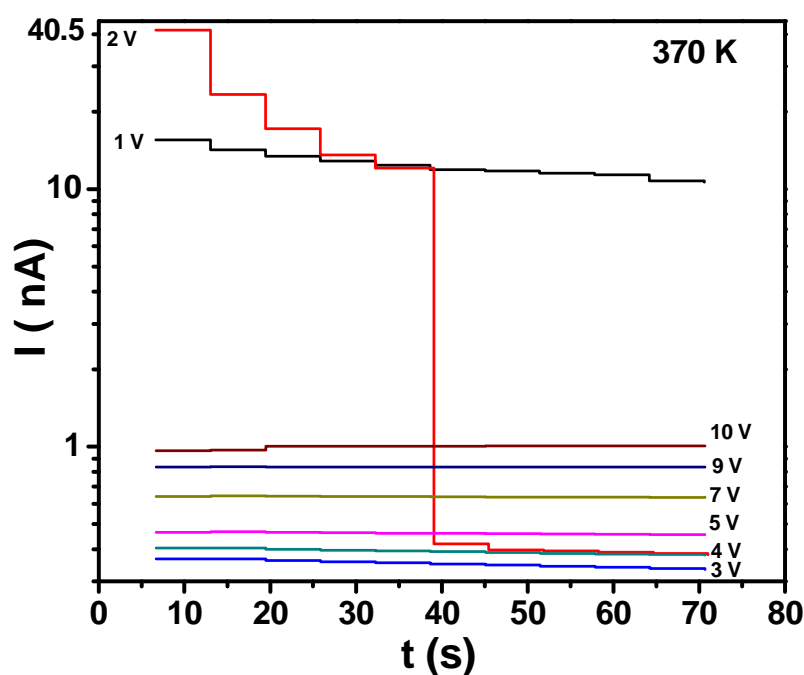***Fig.II.46:*** *Electric current measurement as a function of the time with bias on the device.*

II.3.4 Conclusions

In this chapter we discussed the electrical properties of the singular spin crossover complex $[Fe(HB(pz)_3)_2]$ in the bulk as well as thin film form. We have revealed that the bulk $[Fe(HB(pz)_3)_2]$ as well as the thin film of this compound exhibit an electrical conductivity,

which is moderate on an absolute scale, but relatively high in the family of spin crossover complexes. Even more importantly **the conductivity changes by *ca.* 4 orders of magnitude in the bulk solid and by ca. 2 orders magnitude in the thin film when the material goes through the first (irreversible) transition**. This property together with the facts that this thermochromic compound is stable to light, air and water encouraged us to build an active element in ROM type devices, where **the writing process can be performed by heating** the cell either by increasing the temperature of the whole device or by passing a current (Joule effect) at a given temperature. **The read out can be performed even at room temerature by simple measurements of the resistivity** of the device.

II.4 References

I. G. Austin; N. F. Mott. *Adv. Phys. 18*, **1969**, 41.

A. Bleuzen, V. Escax, JP. Itié, P. Mùnsch, M. Verdaguer, *C. R. Chim.*6. **2003**. 343-352.

A. Bleuzen,. *et al.*, Thermally induced electron transfer in a CsCoFe Prussian blue derivative: the specific role of the alkali-metal ion*, Angew. Chem. Int. Ed. 43*, **2004**, 3728-3731.

S. Bonhommeau. *et al.*, Metal-to-ligand and ligand-to-metal charge transfer in thin films of Prussian blue analogues investigated by X-ray absorption spectroscopy, *Phys. Chem. Chem. Phys.* 10, **2008**, 5882-5889.

K. Boukheddaden, M. Nishino, & F. Varret, Unified theoretical description of the thermodynamical properties of spin crossover with magnetic interactions, *Phys. Rev. B* 72, **2005**, 014467.

A. Bousseksou, G. Molnár, P. Demont, J. Menegotto, *J. Mater. Chem.*, 13, **2003**, 2069.

M. K. Carpenter, & R.S. Conell, A single-film electrochromic device, *J. Electrochrom.* Soc. 137, **1990**, 2464-2467.

S. Cobo; R. Fernández; L. Salmon,; G. Molnár,; A. Bousseksou, Correlation between the stoichiometry and the bistability of electronic states in valence-tautomeric $Rb_xMn[Fe(CN)_6]_y \cdot zH_2O$ complexes, *Eur. J. Inorg. Chem.* **2007**, 1549-1555.

L.R. Dalton, *et al.*, From molecules to opto-chips: organic electro-optic materials, *J. Mater. Chem.* 9, **1999**, 1905-1920

J. R. Durig; M. M. Bergana; W. M .Zunic., *J. Raman Spectroc.*, 23, **1992**, 357.

J. C. Dyre; T. B Schroder, *Rev. Mod. Phys. 72*, **2000**, 873.

F. Grandjean, G. J. Long, B. B. Hutchinson, L. Ohlhausen, P. Neill, J. D. Holcomb, *Inorg. Chem., 28*, **1989**, 4406

T. Guillon, PhD.thesis, **2007**, Université Paul Sabatier Toulouse III.

S. Havriliak,; S. Negami, *Polymer 8*, **1967**, 161.

B. Hutchinson, L. Daniels, E. Henderson, P. Neill, G. J. Long, L. W. Becker, J. Chem. Soc., Chem. Commun., **1979**, 1003.

J. P. Jesson, S. Trofimenko, D.R. Eaton, J. Am. Chem. Soc., 89, **1967**, 3158.

J. P. Jesson, J. F. Weiher, S. Trofimenko, J. Chem. Phys., *48*, **1968**, 2058.

A. K. Jonscher, *Dielectric Relaxation in Solids*, Chelsea Dielectric Press, London, UK **1983**.

O. Kahn, C. J. Martinez, Science, 279, **1998**, 44.

T. Kanki, *et al.*, Electrical-field control of metal-insulator transition at room temperature in $Pb(Zr_{0.2}Ti_{0.8})O_3/La_{1-x}Ba_xMnO_3$ field-effect transistor, *Appl. Phys. Lett.* 83, **2003**, 4860-4862.

K. Kato, *et al.*, Direct observation of charge transfer in double-perovskite-like $RbMn[Fe(CN)_6]$, *Phys. Rev. Lett.* 91, **2003**, 255502.

C.M., Lampert, Smart switchable glazing for solar energy and daylight control, *Sol. Energ. Mat. Sol. C.* 52, **1998**, 207-221.

G. J. Long, F. Grandjean, D. L. Reger, *Top*. Curr. Chem. 233, **2004**, 91.

E.D. Loutete-Dangui,. *et al.*, Spectroscopic ellipsometry investigations of the thermally induced first-order transition of $RbMn[Fe(CN)_6]$, *Phys. Rev. B* 78, **2008**, 014303.

Y. Luo, *et al.*, Two-dimensional molecular electronics circuits, *ChemPhysChem* 3, **2002**, 519-525.

P. B. Macedo; C. T. Moynihan; R. Bose; *Phys. Chem. Glasses 13*, **1972**, 171.

Molnár, G. *et al.*, Interplay between the charge transport phenomena and the charge-transfer phase transition in $Rb_xMn[Fe(CN)_6]_y \cdot zH_2O$, *J. Phys. Chem. C* 113, **2009**, 2586-2593.

N. F. Mott; E. A. Davis, *Electronic Processes in Non-Crystalline Materials,* Clarendon: Oxford, **1979**.

K. Nakamoto, Infrared and Raman Spectra of Inorganic and Coordination Compounds – Part B, *Wiley-Interscience*, **1997**.

S. Ohkoshi, H. Tokoro, & K. Hashimoto, Temperature and photo-induced phase transition in rubidium manganese hexacyanoferrate, *Coord. Chem. Rev.* 249, **2005**, 1830-1840.

S. Ohkoshi, T Nuida, T. Matsuda, H. Tokoro, K. Hashimoto, *J. Mater. Chem. 15*, **2005**, 3291.

S. Ohkoshi *et al.*, Photo-induced magnetization with a high Curie temperature and a large coercive field in a cyano-bridged cobalt-tungstate bimetallic assembly, *J. Am. Chem. Soc.* 128, **2006**, 5320-5321.

S. Ohkoshi *et al.*, Coexistence of ferroelectricity and ferromagnetism in a rubidium manganese hexacyanoferrate, *Angew. Chem. Int. Ed.* 46, **2007**, 3238-3241.

S. Ohkoshi, *et al.*, Crystal structure, charge-transfer-induced spin transition, and photoreversible magnetism in a cyano-bridged cobalt-tungstate bimetallic assembly, *Chem. Mater.* 20, **2008**, 3048-3054.

S. Ohkoshi, *et al.*, Observation of ferroelectricity in paramagnetic copper octacyanomolybdate, *Inorg. Chem.* 47, **2008**, 10810-10812.

M. Poulsen, *et al.*, Effect of an external electric field on the ferroelectric-paraelectric phase transition in polyvinylidene fluoride trifluoroethylene copolymer Langmuir-Blodgett films, *J. Appl. Phys.* 103, **2008**, 034116.

D. R. Rosseinsky; J. S. Tonge; J. Berthelot; J. F Cassidy, *J. Chem. Soc., Faraday Trans. 1* **1987**, *83*, 231.

L. Salmon, E.J. M. Vertelman, C. B. Murgui, S. Cobo, G. Molnár. P. J. van Koningsbruggen, A. Bousseksou, *European Journal of Inorganic Chemistry*, 6, **2009**, 760-768.

O. Sato, T. Kawakami, M. Kimura, S. Hishiya, S. Kubo, Y. Einaga, Electric-field-induced conductance switching in FeCo Prussian blue analogues, *J. Am. Chem. Soc.* 126, **2004**, 13176-13177.

O. Sato, J. Tao, & Y.Z. Zhang, Control of magnetic properties through external stimuli, *Angew. Chem. Int. Ed.* 46, **2007**, 2152-2187.

M. Sayer; A Mansingh. *Phys. Rev.B. 6*, **1972**, 4629.

N. Shimamoto, S-I. Ohkoshi, O. Sato, K. Hashimoto, Inorg. Chem. 41, **2002,** 678-68.

K. Tennakone, W. G. D. Dharmaratne, *J. Phys. C: Solid State Phys. 16*, **1983**, 5633.

S. Trofimenko, J. Am. Chem. Soc., *89*, **1967**, 3170.

S. Trofimenko, Scorpionates: The Coordination Chemistry of Polypyrazolylborate Ligands. *Imperial College Press, London, UK*, **1999**.

E, J, M. Vertelman, Ph.D. thesis, **2009**, University of Groningen, Zenike Insitute for Advanced Materials, Netherland.

E. J. M. Vertelman, T. T. A Lummen, A. Meetsma, M. W. Bouwkamp, G. Molnar, P. H. M. van Loosdrecht, P. van Koningsbruggen, Light- and temperature-induced electron transfer in single crystals of RbMn[Fe(CN)$_6$]·H$_2$O. J. *Chem. Mater. 20*, **2008**, 1236.

E. J. M. Vertelman, E. Maccallini, D. Gournis, P. Rudolf, T. Bakas, J. Luzon, R. Broer, A. Pugzlys, T. T. A. Lummen, P. H. M. van Loosdrecht, P. van Koningsbruggen, J. *Chem. Mater. 18*, **2006**, 1951.

R. Waser, (ed.), Nanoelectronics and Information Technology, *Wiley-VCH*, **2003**.

JL. Wootton, JI. Zink, *Inorg. Chem.* **1997**, 36, 789-795

A. Xidis, V. D. Neff, *J. Electrochem. Soc. 138*, **1991**, 3637.

Chapter III: Optical investigation of Spin Crossover thin films by Surface Plasmon Resonance spectroscopy

Utilisation of nanoscale spin crossover materials represents an extremely appealing approach for the development of new tools for potential applications, such as memories, switching devices and sensors. However, the usual optical methods (Raman spectroscopy for example) devoted to investigate the SCO phenomenon become limited and inappropriate when one reaches the nanoscale (thin film as well as nanoparticles). To overcome this limitation we propose to develop alternative methods where sensing is based on surface plasmon resonance (SPR) detection of refractive index changes. Indeed, as a result of the spin state change, SCO complexes may display a large variation of their refractive index ($\Delta n = 10^{-1} - 10^{-2}$) in the UV-VIS-NIR range [Ohkoshi 05, Loutete-Dangui 07, Hauser 93] and hence the measurement of this change can be applied to the detection of thermal spin crossover (as a function of temperature). In principle the measurement of the change of this physical property (Δn) can be observed with high sensitivity and accuracy even on very thin samples using surface plasmon spectroscopy.

This chapter is organized as follows. First we introduce the principle of attenuated total reflection method based on the Kretchmann configuration and Fresnel equations for determination of optical properties (thickness and refractive index). Then we will study the temperature dependence of the reflectivity of the metal (gold) substrate, which depends mainly on the change of the thickness and the metal dielectric function. After that we will carry out theoretical simulations to predict the effect of the spin state change on the SPR curves and to determine the optimal experimental conditions. Finally we will discuss the experimental results reporting the ability of SPR to characterize thin films (thickness and complex refractive index) and to provide a quantitative determination of the high spin fraction as a function of temperature. At the end of this chapter we will summarize our work and discuss the prospects of the feature research.

III.1 Theory and background

Attenuated total reflection (ATR) occurs at the critical angle where light is totally reflected at the interface. Resonance occurs at angles larger than the critical angle by matching the parallel momentums of the incoming beam with a SP mode or a waveguide mode, depending on the configuration of the layered structure.

III.1.1 Evanescent wave

Before we discuss SPs in more detail, it may be appropriate to define the evanescent wave, which is so central in the concept of SPR sensing. The simplest case for the existence of an evanescent wave is the well-known total internal reflection of a plane electromagnetic wave at the base of a prism (refractive index n_1) in contact with an optically less dense medium (with $n_2 < n_1$). This geometry is schematically sketched in Fig III.1. If the reflected light is recorded as a function of the angle of incidence, θ, the reflectivity R reaches unity as one reaches the critical angle, θ_c, for the total internal reflection (Fig.III.1). A closer inspection of the E-field distribution in the immediate vicinity of the interface shows that above θ_c the light intensity does not fall abruptly to zero in the less dense medium, but there is instead a harmonic wave traveling parallel to the surface with an amplitude decaying exponentially normal to the surface.

The penetration depth l is given by:

$$l = \frac{\lambda}{2\pi}\sqrt{(n_1\sin\theta)^2 - 1} \quad \text{\textit{[Z. Sekkat 1996]}} \tag{III.1}$$

and found to be on the order of half a wavelength of light. This type of wave is called evanescent wave. This explains the interface sensitivity of the evanescent field: only close to the interface is an electromagnetic field present; therefore, only a changing dielectric property (e.g. a changing refractive index) in the vicinity of the interface will influence this field.
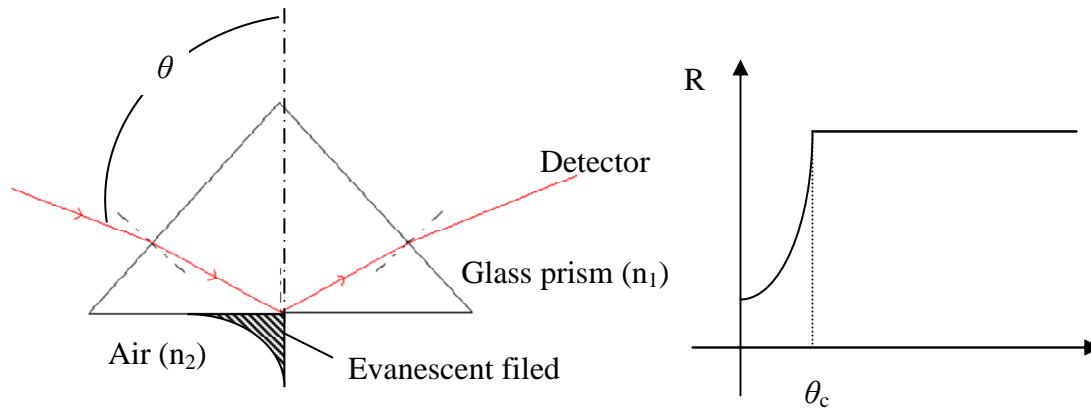
Fig.III.1: Total internal reflection of a plane wave at the base of a prism (left), and the reflectivity as a function of the angle of incidence (right). The reflectivity increases to unity at the critical angle for total internal reflection.

III.1.2 Surface plasmons

Since its first observation by Wood in 1902 [Wood 1902], the physical phenomenon of surface plasmon resonance (SPR) has found its way into practical applications in sensitive detectors, capable of detecting sub-monomolecular coverage. However a complete explanation of the phenomenon was not possible until 1968, when Otto [Otto 68] and in the same year Kretschmann and Raether [Kretschmann 68] reported the excitation of surface plasmons. This was a breakthrough to a new technology that recently emerged and has been termed "Plasmonics". Plasmonics typically cover all plasmon phenomena, including bulk, surface (wave propagates along the surface) and particle plasmons (localized to the particle) [Raether 88]. **Delocalized surface plasmon polaritons** (SPPs, often called loosely "surface plasmons", SPs) which will mainly concern us in this thesis are electromagnetic waves that propagate along the surface of a metal, usually a noble metal (such as Au, Ag, Cu, etc…). They are essentially light waves that are bound to the surface by the interaction with the free electrons of the metal. As a result, the free electrons respond collectively by oscillating in resonance with the light wave.

There are several approaches that all result in the dispersion relation for an SP, that is a relation between the angular frequency ω and the wavevector k. Here we adopt the approach of Raether [Reather 88]. Raether calculated the SP dispersion relation from first principles, viz. Maxwell's equations which are given by:

$$\nabla.\vec{D} = 0 \qquad \nabla \times \vec{E} = -\frac{\partial \vec{B}}{\partial t} \qquad \text{(III. 2)}$$
$$\nabla.\vec{B} = 0 \qquad \nabla \times \vec{H} = -\frac{\partial \vec{D}}{\partial t}$$

Here, $\vec{E}$ is the electric field and $\vec{H}$ is the magnetic field. They are related to the electric displacement $\vec{D}$ and magnetic induction $\vec{B}$ as:

$$\vec{D} = \varepsilon\varepsilon_0\vec{E}$$
$$\text{(III.3)}$$
$$\vec{B} = \mu\mu_0\vec{H}$$

where ε and ε_0 are the dielectric constant (without dimension) and the electric permittivity of free space, respectively. μ and μ_0 are the magnetic permeability (without dimension) and the magnetic permeability of free space respectively.

The solution of Maxwell's equations for the electric field $\vec{E}$, in the case of plane waves, is presented by the equation:

$$\vec{E} = \vec{E}_0 \; e^{i(\vec{k}.\vec{r}-\omega t)} \qquad \text{(III.4)}$$

where $\vec{E}_0$ is the electric field amplitude, $\vec{r}$ is the position vector, ω is the angular frequency ($\omega=2\,\pi f$, f: frequency), t is the time, and $\vec{k}$ is the wavevector, which is in the direction of the propagation. The magnitude of $\vec{k}$ is given by:

$$|k|= \sqrt{\mu\mu_0\varepsilon\varepsilon_0\omega^2} \qquad \text{(III.5)}$$

in vacuum (or in air as a first approximation), $\varepsilon=1$, $\mu=1$ and $\lambda =2\pi c/\omega$, $k=2\pi/\lambda=\omega/c$, then:

$$c = 1/\sqrt{\mu_0\varepsilon_0} \qquad \text{(III.6)}$$

The electron charges on a metal boundary can perform coherent oscillations, which are called surface plasmon polaritons. These charge oscillations can be localized in the z direction, and accompanied by a mixed transversal and longitudinal electromagnetic field that propagates along the x-axis and vanishes at $|z| \to \infty$ on both sides of the metal/dielectric interface, and has its maximum at $z = 0$ (Figure III.2). The plasmon waves have **p-character** because only transverse magnetic plane waves (i.e. TM waves) can be applied to excite SPPs.
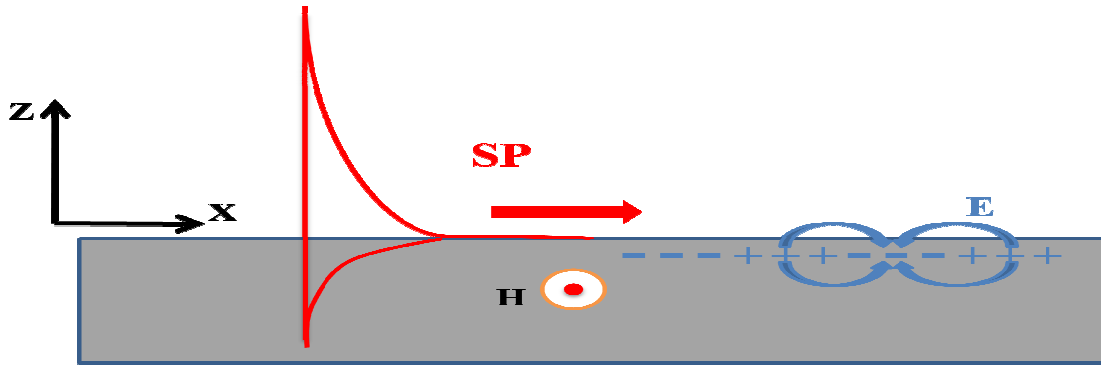

Fig.III.2: *The electromagnetic field of SPs propogating on a surface in the x-direction and the exponential dependence of the field E_z on both +z and –z sides are schematically depicted in the image.*

Considering the dielectric ($\varepsilon_1 > 0$, medium 1)/metal ($\varepsilon_2 = \varepsilon_2'+i\,\varepsilon_2''$, medium 2) interface, the electromagnetic fields on both sides are expressed as:

$Z > 0$

$$H_1 = (0, H_{y1}, 0)\, e^{i(k_{x1}X+k_{z1}Z-\omega t)}$$

$$E_1 = (E_{x1}, 0, E_{z1})\, e^{i(k_{x1}X+k_{z1}Z-\omega t)}$$

(III.7)

$Z < 0$

$$H_2 = (0, H_{y2}, 0)\, e^{i(k_{x2}X-k_{z2}Z-\omega t)}$$

$$E_2 = (E_{x2}, 0, E_{z2})\, e^{i(k_{x2}X-k_{z2}Z-\omega t)}$$

k_{x1} and k_{x2} are the wavevectors in x-directions and k_{z1} and k_{z2} the ones along the z-axis.
Considering the continuity relations of the in-plane components:

$E_{x1} = E_{x2}, \quad H_{y1} = H_{y2}$ and $\quad k_{x1} = k_{x2} = k_x$ (III.8)

and inserting (III.7) into (III.2), together with (III.6) one obtains:

$$- k_{z1}H_{y1} = +\frac{\omega}{c}\varepsilon_1 E_{x1}$$

$$\text{(III.9)}$$

$$+k_{z2}H_{y2} = +\frac{\omega}{c}\varepsilon_2 E_{x2}$$

Together with the continuity relations (III.8), one obtains:

$$k_{z1}/\varepsilon_1 + k_{z2}/\varepsilon_2 = 0 \qquad\qquad \text{(III.10)}$$

This reveals that SPs can only exist at the interface between two materials that have dielectric constants of opposite sign, e.g., a metal/dielectric interface. The wavevector k_i can be decomposed into k_{xi} and k_{zi}, together with (III.8), one obtains:

$$k^2_x + k^2_{zi} = \varepsilon_i \, (\omega/c)^2 \qquad\qquad \text{(III.11)}$$

From (III. 10) and (III.11) one yields the dispersion relation of SPs:

$$k_x = \frac{\omega}{c}\left(\frac{\varepsilon_1\varepsilon_2}{\varepsilon_1 + \varepsilon_2}\right)^{1/2} \qquad\qquad \text{(III.12)}$$

In the case of the dielectric ($\varepsilon_1 > 0$, medium 1)/metal ($\varepsilon_2 = \varepsilon_2'+i\,\varepsilon_2''$, medium 2) interface, and assuming $\varepsilon_2'' < |\,\varepsilon_2'|$, the complex k_x is expressed by:

$$k_x = k_x' + ik_x'' \qquad\qquad \text{(III.13)}$$

with

$$k_x' = \frac{\omega}{c}\left(\frac{\varepsilon_1\varepsilon_2'}{\varepsilon_1 + \varepsilon_2'}\right)^{1/2} \qquad\qquad \text{(III.14)}$$

$$k_x'' = \frac{\omega}{c}\left(\frac{\varepsilon_1 \varepsilon_2'}{\varepsilon_1 + \varepsilon_2'}\right)^{3/2} \frac{\varepsilon_2''}{2\varepsilon_2'^2}$$

(III.15)

We should notice that the dispersion relation of a free photon in a homogenous dielectric is

$k_{ph} = \omega/c \sqrt{\varepsilon_1}$

(III.16)

which is always smaller than the wavevector of SPs at the dielectric/metal interface, k_{sp}. This is shown graphically as $\omega(k_x)$ plots in Figure III.3.
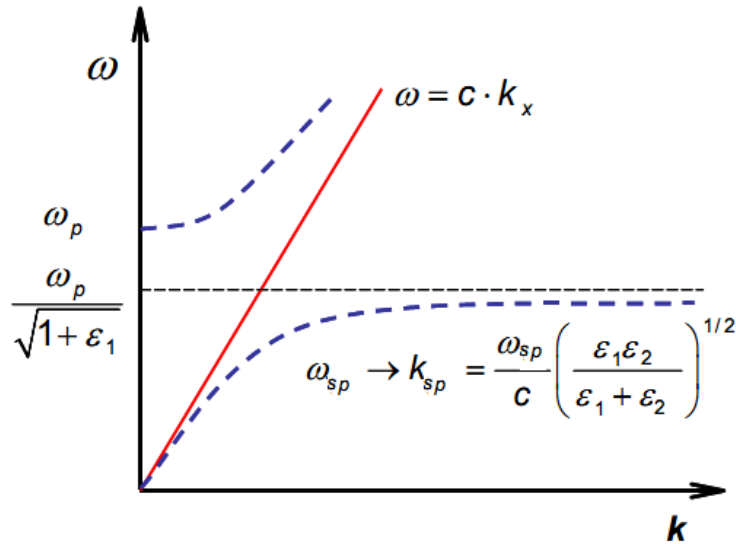

Fig.III.3: *The dispersion relation of surface plasmons at the metal/dielectric interface and the light line $\omega = c.k_x$. ω_p is the plasma frequency.*

The $\omega(k_x)$ curve of SPs approaches asymptotically the dispersion curve of the free photon with no intersection of the curves. Thus, SPs cannot directly transform into light on a smooth surface, i.e. it is a non-radiative wave. Another consequence is that, the SPs cannot be excited directly by light, due to its insufficient k_{ph}. In order to match the optical momentum at the interface, experimentally there are two principal coupling techniques to enhance k_{ph}, namely, the **prism coupling** and the **grating coupling** [Raether 88]. In the case of prism coupling the enhancement occurs if the projection of the wavevector $\omega/c \sqrt{\varepsilon_p}$ on the x-axis matches the x component of k_{sp} at certain wavelength of the laser ω_{laser} (fig.III.4). That means, when light is coupled into the SP mode via a prism; the wavevectors that describe both the light and the SP are equal to one another (**wavevector matching**). SPR cannot be achieved by the direct

illumination of a suitable support surface with light. Wavevector matching does not occur in this situation because the light wavevector is always smaller than the wavevector that describes the SP. The prism is used to increase the light wavevector so that wavevector matching is possible. Equation III.18 describes a wavevector, k_x, which characterizes the component of light propagating parallel to the metal surface.

$$k_x = \frac{2\pi}{\lambda} n_p \sin\theta$$

III.18

Here, θ is the angle of incidence of the light with the metal surface, n_p is the refractive index of the prism, which is proportional to the square root of the dielectric permittivity ε (within the region of optical wavelengths), and λ is the wavelength of the excitation light.

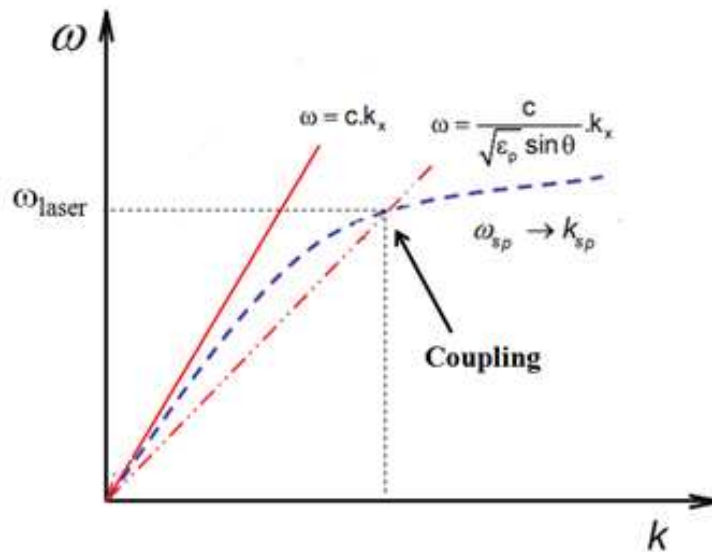***Fig.III.4:*** *Illustration of the dispersion relation of free photons in a coupling prism and the dispersion relation of non-radiative surface plasmons at the metal/dielectric interface.*

We are dealing with the resonant excitation of a coupled state between the plasma oscillations and the photons, that is, "surface plasmon polaritons". This resonance phenomenon can be clearly seen in the ATR scan (see fig.III.5).

In the ATR scan, the incident light is totally reflected above a critical angle θ_C, and the dip in the reflectivity curve above θ_C (at θ_0) indicate the resonant excitation of SPs at the metal air-interface. The coupling angle depends on the resonance condition for SP waves, and the study of the resonance angles allows for the accurate determination of the optical thickness (refractive index × thickness) of thin coatings by SPs [Sekkat 96].
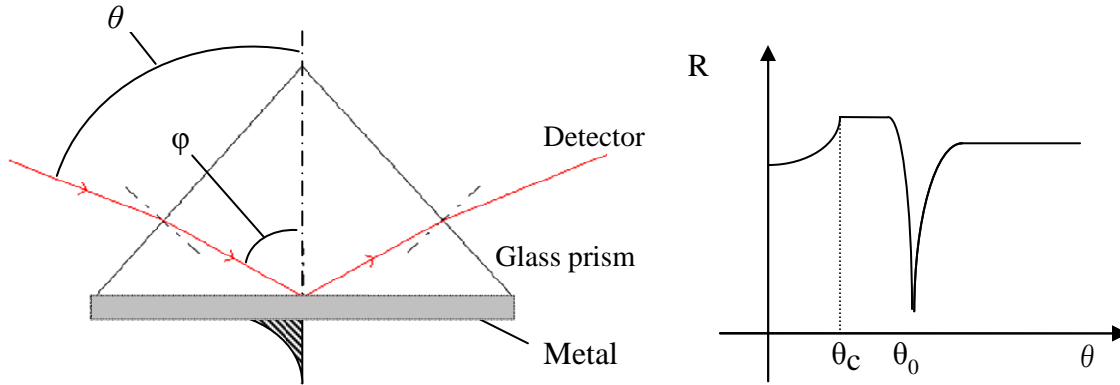

Fig.III.5: *ATR setup for the excitation of surface plasmons in Kretschmann geometry. Left: a thin metal film (thickness ≈ 50 nm) is evaporated onto the base of the prism and acts as a resonator driven by the photon field, and right: the resonant excitation of the surface plasmon wave is seen in the reflectivity curve as a sharp dip at coupling angle θ_0.*

III.2 SPR modeling with Fresnel equations

III.2.1 Theories

Fresnel equations can be used to predict reflected and transmitted light intensity from multilayered structures. To obtain the expression for the amplitude of the reflection coefficient for p-polarized incident beam N-layer models are considered [Macleod 00, Gupta 05]. The layers are assumed to be stacked along the z-axis. The arbitrary medium layer is defined by thickness d_k , dielectric constant ε_k , permeability μ_k , and refractive index n_k . The tangential fields at the first boundary $Z = Z_1 = 0$ are related to those at the final boundary $Z = Z_{n-1}$ by:

$$\begin{bmatrix} U_1 \\ V_1 \end{bmatrix} = M \begin{bmatrix} U_{N-1} \\ V_{N-1} \end{bmatrix},$$

where U_1 and V_1, respectively, are the tangential components of electric and magnetic fields at the boundary of first layer. U_{N-1} and V_{N-1} are the corresponding fields at the boundary of the N_{th} layer. Here M is known as the characteristic matrix of the combined structure and is given by:

$$\prod_{k=2}^{N-1} M_k = \begin{pmatrix} M_{11} & M_{12} \\ M_{21} & M_{22} \end{pmatrix}$$

with

$$M_k = \begin{pmatrix} \cos\beta_k & (-i\sin\beta_k)/q_k \\ -iq_k\sin\beta_k & \cos\beta_k \end{pmatrix}$$

where

$$q_k = \left(\frac{\mu_k}{\varepsilon_k}\right)^{1/2} \cos\theta_k = \frac{(\varepsilon_k - n_1^2 \sin^2\theta_1)^{1/2}}{\varepsilon_k}$$

and

$$\beta_k = \frac{2\pi}{\lambda} n_k \cos\theta_k (z_k - z_{k-1}) = \frac{2\pi d_k}{\lambda}(\varepsilon_k - n_1^2 \sin^2\theta_1)^{1/2}.$$

The amplitude of the reflection coefficient for p-polarized incident wave is given by:

$$r_p = \frac{(M_{11} + M_{12}q_N)q_1 - (M_{21} + M_{22}q_N)}{(M_{11} + M_{12}q_N)q_1 + (M_{21} + M_{22}q_N)}$$

Finally, the reflection intensity for p-polarized light is

$$R_p = \left|r_p\right|^2.$$

III.2.2 Simulations at fixed temperature

The Fresnel SPR model described above was used to calculate the effects of film thickness and refractive index of a SCO layer on SPR signal transduction. The model was originally designed to work with a fixed wavelength and modulated angle of incidence or a fixed angle of incidence and modulated wavelength.

In general the SPR response curve is affected by the choice of metal due to the inherent optical properties of the material. For a given sensing system silver exhibits a sharper angular resonance peak than gold and provides a more precise measurement of the coupling angle (Figure III.6). Silver is also less prone than gold to refraction losses [Raether 88].
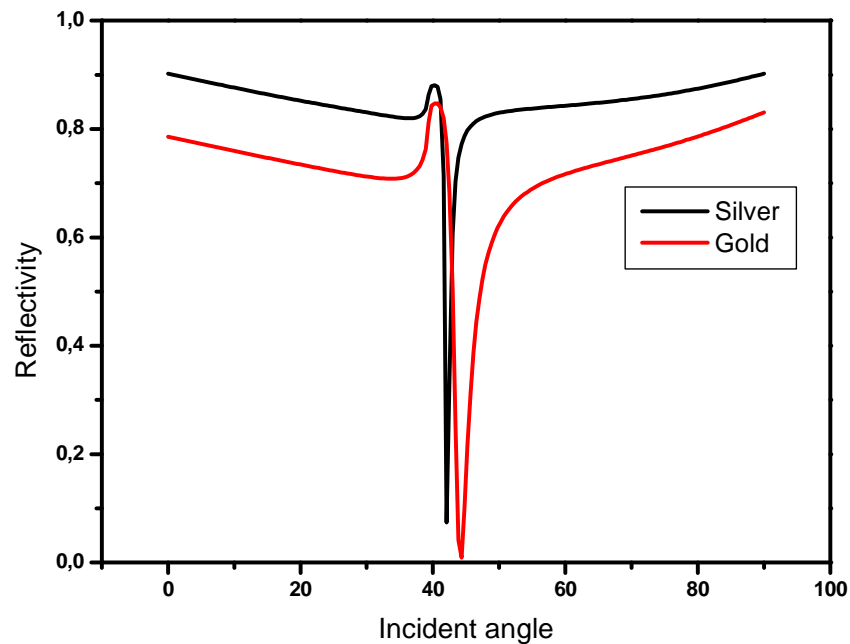
Fig.III.6: *Theoretical SPR response curve of silver (n*=0.135+3.98i)/air and gold (n*=0.197+3.09 i)/air interfaces. The metal thickness considered in this simulation is 50 nm.*

The different widths of the resonance peaks are due to the intrinsic damping of the surface plasmon oscillations on the metal films. The best indicator of the degree of damping that will be observed experimentally is the magnitude of the imaginary part of the permitivity value of

the material. Damping increases with larger imaginary dielectric values. Gold and silver have imaginary dielectric values that are 20 times lower than any other support metal, with silver having a slightly lower value than gold [K.A. Horne 94]. Hence, these materials are the best SP support metals available and are the most commonly used. **Although silver exhibits better optical properties for coupling light into the SP mode, it is not always the best support surface** for sensing applications. Silver is chemically unstable (more reactive than gold) and care must be taken to use it in the experiment.

The metal film thickness to properly optimize the SPR coupling has been a subject of intense studies [C. KoBlinger 95]. The optimal thickness to support SPR has been both experimentally and theoretically determined to lie in the range of 50-60 nm. As the film thickness increases, the depth of the resonance peak decreases, indicating reduced coupling efficiency of light into the SP mode on the film. This is due to the fact that the film essentially begins acting as a reflectance plane when its thickness increases to a point where light cannot couple into the surface charge oscillations that make up the plasmon mode. Very thin films (e.g. 20-30 nm) result in more coupling into the SP mode, but promote a much wider peak width due to light scattering, reducing the sensitivity. **A metal film thickness of 50 nm typically yields the most desirable resonance peaks** [Reather 88]. With a thickness of ~50 nm (silver or gold) the losses caused by absorption and scattering are both minimized, thus increasing sensitivity.

Another important issue is the thickness of the dielectric (spin-crossover) material deposited on the metal. In the simulated curves of figure III.7 we studied the SPR response for different thicknesses in a Au/Ti/ SCO system. We supposed a fixed thickness (ranging from 1 to 65 nm) of the SCO deposit on gold-titanium coated glass slides (5 nm titanium, followed by 50 nm gold). The refractive index of the SCO film was assumed as $n^* = n + ik$, with $n = 1.6$ and $k = 0.06$, which is typical for these type of compounds. The refractive index of the SCO thin film used for the simulation is obtained experimentally from the SPR measurements (see later), and the metal's refractive index was obtained from literature data [refractive index data base].
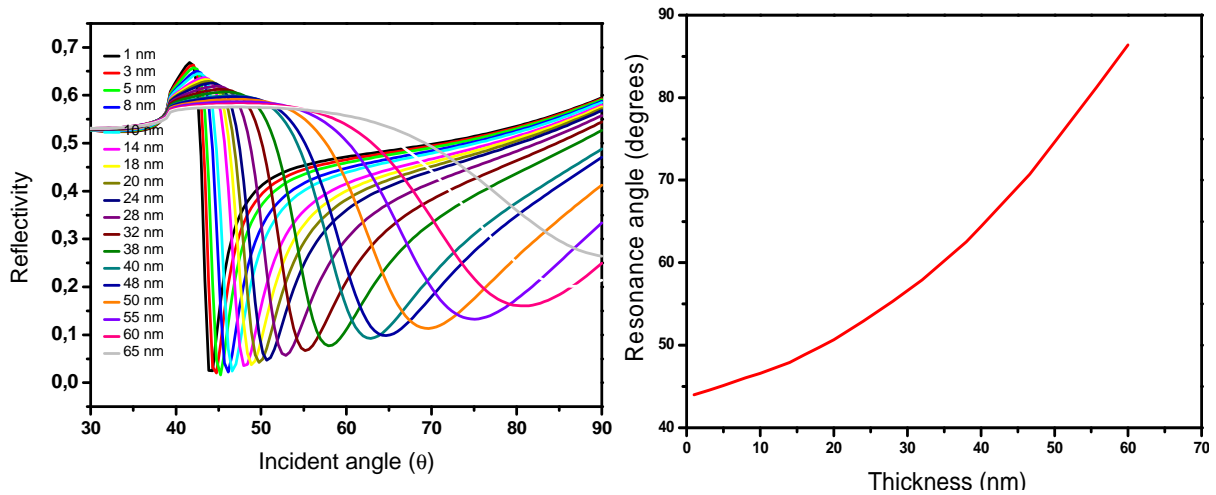
Fig.III.7: *Simulated curves showing the effect of the thickness of the SCO film on the SPR signal on the multilayer system: prism/Ti/Au/SCO/air.*

Plotting the SPR minimum shift versus the film thickness for the system, we can say that SPR is very sensitive to the SCO film thickness change. Therefore from a SPR scan one can determine accurately the film thickness. As can be seen from the figure above, the resonance curve shifts to a higher resonance angle and becomes much wider when the SCO film thickness increases. The broadness observed at large thicknesses is due to losses in the compound.

The effect of refractive index change on the SPR signal has been also simulated (figure III.8, figure III.9). Due to the clear sensitivity of the refractive index either in real (**36 degrees / RIU**, where RIU refers to refractive index unit) or imaginary part on the SPR signals, these theoretical spectra allowed an assessment of the applicability of the model to predict the occurrence of spin transition or sensor response based on refractive index changes. In this theoretical study we supposed a 30 nm thick layer of SCO compound deposited on gold-titanium coated glass slides (5 nm of titanium, followed by 50 nm of gold).

As expected the SPR signals is relatively less sensitive (7.2 degrees / RIU) to the refractive index change, when one assumes a system with a thinner SCO layer (10 nm) deposited on 50 nm of gold (see figure III.9).
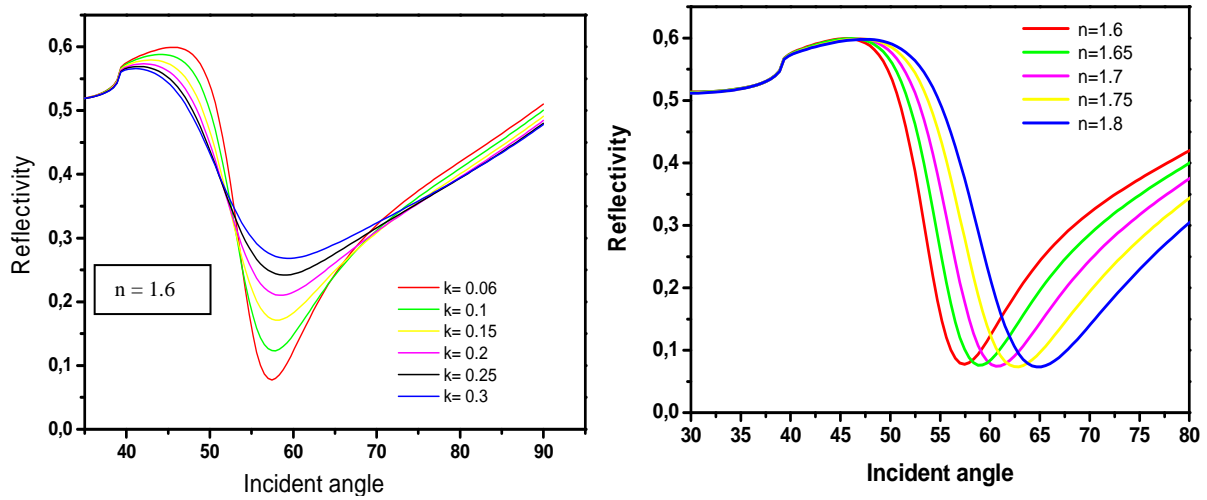
Figure.III.8: *Simulated curves showing the effect of the change of refractive index, real part (right curves) and imaginary part (left curves) on the SPR transduction signal; assuming 30 nm of SCO layer deposited on 50 nm of gold.*
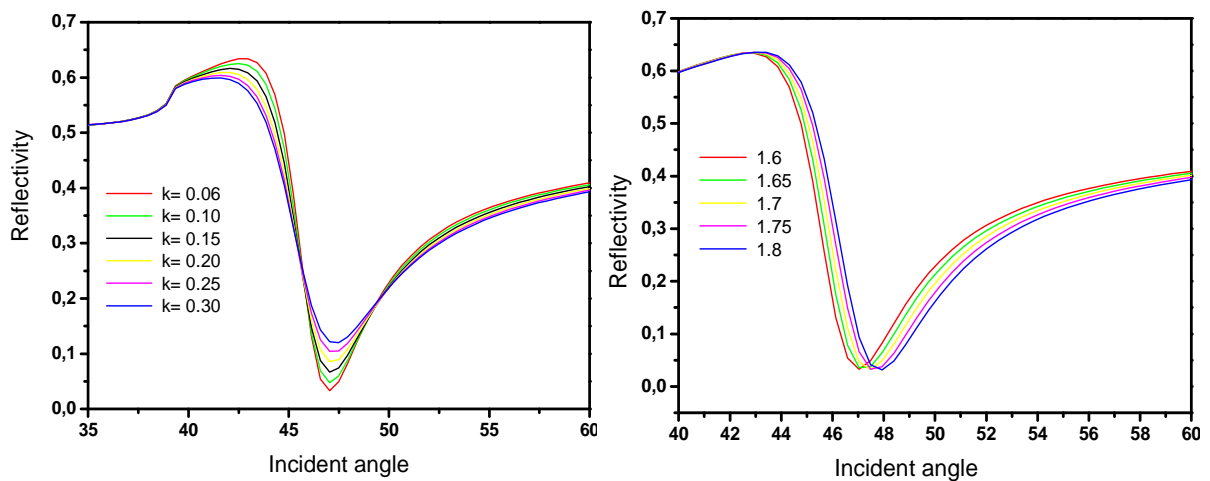
Figure.III.9: *Curves showing the effect of the change of refractive index, real part (right) and absorption coefficient (left) on the SPR transduction signal; assuming 10 nm of SCO layer deposited on 50 nm of gold.*

III.2.3 Temperature-dependent sensitivity of surface plasmon resonance spectroscopy at the gold–air interface

In this section we will study the temperature dependence of reflectivity, which depends mainly on the change of the thickness and the metal dielectric function as a function of

temperature. The variation of the optical constants with temperature for the glass prism is completely negligible in comparison with that for the metal film. For simplicity, we start by adopting the Drude model:

$\varepsilon = 1 - \omega_p^2/[\omega(\omega + i\omega_c)]$, where ω_c is the collision frequency and ω_p is the Plasma frequency given by:

$$\omega_p = \sqrt{\frac{4\pi N e^2}{m^*}},$$

with N and m* the density and effective mass of the electrons, respectively. The collision frequency will have contributions from both phonon-electron and electron-electron scattering: $\omega_c = \omega_{c\,p} + \omega_{ce}$. As reported in ref [Chiang 01], for a resonance phenomenon like SPR, one must account for the temperature (T) variation of ω_p besides that for ω_c. The plasma frequency (ω_p) depend on T via a volumetric effect as follows [Chiang 04]:

$\omega_p = \omega_{p0}[1+\gamma(T - T_0)]^{-1/2}$,

where γ is the expansion coefficient of the metal and T_0 is the reference temperature taken to be the room temperature. ω_c can then be modeled using the phonon-electron scattering model of Holstein [Holstein 54] and the electron-electron scattering model of Lawrence [Lawrence 76], respectively. We thus obtain:

$\omega_{c\,p}(T) = \omega_0[2/5+4(T/\theta)^5\int_\theta^{\theta/T} z^4 dz /(e^z-1)]$,

where θ is the Debye temperature and ω_0 is a constant to be determined from the static limit of the above expression together with the knowledge of the d.c. conductivity [McKay 76, Beach 77].

In addition, we have:

$\omega_{ce}(T) = 1/12 * \pi^3\Gamma\Delta/\hbar E_f *[(k_BT)^2 + (\hbar\omega/2\pi)^2]$, where Γ and Δ are constants giving the average over the Fermi surface of the scattering probability [McKay 76, Lawrence 76]. These equations together describe completely the temperature dependent dielectric constant of the metal.

To predict numerically the temperature effect on the sensitivity of the SPR measurement (*Figure*.III.10), we have considered a thickness of 50 nm of Au thin film at three different temperatures (278, 298 and 323 K) and we used the simulation parameters given in table.III.1.

	Gold (Au)
Plasma frequency at room temperature ω_{p0}	1.3754×10^{16} rad/s
Thermal expansion coefficient γ	1.42×10^{-5} K^{-1}
Debye temperature	170 K
Fermi energy E_F	5.53 eV
ω_0	2.0477×10^{13} rad/s
Δ	0.77
Γ	0.55

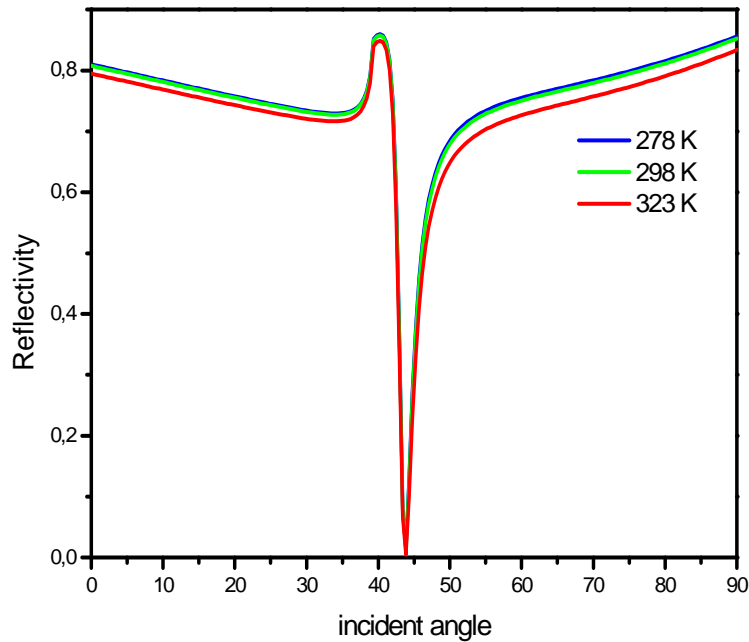***Table.III.1****: Parameters used for the numerical simulation of the temperature effect on SPR* [Sharma 06].

Figure.III.10: *SPR reflectance (R) curve changes with temperature at fixed incident wavelength (λ= 633 nm) and at a fixed gold film thickness (d=50 nm at room T). The resonance angle shift with temperature is negligible in this temperature range (278 – 323 K).*

From the curves of *Figure*.III.10, we notice that **the effect of temperature on the incident angle-dependence for surface plasmon resonance at the gold-air interface is a relatively minor shift of the plasmon resonance angle**. This result agrees qualitatively with those obtained in reference [Chiang 01, Chiang 04]. Note that we have here considered a wide range of temperatures (278–323 K) which is realistic for an experimental investigation of the SCO phenomenon in thin films.

III.2.4 Theoretical simulation of the effect of the spin transition on the SPR signal

In order to predict the effect of the spin state change on the SPR curves and to determine the optimal experimental conditions, we have carried out a theoretical calculation (See Fig.III.11) assuming that the refractive index of the SCO film changes by: Δn = 0.2 and Δk= 0.08. It turned out that the spin transition results in **easily measurable resonance shifts (0.29 degrees) even in an ultra-thin layer (3 nm) of SCO complex**. The experimental validation of these results will be discussed elsewhere (section III.4.2).

Fig.III.11: *Calculated angular reflectivity SPR spectra of a multilayer comprised of a gold film and a thin film of a spin crossover complex. HS and LS stand for High Spin and Low Spin, respectively. Excitation: 633 nm, BK7 prism covered with a gold layer (50 nm, n=0.1971, k=3.0899) and with a thin film of the spin crossover complex (3 nm, n=1.4(HS)/1.6(LS), k=0.04(HS)/0.12(LS)) in air.*

It should be noted that if one takes into account the thickness change upon the SCO (~5% as a typical value), the SPR transducer signals is less sensitive to the SCO and we calculate 0.08 degrees shift upon the SCO (see figure III.12). Obviously when the sample thickness becomes higher, the angle corresponding to maximum SPR coupling tends to shift to the higher value and this compensates for the effect the refractive index change.
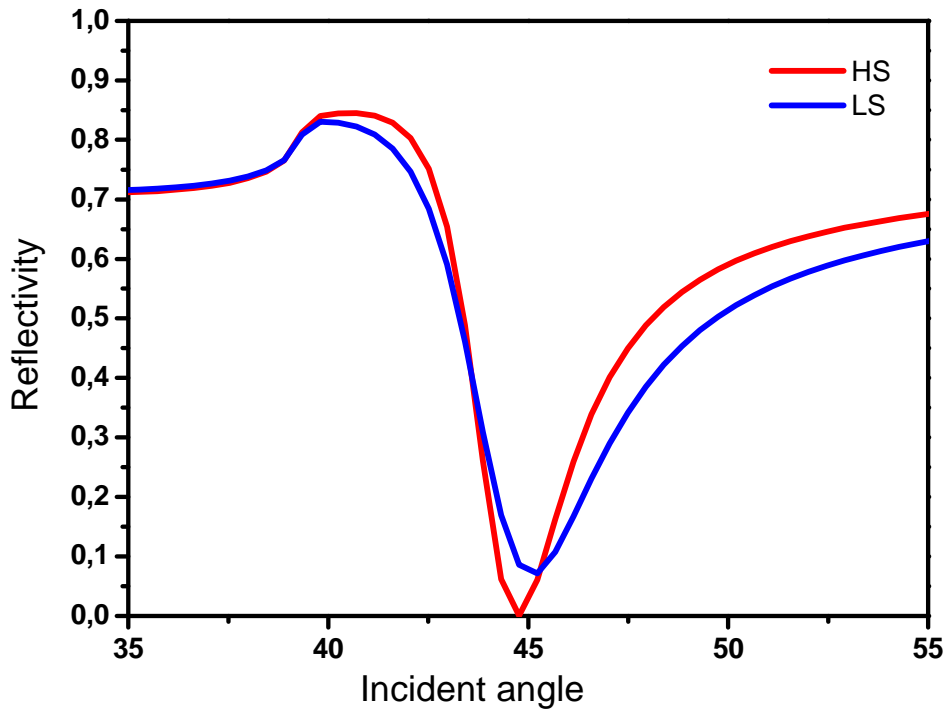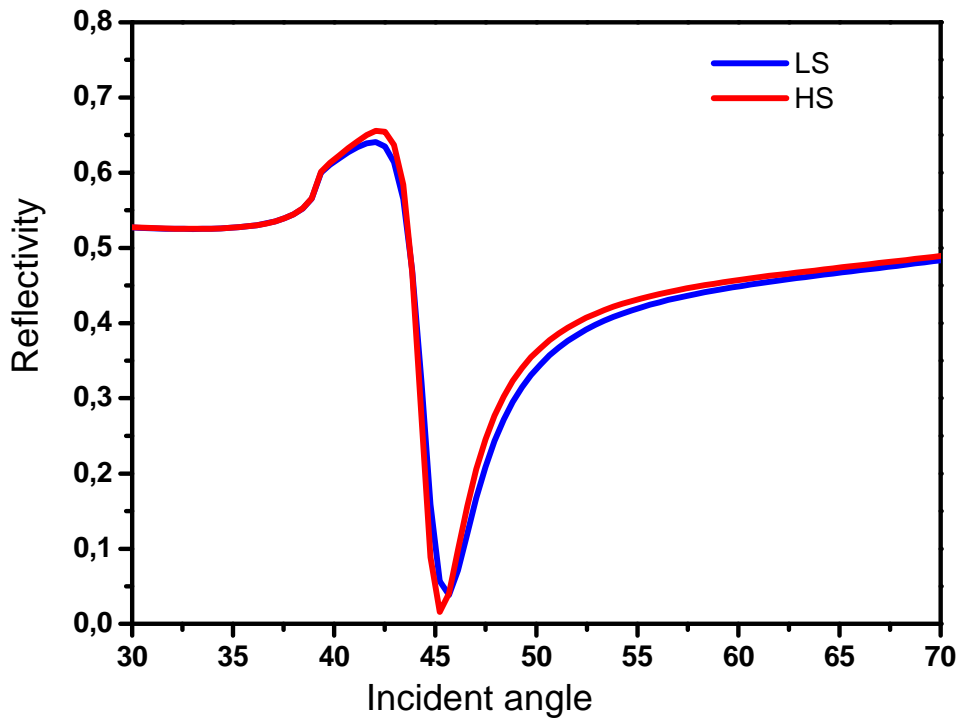
Fig.III.12: *Calculated angular reflectivity SPR spectra of a multilayer comprised of a gold film and a thin film of a spin crossover complex assuming 5% film thickness change upon the spin transition (thickness (LS) = 3 nm, n=1.6(LS), k=0.12(LS); and thickness (HS) = 3.15 nm, n=1.4(HS), k=0.04(HS)) in air.*

We carried out another theoretical simulation assuming that the first layers at the surface do not undergo spin transition (see figure III.13). We supposed three configurations:

1) The whole film in the HS state (20 nm).

2) Multilayer where no ST occurred at the surface (14 nm of a thin film in the LS state sandwiched between two layers of 3 nm which remained in the HS state).

3) The whole film in the LS state (20 nm).

From figure III.13 we can conclude that the SCO is detectable by surface plasmon spectroscopy even in an ultra-thin layer and even on multilayers.
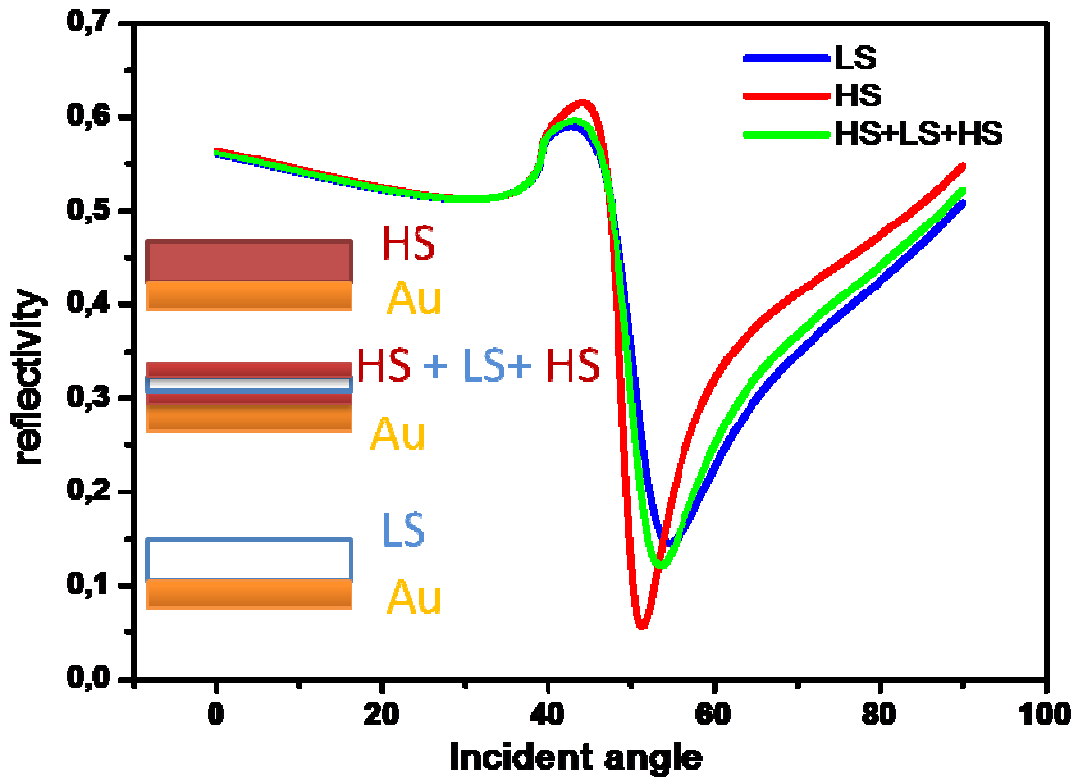
Fig.III.13: *Calculated angular reflectivity SPR spectra of a multilayer assuming that no SCO occurred at the surface (HS + LS + HS).*

III.3 Experimental setup

Using Kretscmann's configuration, there is in general two possibilities to build an SPR setup. The first possibility is to measure at a fixed wavelength the reflectance as a function of the incident angle by using a scanning rotational stage [C. Nylander, 82] or a photodiode array in a compact system having no moving part (based on Fourier transformer) [K.Matsubara 88]. The second possibility is to measure the reflectance at a fixed angle as a function of the wavelength (modulated wavelength) [Reather 88]. In our case, surface plasmon spectroscopic (SPR) measurements were carried out on a custom made fixed wavelength set-up. Gold-titanium coated glass slides (5 nm titanium, followed by 50 nm gold vacuum evaporated onto a microscope slide) were used for reflection measurements. The uncoated side of the slide was brought into optical contact with the base of an equilateral right angle prism (BK7) by an index matching oil. A monochromatic laser light beam from a He-Ne laser (632.8 nm) was first passed through a neutral density filter to adjust the laser intensity, and then a half-wave plate to be able to set TM polarization. After that, the beam is split by a beam splitter into two

beams; one of which serves as a reference, while the other beam was directed to the base of the prism which was mounted on a stepping motor. The intensities of both beams are detected by separate photo-detectors. The reflected light beam which emerged from the lateral face of the prism was collected for incidence angles ranging from 35° to 60°. The incidence angle is controlled by a goniometer with an angle resolution of 0.01°. Both photo-detectors and the goniometer are connected to a computer to run the experiment using a C++ program (see figure III.14).
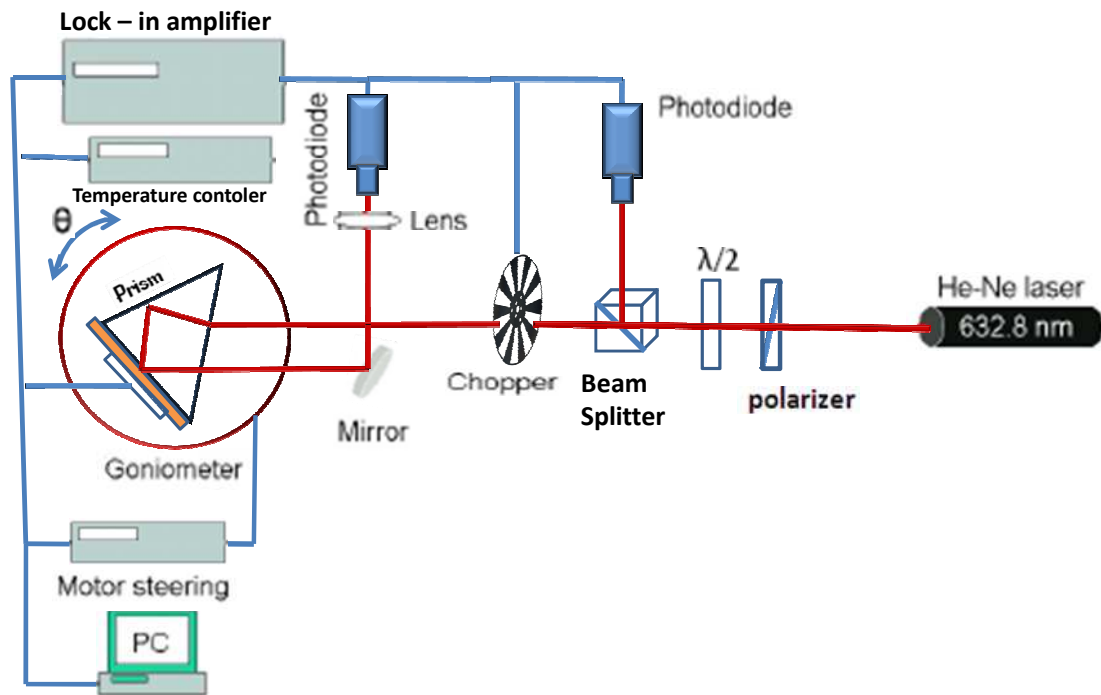
Fig.III.14: *SPR setup based on the Kretchmann configuration.*

To this setup, we added a sample heating / cooling system using a Peltier element which have a hole in the center (to keep the air as the last dielectric layer). The temperature could be adjusted by connecting the Peltier element to a controller, or directly by passing the electrical current through the Peltier element. The temperature was measured with a thermocouple (type K) sensor connected to the sample via the Peltier hole. Using this setup, the sample temperature can be changed from + 10 to + 70 °C.

The substrates used for the thin films growth were fabricated at the "Laboratoire d'Architecture et Analyse de Systèmes" (LAAS, CNRS) in Toulouse. Initially a microscope glass slide was covered by 5 nm of titanium and 50 nm of gold deposited by thermal

evaporation at a pressure of 5×10^{-7} mbar (1 mbar = 100 Pa) using a Veeco 770 thermal evaporator apparatus.

Concerning the deposition of SCO thin films, different thicknesses of the compound {Fe(pyrazine)[Pt(CN)$_4$]} were elaborated by Carlos BARTUAL in our team using a layer-by-layer assembly method [Cobo 06]. First, the anchoring layer (asymmetric ethyl-(4-pyridyl) disulfide) was deposed on the gold-titanium coated glass slide in order to allow the link between the gold substrate and the SCO compound via Au-S and N-Fe bonds. After that, the substrate was dipped into a solution of Fe(II) and $[Pt(CN)_4]^{2-}$ salts and finally into a pyrazine solution with intermediate rinsing in pure ethanol solutions. This cycle (immersion into the three solutions) can be repeated several times as a function of the desired thickness. Schemes I.16 and III.15 represent, respectively, the film growth process and the experimental conditions for the elaboration of the thin films.

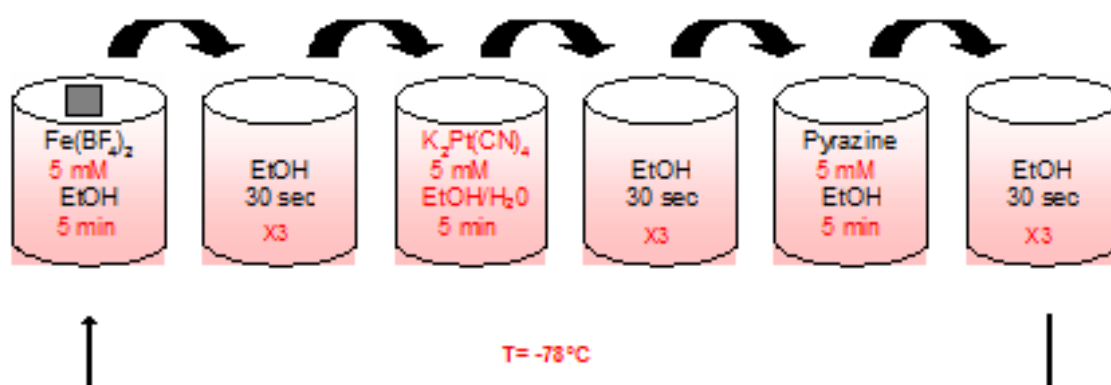**Fig.III.15:** *Experimental conditions of the deposition of thin layers of the SCO complex {Fe(pyrazine)[Pt(CN)$_4$]}.*

The Fe(pz)[Pt(CN)$_4$] thin films were characterized by atomic force microscopy (AFM) with a Nanoscope III instrument (Veeco). AFM scans were preformed in air at room temperature at 1 Hz rate in the tapping mode.

III.4 Results and discussion

III.4.1 Thin films investigation

The resulting $\{Fe(pyrazine)[Pt(CN)_4]\}$ film surfaces were characterized by atomic force microscopy (AFM) and by surface plasmon resonance. We used surface plasmons (SPs) to evaluate its applicability to investigate the SCO phenomenon by measuring the optical thickness and refractive index of the $\{Fe(pyrazine)[Pt(CN)_4]\}$ layers at room temperature (296 K).

The measurement was performed in three steps. First we obtained the total internal reflection, which can be helpful for the alignments and data normalization. The second step is to scan the four-layer system: prism (BK7), Ti layer (5 nm), gold metal layer (50 nm) and air. This second step is used to confirm the refractive indices and thicknesses of the layers which are already known; and also to simplify the simulation in the final step by inserting directly these parameters into the model described in III.2. The third step is to scan the whole system including the $\{Fe(pyrazine)[Pt(CN)_4]\}$ SCO layer. As the response curves indicate (fig.III.16), there is an increasing trend toward larger SPR coupling angles as the thickness of the sample increases. The peak shapes are similar for each of the samples except the curve obtained for 15 deposition cycles. The broadness of this curve might be due to slight losses in the sample. All the parameters extracted from the Fresnel theoretical fits of the reflectivity versus the incident angle curve for the bare titanium/gold surface (reference sample) and the various thickness depositions are reported in Table III.2. The thickness values of 4.8, 6.5 and 15.0 nm obtained for 5, 10 and 15 layers of the polymer, respectively, are in close agreement with the theoretical thickness. Indeed, considering on one hand, the *c* parameter of the unit cell measured by X-ray diffraction for a $\{Fe(pyrazine)[Pt(CN)_4]\}$ single crystal [Cobo 08] of 7.5 Å which corresponds to the thickness of one layer of the 3D coordination polymer and on the other hand, the thickness of about 1 nm for the anchoring layer between the gold substrate and the 3D polymer, the theoretical thickness values for 5, 10 and 15 deposition cycles are 3.9, 8.5 and 12.3 nm, respectively.
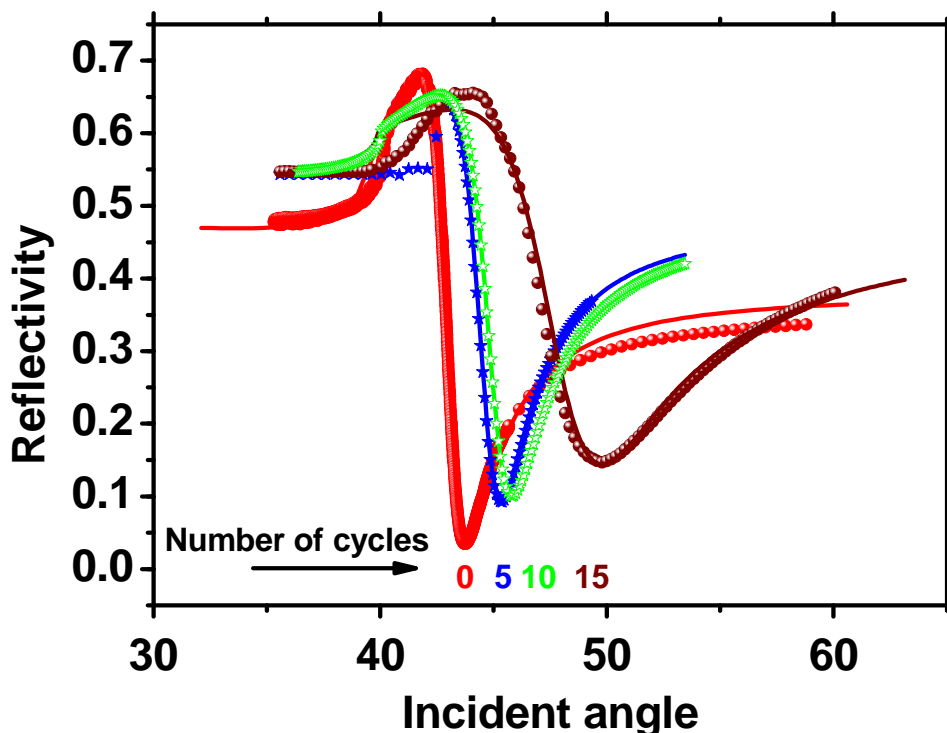
Figure.III.16: *Surface plasmon resonance of the glass/Ti/Au substrate before (indicated by 0) and after coating with {Fe(Pz)[Pt(CN)₄]} layers (indicated by 5, 10, and 15 corresponding to the number of deposition cycles). Scatters are experimental data points acquired in ambient conditions and the full lines are Fresnel theoretical fits.*

Layer	SPR			AFM
	thickness (nm)	n	k	thickness (nm)
Prism (BK7)	-	1.5189	0	-
Ti	5 ± 0.2	2.22 ± 0.02	2.92 ± 0.01	-
Au	50 ± 0.2	0.17 ± 0.02	3.15 ± 0.01	-
{Fe(pyrazine)[Pt(CN)₄]} 5 deposition cycles 10 deposition cycles 15 deposition cycles	4.8 ± 0.2 6.5 ± 0.2 15.0 ± 0.2	1.6 ± 0.02 1.6 ± 0.02 1.6 ± 0.02	0.06 ± 0.01 0.06 ± 0.01 0.07 ± 0.01	3.8 ± 0.7 8 ± 2 12 ± 2
Air	-	1	0	-

Table.III.2: *The fitted geometrical thicknesses as well as the real (n) and imaginary (k) parts of the refractive index of the different {Fe(pyrazine)[Pt(CN)₄]} multilayers determined from the SPR measurements. The corresponding AFM data are also shown.*

The results obtained by surface plasmons agree also quite well with those obtained by atomic force microscopy; e.g. the layers thicknesses obtained separately by both techniques are the same within experimental errors. Continuous films were used to evaluate the average roughness of the surface while the study of the corresponding patterned films provides an efficient way for measuring the average film thickness by AFM. A homogeneous and regular surface with a calculated roughness of *ca.* 0.7 nm can be observed (fig.III.17). The mean value is obtained within a 1 μm^2 surface from 512×512 data points. Similar surface topographies were obtained when 5 - 15 deposition cycles were realized.
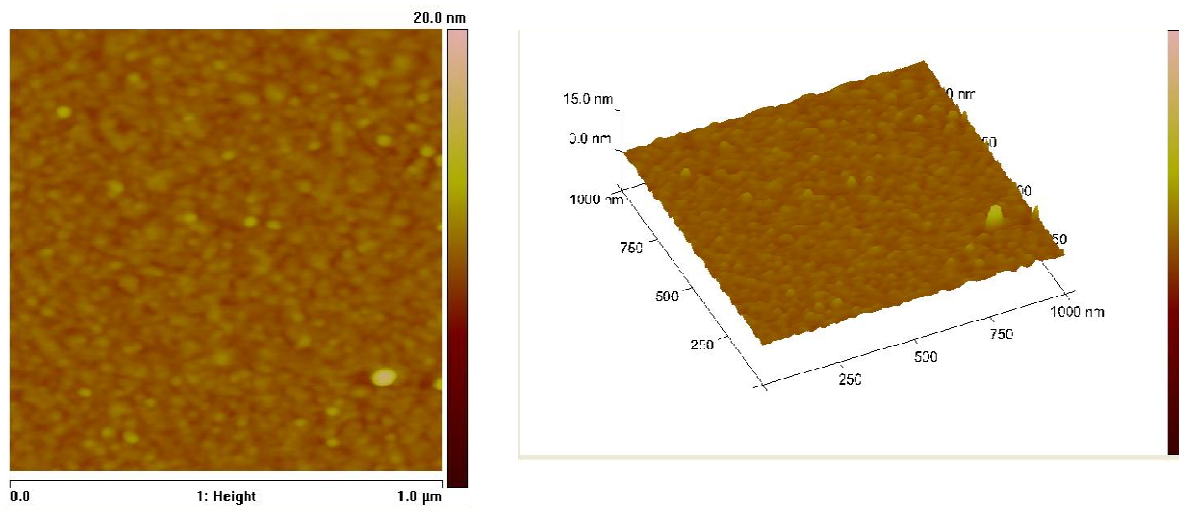

Fig.III.17: *AFM images of a continuous film following 20 deposition cycles*

Figure III.18 shows the AFM images of patterned thin films for different numbers of deposition cycles. In these images, residual artefacts are present on both the surface of the film and that of the gold substrate as well. These correspond to impurities deposited during the final lift off step. The study of the film thickness was carried out by considering the whole area inside the dashed lines including large patterns (several μm^2). The mean value of the thickness was obtained as the peak-to-peak distance between the two maxima of the surface height distribution histogram obtained within this area; the reference peak corresponding to the bare gold surface. The mean thickness measured this way was 3.8, 7.9 and 12.3 nm for 5, 10, and 15 deposition cycles, respectively. The mean roughness- defined as the half-height half width of the peak in the height distribution histograms - within a 4 μm^2 surface was found 0.7, 1.8 and 1.9 nm, respectively.
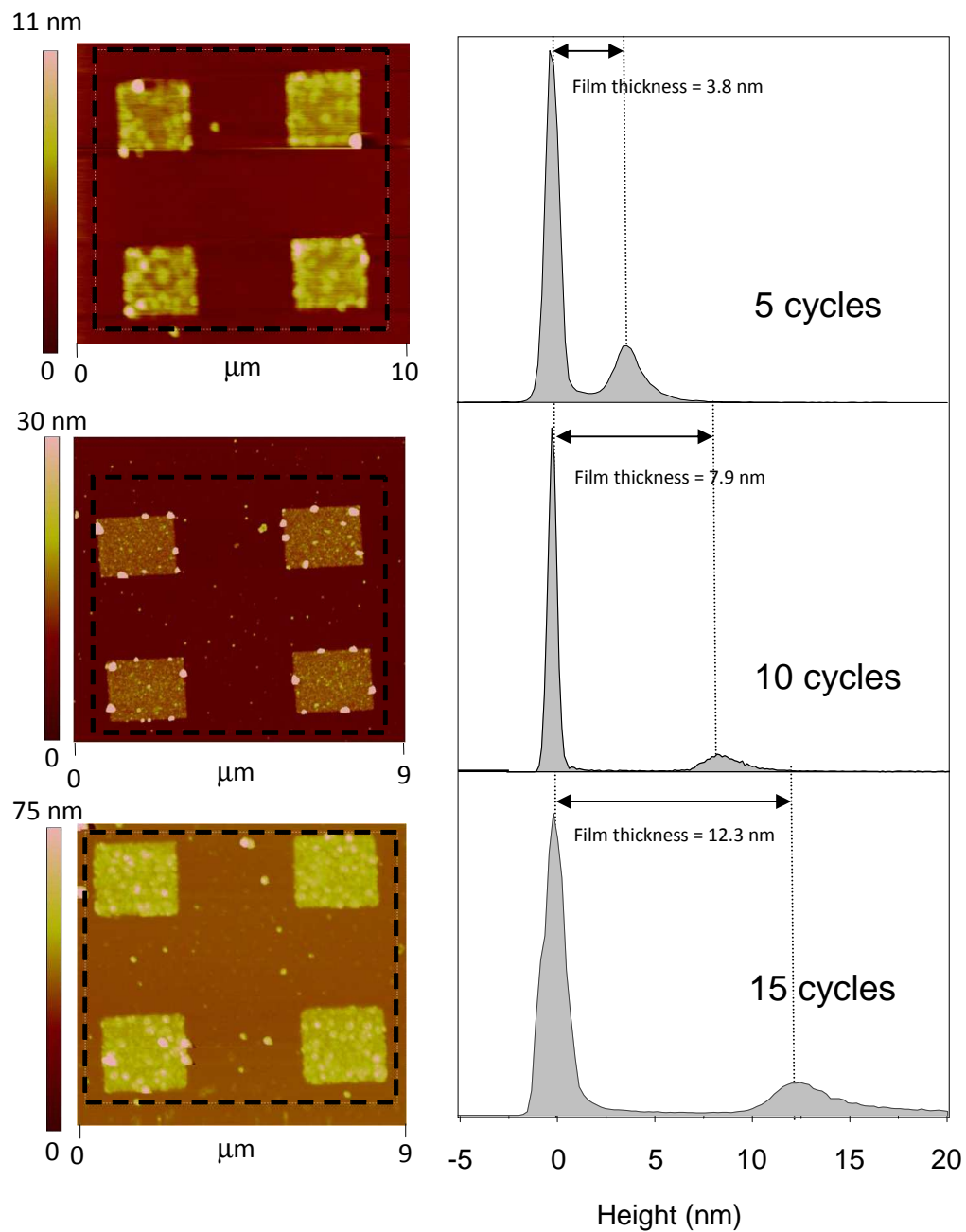
Fig.III.18: *AFM images of micrometric patterns of {Fe(pyrazine)[Pt(CN)₄]} for 5, 10 and 15 deposition cycles. The right panels show the height distribution histograms for the area inside the dashed lines in the images.*

Besides the thickness investigation, the surface plasmon experiments yield, when the geometrical thickness is known, the refractive index and the losses in the layers. We have found that the refractive index at room temperature (296 K) is about 1.6 ± 0.02, whereas the

absorption coefficient is negligible at 632.8 nm (laser wavelength). These last results reveal that the films are of good optical quality.

III.4.2 Investigation of nanoparticle layers

To achieve our ultimate goal, which is the investigation of the thermal spin crossover phenomenon on thin films, we have spin coated nanoparticles of the compound tris (4-hyptyl-1,2,4-triazole) iron(II) tosylate on the typical substrate for SPR studies (glass + 3 nm of Ti + 45 nm of Au). The $[Fe(hptrz)_3](OTs)_2$ SCO nanoparticles were synthesized by I.A. Guralskyi in our team.

Figure.III.19 shows χT vs. T dependence for the $[Fe(hptrz)_3](OTs)_2$ bulk sample during the first and second thermal cycles (χ stands for the molar magnetic susceptibility). The transition temperature $T_{1/2}$ shifts from 310 to 300 K and the hysteresis loop becomes smaller after the first cycle, which could be related to the dehydration of the sample.
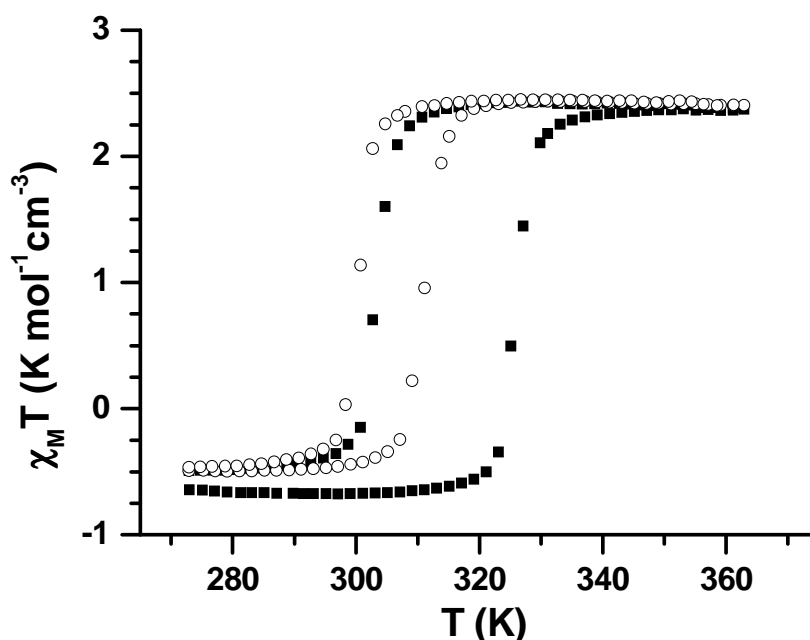

Figure.III.19: *Temperature dependence of χT for **[Fe(hptrz)₃](OTs)₂** bulk sample during the first (■) and second (○) thermal cycles. During the first cycle a dehydration occurs in the sample.*

Before starting the SPR studies and in order to make sure that these deposited SCO nanoparticles as a thin film retain the SCO properties, we have carried out a series of temperature dependent UV-VIS absorption measurements of a *ca.* 85 nm SCO thin film. (The film thickness was measured by AFM.) The spin transition occurs around 325-330 K (figure III.20) and it is almost complete at 340 K as it can be deduced from the negligible absorption intensity at 280 nm. This intense absorption peak at 280 nm in the LS state is assigned to metal-ligand charge transfer. Let us note also that the expected LS absorption peak ($^1A \rightarrow {}^1T$) in the visible region was not detectible due to the low value of molar extinction coefficient for this forbidden *d-d* transition. The observed hysteresis occurs mainly due to the dehydration of the sample.
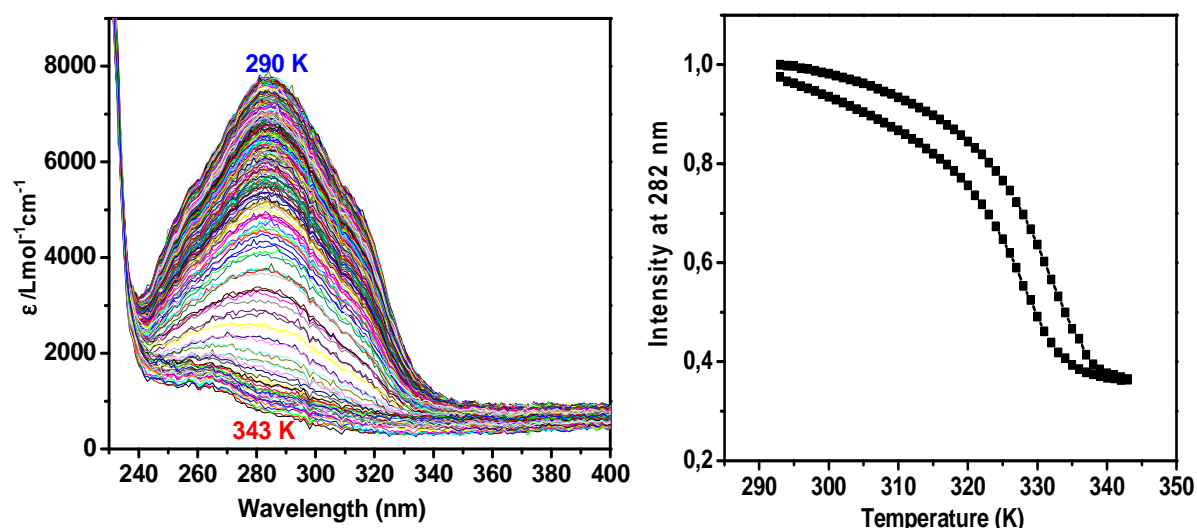

Figure.III.20: *Variable temperature absorption spectra of a [Fe(hptrz)$_3$](OTs)$_2$ SCO thin film in the UV range and the temperature dependence of the absorbance at 282 nm in the heating and cooling modes.*

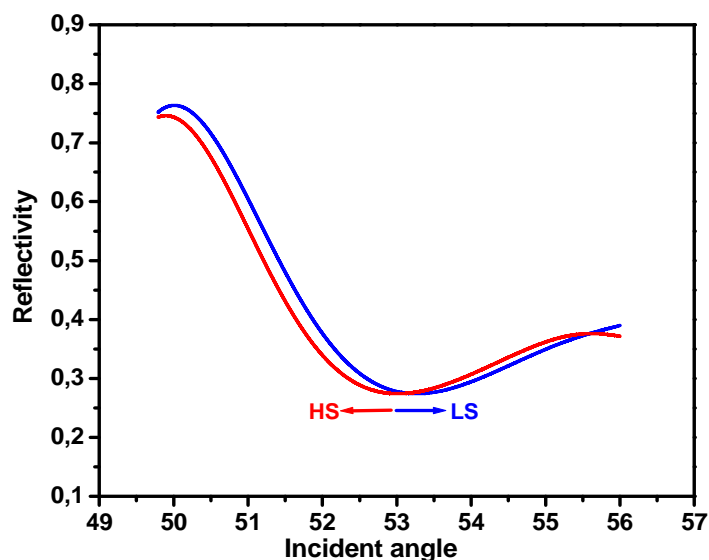Figure III.21 shows the SPR response signal of the [Fe(hptrz)$_3$](OTs)$_2$ SCO thin film at 308 and 343 K.

Figure.III.21: *Surface plasmon resonance of the spin-coated [Fe(hptrz)₃](OTs)₂ SCO thin film on glass/Ti/Au substrate at 308 K (LS) and 343 K (HS).*

As it was predicted theoretically, the SPR resonance shifts to lower angles when the SCO complex is switched from the low to the high spin state. As shown in figure Figure.III.21 the SPR minimum angle shifts from 53.28° (at 308 K) to 52.96° (at 343 K) indicating a refractive index change of *ca.* 0.05. The optical parameters obtained by the Fresnel theoretical fits are: $n_{LS} = 1.57$, $n_{HS} = 1.52$, while the film thickness was evaluated as *ca.* 50 nm.

Figure.III.22 shows the temperature dependence of the SPR resonance angle in the heating and cooling modes for the [Fe(hptrz)₃](OTs)₂ SCO thin film. A linear thermal variation of the resonance angle is observed in the temperature range where no spin crossover occurs. This variation is related to the thermal dilatation of the sample and the associated change of the refractive index. The thermal SCO of [Fe(hptrz)₃](OTs)₂ is characterized by an abrupt transition around T= 325 K. The observed resonance angle shift (*ca.* 0.12°) associated with the SCO is reversible. Similar to the absorption measurements, the small difference in the heating and cooling curves can be explained by the dehydration of the sample. Therefore measurements in a closed chamber with controlled atmosphere (dry N₂) will be necessary in order to draw more quantitative conclusions. This work is under progress.
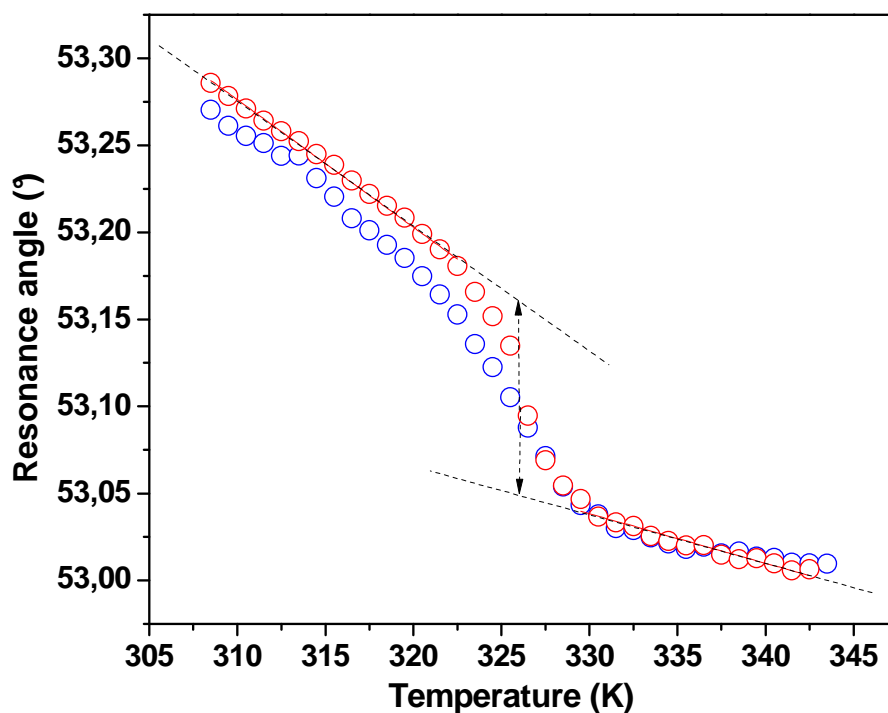
Figure.III.22: *Temperature dependence of the SPR resonance angle in the heating (red) and cooling (blue) modes for a [Fe(hptrz)$_3$](OTs)$_2$ SCO thin film. The arrow indicates the resonance angle shift associated with the spin crossover phenomenon ($\Delta\theta_{SCO} = 0.12°$).*

III.5 Conclusions

This chapter confirmed the potential of the SPR technique to investigate the spin crossover phenomenon in thin films.

In the first part of this study we introduced the principle of attenuated total reflection method based on the Kretchmann configuration and Fresnel equations for determination of optical properties (thickness and refractive index). The theoretical simulations allowed us to optimize the geometry of our gold resonator and revealed that the **intrinsic temperature dependence of the SPR signal from this prism-based gold resonator is negligible** in the temperature range of interest. On the other hand these simulations predicted **a very high sensitivity of the SPR technique** to detect the SCO phenomenon even in ultra-thin (3 nm) films.

In the second part of this study we used surface plasmon resonance spectroscopy to investigate {Fe(pyrazine)[Pt(CN)$_4$]} thin films. This investigation allowed us to **determine the optical thickness of these films**. Moreover we found that the films are of good quality

and the results of both SPR and AFM experiments are in good agreement with the theoretical predictions of the films thicknesses. The spin crossover in these {Fe(pyrazine)[Pt(CN)$_4$]} films is expected to occur at temperatures which are not accessible with our experimental setup for the moment. For this reason we have decided to validate our approach using thin films (50 nm) of the [Fe(hptrz)$_3$](OTs)$_2$ complex, which display spin crossover above room temperature. Using this sample, **we were able to observe – for the first time - the thermal spin crossover phenomenon by means of SPR spectroscopy**. This work is still under progress in order to be able to use our experimental setup under a controlled atmosphere. This development should allow us to carry out more accurate investigations as a function of the films thickness and other parameters (presence of different gas and vapor molecules, etc.).

III.6 References

R.T. Beach, R.W. Christy, *Phys. Rev. B*, 16, **1977**, 5277.

H.-P. Chiang, et al, *Optics Communication,* 188, **2001**, 283-289.

H.-P. Chiang, et al, *Optics Communication,* 241, **2004**, 409-418.

S. Cobo, G. Molnar, J. A. Réal, A. Bousseksou, *Angew. Chem. Int. Ed.* **2006**, 45, 5786.

S. Cobo, D. Ostrovskii, S. Bonhommeau, L. Vendier, G. Molnár, L. Salmon, K. Tanaka, A. Bousseksou, *J. Am. Chem. Soc.* 130, **2008**, 9019.

A. Hauser, *Chemical Physics Letters*. 202, **1993**, 173.

T. Holstein, *Phys. Rev*. 96, **1954**, 535.

K.A. Horne, M. Printz, W.L. Barnes, J.R. Sambles, *Optics Communications*, 110, **1994**, 80-86.

B.D. Gupta, A.K. Sharma, Sens. *Actuat. B*, 107, **2005**, 40.

W.E. Lawrence, *Phys. Rev. B*, 13, **1976**, 5316.

E. D. Loutete-Dangui, F. Varret, E. Codjovi, P. R. Dahoo, H. Tokoro, S-I. Ohkoshi, C. Eypert, J. F. Létard, J. M. Coanga, K. Boukheddaden, *Phys. Rev. B*, 75, **2007**, 184425.

H. A. Macleod, Thin Film Optical Filters, (Bristol, England; Philadelphia, PA: Institute of Physics Pub., **2000**).

Koji Matsubara, Satoshi Kawata, Shigeo Minami, *Applied Optics*, 27, **1988**, 1160.

J.A. McKay, J.A. Rayne, *Phys. Rev. B* 13, **1976**, 673.

C. Nylander, B. Liedberg, T. Lind, "Gas Detection by Means of Surface Plasmon Resonance," *sensors Acuators*, 3, **1982**, 79.

S-I. Ohkoshi, T. Nuida, T. Matsuda, H. Tokoro, K. Hashimoto, *J. Mater. Chem* 15, **2005**, 3291.

A. Otto, Exitation of nonradiative surface plasma waves in silver by the method of frustrated total reflection, *Z. Phys*., 216, **1968**, 398–410.

C. KoBlinger, E. Uttenhaler, S. Drost, F. Aberl, H. Wolf, G. Brink, A. Stanglmaier, E. Sackmann, *Sensors and Actuators B*, 24-25, **1995**, 107-112.

E. Kretschmann and H. Reather, Radiative decay of nonradiative surface plasmons excited by light, Z. Naturforsch., Teil A, 23, **1968**, 2135–2136.

Raether, H. Surface plasmons on smooth and rough surfaces and on gratings, *Springer - Verlag; Berlin*, **1988**.

http://refractiveindex.info

Z. Sekkat, J. Wood, Y. Geerts, W. Knoll, *Langmuir,* 12, **1996**, 2976.

A. K. Sharma, B. D. Gupta, *Optical Fiber Technology*, 12, **2006**, 87- 100.

R.W. Wood, *Philos. Mag*., 4, **1902**, 396–402.

IV Conclusions and perspectives

The aim of the present work was to investigate the electrical and optical properties of switchable molecular complexes - such as spin crossover or valence-tautomeric compounds - in which a switching between two electronic states can be induced by various external stimuli (temperature, pressure, magnetic field, light, …). Recent studies revealed that such compounds are expected to show an important variation of their dielectric constant (ε) in a wide frequency range ($\varepsilon_0 \rightarrow \varepsilon_\infty$). The objectives of our research were inspired by this property and - in the context of this thesis - two main questions were proposed:

 - Is it possible to use an external electric field to switch the properties of bistable molecular complexes?

- Can we use the variation of the complex permittivity (ε^*) to investigate the switching phenomena in these complexes at the nanometric scale?

Concerning the first question, we have focused on valence-tautemeric complexes exhibiting charge transfer phase transition phenomena (RbMnFe and NaCoFe type Prussian blue analogues as well as a Co–W bimetallic complex). We performed a detailed Raman spectroscopic study on three different valence-tautomeric compounds under an applied external electric field. One of the most important outcomes of this work is that **we have been able to provide experimental evidence for a new type of electric field-induced transition in these compounds,** which occurs around room temperature within the thermal hysteresis region. We have shown that this EFI transition takes place always from the high-temperature phase towards the low-temperature phase. We proposed a mechanism for this phenomenon where the field-induced stabilization of the low-temperature phase was related to a paraelectric-ferroelectric transition.

An important prospect of this work on the valence-tautemeric complexes would be the further investigation of the mechanism of the field effect using microscopic and structural probes such as X-ray diffraction. Furthermore, for the applicative aspects, the synthesis of thin films of these materials exhibiting thermal hysteresis would be also highly desired.

In the context of the electric investigations, we have also carried out a detailed investigation of the charge transport properties of the valence-tautemeric complexes with the aim to understand the charge transport mechanism and to elucidate the interplay between the charge transport and the valence-tautomerism:

- We observed a charge transport typical of disordered solids and we concluded that the charge transport occurs in these compounds by **small poalron hopping which we assigned to the intermetallic electron transfer**. A dipole relaxation process displaying the same thermal activation energy as the conductivity has been observed in each case. As an interesting future perspective, we should underline that this property opens up a very efficient possibility to determine inter-valence electron transfer rates in these compounds in a wide frequency range (mHz to MHz) using frequency-domain dielectric spectroscopy, instead of the usually applied lengthy time-domain methods (pump-probe optical spectroscopy, …).

- We have shown that **the transition between the valence-tautomeric forms does not modify the charge transport mechanism and modulates only slightly the conductivity** and thus the dielectric relaxation rate. (The highest variation of conductivity - *ca.* one order of magnitude - was observed for the RbMnFe-type Prussian blue analogues.) On the basis of the proposed transport mechanism, the relatively small conductivity changes were related to the variation of the phonon frequencies upon the valence-tautomeric phase transition.

We have also investigated the electrical properties of the spin crossover complex $[Fe(HB(pz)_3)_2]$. Remarkably, the electrical conductivity of the sample measured at 293 K dropped by 4 orders of magnitude following the first thermal cycle through the spin transition. This property, together with the fact that this compound can be deposited on surfaces by sublimation, allowed us to construct a **ROM-type microelectronic device** with the $[Fe(HB(pz)_3)_2]$ complex as an active element. Information is stored in the device by heating the complex and thus switching the device from the high to the low conductivity state. The readout can be performed at room temperature by measuring the resistivity of the device.

Concerning our second objective, we developed a novel approach for the detection of spin crossover in nanometric thin films where sensing is based on surface plasmon resonance (SPR) detection of refractive index changes in the films. Indeed, the conversion between the electronic states of the molecules is accompanied by a large variation of the refractive index ($\Delta n = 10^{-1} - 10^{-2}$) in both spin crossover and charge transfer complexes. **We demonstrated theoretically as well as experimentally that these changes in terms of refractive index (dielectric constant) can be easily detected by surface plasmon spectroscopy.** Using this technique we have been able to determine the thickness and the optical constants of ultra-thin films of the {Fe(pyrazine)[Pt(CN)$_4$]} complex at room temperature. In the case of a thin film of the [Fe(hptrz)$_3$](OTs)$_2$ complex, we have determined the optical thickness of the film in a wide temperature range and we could clearly evidence the thermal spin transition around 325 K.

The SPR spectroscopy appears thus as a powerful method to investigate our materials even in the case of very thin films (down to 2-3 nm) using the angular SPR shifts as a signal transducer. The results reported here represent an important step towards the investigation of size-reduction effects on the physical properties of bistable molecular materials and thus bridging the gap between the molecular and bulk phenomena. Moreover, these results open up prospects for integration of these materials in photonic devices with the aim of their possible applications as memory devices, switches and sensors.

Résumé en français

Table des matières

I)   <u>Introduction générale</u>

De nos jours, les demandes technologiques en terme de miniaturisation de composants telles que les capteurs, les dispositifs pour l'électronique et l'optique stimulent de plus en plus l'activité scientifique des laboratoires à l'échelle mondiale. A cet effet, les matériaux moléculaires bistables semblent prometteurs dans la perspective de telles applications. L'adressage et la détection de la bistabilité dans ces matériaux à l'échelle nanométrique est une étape incontournable dans la conception de tels dispositifs.

Dans ce contexte, le phénomène de la transition de spin constitue un exemple typique de cette voie d'une actualité grandissante. Il est possible dans ce cas de commuter le système entre ses états de spin haut et bas. Un autre exemple est celui des tautomères de valence dans lesquels la commutation est liée à un transfert d'électron. La bistabilité dans ces matériaux peut présenter des cycles d'hystérésis de la susceptibilité magnétique, de la réflectivité optique et de la constante diélectrique *[Bousseksou 03, Ohkoshi 05]* dus à la présence d'une transition de phase du premier ordre liée à une forte coopérativité d'origine magnéto-élastique. Cela laisse entrevoir des applications telles que les dispositifs de stockage d'information dans le matériau, les dispositifs capteurs ou actionneurs à l'échelle moléculaire.

Le phénomène de transition de spin (ou de transfert de charge) peut être induit par une variation de température, de pression, de champ magnétique ou une irradiation lumineuse. Il a été montré que le phénomène de transition de spin peut être mesuré par une variation des propriétés électriques, ce qui laisse entrevoir des applications basées sur une lecture électrique. Dans le cadre de ces travaux de thèse, nous souhaitons étudier en plus la possibilité d'induire ces transitions par l'application d'un champ électrique. Ainsi, l'écriture et la lecture pourraient être tout électrique. Outre son intérêt pour des applications potentielles, l'étude des matériaux bistables de tailles nanométriques constitue un enjeu majeur du point de vue fondamental : l'objectif est de comprendre les effets spécifiques liés aux objets de petites tailles. Par exemple, dans le cas des complexes à transition de spin, une des questions les plus importantes est de savoir comment la réduction de taille influencera sur la largeur de l'hystérésis observée à l'échelle macroscopique ainsi que sur l'établissement même du

phénomène via les processus coopératifs. Pour cette raison la spectroscopie des plasmons de surface a été choisie pour suivre le changement de l'indice de réfraction lors de la transition de spin (liée aux changements de la constante diélectrique).

Ce manuscrit est structuré en trois chapitres :

- Le premier chapitre expose une introduction générale sur les systèmes bistables tels que les complexes à transition de spin et les tautomères de valence et les différents perturbateurs externes (température, pression, champ magnétique, irradiation lumineuse) qui peuvent induire une transition de spin ou une transition de phase ainsi que les méthodes expérimentales pour détecter la transition de spin. L'état de l'art sur la réduction de la taille de ces matériaux sous formes de couches minces et de nanoparticules est également introduit.

- Le deuxième chapitre est consacré aux études électriques. Nous proposons pour la première fois l'application d'un champ électrique externe pour induire une transition de phase dans les complexes tautomères de valences. En parallèle, nous allons étudier le transport de charges et les propriétés diélectriques de ces complexes. Nous allons également proposer un dispositif de mémoire non-volatile pour le stockage de l'information en se basant sur le changement de la résistivité qui accompagne la transition de spin (TS).

- Dans le troisième chapitre nous allons introduire le phénomène de résonance des plasmons de surface (RPS). Nous allons démontrer théoriquement et expérimentalement que la RPS est une méthode performante pour déterminer l'indice optique des films ultra - minces et détecter la TS.

Enfin, nous conclurons ce manuscrit en rappelant les principales avancées que nous avons apportées aux différentes questions abordées puis nous proposerons quelques perspectives de recherche.

II) <u>Introduction à la bistabilité moléculaire</u>

II.1) <u>Le phénomène de la transition de spin</u>

Certains métaux de la première série de transition, de configuration électronique $3d^n$ ($4 < n < 7$) peuvent exister dans deux états électroniques stables, selon la force du champ cristallin : l'état HS et l'état BS. Pour ces systèmes, l'effet d'un champ de ligand octaédrique provoque l'éclatement des niveaux d'énergie des orbitales d (dégénérés dans le cas de l'ion libre) en deux niveaux d'énergie : un premier niveau comportant trois orbitales t_{2g} non liantes (d_{xy}, d_{yz}, d_{zx}) et un second composé de deux orbitales e_g antiliantes (d_{z2}, d_{x2-y2}). Ces deux niveaux sont séparés par un éclatement 10 Dq, caractérisant la force du champ de ligand. Cet éclatement dépend de la nature de l'ion et des ligands qui l'entourent.
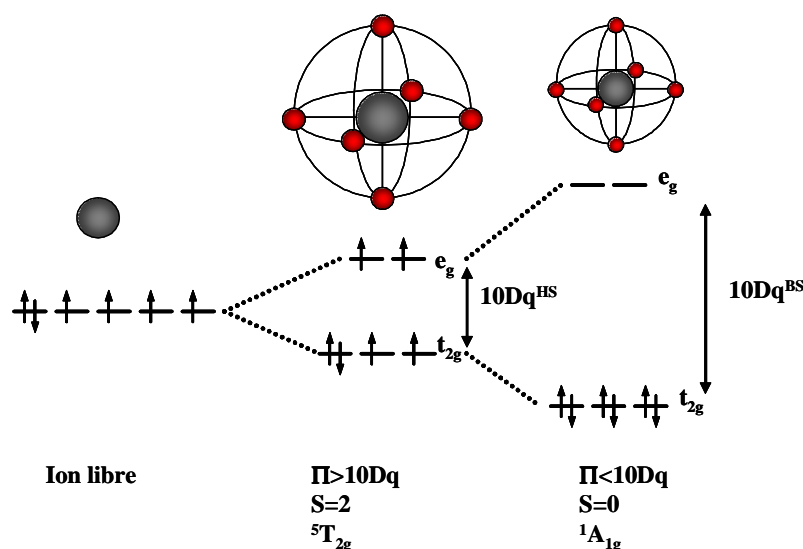
Figure.2.1 : Levée de dégénérescence et configuration électronique des états HS et BS dans le cas d'un complexe octaédrique du Fe^{II}.

II.2) <u>Transition de spin induite par différentes perturbations physiques</u>

II.2.a) <u>Transition de spin thermique</u>

La condition pour que la transition de spin thermique se produise, est que la différence des énergies des niveaux de point zéro entre les états HS et BS soit de l'ordre des énergies thermiquement accessibles $k_B T$: $\Delta E^0 = E_{HS}^0 - E_{BS}^0 \sim k_B T$; la variation d'entropie jouant un

rôle de « moteur » de la transition de spin. En effet, si la transition de spin est quantitative à haute température c'est parce que la densité d'états est largement supérieure dans l'état HS par rapport à l'état BS.

II.2.b) Transition de spin induite par la pression

L'application d'une pression va favoriser l'état de moindre volume c'est-à-dire l'état BS ou, en d'autre terme, accroître la température de transition. L'action de la pression se traduit par le terme de travail $P\Delta V$ (avec $\Delta V = V_{HS} - V_{BS}$) dans les équations thermodynamiques selon : $\Delta E^0(P) = \Delta E^0 + P\Delta V$, soit : $\Delta G = \Delta H - T\Delta S + P\Delta V$ avec ΔE^0 le gap d'énergie entre état HS et LS à pression atmosphérique. G, H, P et S sont respectivement l'énergie libre de Gibbs, l'enthalpie, la pression et l'entropie.

II.2.c) Transition de spin induite par un champ magnétique

L'application d'un champ magnétique extérieur peut induire une transition de spin magnéto-induite. [Bousseksou 04] Dans ce cas, l'application d'un champ magnétique va stabiliser l'état HS et diminuer la température de transition $T_{1/2}$ vers les basses températures, dû à l'éclatement des niveaux d'énergie par l'effet Zeeman (le terme $-\frac{1}{2}\chi B^2$ est ajouté à l'énergie libre de Gibbs).

II.2.d) Transition de spin induite par irradiation lumineuse

Le phénomène de transition de spin peut être également induit par la lumière (transition de spin photo-induite). La photo-commutation de complexes du Fe(II) à transition de spin, fut rapportée pour la première fois par McGarvey *et al.* en 1982. [McGarvey 82] Cet effet sera attribuable à l'effet LIESST (Light-Induced Excited Spin State Trapping) découvert par Descurtins *et al.* en 1984 qui consiste à piéger le système dans l'état HS métastable par pompage optique à très basse température. [Decurtins 84] Notre équipe a réalisé et rapporté des effets de photo-commutation à température ambiante. [Bonhommeau 05] Le procédé consiste à envoyer un « pulse » de lumière dans la zone métastable à l'intérieur de la boucle d'hystérésis thermique. L'application d'un « pulse » laser peut faire basculer totalement et réversiblement la partie irradiée du composée d'un état à un autre (HS ⇄ BS).

II.3) Les différentes techniques expérimentales pour caractériser un changement d'état de spin

Une transition de spin peut être caractérisée par la fraction molaire ou fraction représentant le nombre de molécules dans l'état HS, notée n_{HS} en fonction des divers paramètres thermodynamiques (T, p, H, ..). Cette fraction n_{HS} peut être mesurée à partir de différentes techniques expérimentales conduisant à des réponses différentes suivant l'état de spin. Le changement d'état de spin est associé ou entraîne des modifications relativement importantes des propriétés physiques du composé. Ainsi, plusieurs voies, plus ou moins directes, sont possibles pour caractériser la transition de spin et déduire plus ou moins directement et facilement la fraction n_{HS} en fonction de la température.

- Les méthodes de mesures de la susceptibilité magnétique statique molaire χ_M en fonction de la température sont le plus souvent utilisées pour caractériser la transition de spin d'un matériau.[König 91, Gütlich 94]

- Une autre méthode expérimentale, plus quantitative est très utilisée pour les complexes de fer, la spectroscopie Mössbauer. Cette méthode résulte de l'absorption sans recul de photons γ provenant d'une source radioactive par la faible quantité d'isotope atomique ^{57}Fe contenu dans le composé étudié.[Greenwood 71]

- Les méthodes cristallographiques, telles que la diffraction des rayons X, permettent d'obtenir des données structurales distinctes suivant l'état de spin, en particulier l'élongation des distances métal-ligand et donc la variation de volume, ainsi que les changements d'angles de la maille cristalline ...

- Deux types de spectroscopie vibrationnelle sont également utilisés, la spectroscopie infrarouge et la spectroscopie Raman. Chaque état de spin peut être caractérisé : les quanta de vibrations de déformation métal-ligand sont systématiquement plus hauts en énergie dans l'état LS que dans l'état HS.

- La spectroscopie électronique par absorption comme la spectroscopie UV-Vis, le nombre de bandes d'absorption permises ainsi que leur longueur d'onde étant différents suivant la configuration électronique et donc d'état de spin.

- D'autres méthodes peuvent être utilisées comme la calorimétrie, la spectroscopie dynamique diélectrique, et la Résonance Paramagnétique Electronique.

II.4) Le besoin de la nano-structuration des matériaux à transition de spin

Pour l'application des matériaux à transition de spin comme dispositifs mémoires ou capteurs il est requis leur mise en forme en couche mince ou en nanoparticules. La nano-structuration de ces composés ouvre la porte à de nombreuses possibilités d'applications. Néanmoins, il faut souligner que la réduction de taille au niveau nanométrique peut entrainer une diminution de la taille des domaines de spin dans le même état, et par conséquent peut affecter le comportement de ces systèmes. Ainsi, l'objectif est d'une part, d'étudier l'effet de réduction de taille sur les propriétés physiques du matériau et d'autres part, de structurer ces composés en réseaux nanométriques, homogènes et périodiques pour des applications en nano-photonique et en nano-électronique. L'état de l'art dans la synthèse et la nano structuration des matériaux à transition de spin est actuellement très avancé. [Bousseksou 2011]

II.5) Tautomères de valence : Introduction

La bistabilité des états électroniques observée pour certains complexes de métaux de transition constitue un domaine important dans le champ de recherche de la chimie de coordination. Les complexes à **transition de spin** et les **tautomères de valence** constituent deux exemples importants et typiques de ce phénomène.

II.5.a) Les analogues du bleu de Prusse (BP)

Les analogues du bleu de Prusse (BP) de formule générale $A_x M^{II}_y [M'^{III}(CN)_6] \cdot n H_2 O$ (où A est un cation alcalin, et M et M' sont des cations de métaux de transition divalents et trivalents,

respectivement) ont fait l'objet d'un très grand intérêt du fait de leurs propriétés magnétiques et photomagnétiques. Certains de ces complexes présentent, en outre, une transition thermique du premier ordre, associée au transfert d'un électron d'un métal à l'autre.

Certaines recherches se sont orientées vers l'étude des possibilités de contrôle des propriétés magnétiques de ces analogues de BP par un stimulus extérieur. Le composé $Na_xCo[Fe(CN)_6]_y \cdot zH_2O$ est un bon exemple qui montre une bistabilité thermique entre la phase à haute température (HT) $Co^{II}(S = 3/2)$–$Fe^{II}(S = 1/2)$ et la phase à basse température (BT) $Co^{III}(S = 0)$–$Fe^{III}(S = 0)$. Son étude montre que l'état électronique stable dépend fortement de la quantité de défauts de $Fe(CN)_6$ et que la transition thermique est due au transfert d'un électron d'un métal à l'autre (figure.2).
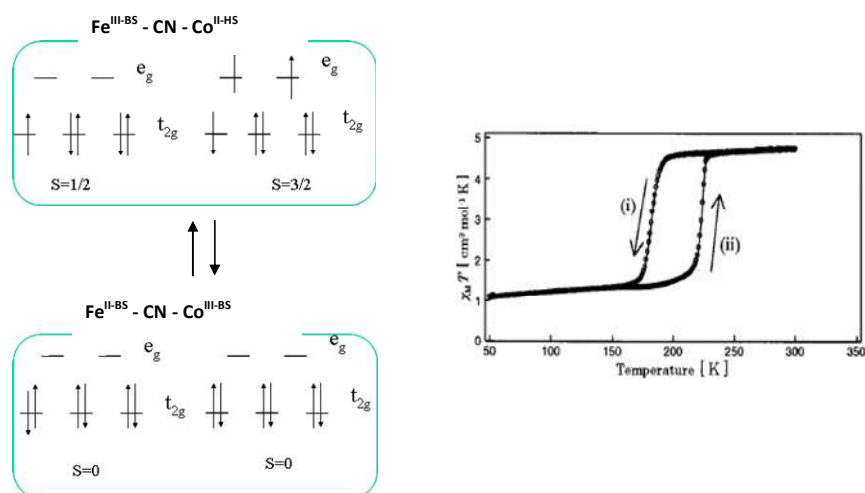

Figure.2 : a) bistabilité des états électroniques et b) propriétés magnétiques du complexe $Na_{0.53}Co_{1.32}[Fe(CN)_6] \cdot 4.4H_2O$.

III) **Matériaux moléculaires bistables : Etudes électriques**

Ce travail de thèse présente une approche originale, non seulement pour l'adressage des matériaux moléculaires bistables par voie électrique, mais aussi pour la lecture de l'information stockée dans les matériaux moléculaires bistables à l'échelle nanométrique. A cet effet, nous avons étudié les propriétés de transport des complexes de coordination (**$Rb_xMn[Fe(CN)_6]_y \cdot zH_2O$**, **$Na_xCo[Fe(CN)_6]_y \cdot zH_2O$**, **$Co_3[W(CN)_8]_2(pyrimidine)_4 \cdot 6H_2O$** et

{Fe(HB(pz)₃)₂}) et nous avons pu mettre en évidence une commutation entre leurs deux états bistables par l'application d'un champs électrique.

III.1) Transport de charge dans les tautomères de valence.

Nous avons étudié le transport de charges dans les tautomères de valence $Rb_xMn[Fe(CN)_6]_y.zH_2O$, $Na_xCo[Fe(CN)_6]_y.zH_2O$ et $Co_3[W(CN)_8]_2(pyrimidine)_4 \cdot 6H_2O$ pour différentes stœchiométries. Le large domaine de bistabilité thermique nous a permis d'étudier le transport de charge des deux phases tautomèriques dans des conditions expérimentales identiques. Généralement nous avons observé que :

- La dépendance fréquentielle de la conductivité suit la même loi que celle des solides désordonnés.
- Pour des températures élevées, la conductivité (dans le régime continue) à un comportement gouverné par la loi d'Arrhenius.

Dans le cas du composé $Rb_xMn[Fe(CN)_6]_y.zH_2O$ nous avons obtenu des résultats très intéressantes par rapport aux autres composés étudiés. Nous avons conclu que :

- La relaxation dipolaire est thermiquement activé (figure 4), la valeur de l' énergie d'activation est identique à celle de la conductivité ($E_a(\sigma T) \approx E_a(\omega) \approx 0.55$ eV).

- Nous avons attribué **le saut de petits polarons** comme mécanisme pour la conductivité électrique (transfert d'électron entre les deux centres métalliques : Mn^{2+}-NC-$Fe^{3+} \leftrightarrow Mn^{3+}$-NC-$Fe^{2+}$).

- L'ensemble des résultats expérimentaux ont bien été reproduit par l'équation $\sigma_{dc} = (n_c e^2 a^2/6k_B T)\nu_p$; n_c, a, k_B, T, υ_p sont respectivement la densité des paires de centres métalliques, la distance ente centres, la constante de Boltzmann, la température et la fréquence de saut.

L'allure de la transition de phase dans les tautomères de valence correspond bien à l'hystérésis thermique de la conductivité électrique mesuré (figure 3). Cependant, le mécanisme de la conductivité varie avec la température. Il est thermiquement activé pour les

hautes températures et gouverné par l'effet tunnel pour les basses températures. A partir des études sur les échantillons qui ne présentent pas de transition de phase, nous pouvons conclure sans ambiguïté que les deux phénomènes, la transition de phase et le changement de mécanisme de la conductivité sont indépendants. Le fait qu'ils se produisent dans la même gamme de température pour certains échantillons n'est que pur hasard. En fait, la transition de phase ne modifie ni le mécanisme du transport, ni celui de la relaxation diélectrique, mais fait varier la conductivité et le taux de relaxation. Étonnamment, l'énergie d'activation de la conductivité a été trouvée assez similaire dans les deux phases (HT et BT) dans le cas des composés $Rb_xMn[Fe(CN)_6]_y z \cdot H_2O$ mais est légèrement différente dans les deux phases des composés $Na_xCo[Fe(CN)_6]_y.zH_2O$ et $Co_3[W(CN)_8]_2(pyrimidine)_4 \cdot 6H_2O$. D'autre part, le taux de transfert de charge et par conséquence la conductivité est plus élevée dans la phase BT. Cette différence correspond au facteur pré-exponentiel de la fréquence de saut, qui est lié à la forte contraction du réseau lors de la transition de phase HT $\rightarrow$ BT.
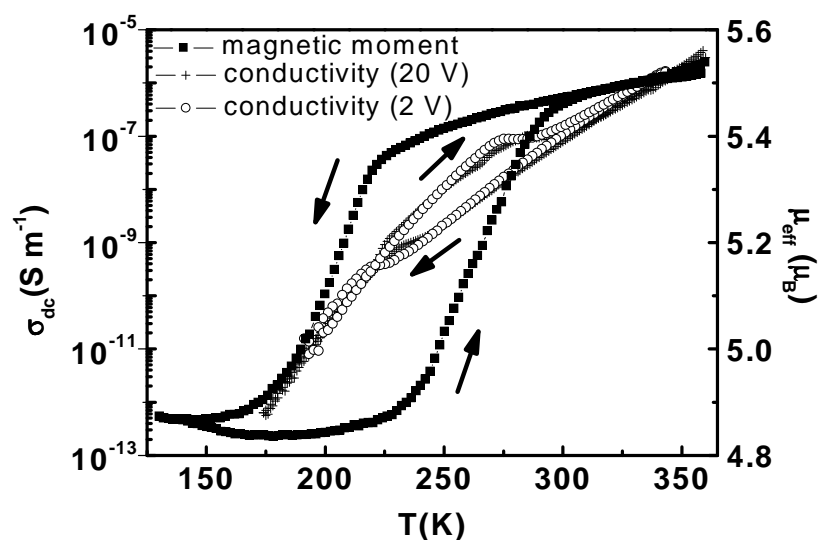

Figure.3 : Dépendance thermique de la conductivité dc (mesuré à 2 et 20 V) et moment magnétique effectif du composé $Rb_{0.76}Mn[Fe(CN)_6]_{0.91}.1.6H_2O$.
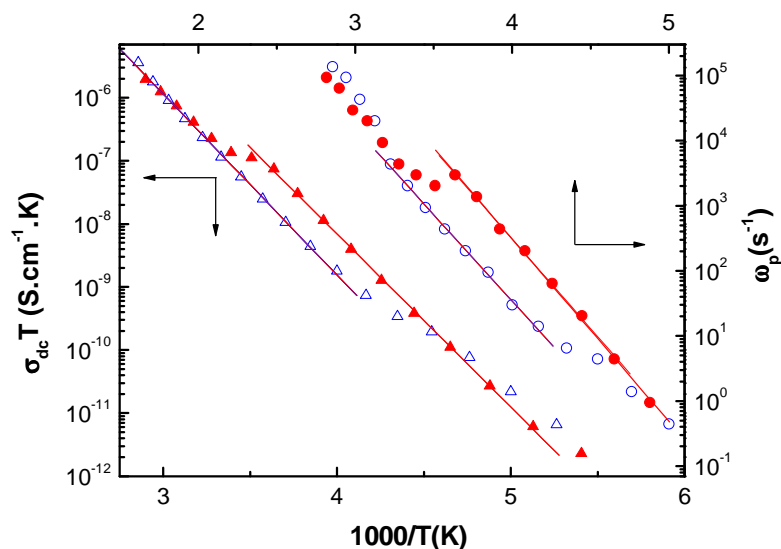
Figure.4 : Dépendance thermique de la conductivité dc (triangles) et fréquences de relaxation de la conductivité (cercles). Les symboles ouverts correspondent au mode refroidissement et les symboles fermés correspondent au mode chauffage.

III.2) Adressage électrique des matériaux moléculaires bistables

Nous avons déjà vu que le phénomène de transition de spin ainsi la transition de phase induite par le transfert de charge (tautomère de valence) peut être induit par la température, une pression, un champ magnétique ou une irradiation lumineuse. Suite à l'étude des propriétés électriques des tautomères de valence et des composés à transition de spin, nous avons cherché à étudier une transition éventuellement induite par un champ électrique statique conduisant à l'adressage électrique de ces matériaux.

Après une série d'expériences nous avons réussi à mettre en évidence une transition de phase dans la famille des tautomères de valences par application d'un champ électrique statique. Pour un champ électrique d'environ 1.2 kV/mm autour de la température ambiante et à l'intérieur du cycle d'hystérésis, nous avons pu commuter irréversiblement les composés étudiés de la phase haute température vers la phase basse température (figure 5). Malgré tout, le processus inverse (de la phase basse température vers la phase haut température) est possible en chauffant le matériau par effet Joule.
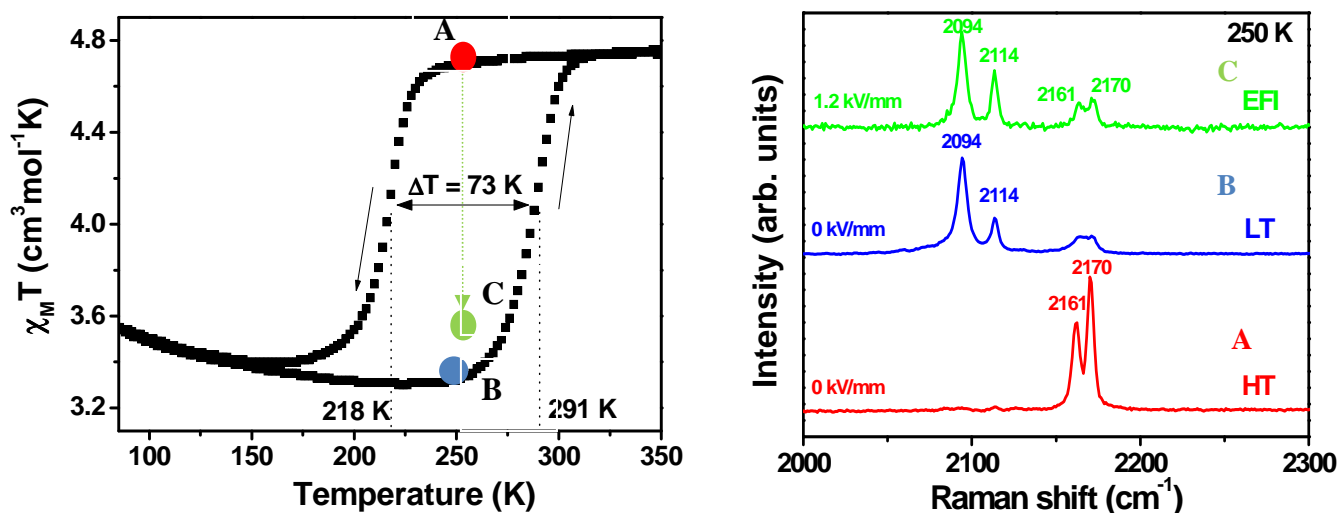
Figure.5 : Propriétés magnétiques du complexe $Rb_{0.8}Mn[Fe(CN)_6]_{0.93}\cdot1.62H_2O$ (à gauche). La flèche en pointillée montre l'effet de l'application d'un champ électrique de 1.2 kV/mm. Spectres Raman du même composé enregistrés à 250 K dans l'état HT et l'état BT sans application du champ électrique et après application d'un champ électrique de 1.2 kV/mm dans la branche descendante du cycle d'hystérésis (à droite).

Nous avons proposé une transition de phase paraélectrique à ferroélectrique comme mécanisme pour expliquer nos observations dans cette famille de composés (tautomères de valence). En effet, l'application d'un champ électrique favorise la phase BT par déplacement de la température de transition vers les hautes températures par le terme : $\Delta T_{eq} = \dfrac{p^2 E^2}{\Delta H(0)}$ avec p le moment dipolaire électrique, E le champ électrique appliqué et H l'enthalpie.
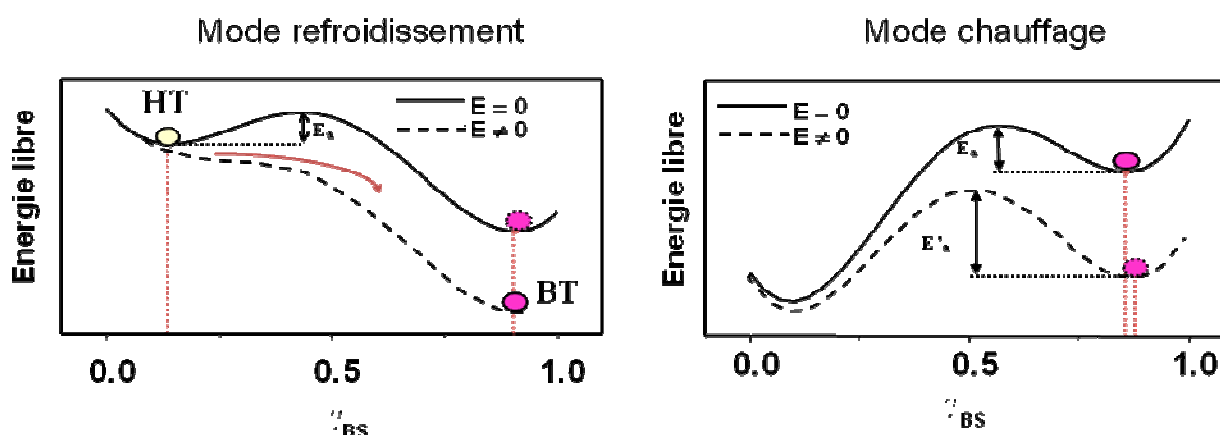

Figure.6 : Dépendance en champ électrique de l'énergie libre (F) en fonction de la fraction de la forme basse température (BT). L'application d'un champ électrique favorise toujours l'état basse température.

III.3) De la molécule vers les dispositifs électroniques

Dans le cadre de cette thèse nous avons observé que le complexe [Fe(HB(pz)$_3$)$_2$] possède une propriété remarquable : il présente une transition thermique irréversible. La variation thermique du moment magnétique ainsi que les propriétés électriques sont irréversibles. La partie réelle de la conductivité change de quatre ordres de grandeur. Cette propriété intéressante nous a encouragé à étudier les couches minces de ce composé dans le but de l'utiliser comme dispositif de mémoire électronique. La lecture et l'enregistrement de l'information stockée dans ce matériau moléculaire bistable sont envisagés par voie électrique (figure.7). L'enregistrement est basé sur le chauffage indirect ou direct du matériau par effet Joule.

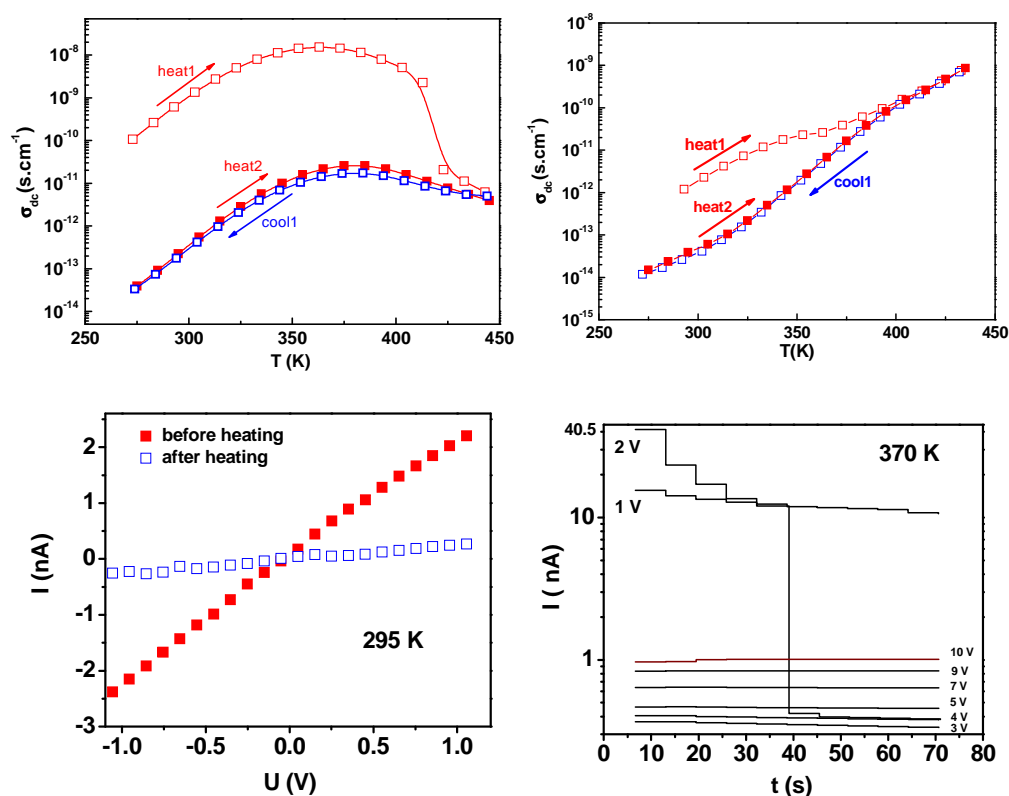*Figure.7 : Les figures du haut présentent la dépendance thermique de la conductivité électrique (conductivité σ' enregistré à 10 mHz pour deux cycles thermiques) du complexe [Fe(HB(pz)$_3$)$_2$] (gauche) et de la couche mince (droite). Les figures du bas sont des mesures I(V) sur le film de [Fe(HB(pz)$_3$)$_2$] qui démontrent la possibilité d'utiliser ces couches minces pour fabriquer une mémoire électronique non volatile (ROM).*

IV) Détection de la transition de spin dans des couche ultra-minces à l'aide des plasmons de surface

IV.1) Résonance des plasmons de surface (RPS)

Lorsqu'un matériau interagit avec une onde électromagnétique, un couplage fort entre cette onde et la polarisation induite locale de ce matériau peut se produire. Cette excitation couplée est appelée polariton. Dans un métal, le couplage se produit avec les oscillations électroniques collectives et quantifiées. On utilise alors le terme de plasmon-polariton ou plus simplement plasmon. En effet, pour qu'un couplage entre les plasmons de surface et la lumière puisse être observé, il faut que la condition dite de couplage soit satisfaite. Cette condition s'exprime très simplement par l'égalité entre la norme du vecteur d'onde des plasmons de surface k_{ps} et la projection dans le plan de la surface du vecteur d'onde k_x de la lumière incidente.

Il existe principalement 2 types de coupleurs permettant de réaliser la condition de couplage :
- Le prisme
- Le réseau de diffraction
Dans ce travail de thèse nous avons utilisé le prisme comme coupleur.

Lors du passage de la lumière à travers un prisme, si l'angle d'incidence est supérieur à l'angle critique (θ_c dans la figure 8) défini par la loi de Snell, une réflexion interne totale (RIT) est observée. L'onde réfractée ne peut plus se propager et il y a apparition d'un champ évanescent à l'interface prisme-milieu extérieur. Ce champ est qualifié d'évanescent, car son amplitude décroît exponentiellement suivant l'axe z perpendiculaire à l'interface. Dans le cas où le prisme est recouvert d'une couche métallique (Au Ag …), le phénomène de réflexion interne totale se produit également. Si l'épaisseur de cette couche métallique est suffisamment faible, alors l'amplitude du champ associée à l'onde évanescente sera encore suffisamment importante au niveau de la seconde interface métal/milieu extérieur. Le champ évanescent pourra alors se coupler avec les plasmons de surface présents à l'interface métal/milieu extérieur, sous réserve que la condition de couplage soit satisfaite. En effet, pour un angle

d'incidence particulier, que nous appellerons angle de résonance (θ_0 dans la figure 8), il pourra y avoir égalité entre la composante longitudinale du vecteur d'onde du champ évanescent et le vecteur d'onde du plasmon. Ce couplage se manifestera par un minimum sur la courbe de réflectivité du à l'absorption de l'énergie par le métal, énergie qui pourra se propager sous forme de plasmon de surface à l'interface entre le métal et le milieu extérieur. Ce phénomène est appelée réflexion totale atténuée (RTA).
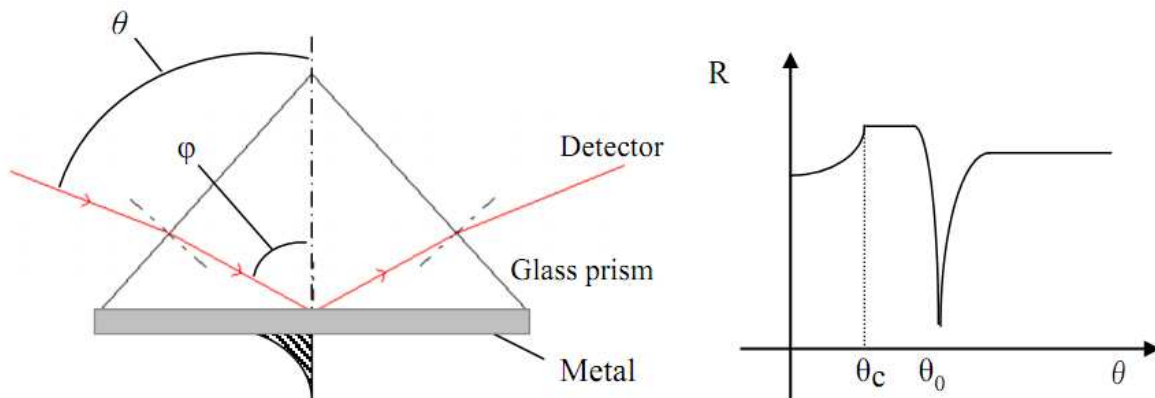

Figure.8 : Schéma explicatif du principe d'excitation de plasmon de surface selon la configuration de Krechmann.

IV.2) Simulation théorique

En utilisant les équations de Fresnel, nous avons étudié théoriquement la possibilité de détecter la transition de spin dans des couches minces à l'aide de la résonance des plasmons de surface. Nous montrons que cette technique peut détecter des variations d'indice optique associées à la bistabilité même pour des couches ultra-minces (<10 nm).

IV.3) Caractérisation des couches minces par RPS

L'échantillon étudié est formé du composé [Fe(pyrazine) Pt(CN)$_4$] déposé sur une couche de titane/or (5/50 nm). Le titane permet l'accroche de l'or sur le verre. Cette géométrie est à prendre en compte dans les simulations de spectres. Les couches minces à transition de spin ont été élaborées par une méthode d'assemblage multicouche séquentiel. [Bartual 11]
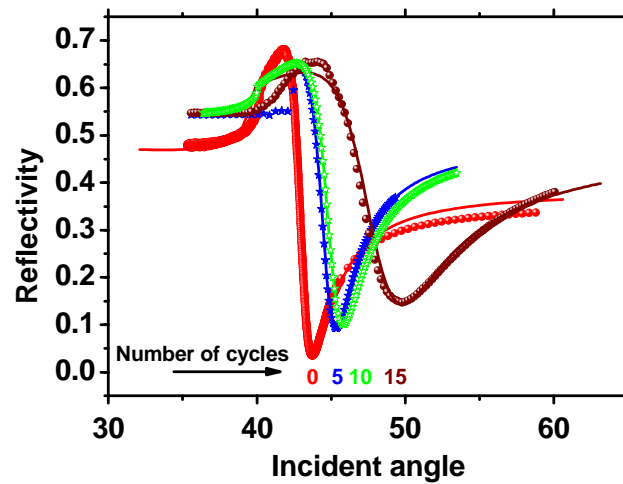
Couche mince : {Fe(pyrazine)[Pt(CN)$_4$]}	SPR			AFM	Epaisseur théorique (nm)
	Epaisseur (nm)	n	k	Epaisseur (nm)	
5 cycles	4,8 ± 0,2	1,6 ± 0,02	0,06 ± 0,01	3,8 ± 0,7	3,9
10 cycles	6,5 ± 0,2	1,6 ± 0,02	0,06 ± 0,01	8 ± 2	8,5
15 cycles	15,0 ± 0,2	1,6 ± 0,02	0,07 ± 0,01	12 ± 2	12,3

Figure.9 : Courbes RPS expérimentales et ajustements théoriques. Le tableau rassemble les données expérimentales mesurées par AFM (microscopie à force atomique) et RPS qui sont comparées aux valeurs théoriques.

Ce résultat expérimental montre que la RPS est une technique puissante non seulement pour mesurer les épaisseurs des couches minces mais aussi pour déterminer les constantes optiques du matériau étudié.

IV.4) Détection de la transition de spin dans les couches minces par SPR

La température a un effet sur les indices de réfraction des matériaux. Cependant dans le domaine d'étude thermique qui nous intéresse, la variation d'indice de réfraction du prisme est négligeable. La variation de l'absorption de l'or est aussi nulle, mais son indice de réfraction n_{Au} varie de $\Delta n_{Au} = 0,05$ sur 100 °C.

Pour vérifier l'influence de ce changement d'indice sur les courbes plasmoniques, une simulation a été réalisée. Elle consiste à étudier le système : prisme (BK7) - Ti 5 nm - Au 45 nm
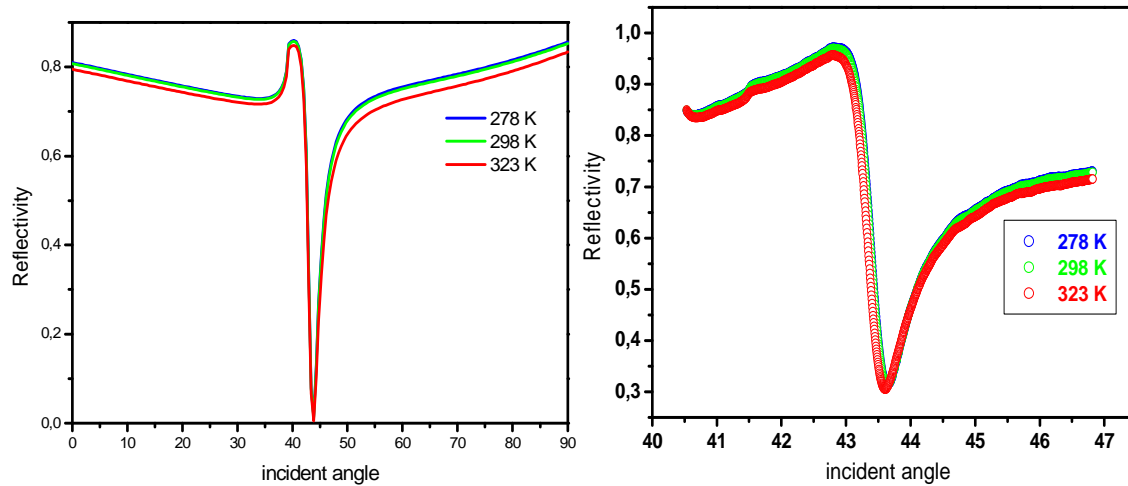

Figure.10 : simulations théoriques et courbes RPS expérimentales qui montrent l'influence de la température sur notre capteur plasmonique.

D'après ces résultats nous avons pu confirmer que la réponse de l'ensemble du capteur (prisme + couche Au/Ti) est stable avec la température et n'aura donc aucune influence sur les mesures des composés dans cette gamme de température.

Comme nous avons déjà indiqué dans la première partie, une transition de spin peut être provoquée par variation de la température du matériau. Ainsi en suivant la variation thermique du minimum de la courbe de réflectivité, nous pouvons suivre la variation de l'indice de réfraction du matériau déposé.

La figure 11 montre le résultat de l'étude expérimentale réalisée sur une couche mince de 50 nm du composé $[Fe(hptrz)_3](OTs)_2$. Entre 305 à 320 K, le matériau est dans l'état bas spin et l'angle de résonance plasmon varie de façon linéaire avec la température. De 320 à 330 K, la linéarité de la courbe est rompue car le phénomène de transition de spin se superpose à la variation thermique. Enfin, de 330 à 345 K, la variation de l'angle de résonance plasmon redevient linéaire, mais avec des coefficients de linéarité différents, le matériau est dans l'état haut spin. La transition de spin du matériau se situe donc autour de la température ambiante (~ 325 K). Le positionnement de la température de transition est en accord avec les autres

mesures expérimentales sur ce matériau. D'autre part, la présence de la discontinuité confirme que le changement d'indice de réfraction non - linéaire est bien lié à la transition de spin et non à d'autres phénomènes physiques.
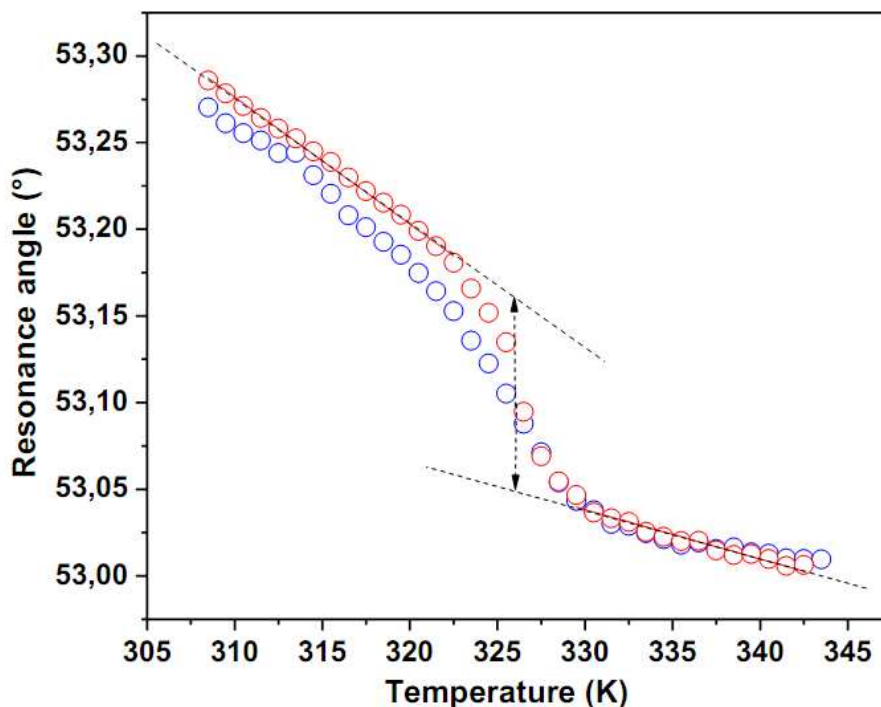

Figure.11 : Suivi de la résonance plasmon : angles de résonance expérimentales en fonction de la température (rouge : chauffage, bleu : refroidissement), pour un système BK7, 5nm Ti, 45 nm Au, 50 nm composé [Fe(hptrz)₃](OTs)₂, air.

Ces résultats ouvrent de sérieuses perspectives pour l'intégration des complexes à transition de spin dans des dispositifs photoniques dont l'objectif est leurs possibles applications comme capteurs ou dispositifs optiques adressables.

V) Conclusion générale

L'objectif du présent travail a été d'étudier les propriétés électriques et optiques des complexes moléculaires bistables tels que les composés à transition de spin ou tautomères de valence dans lequel une commutation entre deux états électroniques peut être induite par différents perturbateurs externes (température, pression, champ magnétique, de lumière, ...). Des études récentes ont révélé que ces composés sont susceptibles d'avoir une variation importante de leur constante diélectrique (ε) dans une large gamme de fréquences ($\varepsilon_0 \rightarrow \varepsilon_\infty$). Les objectifs de

notre recherche ont été inspirés par cette dernière propriété remarquable. Deux questions principales ont été abordées dans le cadre de cette thèse:

- Est-il possible d'induire la transition de spin de ces composés bistables par application d'un champ électrique externe?

- Est- il possible d'utiliser la commutation de la permittivité électrique (ε^*) de ces matériaux pour détecter la transition de spin à l'échelle nanométrique ?

Pour la première question, nous nous sommes focalisés sur les tautomères de valence (les analogues de bleu de prusse RbMnFe et NaCoFe et le complexe bimétallique Co-W). Nous avons étudié par la spectrométrie Raman sous champ électrique trois composés qui appartiennent à la famille des tautomères de valences. Ces études nous ont amené à des résultats très marquants. Nous avons démontré expérimentalement la possibilité d'adressage des matériaux moléculaires bistables par voie électrique autour de la température ambiante et à l'intérieur du cycle d'hystérésis thermique. Nous avons montré que l'application du champ électrique favorise toujours la phase basse température. Nous avons proposé un mécanisme pour expliquer ce phénomène : la stabilisation de la phase basse température sous l' effet d'un champ électrique est relié à une transition paraélectrique-ferroélectrique.

Dans le cadre des études électriques, nous avons étudié les propriétés de transport des complexes de coordination $Rb_xMn[Fe(CN)_6]_y \cdot zH_2O$, $Na_xCo[Fe(CN)_6]_y \cdot zH_2O$, $Co_3[W(CN)_8]_2(pyrimidine)_4 \cdot 6H_2O$ et $\{Fe(HB(pz)_3)_2\}$:

- Nous avons observé un transfert de charge caractéristique des solides désordonnés et nous avons conclu que le transport de charge dans ces composés se produit par sauts de petits polarons correspondant aux transferts d'électrons intermétalliques. Le processus de relaxation dipolaire a une énergie d'activation thermique équivalente à celle de la conductivité.

- Nous avons conclu que la transition dans les tautomères de valence ne modifie pas le mécanisme de transport de charge, mais module légèrement la conductivité ainsi le taux de relaxation diélectrique. A partir du mécanisme de transport proposé, les changements de conductivité, qui sont relativement faibles (un ordre de grandeur), sont liés à la variation des fréquences des phonons associée à la transition de phase des tautomères de valence.

Ce travail de thèse présente une approche originale, non seulement pour l'adressage des matériaux moléculaires bistables par voie électrique, mais aussi pour la lecture de l'information stockée dans les matériaux moléculaires bistables à l'échelle nanométrique par voie électrique ou optique.

Pour la deuxième question posée, nous avons étudié théoriquement et expérimentalement la possibilité de détecter cette commutation dans des couches minces à l'aide de la résonance des plasmons de surface. Nous montrons que cette technique peut détecter des variations d'indice optique associées à la bistabilité même pour des couches ultra-minces (<10 nm). Par exemple dans le cas d'une couche mince du complexe $[Fe(hptrz)_3](OTs)_2$ de 50 nm, nous avons détecté la transition de spin autour de 325 K.

Ces résultats représentent une étape très importante pour la compréhension de l'effet de réduction de taille dans les matériaux moléculaire bistables et ouvrent de sérieuses perspectives pour l'intégration des complexes à transition de spin ou à transfert de charge dans des nano-circuits électriques et des dispositifs photoniques dont l'objectif est leurs possibles applications comme mémoire, capteurs ou dispositifs optiques adressables.

VI) Articles liés à cette thèse

- G. Molnár, S. Cobo, <u>T. Mahfoud</u>, et al, Interplay between the charge transport phenomena and the charge-transfer phase transition in $Rb_xMn[Fe(CN)_6]_y.zH_2O$, **J. Phys. Chem. C** 133 (2009), 2586.

- Tarik Mahfoud, et al, Electric-Field-Induced Charge-Transfer Phase Transition: A Promising Approach Toward Electrically Switchable Devices, **J. Am. Chem. Soc,** 131 (2009), 15049.

- L. Salmon, G. Molnár, S. Cobo, T. Mahfoud, et al. Re-investigation of the spin crossover phenomenon in the ferrous complex [Fe(HB(pz)$_3$)$_2$)], **New J. Chem**, 33 (2009), 1283.

- Carlos Bartual-Murgui, Lionel Salmon, Amal Akou, Christophe Thibault, Gabor Molnar, Tarik Mahfoud, Zouheir Sekkat, Jose Antonio Real and Azzedine Bousseksou, high quality nano-patterned thin films of the coordination compound {Fe(pyrazine)[Pt(CN)$_4$]} deposited layer-by-layer, **New J. Chem**., (2011), DOI:10.1039/c1nj20212j.

- T. Mahfoud, et al. Thin films of the [Fe(HB(pz)$_3$)$_2$] spin crossover complex: electrical properties and non-volatile memory effect, **Appl. Phys. Lett.** soumis.

VII) Références

[Bartual 11] C. Bartual-Murgui, L. Salmon, A. Akou, C, Thibault, G. Molnar, T. Mahfoud, Z. Sekkat, JA. Real, A. Bousseksou, *New J. Chem*., (2011), DOI:10.1039/c1nj20212j.

[Bonhommeau 05] S. Bonhommeau, G. Molnár, A. Galet, A. Zwick, J.A. Real, J.J. McGarvey, A. Bousseksou, *Angew. Chem. Int. Ed*. 44, **2005**, 4069.

[Bousseksou 03] A. Bousseksou, G. Molnár, P. Demont, J. Menegotto, *J. Mater. Chem. 13*, **2003**, 2069.

[Bousseksou 04] A. Bousseksou, F. Varret, M. Goiran,K. Boukheddaden, J. –P. Tuchagues, *Top. Curr. Chem,* 235, **2004**, 65.

[Bousseksou 11] A. Bousseksou, G. Molnar, L. Salmon, W. Nicolazzi, Chem. Soc. Rev, 40, **2011**, 3313.

[Decurtins 84] S. Decurtins, P. Gütlich, C. P. Köhler, H. Spiering, A. Hauser, *Chem. Phys. Lett. 105*, **1984**,1.

[Ohkoshi 30] S.-I. Ohkoshi, H. Tokoro, K. Hashimoto, *Coord. Chem. Rev.*, 249, 2005, 1830.

[Greenwood 71] M. N. Greenwood, T. G. Gibb, *Mössbauer Spectroscopy*, **1971**, Chapman and Hall Ltd, London.

[Gütlich 04] P. Gütlich, H. A. Goodwin, *Top. Curr. Chem.* 233, **2004**, 1.

[König 91] E. König, "Nature and dynamics of the spin-state interconversion in metal complexes", in Struct. Bonding, *Springer-Verlag, Berlin Heidelberg New York*, 76,**1991**, 51.

[McGarvey 82] J. J. McGarvey, I. Lawthers, *J. Chem. Soc., Chem. Comm*, **1982**, 906.